Acta Materialia xxx (2017) 1–80

Contents lists available at ScienceDirect

Acta Materialia

journal homepage: www.elsevier.com/locate/actamat

By invitation only: overview article

Twinning-induced plasticity (TWIP) steels

Bruno C. De Cooman [a, *], Yuri Estrin [b, c], Sung Kyu Kim [d]

[a] Graduate Institute of Ferrous Technology, Pohang University of Science and Technology, Pohang, Republic of Korea
[b] Department of Materials Science and Engineering, Monash University, Clayton, Australia
[c] Laboratory of Hybrid Nanostructured Materials, NUST MISiS, Moscow, Russia
[d] POSCO Technical Research Laboratories, Gwangyang, Republic of Korea

ARTICLE INFO

Article history:
Received 14 February 2017
Received in revised form
19 June 2017
Accepted 21 June 2017
Available online xxx

Keywords:
Mechanical twinning
Dislocation glide
High manganese steel
Stacking fault energy
Strain hardening

ABSTRACT

This article reviews original work and important new developments in the field of deformation behavior of high manganese face-centered cubic γ-Fe alloys. Owing to their exceptional mechanical properties, these alloys, referred to as twinning-induced plasticity, or TWIP, steels, have come to the fore as prime candidate materials for light-weight applications, notably in automotive, shipbuilding, and oil and gas industries. It is established that a superior combination of strength and ductility exhibited by TWIP steels is associated with a specific character of the variation of the dislocation density. The defining feature of TWIP steels is the small magnitude of the intrinsic stacking fault energy. In addition to limiting the dynamic recovery rate, the low stacking fault energy of TWIP steels results in the formation of isolated stacking faults and deformation twins, which reduces the dislocation mean free path. Both effects lead to an increased strain hardening rate. Despite the progress made, there are still considerable differences between the models proposed for the microstructural evolution during the deformation of TWIP steels and the concomitant strain hardening behavior. The review surveys the experimental literature, summarizes the current modeling concepts, and identifies the outstanding issues with TWIP steels that require the attention of the materials science community. Suggestions for the directions of future research on twinning-induced plasticity steels are offered.

Contents

* Corresponding author.
E-mail address: decooman@postech.ac.kr (B.C. De Cooman).

http://dx.doi.org/10.1016/j.actamat.2017.06.046
1359-6454/

Please cite this article in press as: B.C. De Cooman, et al., Twinning-induced plasticity (TWIP) steels, Acta Materialia (2017), http://dx.doi.org/10.1016/j.actamat.2017.06.046

1. Introduction

Some iron alloys and steels have impressive plasticity-enhancing potential, which is not yet fully exploited in engineering applications, as it requires a thorough understanding of the underlying mechanisms and their activation during straining. This necessitates an approach to steel design incorporating a selection of composition, microstructure, and processing parameters based on sound theoretical principles. Most formable ferritic steels exhibit uniform engineering elongation less than 25% and relatively low ultimate tensile strength ($\ll$1 GPa). The formability of these steels is based on the control of their crystallographic texture, rather than the strain hardening. As a consequence, higher strength is usually achieved at the cost of ductility. There is a way to resolve this conflict of properties, though: by designing fully austenitic steels or austenite-containing multi-phase steels with an enhanced strain hardening rate, both high strength and good formability can be achieved. Twinning-induced plasticity, or TWIP, steels belong to this category of ferrous alloys. They are characterized by a high strain hardening, large uniform elongation and high ultimate tensile strength levels. These properties make them candidate light-weighting materials for large scale use in the automotive industry, LNG-shipbuilding, oil-and-gas exploration and non-magnetic structural applications. The rapid progress made in the fundamental understanding of the mechanical behavior of TWIP steels is a result of a tremendous global research effort. It is a convincing illustration of what materials research can achieve through consequent use of computational thermodynamics and first principle calculations. The experimental analysis of the properties of TWIP steels has also profited from the use of advanced techniques for microstructural characterization of materials, such as synchrotron X-ray diffraction, electron backscattering diffraction, 3D atom probe tomography, and micromechancial testing methods (nano-hardness, micro-pillar testing). Finally, a more sophisticated analysis of the results of standard macroscopic mechanical tests involving the strain rate and temperature dependence of the mechanical properties has contributed to a better understanding of the mechanisms underlying strength and plasticity of TWIP steels. In this article, a historical overview and an assessment of the current state of our understanding of the mechanical properties of TWIP steels are given.

The ground breaking contributions of Grässel et al. [1–4] and Frommeyer et al. [5] to the science of Fe-Mn-Si-Al TWIP steels with a very low carbon content (<100 ppm) prompted a global research effort aimed at developing a better understanding of the plasticity-enhancing mechanisms which are activated during the plastic deformation of these steels and similar C-alloyed high Mn face-centered cubic (fcc) γ-Fe. Grässel and Frommeyer observed that large scale deformation twinning occurred in a TWIP steel when its Mn content was larger than 25%, the Al content was in excess of 3%, and the Si content was in the range of 2–3% (by weight). A very favorable strength-ductility balance was attained. An important quantity that characterizes this balance is the product of the ultimate tensile strength and the total elongation (UTS $\times$ TE value, or $R_m \times A$ value, in European publications). A very large value of this quantity in excess of 50,000 MPa $\times$ %, resulting mainly from an

Please cite this article in press as: B.C. De Cooman, et al., Twinning-induced plasticity (TWIP) steels, Acta Materialia (2017), http://dx.doi.org/10.1016/j.actamat.2017.06.046

extremely large total tensile elongation of 80%, was reported.

Contemporary TWIP steels exhibit high ultimate tensile stresses paired with exceptionally large tensile elongations (60%) over a wide range of strain rates (10^{-3}-10^{3} s^{-1}). The importance of TWIP steels as breakthrough structural materials cannot be underestimated as the TWIP steel concept has also opened up the possibility of creating new steel grades with a very wide range of properties. These developments have already been addressed in the literature [6–8]. The present review aims at critically evaluating our current understanding of TWIP steels and accounting for the most recent developments in this area. The review focusses on the *strain hardening behavior* of TWIP steels, as a better understanding of many aspects of this fundamental property has evolved in the recent years, which makes it necessary to review its defining role in the strength and plasticity enhancement in TWIP steels. Other aspects of the mechanical performance of TWIP steels are also discussed in relation to their strain hardening behavior.

2. Strain hardening of TWIP steels – phenomenology and early models

2.1. The taxonomy of strain hardening stages

Figs. 1 and 2 illustrate an exceptional strength-ductility combination of TWIP steels, as exemplified by 18%Mn-0.6%C-1.5%Al TWIP steel, by comparing its properties with those of Ti-stabilized interstitial-free (Ti-IF) ferritic steel. The latter is considered as one of the most formable industrial steel grades. The formability of these steels is controlled by their crystallographic texture, their grain size and the presence of precipitates. The development of a pronounced ND//⟨111⟩ fiber texture results in an improved formability and some limited texture hardening. Higher levels of strength attained through grain size reduction and precipitation hardening are always achieved at the cost of ductility. The stress-strain curves of Ti-IF and TWIP steel are presented in Fig. 2 in terms of engineering (s,e) and true (σ,ε) stresses and strains, respectively. It is obvious that compared to the Ti-IF steel, the TWIP steel exhibits a higher strain hardening rate (defined throughout this paper as the slope of a stress-strain curve, $d\sigma/d\varepsilon$), larger uniform elongation ε_u, and a greater ultimate tensile strength. It also has a relatively low yield strength and shows virtually zero post-uniform elongation. In addition, some serrations are visible on the stress-strain curve at large strains. Due to its relation to dynamic strain aging, this region of the stress-strain curve is designated as DSA. The superior forming properties of specific TWIP steels, such as the Fe-18%Mn-0.5%C-1.5%Al TWIP steel, have already been reviewed in great detail [9]. In fact, this class of highly ductile, high or ultra-high strength steels has been the subject of a substantial effort aimed at their commercial development. In the case of automotive materials, the main motivation for current research into the development of high-performance Fe-Mn-Al-C TWIP steel is the expectation that it can offer ultra-high strength for structural reinforcement, a superior ductility for the ease of press forming, and a great energy absorption capability for improved crashworthiness, which is crucial for a vehicle. In addition, their large scale use will result in a reduction of a vehicle's mass, a lowering of greenhouse gas emissions, a drastic increase of gas mileage, and an improvement of passenger safety.

The alloy content of TWIP steels is typically 15–30% Mn, 0–1% C, 0–3% Al, and 0–3% Si. Secondary alloying additions include Cr, Cu, N, Nb, Ti and/or V. The composition critically influences the magnitude of the stacking-fault energy of TWIP steels – a quantity that will be shown to be decisive for their special mechanical properties. The intrinsic stacking fault energy of TWIP steels, γ_{isf}, is commonly in the range of 15–45 mJm^{-2} at room temperature. In this γ_{isf}-range, deformation twinning is activated during deformation. A subtle interaction between glide dislocations, grain boundaries, wide stacking faults, and deformation twins results in a sustained high strain hardening during deformation. Strain hardening rates as high as G/20, where G is the shear modulus, large uniform elongations, and high ultimate tensile strength levels have been reported. In this section, we present experimental facts and theoretical considerations that contribute to a current picture of the deformation processes in TWIP steels, in which deformation twinning plays an important role.

Assessing the contribution of the twinning mode to strain, Qin [10] showed that the contribution of twinning to the overall strain in TWIP steels depends on the twin volume fraction and the crystallographic texture. Assuming that twinning was the only deformation mode, and considering the twinning shear to be given by $\frac{b_{<112>}}{d_{\{111\}}} = \sqrt{\frac{3}{6}} = 0.707$, where $b_{<112>}$ and $d_{\{111\}}$ denote the atomic spacing in the crystallographic direction $<112>$ and the distance between the crystallographic planes $\{111\}$, respectively, Qin estimated that the true strain resulting from twinning was less than 0.15. This figure is much lower than the uniform true strain for

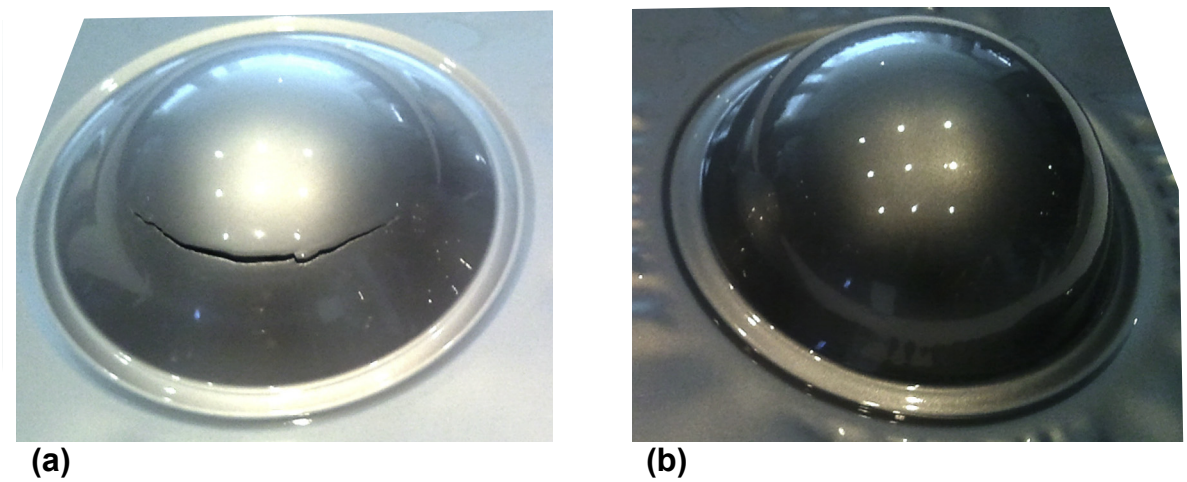

Fig. 1. Comparison of a bulge test carried out on (a) Ti-stabilized interstitial-free (IF) ferritic steel and (b) austentic Fe-18%Mn-0.6%C-1.5%Al TWIP steel. The TWIP steel is still undamaged at a dome height that is 31% larger than the IF steel dome height at failure.

Please cite this article in press as: B.C. De Cooman, et al., Twinning-induced plasticity (TWIP) steels, Acta Materialia (2017), http://dx.doi.org/10.1016/j.actamat.2017.06.046

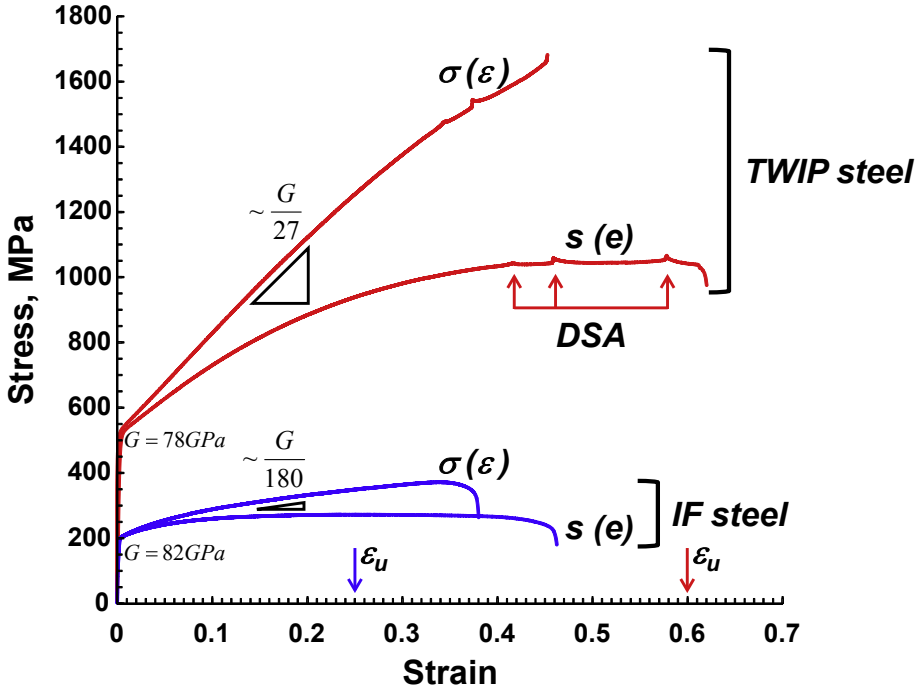

Fig. 2. Comparison of the uniaxial tensile stress-strain curves for a Ti-stabilized interstitial-free (IF) ferritic steel (bcc crystal structure) and an austentic Fe-18%Mn-0.6%C-1.5%Al TWIP steel (fcc crystal structure), illustrating a considerable difference in mechanical properties resulting from the more than six times larger strain hardening rate of the TWIP steel as compared to the IF steel.

TWIP steel, which is typically larger than 0.5. As the volume fraction of mechanical twins is typically in the range of 0.1–0.2, the contribution of mechanical twinning to plastic strain for TWIP steel does not exceed 3%. This implies that the plastic flow of a TWIP steel is dominated by dislocation glide, whilst the deformation twins have a secondary, albeit very important, effect on the mechanical properties. As will be shown below, the positive influence of deformation twinning on the mechanical performance of TWIP steels is chiefly through its effect on the evolution of the dislocation density.

The deformation curve of fcc metals is dominated by stage III hardening, and polycrystalline TWIP steels are no exception to that. In the Kocks-Mecking-Estrin one internal variable model [11] the description of stage III strain hardening is based on the evolution of the average dislocation density regarded as a single internal variable. In their work on the strain hardening of fcc metals, Kocks and Mecking, as well as the followers of their modeling approach [12–14], highlighted the central role of the normalized stacking fault energy, $\frac{\gamma_{isf}}{Gb}$, as a key scaling parameter for the strain hardening of metals as different as Al, which has a high γ_{isf} and deforms by dislocation glide only, and Ag, in which deformation twinning is common due to its low magnitude of γ_{isf}. Here b denotes the magnitude of the dislocation Burgers vector.

Changes in the composition of single phase fcc Fe-alloys, such as TWIP steels, result in variations in stacking fault energy, and, as a consequence, in strain hardening and strength. In TWIP steels the combination of strengthening by solute interstitial atoms (C and N) and the control of γ_{isf} by suitable alloying additions (Mn, Al, Si, Cr, C and/or N) promotes twinning as an additional deformation mode and leads to an increase of the strain hardening rate.

In their report on the strain hardening response of low γ_{isf} fcc alloys, Kalidindi and co-workers [15,16] suggested that the strain hardening of alloys for which the plastic deformation includes both dislocation glide and deformation twinning goes through four distinct stages. Fig. 3 identifies these four stages of strain hardening in the strain hardening curve of Fe-18%Mn-0.6%C-1.5%Al TWIP steel. Note that the strain hardening rate reaches a maximum magnitude of approximately G/30, a value which is close to G/20~4 GPa given by Kocks and Mecking as the highest strain hardening rate for steel [14].

While the mentioned general trend of a continual drop of the strain hardening coefficient characteristic of stage III strain hardening of fcc metals is largely observed for TWIP steels as well, the latter exhibit a greater complexity of strain hardening. Accordingly, the taxonomy of the strain hardening stages in TWIP steels proposed by Kalidindi et al. is different from the classical one that applies for materials whose plastic deformation is governed by dislocation glide alone [14]. According to this taxonomy, stage A is the initial strain hardening stage, which is controlled by the dislocation density evolution in the absence of twin formation. It is equivalent to the standard stage III of strain hardening of high γ_{isf} fcc metals and alloys, in which the strain hardening rate decreases continuously. This behavior is associated with the evolution of the dislocation density characterized by a continuously decreasing rate of dislocation storage. This results from a relatively constant dislocation generation rate and an increasing rate of dislocation annihilation (dynamic recovery), chiefly by cross slip and annihilation of screw dislocations of opposite sign. Stage A is usually observed during a relatively short strain interval. According to Asgari et al. [15], no twinning takes place in stage A. At this deformation stage, overlapping stacking faults are usually observed, and it can be considered as an incubation stage in which dislocation interactions generate twin nuclei.

Stage B is the primary twinning stage, which is characterized by an increasing strain hardening. It starts when primary deformation twinning is initiated in favorably oriented grains. Over this stage the strain hardening rate initially increases and then remains more or less constant during straining. Stage B typically starts in the true strain range of 0.03–0.04, which indicates that dislocation slip activity and dislocation-dislocation interactions occur prior to

Please cite this article in press as: B.C. De Cooman, et al., Twinning-induced plasticity (TWIP) steels, Acta Materialia (2017), http://dx.doi.org/10.1016/j.actamat.2017.06.046

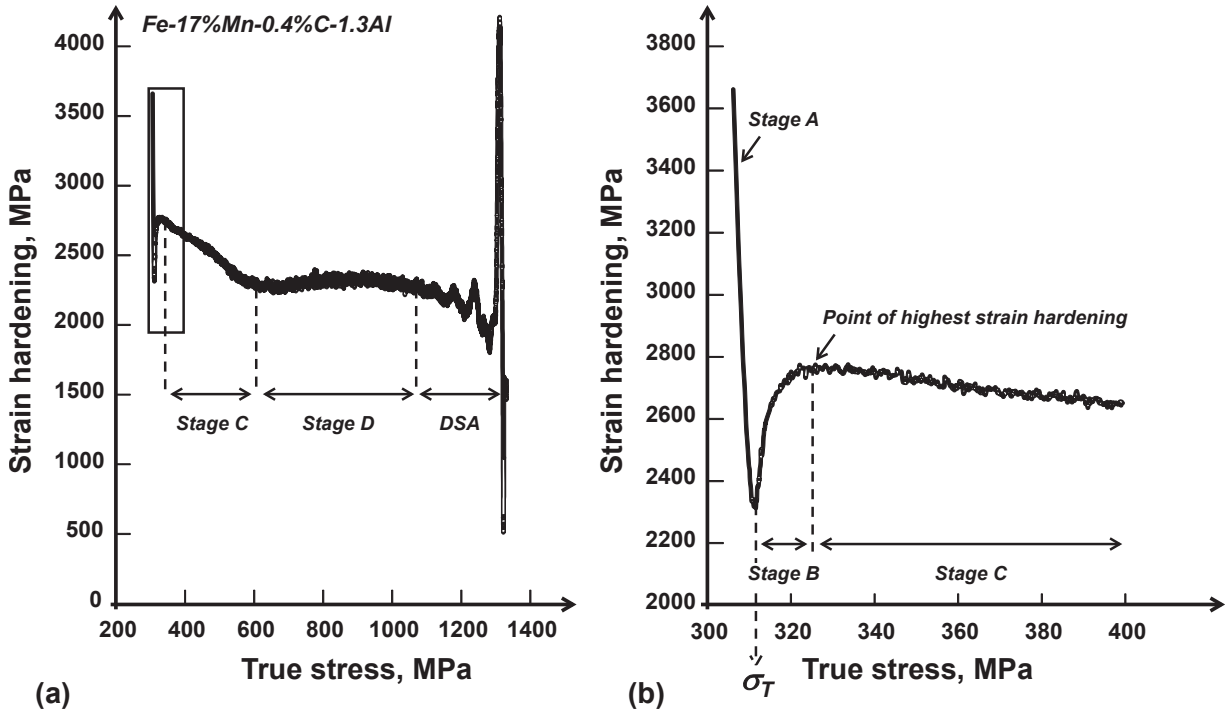

Fig. 3. (a) Strain hardening of Fe-17%Mn-0.4%C-1.3%Al TWIP steel showing four strain hardening stages. (b) Enlargement of the initial strain hardening range. The transition from stage A to stage B corresponds to the onset of deformation twinning, and the minimum in strain hardening determines the twinning stress σ_T. The point of maximum strain hardening is reached at the transition from stage B to stage C. The fourth strain hardening stage, stage D, as well as the section of the curve in (a) associated with dynamic strain aging (DSA) are discussed later in the text.

twinning. This also suggests that dislocations play a role in the creation of twin initiation sites. The experimental twinning stress reported in the present article corresponds to the stress at the onset of stage B. Fig. 4 shows that the twinning stress, defined in this way, i.e. at the minimum of the strain hardening rate in Fig. 3b, is only slightly higher than the yield stress. The difference between the two quantities for the Fe-18%Mn-0.6%C-1.5%Al TWIP steel is approximately 46 MPa. The critical strain for the onset of deformation twinning is in the range of 0.006–0.012. Bracke et al. report the observation of deformation twins by transmission electron microscopy in Fe-22%Mn-0.5%C TWIP steel deformed to a strain of 0.02 [17]. According to Kim et al. [18], the critical strain for deformation twinning is slightly higher, 0.045 and 0.055, for Fe-18%Mn-0.6%C and Fe-18%Mn-0.6%C-1.5%Al TWIP steel, respectively. Mahato et al. [19] also report that in Fe-27%Mn-2.5%Si-3.5%Al TWIP steel, twinning is initiated at the start of stage B of the strain hardening curve. It should be noted, however, that a sharp increase in the strain hardening upon the onset of stage B depicted in Fig. 3 is not always observed. There is also no general consensus in literature that stage B can be unequivocally linked to the initiation of deformation twinning. Thus, in their report on the strain hardening of Fe-15%Mn-0.7%C-2%Al-2%Si TWIP steel, Rahman et al. [20] suggest that in stage B, which they refer to as stage 2, the rise of the hardening rate is due to an increase in the twinning rate, rather than the initiation of deformation twinning. Barbier et al. [21] and Lebedkina et al. [22] attribute the increase in the strain hardening rate, or the “bump in hardening”, in Fe-22%Mn-0.6%C TWIP steel to the activation of a secondary twin system.

The highest strain hardening rate is observed at the transition from stage B to stage C. In stage C the strain hardening rate diminishes gradually with strain. This decreasing strain hardening is attributed to a reduction in the rate of primary twin formation. As the original grain size is reduced by the progressive segmentation of the grains by the deformation twins, higher stresses are required to generate more twins. The first three stages of strain hardening have been correlated experimentally with the strain dependence of the twinning kinetics in Fe-20%Mn-1.2%C TWIP steel by Renard and Jacques [23]. According to the work of Kalidindi's group [15,16], the slowly decreasing strain hardening observed in stage C is terminated when extensive twinning is initiated on secondary twin systems, but in certain cases diffuse necking has been reported to set in at the end of stage C.

In a scenario proposed by Kalidindi and co-authors, secondary twin systems are activated during stage D. Multiple twin-twin intersections are formed which considerably limit dislocation glide distances. This lead to a reduction of the rate at which the strain hardening decreases with strain, and a more or less constant strain hardening rate is observed over stage D. Note that stage D is not observed in the strain hardening curve of some TWIP steels. Mahato et al. [19] consider the absence of stage D in the strain hardening curve for Fe-27%Mn-2.5%Si-3.5%Al TWIP steel to be an indication of the absence of secondary twinning.

Some reports consider more than four strain hardening stages. Barbier et al. [21,24] introduce a fifth stage, stage E, during which a continuous decrease of the strain hardening rate occurs. They report that the twin volume fraction grows significantly in this stage, with twin bundles becoming denser and thicker. This observation appears to be at odds with the well documented saturation of deformation twinning. The same authors report the development of large intra- and inter-granular regions with high dislocation density, which result in a pronounced strain localization prior to fracture.

In multi-component alloys, such as TWIP steels, relatively small compositional differences are expected to influence the value of γ_{isf}, and hence the strain hardening behavior. Some of the differences in strain hardening behavior discussed in this section may therefore

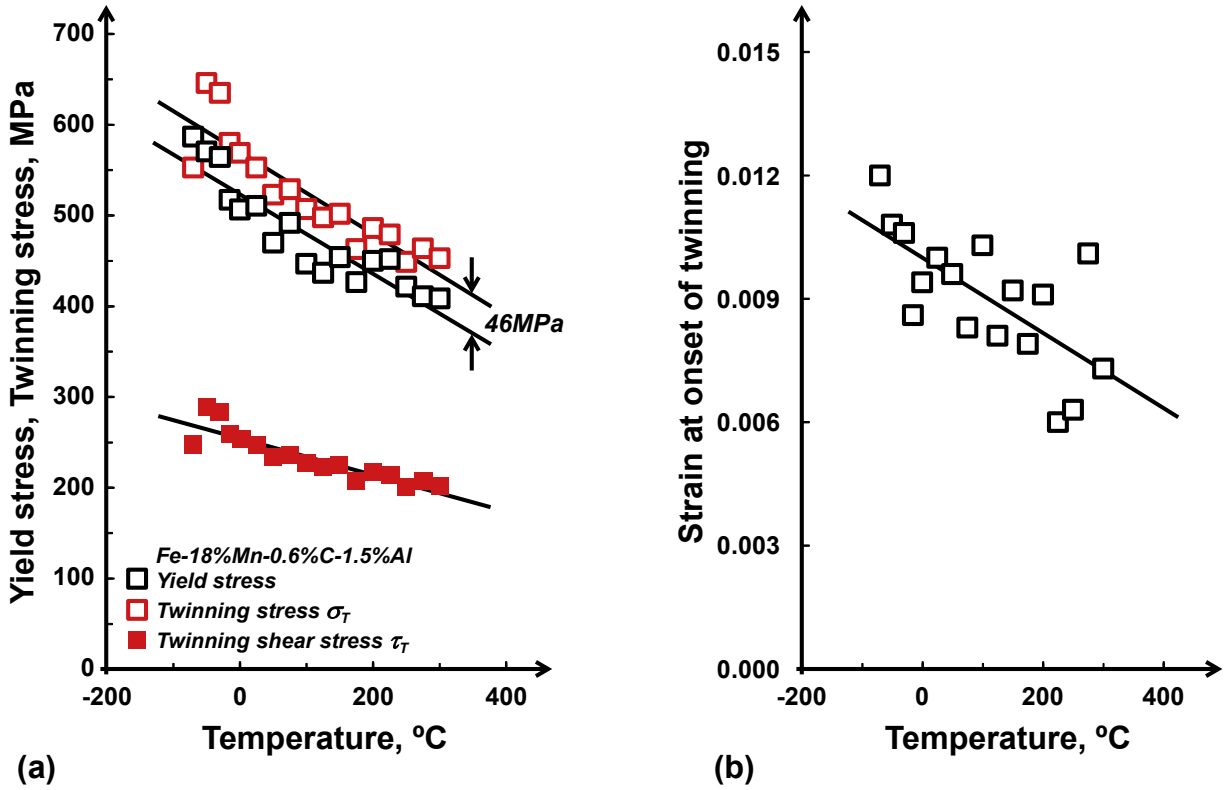

Fig. 4. (a) Temperature dependence of the yield stress, the twinning stress and the twinning shear stress of Fe-18%-0.6%C-1.5%Al TWIP steel. (b) Temperature dependence of the strain at the onset of deformation twinning in this steel.

be due to minor differences in alloy composition.

2.2. Modeling approaches involving deformation twinning

Guttierez-Urrutia and Raabe [25] and Saeed-Akbari et al. [26], who studied Fe-22%Mn-0.6%C TWIP steel and Fe-(19–27)%Mn-(0.3–1.2)%-(0.0–3.5)%Al TWIP steels, respectively, provided in-depth analysis of strain hardening data and correlated these with microstructural observations. They proposed a slightly different interpretation of the first three stages of strain hardening. While they agree with the view of Kalidindi and co-workers that stage A is dominated by dislocation dynamic recovery, their conclusion is that deformation twinning initiates already in this early deformation stage. In fact, according to Guttierez-Urrutia et al. [27] yielding and twinning occur simultaneously, i.e. the critical resolved shear stress for glide and twinning are equal, *i.e.* $\tau_{crss} = \tau_T$. Guttierez-Urrutia et al. argue that the strain hardening in stage B is related to the evolution of the dislocation ensemble to a dislocation cell/dislocation wall structure. These dislocation arrangements act as very effective obstacles to dislocation glide. According to these authors, the influence of the deformation twins on the strain hardening comes to bearing in stage C with the formation of dense deformation twin substructures, which are formed by deformation twins cutting through the already present dislocation substructure.

Rahman et al. [20] report that, in cyclically tested Fe-15%Mn-0.7%C-2%Al-2%Si TWIP steel, the nucleation of twins could even occur at stresses below the yield stress. Their results have however been critically re-evaluated by Saleh and Gazder [28], who argue that the conclusions of Rahman et al. were based on the failure to recognize a number of significant differences between plasticity in cyclic tests and monotonic tensile tests. Saleh and Gazder claim that this resulted in a number of modeling assumptions, such as unrealistically low twinning stresses and excessively large twin volume fractions, which were not compatible with the experimental observations.

Using electron channeling contrast imaging (ECCI) Gutierrez-Urrutia and Raabe [25] and Zaefferer and Elhami [29] were able to observe the evolution of both the deformation twinning and the dislocation substructure in great detail. They argue that the dislocation mean free path is determined by both the twin spacing and the characteristic length scale defined by the dislocations substructure. In their investigation of samples deformed under uniaxial tensile loading, they observed three types of grains in the deformed microstructure. Type I grains, with a ⟨001⟩-type direction aligned with the tensile axis, have a low density of deformation twins. Type I grains also develop a clear equiaxed dislocation cell substructure. Wavy slip is promoted in type I grains. The orientation of type I grains also favors multiple slip. Type II grains have a higher density of twins belonging to the primary deformation twin system. Finally, type III grains, whose ⟨111⟩-type direction is parallel to the tensile axis, have a high density of deformation twins of both the primary and the secondary twin systems. Type III grains also contain a developed dislocation cell structure. High dislocation density walls are a typical feature of planar dislocation glide. The twins appear to encounter little or no resistance from this dislocation substructure as they are often seen to cross the entire grains.

Based on their observations, Gutierrez-Urrutia and Raabe [25] proposed a physical model of strain hardening that accounts for dislocation glide and deformation twinning. They argued that the strain hardening is determined by both the deformation twin spacing and the characteristic length scale of the dislocation substructure. In particular, the dislocation substructure provides a large strain hardening rate in stage A. Using the Kuhlmann-

Please cite this article in press as: B.C. De Cooman, et al., Twinning-induced plasticity (TWIP) steels, Acta Materialia (2017), http://dx.doi.org/10.1016/j.actamat.2017.06.046

Wilsdorf similitude principle [30], they calculate the contribution of the dislocation cells to stress in type I grains as follows:

$$\sigma = M \cdot f_I \cdot \frac{K \cdot G \cdot b}{D} \quad (1)$$

Here M is the Taylor factor ($M = 2.44$ for type I grains), f_I is the fraction of type I grains, D is the dislocation cell size, which varies from 750 nm to 180 nm when the strain increases from 0.05 to 0.40, and the *similitude* constant K is a numerical parameter. A low K value is indicative of a high rate of dislocation storage. Gutierrez-Urrutia and Raabe [25] note that for the TWIP steel they investigated the refinement of the cell structure with strain corresponds to a smaller similitude constant, $K = 3.7$, than in the case of high stacking fault alloys ($7 < K < 8$), and ascribed this to the influence of the stacking fault energy on the cell formation.

The strain hardening behavior of TWIP steels has also been considered by means of micro-mechanical models, such as the crystal plasticity finite element (CPFE) and visco-plastic self-consistent (VPSC) models. The important feature of these approaches is that they offer a physically based picture of the behavior of the material at the grain scale. Shiekhelsouk et al. [31] consider a polycrystal of a low stacking fault energy material such as TWIP steel to be equivalent to a representative volume element (RVE) comprised by a limited number of grains with specific orientations, which are subjected to homogeneous stress and strain rate boundary conditions. The constitutive equations for the individual grains take into account three grain orientation-dependent strain mechanisms, *viz.* instantaneous elasticity, viscous or rate-dependent thermally activated crystallographic slip, and rate-independent mechanical twinning, in well-defined imposed conditions of stress, strain and temperature. In polycrystalline TWIP steel intergranular interactions due to non iso-strain conditions at the grain boundaries lead to internal stresses. In the self-consistent approach, each grain is considered to be embedded in a homogeneous matrix, which represents a homogenized effective continuum interacting with that grain regarded as an inclusion.

The model proposed by Shiekhelsouk et al. [31] shows that at a strain of 15%, some 90% of the grains in a TWIP steel contain twins. Predominantly, two twin systems operate within a grain. The twin volume fraction remains low, e.g. only 6% at 30% strain. This is consistent with the experimental observation that twinning does not influence the development of the crystallographic texture. It also implies that the contribution of the twinning strain to the total plastic deformation is very small, e.g. 3% at 35% strain. Therefore, the twinning strain as such does not contribute significantly to the uniform elongation prior to necking. However, the occurrence of deformation twinning can influence the evolution of the dislocation density indirectly, by controlling the dislocation mean free path (MFP). In the initial stages of deformation this quantity is mainly determined by the grain and/or dislocation cell size. Accordingly, the dislocation MFP decreases due to an increase of the dislocation density. The onset of deformation twinning at about 5% strain results in an additional reduction of the MFP.

According to Shiekhelsouk et al. [31] the onset of twinning is not discernible in the calculated strain hardening curves as a stop in the decrease of the $d\sigma/d\varepsilon$ vs. ε curves at small plastic strains. They argue that the effect of the dislocation MFP reduction by the deformation twins occurs only at higher strains, when enough grains have two active slip systems, because the twins belonging to the primary twin system are coplanar with it and therefore do not contribute to a decrease in the MFP. The results the mentioned authors obtained on single crystals illustrate two important aspects of deformation twinning at the scale of the individual grains, which appear to have been overlooked in the original Kalidindi model for strain hardening in low γ_{isf} alloys. These are as follows: (a) the primary twins do not contribute to a MFP reduction for the primary slip dislocations, and (b) the effect of the mechanical twins in reducing the dislocation mean free path, and thereby increasing the strain hardening, is not instantaneous as the first effect of the formation of twins is to supply an additional strain which relaxes intergranular stresses. These conclusions are illustrated in the representative single grain response taken from the work of Shiekhelsouk et al. [31] shown in Fig. 5. All grains have three to five active slip systems from the very start of plastic deformation, and no additional slip systems become significant with strain. The primary twin system $(a/2[011](1\bar{1}1)$, in the case of Fig. 5) is usually coplanar with the primary slip system, and non-coplanar with at least one of the other slip systems. As soon as twinning sets in, there occurs a steep drop in the strain hardening due to a contribution of twins to plastic strain. This happens until a reduction of the MFP by the

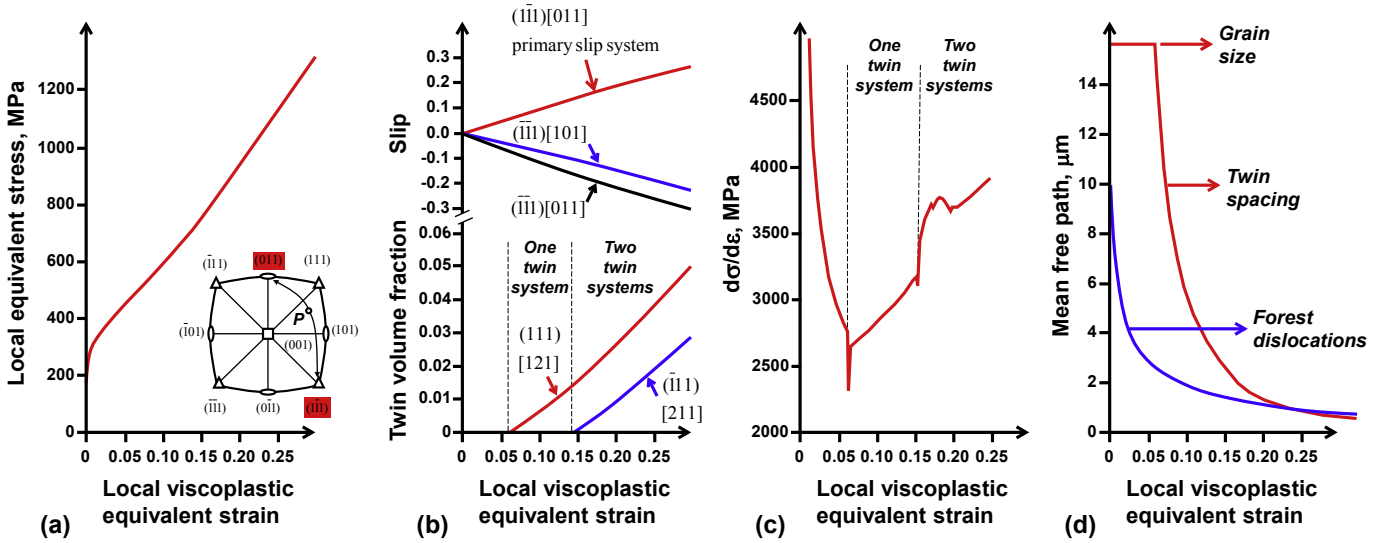

Fig. 5. (a) Calculated stress-strain curve for a grain with the orientation shown in the inset. Three slip systems and two twinning systems are activated during straining. (b) Evolution of the slip for the three activated slip systems and the volume fraction of the activated twin systems in the grain. (c) Strain hardening vs. strain curve. (d) Evolution of the dislocation mean free path with strain: effect of grain size, forest dislocation density, and deformation twins. The figures are based on data published by Shiekhelsouk et al. [31].

twins comes to bearing to give rise to an increase in strain hardening. Thus, twinning contributes to the deformation in two competing ways. As seen from Fig. 5c, the initial steep decrease of the strain hardening occurs up to a strain of 6%. At that strain, a decrease of the dislocation MFP and the concomitant rise of the strain hardening rate sets in due to the activation of three non co-planar slip systems. The primary twin system is activated at about the same strain of 6%. It is co-planar with one of the three slip systems. A secondary twin system is activated at about 15% strain. There is also a small dip in the $d\sigma/d\varepsilon$ vs. ε curve at the onset of the activation of this second twin system. As it is non coplanar with the primary slip systems and the primary twin system, twin-twin interactions inhibit the twin activity and the model predicts that no further twin systems are activated at higher strains.

Another group of authors, Dancette et al., also used crystal plasticity based finite element method to predict the behavior of TWIP steel at the grain level [32]. They showed that in the course of uniaxial tensile deformation the grains get re-oriented towards the stable ⟨100⟩//td and ⟨111⟩//td orientations (td: sample tensile direction). The model predicts a lower, yet non-zero, twin volume fraction in grains ending up close to the ⟨100⟩ orientation. Grains with a high density of twins originate from grains with orientations between ⟨110⟩//td and ⟨111⟩//td.

While the different attempts at modeling the mechanical properties of TWIP steels give generally a good agreement with experimental results, it is important to realize that more work is needed in this area, as the values of some of the key model parameters vary strongly from report to report. For example, the value of the critical resolved shear stress τ_{crss} for slip in Fe-22%Mn-0.6%C TWIP steel obtained through fitting by Shiekhelsouk et al. [31] is 95 MPa; the critical resolved shear stress for twinning is much lower, $\tau_T = 47.5$ MPa, *i.e.* $\tau_T \approx \tau_{crss}/2$. In contrast, Dancette et al. [32] came up with the values of $\tau_{crss} = 125$ MPa and $\tau_T = 230$ MPa for Fe-20%Mn-1.2%C TWIP steel, *i.e.* $\tau_T \approx 2 \times \tau_{crss}$.

The main conclusions that transpire from the studies mentioned above can be condensed to the following statement. The key reason for the combination of high strength and large ductility of TWIP steels owing to deformation twinning is a decrease of the dislocation mean free path, especially for dislocations on slip planes intersecting the twinning plane. A further factor to consider is the high dislocation storage capacity due to the strong inhibition of dislocation cross-slip resulting from the low value of γ_{isf}. Finally, additional strengthening may stem from the very small thickness of the deformation twins (the size effect).

Three types of models put forward to explain the mechanism of enhancement of strain hardening and tensile ductility due to deformation twinning are central to our subject: (a) the "dynamic Hall-Petch effect" [33,34], (b) the back stress effect [35], and (c) the "composite effect" proposed by Guttierez-Urrutia and Raabe [25]. The key aspects of the three types of models are illustrated in Fig. 6. The first one accounts for *isotropic strain hardening*, which is related to the growth of the dislocation density – a scalar quantity controlling the overall level of stress. The other two describe *kinematic hardening* and are associated with the directionality of the strain hardening behavior. We begin with the isotropic strain hardening model due to Allain and Bouaziz, which generated a number of follow-up modeling exercises, and then move on to the kinematic hardening approaches in Section 2.2.2.

2.2.1. Role of deformation twinning in the isotropic strain hardening of TWIP steel

Schematics of the models based on the Allain-Bouaziz dynamic Hall-Petch concept are shown in Fig. 7. The results illustrate the influence of the deformation twinning kinetics on the mechanical properties of a TWIP steel in terms of the two internal variable model proposed by Kim et al. in which the twin boundaries act as impenetrable obstacles for dislocation glide [18,36]. The calculations are based on a constitutive model developed by Estrin and Kubin [37], which accounts for the mobile and forest dislocation density evolution during plastic deformation. The model also allows the computation of the contribution of dynamic strain aging to the strain hardening of TWIP steel. In addition, the model considers the fact that only a certain fraction of the grain population develop deformation twins during straining.

Despite considerable advances in the state of the knowledge of TWIP steels and the wide acceptance of the model for the strain

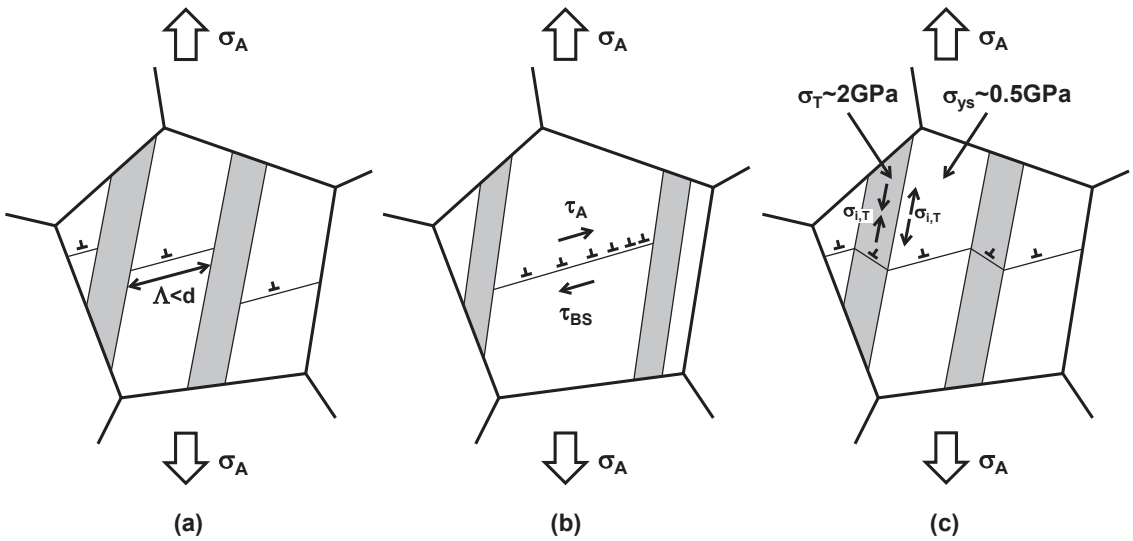

Fig. 6. Mechanisms of plasticity enhancement due to deformation twinning according to (a) the Bouaziz-Allain "dynamic Hall-Petch effect" [33,34], (b) the Bouaziz back stress effect [35], and (c) the "composite effect" introduced by Guttierez-Urrutia and Raabe [25]. Here σ_A and τ_A denote the applied stress and the shear stress, respectively, and τ_{BS} denotes the back stress; σ_{ys} and σ_T represent the yield strength and the twinning onset stress, respectively; d stands for the average grain size and Λ for the average twin spacing. Finally, $\sigma_{i,M}$ and $\sigma_{i,T}$ are the reaction stresses in the composite model that develop to compensate plastic strain incompatibility between the twins and the matrix: $\sigma_{i,M}$ denotes the tensile stress in the matrix, while $\sigma_{i,T}$ is the associated compressive stress in the twins.

Please cite this article in press as: B.C. De Cooman, et al., Twinning-induced plasticity (TWIP) steels, Acta Materialia (2017), http://dx.doi.org/10.1016/j.actamat.2017.06.046

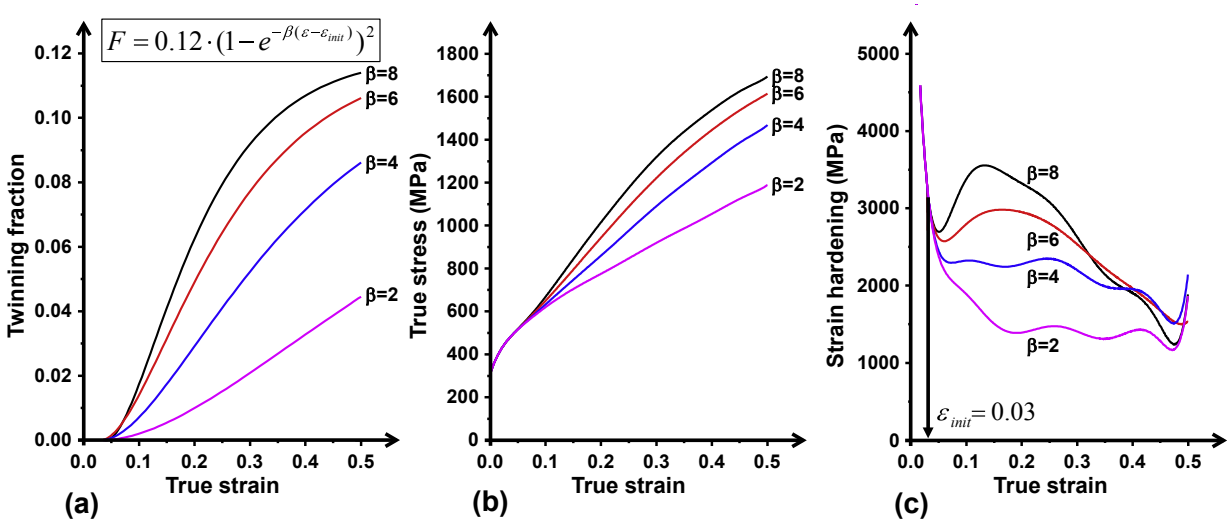

Fig. 7. Effect of a reduction of the twinning kinetics parameter β entering the exponential in the strain dependence of twin volume fraction, F, on (a) the strain dependence of the twin volume fraction, (b) the stress-strain curve, and (c) the strain hardening rate. The figures are based on the model developed by Kim et al. [36].

hardening of TWIP steels based on the dynamic Hall-Petch effect, there is still no consensus on the fundamental mechanisms of strain hardening in TWIP steels. In its simplest form, the basic model for strain hardening assumes that the dominant deformation mode in TWIP steels is dislocation glide, i.e. that strain hardening is controlled by the kinetics of the material's dislocation storage during plastic deformation. The deformation-induced twinning leads to a decrease of the effective dislocation glide distance, or mean free path. This results in a "dynamic Hall-Petch effect", which leads to a pronounced increase of the strain hardening rate, a high tensile strength, and a substantial uniform elongation. This early model has evolved quite considerably, and its more recent versions will be discussed below.

In the original one internal variable model for strain hardening of TWIP steel put forward by Bouaziz and Guelton [33], the key factor enhancing strain hardening is considered to be a decrease of the dislocation mean free path due to progressive segmentation of the grains into smaller microstructural entities by deformation twins. The model is based on the Taylor relation [38] between the shear flow stress, τ, and the dislocation density, $\rho_d(\gamma)$, whose evolution with the shear strain γ can be described by an appropriate version of the Kocks-Mecking equation [14]:

$$\begin{aligned} &\tau = \tau_0 + \alpha G b \sqrt{\rho_d(\gamma)} \\ &\frac{d\rho_d(\gamma)}{d\gamma} = \frac{1}{b\lambda} - f\rho_d(\gamma) \quad = \frac{1}{b}\left(\frac{1}{d} + \frac{1}{t(\gamma)} + k\sqrt{\rho_d(\gamma)}\right) - f\rho_d(\gamma) \end{aligned} \tag{2}$$

Here λ is the effective dislocation mean free path, whose inverse is defined as the sum of the inverse distances between various impenetrable obstacles to dislocation motion and $t(\gamma)$ is the average distance between the deformation twins. The latter quantity is expressed in terms of the twin volume fraction $F(\gamma)$ and the twin thickness t_T by the Fullman relation [39]:

$$t(\gamma) = t_T \cdot \frac{1 - F(\gamma)}{F(\gamma)} \tag{3}$$

A shear strain increment is comprised by the weighted contributions from dislocation glide, $d\gamma_d$, and twinning shear, $d\gamma_T$:

$$d\gamma = (1 - F) \cdot d\gamma_d + F \cdot d\gamma_T \tag{4}$$

This isotropic hardening model takes into consideration the fact that the deformation twins in TWIP steel are initially very thin, and that they do not thicken much with strain. The shape of the twins is usually considered to be plate-like, but close inspection by means of TEM shows that they tend to have a highly variable thickness (Fig. 8). Growth of the volume fraction of twins is mostly furnished by the formation of new twins in the course of deformation. The steady nucleation of new deformation twins results in an increasing fragmentation of the grains by twin lamellae with increasing strain. This is the origin of the *dynamic* Hall-Petch effect. The Kocks-Mecking model originally used by Bouaziz and Allain [33,34] operates with a single internal variable – the total dislocation density. It was refined by Kim et al. [18] to include two dislocation densities: the mobile and the forest ones. In this approach the original Kocks-Mecking equation for the evolution of the dislocation density was replaced by a set of two coupled differential equations based on the work of Estrin and Kubin, modified to take into account the contribution of the grain boundaries and the twin boundaries to the dislocation density evolution [37]:

$$\begin{aligned} \frac{d\rho_m}{d\gamma} &= \frac{C_1}{b^2}\frac{\rho_i}{\rho_m} - C_2\rho_m - \frac{C_3}{b}\sqrt{\rho_i} - \frac{1}{bd} - \frac{1}{bt_T}\frac{F}{1-F} \\ \frac{d\rho_i}{d\gamma} &= C_2\rho_i + \frac{C_3}{b}\sqrt{\rho_i} + \frac{1}{bd} + \frac{1}{bt_T}\frac{F}{1-F} - C_4\rho_i \end{aligned} \tag{5}$$

Here ρ_m and ρ_i are the mobile and immobile (forest) dislocation densities. The terms containing the parameters C_1, C_2, C_3 and C_4 are related to the following physical processes. C_1 specifies the magnitude of the dislocation pinning term, assuming that immobile forest dislocations act as pinning points of fixed dislocation sources. The decrease of the mobile dislocation density by interactions with other mobile dislocations is taken into account through the term $C_2\rho_m$. C_3 describes the immobilization of mobile dislocations with a mean free path proportional to $\rho_i^{-1/2}$, i.e. assuming a spatially organized dislocation forest. C_4 is associated with dynamic recovery, i.e. the annihilation of forest dislocations by cross slip. The approach makes it possible to compute the contribution of dynamic strain aging to the flow stress. This contribution was found to be minor in term of stress, *viz.* approximately 20 MPa. However, through a negative contribution to the strain rate sensitivity of the flow stress, it is very important in the context of strain localization and ductility, see below. The two internal variable

Please cite this article in press as: B.C. De Cooman, et al., Twinning-induced plasticity (TWIP) steels, Acta Materialia (2017), http://dx.doi.org/10.1016/j.actamat.2017.06.046

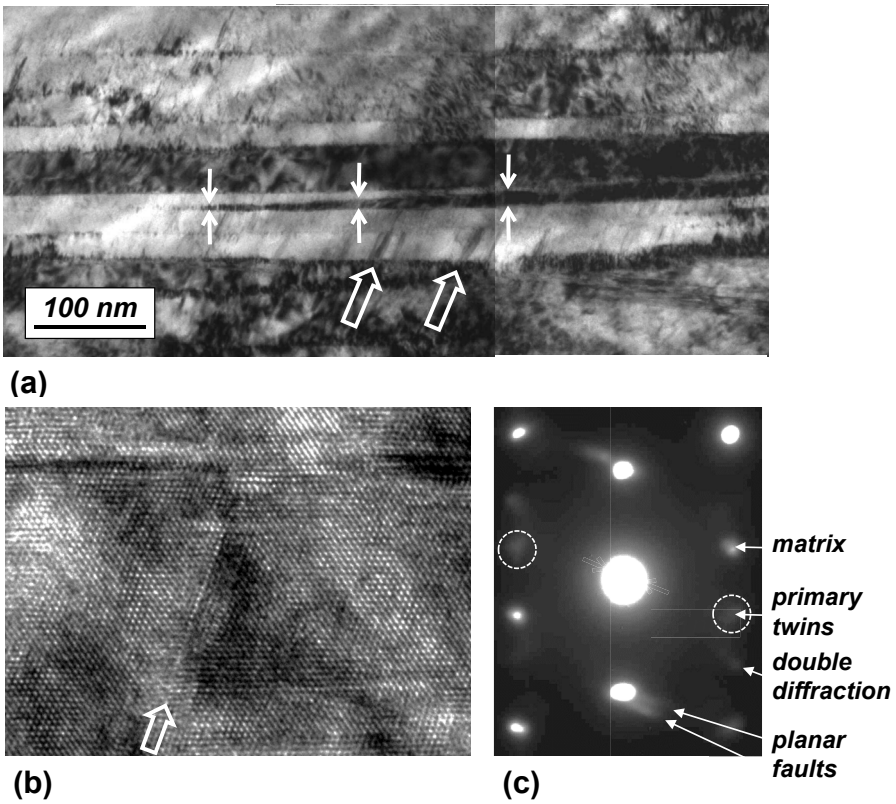

Fig. 8. (a) TEM micrograph of Fe-18%Mn-0.6%C TWIP steel strained to fracture. The twin thickness, typically less than 50 nm, is highly variable and appears to be the results of a chaotic succession of stacking faults. The small white arrows give an indication of the twin thickness variability. The two open white arrows indicate stacking faults in the matrix region between twins. Note that the formation of a 30 nm thick twin requires 144 partials trailing intrinsic stacking fault on successive {111} glide planes. Although the twins are very narrow one must consider the fact that most models for twin nucleation envisage two to three layers thick twin nuclei. A considerable amount of twin thickening must therefore occur via a specific mechanism. (b) High resolution image of a stacking fault inside the matrix region (open white arrow). (c) Diffraction pattern showing evidence for primary twin formation and stacking faults on secondary slip planes.

model due to Kim et al. [18] also took into account that deformation twinning does not occur in some grains as a result of their crystallographic orientation. This aspect of the model will be discussed below.

A somewhat different constitutive model for dislocation-cell forming fcc metals and alloys was proposed by Roters et al. [40]. They considered three distinct dislocation populations: mobile dislocations in the cell interior, mobile dislocations in the cell walls, and immobile dislocation (dipoles) in the cell walls. Their three internal variable model was used by Steinmetz et al. [41] to model the flow stress of Fe-22%Mn-0.6%C TWIP steel. The dislocation density evolution equations of the model by Roters et al. do not contain a mean free path term λ in the sense of the equations of the Kocks-Mecking-Estrin model, cf. Eq. (2). Instead, the mean free path is introduced via the Orowan equation for the strain rate controlled by the thermally activated passing of an obstacle by a dislocation [42]:

$$\dot{\gamma} = v_d b \rho_d = \lambda_i v_0 b \rho_i \cdot \exp\left(-\frac{Q_s}{k_B T} \cdot \left(1 - \left(\frac{\tau_{eff,i}}{\tau_0 + \alpha G b \sqrt{\rho_i}} \right)^p \right)^q \right) \tag{6}$$

Here v_d is the average dislocation velocity, ρ_d is the mobile dislocation density, v_0 is the Debye frequency, Q_s is the activation energy for slip, k_B is the Boltzmann constant, and T is the absolute temperature. The heuristic parameters p and q are related to the force-distance profile for dislocation-obstacle interaction. The subscript i represents c or w, for the cell interior (c) and the cell wall (w), respectively. Distinctly different values of the mean free path were considered for the cell interior (λ_c) and the cell walls (λ_w):

$$\begin{aligned} \frac{1}{\lambda_c} &= \frac{1}{d} + \frac{1}{i_T t} + \frac{\sqrt{\rho_c}}{i_c} \\ \frac{1}{\lambda_w} &= \frac{1}{d} + \frac{1}{i_T t} + \frac{\sqrt{\rho_w}}{i_w} \end{aligned} \tag{7}$$

Here d is the grain size and t is the twin spacing. The quantities i_c and i_w denote, respectively, the average number of dislocation spacings in the cell interior and the cell walls a dislocation travels before being immobilized. Similarly, i_T is the average number of twin spacings a dislocation travels before being immobilized. A rule of mixtures was used by Steinmetz et al. [41] for the flow stress:

$$\tau = f_c \tau_{eff,c} + f_w \tau_{eff,w} \tag{8}$$

where f_c and f_w are the volume fractions of the cell interiors and the cell walls, respectively.

2.2.2. Kinematic hardening models

In the models reviewed so far, the strain hardening was essentially controlled by the dynamic Hall-Petch mechanism, the formation of twins gradually reducing the dislocation mean free path, thereby contributing to enhanced dislocation storage and ensuing isotropic hardening. Bouaziz et al. [35] have identified another important mechanism of strain hardening. By using forward-reverse shear tests, they measured the back stress and

determined that at a strain of 0.2 it contributed about 50% of the flow stress. These results suggest that, in addition to *isotropic hardening* considered above, substantial *kinematic hardening* (giving rise to the Bauschinger effect) was involved. According to Bouaziz et al. [35], the back stress is generated by pile-ups of dislocations arrested at twin boundaries. Fig. 9 shows TEM micrographs of a pile-up of identical partial dislocations at a twin. The progressively increasing interdislocation distance is a clear indication of a repulsive interaction between the dislocations and the twin boundary. The micrograph also suggests that stress amplification at the tip of the pile-up has initiated the formation of a dislocation within the twin and also shows that slip is not transmitted across the twin. From their *in situ* neutron diffraction experiments, Saleh et al. [43] concluded that the back stress stems from a combination of (a) intergranular residual stresses (Type II stresses), arising from the inhomogeneous deformation of grains due to the orientation dependence of the elastic modulus and the yield strength, and (b) dislocation pile-ups at the intersections of stacking faults. They report a back stress of 210 MPa, which amounts to 65% of the stress in forward tension.

It should be noted that precise measurement of the back stress is difficult as it is critically dependent on the offset strain chosen to measure the backward yield stress. This is the most likely explanation for the very different back stress values found in literature. The back stress was reported to be 68%, 65%, 50%, and 20% of the flow stress according to Gil Sevillano [44], Saleh et al. [43], Bouaziz et al. [35], and Guttierrez-Urrutia et al. [45], respectively. Collet [46] determined the back stress by X-ray diffraction studies and reported values similar to those published by Bouaziz et al. The occurrence of a pronounced Bauschinger-type back stress in fcc alloys susceptible to deformation twinning was also observed in Fe-24Mn-3Al-2Si-1Ni-0.06C TWIP steel by Saleh et al. [43] and in Fe-12%Mn-1.2%C Hadfield steel (with $\gamma_{isf} = 35$ mJ/m^2) by Karaman et al. [47]. The data of Chung et al. [9] shown in Fig. 9 (a) shows a small asymmetry for sheet samples of TWIP steel tested in tension and compression along the rolling direction. The tension and compression curves converge rapidly, *i.e.* the same strain hardening behavior in tension and compression is observed after a strain of 0.03. The situation is different when a TWIP steel is first strained in tension and then in compression. In this case a considerable back stress develops, as shown in Fig. 9 (b).

Bouaziz et al. [35] proposed a refinement of their original strain hardening model, which includes a term for the kinematic hardening effect caused by long range internal stresses originating from dislocation pile-ups containing n dislocations in a grain with a dislocation mean free path L. The key equations in the model describe the evolution of the dislocation density and the dislocation mean free path:

$$\frac{d\rho}{d\gamma} = \frac{1-\frac{n}{n_0}}{bL} + \frac{k}{b}\sqrt{\rho} - f\rho$$
$$\frac{1}{L} = \frac{1}{d} + \frac{1}{2t}\frac{F(\gamma)}{1-F(\gamma)} \quad (9)$$

Here n_0 is the largest number of dislocations stopped at a twin boundary. Note that L is independent of d at small strains, and that the number of dislocations n in the pile-ups rapidly reaches its saturation value n_0.

The back stress can also be considered to be a result of the localized shear associated with a twin, the back shear stress stemming from the constraint of the adjacent grain. In other words, an internal forward stress acts on the twins and an internal back stress acts on the matrix. The back stress can be estimated by means of the Brown-Clarke equation [48] for a twin that is considered as a hard Eshelby inclusion in the TWIP steel:

$$\tau_{BS} = 2\cdot\chi\cdot F_T\cdot\gamma^*\cdot D_G\cdot G \quad (10)$$

Here χ is the Eshelby accommodation factor, which depends on the shape and orientation of the twin formed in the softer TWIP steel matrix during forward loading, γ^* is the unrelaxed shear strain built up on a specific slip system during forward loading, and D_G is a correction factor for the shear modulus. Approximating the twins as isotropic spherical inclusions with $G_T = G_M$, *i.e.* assuming the elastic constants of the TWIP matrix and the twins to be equal, the

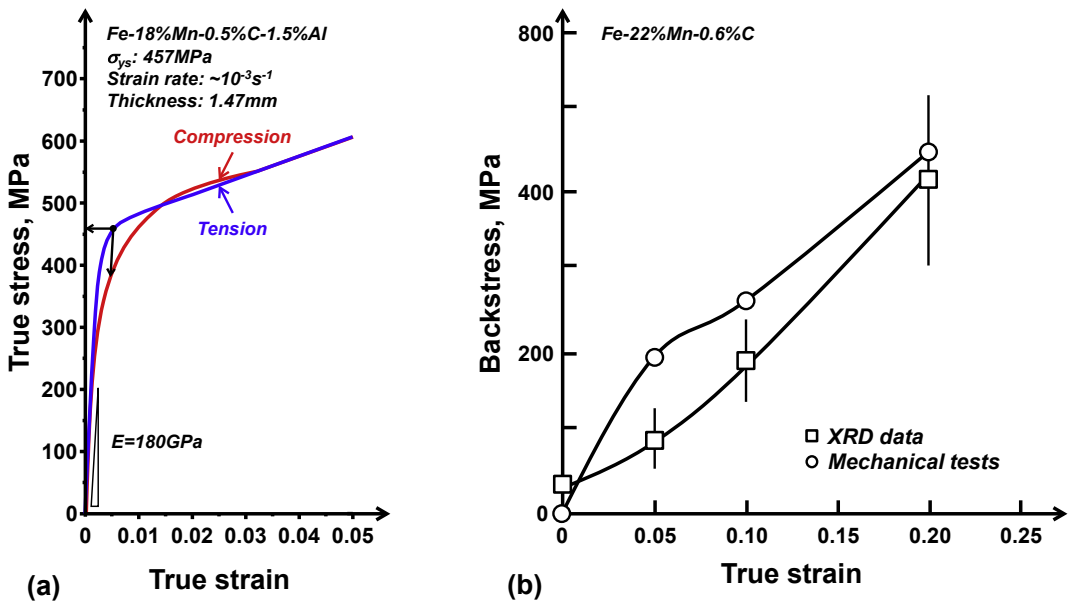

Fig. 9. (a) Tension-compression asymmetry observed for a Fe-18%Mn-0.6%C-1.5%Al TWIP steel. (b) Strain dependence of the back stress as measured by tension-compression tests and X-ray diffraction [35].

parameters χ and D are expressed by

$$\chi = \frac{7-5\nu}{15(1-\nu)} \approx \frac{1}{2}$$
$$D = \frac{G_M}{G_M - \chi(G_T - G_M)} = 1 \quad (11)$$

Combining the previous equations, one obtains the following equation for the back stress:

$$\tau_{BS} \approx G_M \cdot F_T \cdot \gamma^* \quad (12)$$

For tensile tests, one has $\sigma = M\tau$ and $\gamma = M\varepsilon$, where M is the Taylor factor. Taking $M = 3.06$, F_T ~0.1 and $G_M = 78$ GPa, one obtains:

$$\sigma_{BS}(GPa) \approx 73 \cdot \varepsilon_p \quad (13)$$

For a plastic strain ε_p of 0.01, the back stress is about 730 MPa. This estimate suggests that Bauschinger back stresses can also be very substantial in fcc alloys susceptible to deformation twinning if accommodation stresses, rather than dislocation pileups, are considered. Gil Sevillano and de las Cuevas also noted that strain compatibility between twins and the matrix requires the generation of backward and forward internal stresses [49] in the spirit of the two-phase models of Mughrabi [50,51]. Due to the equilibrium condition, the backward stress that develops in the softer austenite matrix in which the twins are formed must be balanced by forward stresses in the hard twins. This leads to a composite strain hardening effect, with the flow stress given by:

$$\sigma_f(\varepsilon) = (1 - F_T(\varepsilon))\sigma_{f,M}(\varepsilon) + F_T(\varepsilon)\sigma_{f,T}(\varepsilon)$$
$$= (1 - F_T(\varepsilon))\alpha G b\sqrt{\rho(\varepsilon)} + F_T(\varepsilon)\sigma_{f,T}(\varepsilon) \quad (14)$$

Here $\sigma_{f,M}$ and $\sigma_{f,T}$ are the flow stresses in the matrix and in the twins, respectively. As $\sigma_{f,M}(\varepsilon) < \sigma_f(\varepsilon) < \sigma_{f,T}(\varepsilon)$, the internal stress in the matrix, $\sigma_{i,M}$, and in the twins, $\sigma_{i,T}$, are given by:

$$\sigma_{i,M}(\varepsilon) = \sigma_f(\varepsilon) - \sigma_{f,M}(\varepsilon) > 0$$
$$\sigma_{i,T}(\varepsilon) = \sigma_f(\varepsilon) - \sigma_{f,T}(\varepsilon) < 0 \quad (15)$$

That is to say, the back stress in the matrix is positive and acts against the external stress, while the 'back stress' in the twins is negative, i.e. it acts in the forward direction – the same direction as the external stress.

The internal stresses must satisfy the equilibrium condition:

$$(1 - F_T(\varepsilon))\sigma_{i,M} + F_T(\varepsilon)\sigma_{i,T} = 0 \quad (16)$$

The back stress results in an increase of the flow stress, thus contributing to strain hardening or to softening when the direction of the stress is reversed. In a Bauschinger experiment the back stress is given by

$$\sigma_{BS} = \frac{\sigma_{f,forward} + \sigma_{ys,backward}}{2} \quad (17)$$

$\sigma_{f,forward}$ (>0) and $\sigma_{ys,backward}$ (<0) are the forward flow stress and the backward yield stress measured during the test, respectively. While σ_{BS} can be measured experimentally, $\sigma_{i,M}$ and $\sigma_{i,T}$ cannot be obtained directly from back stress measurements.

2.2.3. Stress due to size effect

Gil Sevillano and de las Cuevas proposed an additional mechanism for strengthening by deformation twins [44,49]. Namely, the deformation twins are considered to contribute to the strength of the twin-austenite aggregate due to their very small thickness (the size effect). This contribution to stress can be evaluated by noting that the critical flow stress for the activation of a Frank-Read type dislocation source within a twin of thickness t is given by

$$\sigma_T \approx 3 \cdot \frac{G \cdot b_{110}}{t} \quad (18)$$

where b_{110} is the atomic spacing in the direction ⟨110⟩. Assuming t = 30 nm, G = 78 GPa, and b_{110} = 0.255 nm, one obtains $\sigma_T \approx$ 2.0 GPa. High long-range internal stresses will therefore be generated in the grains of TWIP steels which contain very narrow deformation twins ($t \approx$ 20–30 nm). The very hard twins separate regions of softer non-twinned matrix. According to Gil Sevillano there are therefore two contributions adding up to the overall flow stress through a rule of mixtures: (1- f_T) × σ_M, the contribution of the matrix region, which is gradually refined by an increasing volume fraction of deformation twins (f_T), and $f_T \times \sigma_T$, the contribution from the very thin, high strength deformation twins:

$$\sigma = (1 - f_T) \cdot \left(\sigma_0 + \frac{K_{HP}}{\sqrt{\frac{t}{\beta_1} \cdot \left(\frac{1}{f_T} - 1\right)}} \right) + f_T \cdot \sigma_T \quad (19)$$

where $f_T = \frac{\beta_2 \cdot \beta_3 \cdot M \cdot \varepsilon}{\gamma_T}$. In the above equations, K_{HP} is the coefficient in the Hall-Petch relation (257 MPa $\mu m^{1/2}$), β_1 is a numerical factor related to the shape of the twins ($\beta_1 \approx 1/2$, for a high aspect ratio twin), β_2 is a numerical factor associated with the number of deformation systems activated in the individual grains ($\beta_2 \approx 1/5$, assuming five deformation systems, consisting of four slip systems and one twin system), β_3 is a numerical factor related to the degree to which the uniform deformation conditions are relaxed ($\beta_3 = 1$, for full-constraints conditions), M is the Taylor orientation factor ($M = 3.06$), γ_T is the twinning shear ($\gamma_T = \sqrt{2}/2$), and ε is the applied true plastic strain.

Idrissi et al. [52] studied the structure of deformation twins in two TWIP steels and reported that the deformation twins formed in Fe-20%Mn-1.2%C steel were thinner (20 nm < t_T < 70 nm) and contained a much higher density of sessile dislocations as compared to twins in carbon-free Fe-28%Mn-3.5%Si-2.8%Al steel (100 nm < t_T < 700 nm). They argued that this observation, together with the strain hardening rate being considerably higher (close to G/20) for the Fe-20%Mn-1.2%C TWIP steel, supported the strain hardening model proposed by Gil Sevillano and de las Cuevas.

2.2.4. Controversial issues relating to the role of deformation twinning

There are many observations which suggest that the relation between deformation twinning and strain hardening may be more complex than the models outlined in the foregoing sections, which emphasize the relation between the evolution of the density of deformation twins and the strain hardening. Most TWIP steels retain a large ductility when deformation twinning is restricted, *i.e.* by a change in composition, grain refinement or an increase in temperature. For example, two TWIP steels with the same γ_{isf}, *viz.* Fe-30%Mn and Fe-22%Mn-0.6%C, develop a very different dislocation microstructure, with extensive twinning in Fe-30%Mn and no twinning in Fe-22%Mn-0.6%C [53]. Both steels have a large ductility. Nakano [54] suggested that this was related to the sign of the parameter $-\frac{\Delta G_m}{k_B T}$, the dimensionless driving force for the $\gamma \rightarrow \varepsilon$ transformation, where ΔG_m denotes the Gibbs free energy of the transformation. Using an empirical correlation with the mechanical properties of high Mn steels, Nakano argued that this parameter must be positive, as in the case of Fe-22%Mn-0.6%C, to promote

Please cite this article in press as: B.C. De Cooman, et al., Twinning-induced plasticity (TWIP) steels, Acta Materialia (2017), http://dx.doi.org/10.1016/j.actamat.2017.06.046

deformation twinning.

Another case suggesting that deformation twinning may not necessarily play a key role in the strain hardening of TWIP steels is shown in Fig. 10. It compares the flow curves of Fe-18%Mn-0.6%C-1.5%Al TWIP steel at temperatures in the range from −70 °C to 300 °C. Although in this temperature range γ_{isf} varies significantly, from 17 mJ/m^2 to 82 mJ/m^2, the ductility of the material remains high, even when dynamic strain aging is pronounced, as can be concluded from the serrated deformation curves measured in the high temperature part (100 °C-300 °C) of this temperature range. Deformation twinning is suppressed when $\gamma_{isf} = 45$ mJ/m^2, *i.e.* at 108 °C. This suggests that the deformation twins may not be the key factor responsible for the high strain hardening rate observed for TWIP steels. Other processes leading to a favorable dislocation density evolution and large strain hardening have therefore been proposed. These include short range ordering, dynamic strain aging due to the interaction between mobile dislocations and carbon atoms [55], pseudo-twinning, strengthening associated with the lattice distortion due to a change of the position of an interstitial C atom from an octahedral to a tetrahedral site under twinning shear when the carbon atom resides in the glide plane [56], and stacking fault formation. All of these effects will be considered in the following sections.

2.2.5. Short range ordering

Gerold and Karnthaler [57] have argued that short range ordering (SRO) and short range clustering, rather than the value of γ_{isf}, control the occurrence of planar dislocation glide. According to Fisher [58] short range order, i.e. a local deviation from randomness in the arrangement of atoms on the crystal lattice, results in a strain hardening effect. The mechanism is as follows. The first dislocation on a glide plane experiences an increased resistance against its motion due to the SRO. As the SRO is destroyed by the lead dislocation, the resistance to the motion of subsequent dislocations on the same glide plane is reduced, which is tantamount to softening. This softening favors glide on the glide plane of the initial dislocation. Planar glide, which is known to increase strain hardening, is therefore promoted in the systems where SRO occurs.

It should be mentioned that a competition between the destruction of SRO by moving dislocations and its thermally activated restoration may lead to a negative strain rate sensitivity of the flow stress – an effect akin to dynamic strain aging effect discussed in the following section. Referred to as the pseudo-Portevin-Le Chatelier effect [59], it is associated with discontinuous plastic flow manifesting itself in serrations on the deformation curve.

The distribution of the substitutional solutes Mn, Al, etc. in a TWIP steel is usually assumed to be fully random. The C distribution is however influenced by the strong attractive C-Mn interaction which leads to the formation of C-Mn octahedral complexes, and short range order. The repulsive C-C interaction and the attractive C-Al interaction also promotes SRO in Fe-Mn-C-Al TWIP steel by formation of solute complexes with a structure similar to that of κ-carbide. Choi et al. [60] reported electron diffraction evidence for SRO in a Fe-28%Mn-9%Al-0.8%C steel. Park et al. [61], studied Fe-22%Mn-0.6%C ($\gamma_{isf} = 21.5$mJ/m^2), Fe-22%Mn-3%Al-0.6%C ($\gamma_{isf} = 36.5$mJ/m^2) and Fe-22%Mn-6%Al-0.6%C ($\gamma_{isf} = 50.7$mJ/m^2), and Jin and Lee [62], who studied Fe-18%Mn-0.6%C ($\gamma_{isf} = 17$mJ/m^2), Fe-19%Mn-1%Al-0.6%C ($\gamma_{isf} = 29$mJ/m^2) and Fe-19%Mn-2%Al-0.6%C ($\gamma_{isf} = 36.3$mJ/m^2), analyzed the effect of Al-additions on the strain hardening of TWIP steel. Park et al. [61] reported that planar dislocation glide always occurred before mechanical twinning, independently of the value of γ_{isf}. An increase of γ_{isf} by Al-additions resulted in a more pronounced planar glide and less mechanical twinning. The authors argued that the pronounced planar glide was due to short range ordering.

2.2.6. Dynamic strain aging

Dynamic Strain Aging (DSA) is observed in C-added TWIP steels at room temperature, *i.e.* at a temperature at which the diffusivities of solutes, including that of interstitial carbon, is extremely low and diffusion of C to temporarily arrested dislocations is virtually impossible, as the activation energy for C diffusion in γ-Fe is

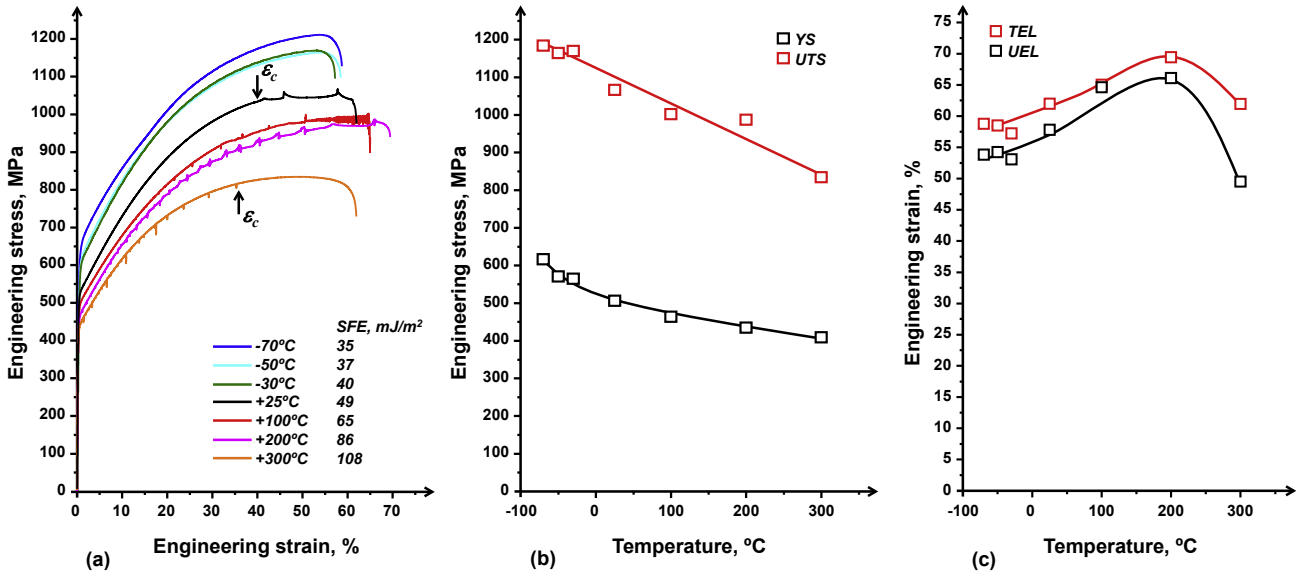

Fig. 10. (a) Engineering stress-strain curves of Fe-18%Mn-0.6%C-1.5%Al TWIP steel in the temperature range of −70 °C to 300 °C as measured at a strain rate of $10^{-3}s^{-1}$. (b) Temperature dependence of the yield stress (YS) and the ultimate tensile stress (UTS). (c) Temperature dependence of the uniform elongation (UEL) and total elongation (TEL). Note in (a) that the stress-strain curves in the range of 25 °C to 300 °C are serrated. The TWIP steel exhibits an inverse behavior for the occurrence of serrations at high temperature: a critical strain (ε_c) of about 40% needs to be reached for the initiation of the serrations at 25 °C, whereas lower onset strains are required at lower temperatures. At 300 °C a critical strain for the termination of serrated yielding is about 35%. It should be noted in (b) that the uniform elongation peaks at a temperature of 200 °C. At this temperature γ_{isf} is approximately 62 mJ/m^2, and deformation twinning is definitely suppressed.

Please cite this article in press as: B.C. De Cooman, et al., Twinning-induced plasticity (TWIP) steels, Acta Materialia (2017), http://dx.doi.org/10.1016/j.actamat.2017.06.046

approximately 1.6 eV. Solute C in fcc Fe-alloys is known to have very low diffusivity at room temperature and interaction of solute C with dissociated dislocations during room temperature deformation will therefore necessarily be of very short range nature. Even if local heating, e.g. due to increased strain rate within a localized deformation band, is taken into consideration, the bulk diffusion of C at room temperature is too limited to allow for a DSA mechanism based on large diffusion distances. Rose and Glover [63] attribute DSA in fcc alloys to the presence of C–vacancy complexes and their rapid reorientation in the stress field of dislocations. They point to the low activation energy for DSA (83 kJ mol^{-1}, or 0.86 eV/atom) and argue that reorientation is due to the movement of a vacancy rather than a C atom. Reorientation of a C atom in a tetragonally distorted $CFe_{6-x}Mn_x$ solute complex by a single diffusional hop to an energetically more favorable neighboring octahedral position relative to the stress field of a partial dislocation or the lattice contraction perpendicular to the stacking fault plane has been proposed as a DSA mechanism [64,65]. DSA is only observed when the C atom reorientation time is shorter than the waiting time of a dislocation at the location of the solute complex. Vacancy-C atom complexes could also cause DSA in TWIP steels, as plastic deformation results in the formation of excess vacancies. DSA associated with such complexes could therefore be observed after a large amount of strain. This is however not observed in practice, as DSA is initiated at very low strains in Fe-22%Mn-0.6%C.

In the semi-empirical analysis of the strain hardening of a wide variety of TWIP steels by Bouaziz et al. [35] the strain hardening appeared to be independent of the stacking fault energy, an observations very aptly referred to as the “carbon paradox” by Allain [66]. Bouaziz et al. [35] see this as an evidence for a mechanism related to solute complexes playing a role in the strain hardening of TWIP steels. Based on a range of TWIP steel compositions, they have proposed the following heuristic equation for the back stress contribution to the strain hardening due to the presence of the deformation twins during uniaxial tensile deformation:

$$\sigma_{BS} = \left[60661 \cdot \left(\frac{\%C}{\%Mn - 5}\right) - 261874 \cdot \left(\frac{\%C}{\%Mn - 5}\right)^2\right] \cdot \varepsilon^{1.75} \tag{20}$$

According to this formula, the back stress is a maximum when the ratio $z = \frac{\%C}{\%Mn-5}$, which the authors refer to as the “equivalent C content”, is equal to 0.016. In this case $\sigma_{BS} = 365$ MPa at a true strain of 0.4. The equation suggests that an increase in the C content beyond this level of m would result in an increase of the strain hardening due to the back stress contribution of the deformation twins. The lines corresponding to constant values of the $\frac{\%C}{\%Mn-5}$ ratio in Fig. 11 are nearly perpendicular to the iso-γ_{isfe} curves, suggesting that strain hardening is γ_{isf}-independent. The effect of C appears to be a result of a complex interplay of multiple effects, involving dynamic strain aging and the effect of C on dislocation mobility and

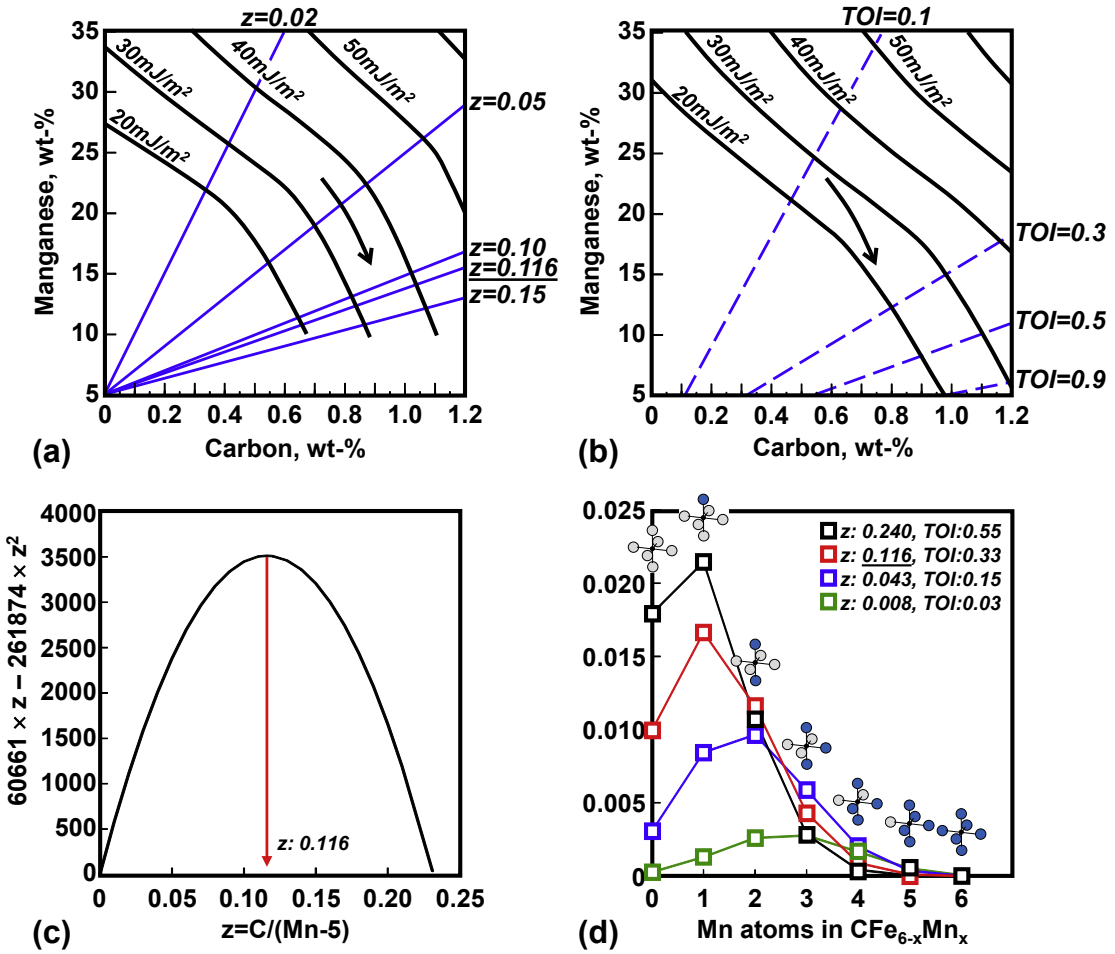

Fig. 11. Iso-γ_{isf} C-Mn composition diagram for Fe-Mn-C showing the direction of increasing strain hardening in C-added high Mn TWIP steels (a) according to Allain et al. [71] and (b) according to Saeed-Akbari et al. [26]. (c) Composition dependence of the m-parameter; and (d) the TOI-parameter dependence of the volume fraction distribution of the various $CFe_{6-x}Mn_x$ complexes.

dislocation patterning. Saeed-Akbari et al. [26] arrived at a similar conclusion regarding the effect of C, which they considered to be related to the formation of C-Mn complexes. They also attempted to relate the strain hardening with the density and distribution of the different $CFe_{6-x}Mn_x$ octahedral complexes, as these are believed to interact with the dislocations. Saeed-Akbari et al. suggested that the population of $CFe_{6-x}Mn_x$ octahedra is a function of the C/Mn atomic ratio, which they refer to as the theoretical ordering index $TOI = \frac{X_C}{X_{Mn}}$. They reported that the highest density of CMn_6 octahedra occurred when TOI was around 0.31.

According to von Appen and Bronkowski [67], the CMn_6 octahedra are the most stable of the various possible $CFe_{6-x}Mn_x$ solute complexes. Lee et al. [64] have used the Grujicic and Owen cell model [68,69] to describe the population of $CFe_{6-x}Mn_x$ octahedra in Fe-18%Mn-0.6%C-1.5%Al. According to that study, the CFe_5Mn_1 and CFe_4Mn_2 octahedra are the most common solute complexes in standard TWIP steels. Internal friction measurements and the occurrence of dynamic strain aging only in C-added TWIP steels, provide experimental support for the presence of $CFe_{6-x}Mn_x$ complexes.

Internal friction measurements are a powerful tool for identifying the nature of point defects and more complex groups of solute atoms in TWIP steels. Thus, it was shown by Lee et al. [64] and Jung et al. [65] that the Finkelstein-Rosin (FR) internal friction peak observed in Fe-18%Mn-0.6%C-x%Al TWIP steel (Fig. 12) can be associated with the stress-induced reorientation of elastic dipoles formed by substitutional–interstitial atom complexes. The presence of point defect complexes involving C which may be the cause of DSA in C-alloyed TWIP steel revealed by internal friction measurements was also confirmed by Mössbauer spectroscopy [64]. This suggests that a pronounced DSA of TWIP steels in the absence of Al additions may result from the interaction of C-Mn complexes

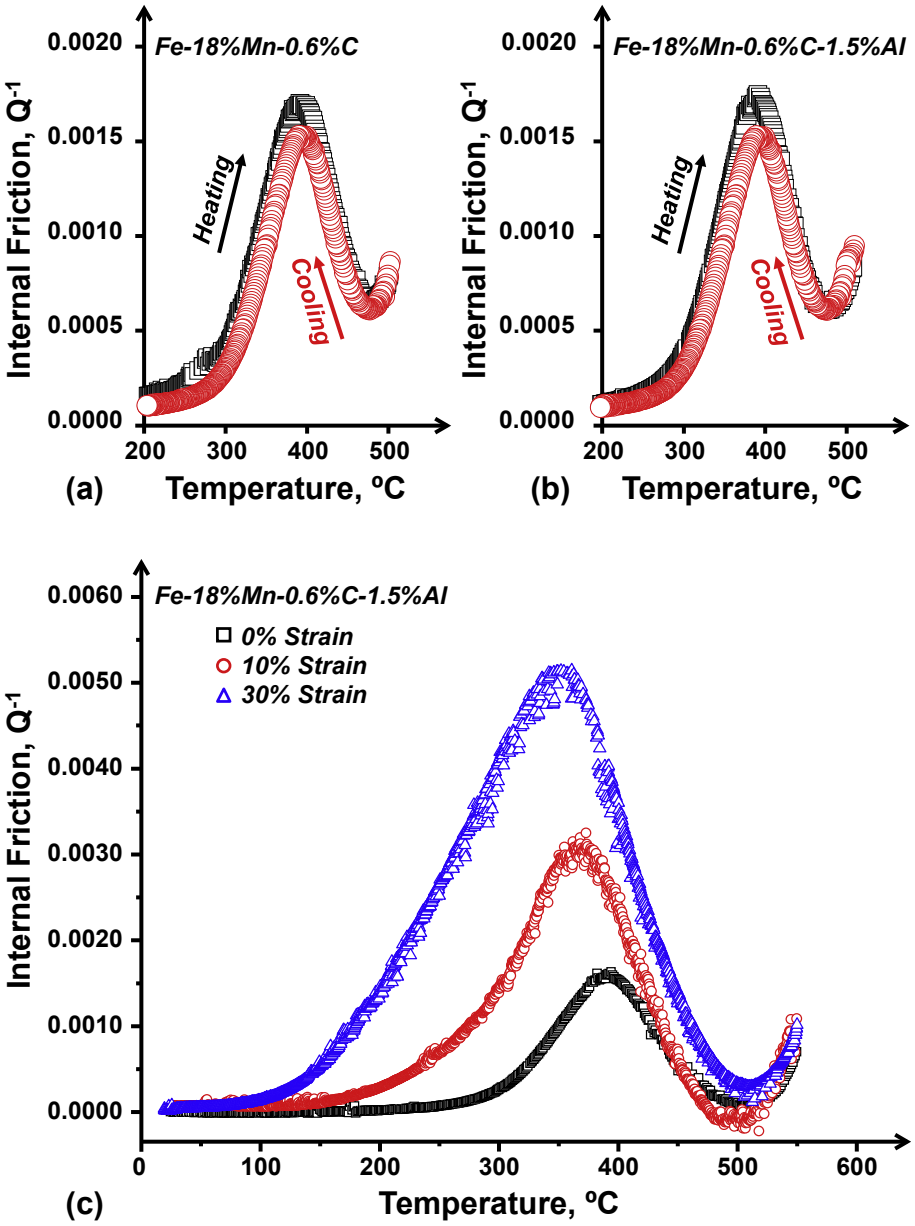

Fig. 12. Internal friction spectrum of TWIP steels [65]. (a) FR relaxation peak in Fe-18%Mn-0.6%C; (b) FR relaxation peak in Fe-18%Mn-0.6%C-1.5%Al at the measurement frequency of about 1 kHz; (c) Enhancement of the FR peak height for Fe-18%Mn-0.6%C-1.5%Al by straining.

Please cite this article in press as: B.C. De Cooman, et al., Twinning-induced plasticity (TWIP) steels, Acta Materialia (2017), http://dx.doi.org/10.1016/j.actamat.2017.06.046

with stacking faults. Indeed, the formation of stable C-Mn complexes due to attractive interaction of C atoms with substitutional Mn atoms leads to a symmetry of the local coordination shells around an interstitial carbon atom which is lower than cubic. This effect gives rise to the formation of an elastic dipole. While an isolated interstitial atom in an fcc metal would not contribute to anelastic relaxation because it occupies an octahedral interstitial site having the same symmetry as the host lattice, an elastic dipole would re-orient under external stress. In the case of fcc lattice of γ-Fe alloys, in which substitutional-interstitial complexes are formed, a FR internal friction peak can be seen as a signature of the resulting elastic dipoles. The peak position at the temperature T_{max} (at the frequency f = 1 kHz) observed in steels is within the temperature range of 470–570 K, depending on the composition of the steel. The activation energy of the FR peak observed in Fe-18%Mn-0.6%C and Fe-18%Mn-0.6%C-1.5%Al (1.2 eV and 1.39 eV, respectively [64,65]) is close to the activation energy for carbon diffusion in alloyed austenitic steels (1.166 eV for γ-Fe-0.6%C [70]). The FR peak was very stable and was not influenced by annealing at high temperatures. It was also not affected by the addition of Al, suggesting that Al atoms are not part of the solute complex giving rise to the peak. The height of the FR peak in the TWIP steels studied was shown to grow with strain, which suggests that the peak stems from the interaction between strain-induced dislocations and solute complexes.

A carbon atom with a shell consisting of one or two manganese atoms is thermodynamically more likely than any other octahedral shell configuration in Fe-18%Mn-0.6%C-1.5%Al TWIP steel. It involves an anisotropic (tetragonal) lattice distortion, which can only be achieved when the solute C is part of a tetragonally distorted point defect complex such as the CFe_5Mn_1 or CFe_4Mn_2 octahedra. The occurrence of serrations on the stress-strain curves also point to dynamic strain aging associated with C-Mn complexes, as no serrations were detected on the stress-strain curves of *C-free* Fe-Mn-Si-Al TWIP steels [3,19,71–74].

Deformation twinning in the presence of interstitial solutes is referred to as pseudo-twinning. In this case C atoms are transferred from octahedral to tetrahedral sites. This mechanism was proposed to cause a strain hardening effect. *Ab initio* calculations show that a random distribution of C results in an increase of γ_{isf} [74], which provides a strong thermodynamic driving force for C to leave the stacking fault plane. This *ab initio* insight has made it possible to understand some apparent inconsistencies in experimental observations. Fig. 13 illustrates how dissociated dislocations incorporate C atoms in the glide plane during their crystallographic glide. This results in a considerable local increase of the stacking fault energy. As the C atoms are transferred to a tetrahedral position during the passage of a stacking fault, they arrive at an intermediate high energy state for interstitial C diffusion. Accordingly, subsequent movement to an octahedral position away from the stacking fault plane does not require the thermally activated overcoming of a high energy barrier associated with this intermediate stage [75]. The passage of a dissociated dislocation will therefore clear its glide plane of all C atoms initially present there, and this will therefore facilitate the glide of subsequent dislocations on the glide plane of this lead dislocation, including the glide on cross slip planes. This results in an increase of the strain hardening due to a limited dynamic recovery and the attendant pronounced planar glide [56] mentioned above. This strain hardening mechanism is dependent on the stacking fault width, the dislocation velocity, and the kinetics of the re-orientation of the C atoms. The mechanism is also expected to be both stress and temperature dependent. It should be noted, however, that there is experimental evidence suggesting that the significance of the pseudo-twinning effect may be overestimated. Indeed C-free TWIP steels studied by Grässel et al. [3] exhibit a high strain hardening *in the absence of C*.

2.2.7. Stacking faults

Perfect dislocations and partial dislocations emitted from grain

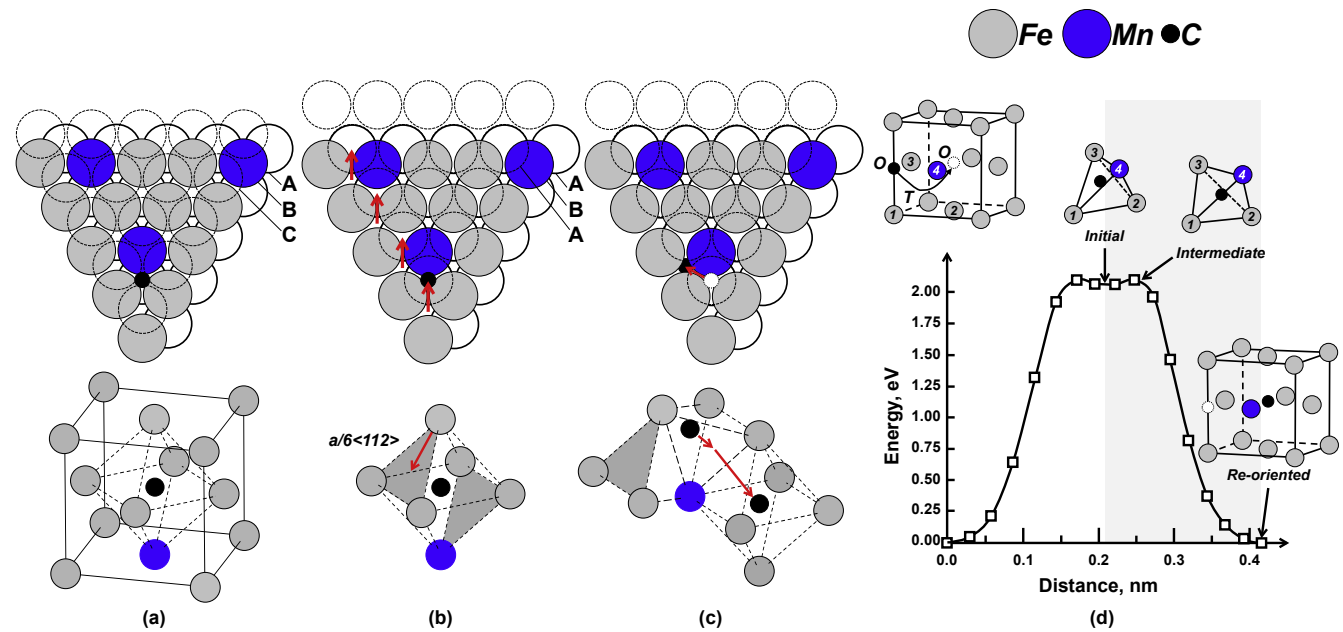

Fig. 13. Schematic illustrating the reorientation of a carbon atom in a tetragonally distorted $CFe_{6-x}Mn_x$ complex during the passage of a partial dislocation. (a) Starting atom arrangement for the $CFe_{6-x}Mn_x$ complex. (b) Lattice shear by a partial dislocation causes the carbon atom to be transferred from an octahedral interstitial position to a high energy tetrahedral position. (c) Single thermally activated hop of the carbon atom to an energetically more favorable neighboring octahedral position out of the stacking fault plane. (d) *Ab initio* calculation of the energy pathway for C atom diffusion in γ-Fe at zero Kelvin temperature. The diagram illustrates that when an interstitial C atom is transferred from an octahedral site to a near-tetrahedral site when it is situated in the stacking fault plane of a leading partial dislocation, no thermal energy needs to be supplied for the C atom to jump to a nearby octahedral site away from the stacking fault plane [75].

Please cite this article in press as: B.C. De Cooman, et al., Twinning-induced plasticity (TWIP) steels, Acta Materialia (2017), http://dx.doi.org/10.1016/j.actamat.2017.06.046

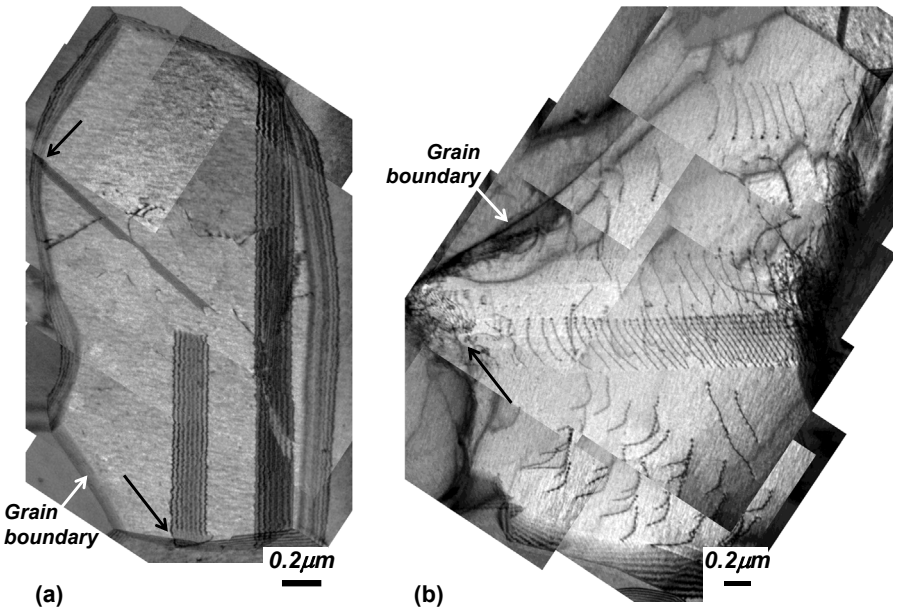

Fig. 14. (a) Stacking faults emitted from grain boundary defect sites (black arrows) in Fe-15%Mn-0.6%C ($\gamma_{isfe} = 14$ mJ/m^2) TWIP steel. (b) Perfect screw dislocation pileup emitted by a grain boundary defect sites (black arrow) in Fe-15%Mn-0.6%C-1.5%Al ($\gamma_{isfe} = 27$ mJ/m^2).

boundary defects and trailing stacking faults are commonly observed in strained TWIP steels (Fig. 14). Isolated stacking faults are known to act as obstacles to dislocations, and they have been reported to contribute to the strain hardening in low stacking fault energy metals and alloys [76]. Although the strain hardening effect of stacking faults *per se* has not yet been analyzed in depth in relation to TWIP steels, it is worthy of note that Meyers et al. [77] and Tian et al. [76] recently proposed that the significant stacking fault contribution to strain hardening in Cu-15%Al ($\gamma_{isfe} = 7$ mJ/m^2) observed from low strains on, may also apply to TWIP steels. They report that while deformation twinning is grain size dependent, twinning being suppressed at small grain size, the strain hardening effect of stacking faults is independent of the grain size. Fig. 15 illustrates the ubiquitous presence of stacking faults in TWIP steels, even at low strains. It also shows that they appear to be emitted from grain boundaries. Thus, Fig. 15 (a), illustrates the emission of a high density of stacking faults from a grain boundary in Fe-18%Mn-0.6%C-1.5%Al TWIP steel at 2% engineering strain. A similar mechanism is also evident in Fig. 14 (a). Clear observations of both stacking faults and twins being emitted form grain boundaries have led Beladi and co-workers [78] to conduct an in-depth analysis of the possible relation between the formation of deformation twins and the boundary characteristics of the grains at which the twins are formed. They report that the 60°{111} annealing twin boundaries were the most likely boundaries to emit deformation twins. This is rather unexpected as 60°{111} twin boundaries are low energy boundaries.

To close this section of the relation between deformation twinning and strain hardening in TWIP steel, it is important to address a number of issues related to the physically-based modeling of the mechanical properties of TWIP steels.

A common problem with the physically-based constitutive equations is the identification of the values of the physical parameters used in the model. An example is the parameter α in the Bailey-Hirsch equation [79]. This parameter enters the relation between the flow stress and the square root of the dislocation density. An overview written by Kang et al. [80] compiles published values for α ranging from 0.1 to 0.5. According to Kuhlmann-Wilsdorf [81], α is equal to 0.3 "within a factor of two". Kuhlmann-Wilsdorf [30] derived the following equation for α for dislocation-cell forming metals:

$$\alpha = \frac{1-\frac{\nu}{2}}{6\cdot\pi\cdot(1-\nu)}\cdot\ln\left(\frac{3}{b\cdot\sqrt{\rho_d}}\right) \tag{21}$$

Assuming $\nu = 0.312$, $b = 0.25$ nm and a value of ρ_d of 10^{13}m^{-2} or 10^{15}m^{-2}, one obtains $\alpha = 0.54$ or $\alpha = 0.39$, respectively. These value are close to $\alpha = 0.4$ used by Allain et al. [34] for Fe-22%Mn-0.6%C TWIP steel, and $\alpha = 0.35$ used by Kim et al. [18] for Fe-18%Mn-0.6% C-1.5%Al TWIP steel.

While constitutive equations that capture the effect of deformation twinning on the mechanical properties of TWIP steels in a semi-phenomenological way are in existence and will be discussed at length below, the models developed so far at the level of dislocation-twin interactions are scarce. They consider only a special case when deformation twinning generates $\Sigma 3\{111\}\langle 110\rangle$-type coherent twin boundaries (CTBs) which act as impenetrable obstacles to dislocations gliding on their slip planes not parallel to the twin plane. The influence of the dislocation-CTB interaction itself is ignored. It is well known that dissociated dislocations which encounter a coherent twin boundary are stopped by the boundary, as illustrated in Fig. 16. As the applied stress increases, the two partial dislocations recombine to a perfect dislocation and the dislocation can either be incorporated in the twin plane or be transmitted through the CTB to form a dissociated screw dislocation in the twin [82–84]. Large scale molecular dynamics (MD) models for the interaction between screw dislocations and CTBs have shown that the spontaneous absorption of the dislocation into the CTB is possible when γ_{isf} is high, as in the case of Al. When γ_{isf} is low, this process requires that a dislocation constriction occurs first. This can result in the absorption of the dislocation into the CTB or transmission into the twin. Sangid et al. [85] have shown by MD simulations and experimental observations that the type of coherent $\Sigma = 3$ twin boundaries created during deformation twinning act as strong obstacles to slip, resulting in a considerable strengthening contribution. Dislocations eventually slip into the

Please cite this article in press as: B.C. De Cooman, et al., Twinning-induced plasticity (TWIP) steels, Acta Materialia (2017), http://dx.doi.org/10.1016/j.actamat.2017.06.046

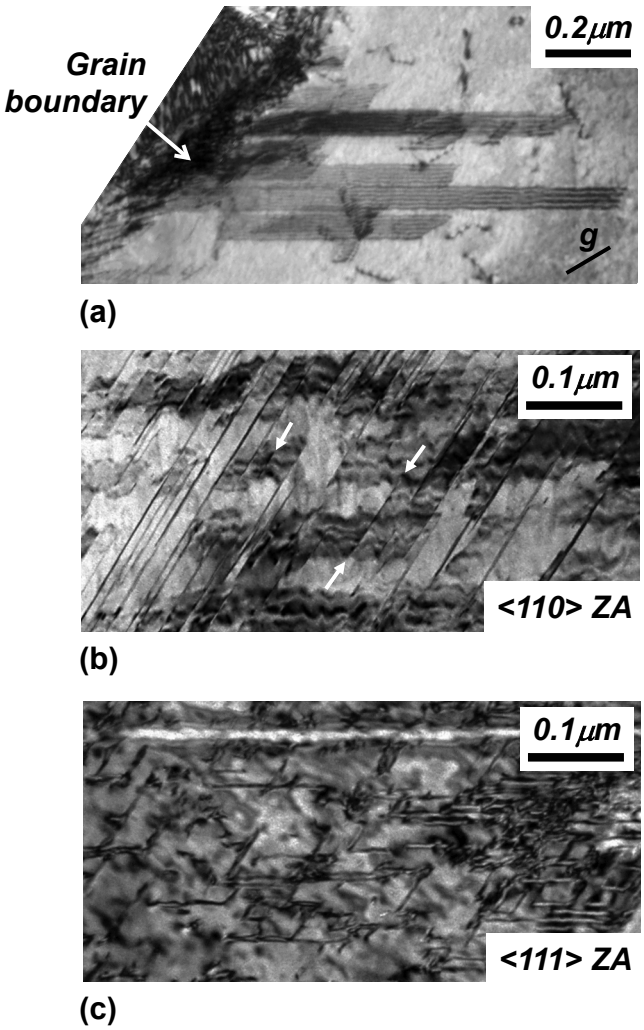

Fig. 15. Illustration of the prevalence of isolated stacking faults in the deformed microstructure of Fe-18%Mn-0.6%C-1.5%Al TWIP steel. (a) Overlapping stacking faults emitted by a grain boundary at low strains. (b) Stacking faults which appear to be associated with the end point of deformation twins at intermediate strains. (c) Regular pattern of interacting stacking faults at high strains.

twin when the imposed load is substantially increased, or when dislocation pileups create a significant local amplification of the imposed stress. Transmission of slip is always associated with the formation of dislocations at the twin boundary. To the best of the authors' knowledge, the TEM observations reported by Idrissi and Schryvers [86] are the only ones which elucidate the interaction between dislocations and deformation twin boundaries in TWIP steels. The authors report that pileups of extended primary dislocations in a Fe-20%Mn-1.2%C TWIP steel impinging on CTBs did not transmit slip into the twins. Neither did they observe transmission of primary screw dislocations into twinned regions by a process which involves the constriction of a dislocation at the CTB and its cross slip into the twin, where it re-dissociates. Extended primary dislocations were, however, found to be incorporated into the CTB plane after recombination of the partial dislocations. The perfect dislocations then nucleated a sessile Frank partial dislocation and a Shockley partial dislocation in the CTB plane (Fig. 17). These observations provide support to some of the MD simulation results reported by Jin et al. [83] for the interaction of non-screw dislocations with CTBs. Idrissi and Schryvers argue that the large number of Frank partial dislocations observed in their TEM analysis of CTBs prevent twin thickening and increase the strain hardening by impeding the interaction between the subsequent dislocations and the CTB.

An additional limitation of the mentioned physically-based constitutive models is that they do not take into account the surprisingly high rate of dislocation multiplication and the activation of multiple glide systems at low strains observed experimentally in TWIP steels. An example is shown in Fig. 18 for a single crystal of a TWIP steel deformed in stage I (easy glide), as documented by the slip lines observed on the sample surface. We note, however, that TEM observations revealed a high density of dislocations in two non co-planar slip systems, which puts in question the identification of strain hardening as being associated with easy glide.

3. The energy of planar faults in a TWIP steel

3.1. Intrinsic vs. extrinsic stacking faults

There are relatively few publications which have addressed the important experimental verification of the character of stacking faults occurring in TWIP steels. Despite the fact that the *intrinsic* and *extrinsic* stacking faults of fcc metals and alloys are believed to be very similar [87] extrinsic stacking faults are not often observed in practice, and a stacking fault in fcc metals and alloys is usually assumed to be intrinsic. Vercammen et al. [88] were the first to report that the stacking faults in C-free Fe-30%Mn-3%Al-3%Si TWIP-steel were extrinsic. Idrissi et al. [89] observed that in C-free Fe-19.7%Mn-3.1%Al-2.9%Si TWIP steel the character of the stacking fault changed with temperature: the stacking faults were extrinsic at low temperature and intrinsic at high temperature. Whereas deformation at room temperature resulted in the strain-induced transformation to ε-martensite and the occurrence of stacking faults which were predominantly extrinsic in nature, deformation at high temperature (160 °C) resulted in the formation of

Fig. 16. Transmission electron micrographs showing a pileup of sixteen identical a/6<112>{111}-type partial dislocations impinging on a deformation twin. (a) Partial dislocation contrast. (b) Stacking fault contrast. (c) Tilted view of a deformation twin showing evidence of the incident slip dislocation pileup generating a dislocation in the twin (arrow A), dislocations crossing the twin between the two coherent twin planes (arrow B), and an array of straight boundary dislocations in the twin/matrix interface plane (arrow C).

Please cite this article in press as: B.C. De Cooman, et al., Twinning-induced plasticity (TWIP) steels, Acta Materialia (2017), http://dx.doi.org/10.1016/j.actamat.2017.06.046

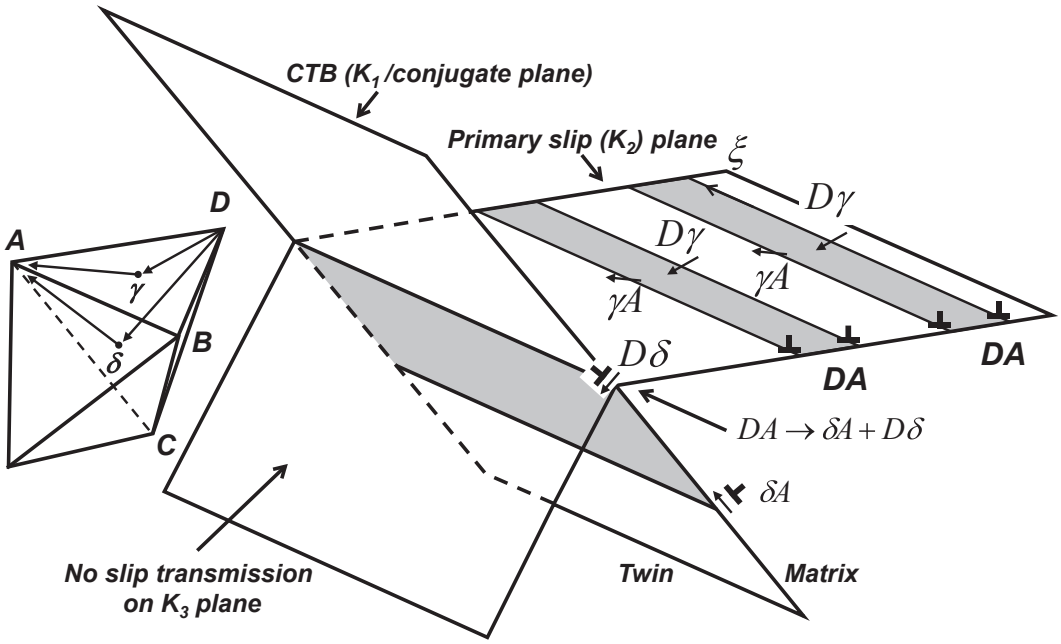

Fig. 17. Schematic of the dislocation/CTB interaction observed by Idrissi and Schryvers [86]. Multiple similar interactions result in a large density of sessile Frank partial dislocations located in the twin boundary.

deformation twins and stacking faults, which were all intrinsic. The authors suggested that at low temperatures ε-martensite is nucleated at extrinsic stacking faults. This viewpoint is at odds with the commonly accepted view that ε-martensite is formed by a specific sequence, *i.e.* the passage of one partial dislocation trailing an intrinsic stracking fault on every other {111} slip plane. Tisone has suggested that this may be due to a difference in the temperature dependence of γ_{esf} and γ_{isf} [90]. Idrissi et al. [91] also claimed, using the analysis of the stacking fault fringe contrast in transmission electron microcopy, that the stacking faults used to determine γ_{isf} for C-alloyed Fe-20%Mn-1.2%C TWIP steel ($\gamma_{isf} = 15$ mJ/m^2) were all intrinsic. Karaman et al. [92] observed extrinsic stacking faults in 12.3%Mn-1.1%C Hadfield steel single crystals ($\gamma_{esfe} = 23$ mJ/m^2). Mahato et al. [19] analyzed dissociated dislocations in Fe-27%Mn-2.5%Si-3.5%Al TWIP steel. These authors frequently observed extrinsic stacking faults, which they considered to be three-layer twin embryos. Pierce et al. [93] used the diffraction contrast method to determine the character of the stacking faults in the Fe-22%Mn-3%Al-3%Si, 25%Mn-3%Al-3%Si, and 28%Mn-3%Al-3%Si alloys, and identified the stacking faults as being intrinsic in all cases.

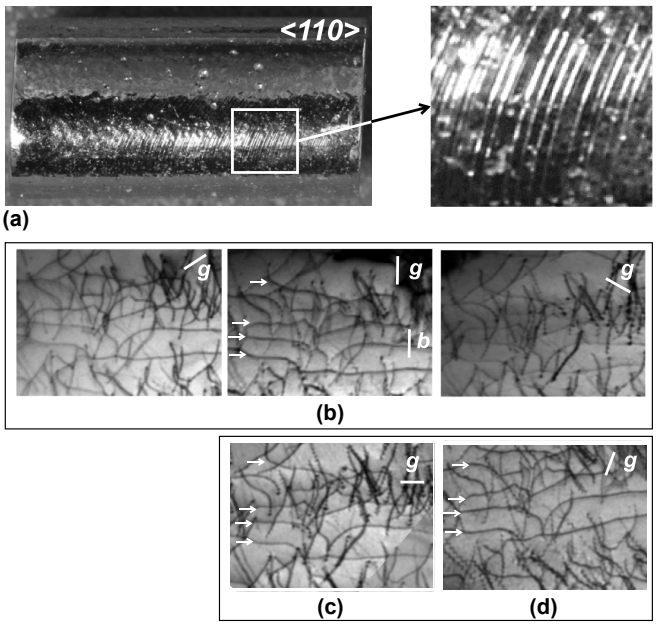

Fig. 18. (a) TWIP steel single crystal after 4% strain under compression in the ⟨110⟩ direction. The parallel slip traces at the crystal surface, indicative of planar dislocation glide, are clearly visible. (b) Transmission electron micrographs using {220}-type reflections showing the presence of long edge-type glide dislocations (white arrows) in the macroscopic primary slip plane of the sample shown in (a). The micrographs also reveal the presence of forest dislocations on an intersecting glide plane. (c) and (d) are views of the same area as in (b) after tilting the sample from the ⟨111⟩ zone axis to two different ⟨112⟩ zone axes. The micrograph shows that the shorter dislocation segments are forest dislocations which intersect the primary glide plane. Note the absence of dislocation pileups. As the sample was strained to just 4%, *i.e.* in the easy glide stage (Stage I hardening), the micrographs are also evidence for multiple slip in the early stages of deformation, despite the fact that the macroscopic single crystal appears to deform in single slip. (Image and micrographs courtesy of Dr.-Ing. Stephanie Sandlöbes, RWTH Aachen).

3.2. Stacking fault energy computations

Classical texts on the mechanical behavior of fcc metals and alloys consider that the intrinsic stacking fault energy, γ_{isf}, is the key parameter controlling the emergence of plasticity mechanisms other than dislocation glide. γ_{isf} is considered to be the parameter which controls whether plasticity is carried by glide of perfect dislocations, dissociated dislocation glide, or deformation twinning resulting from the motion of partial dislocations trailing stacking faults on parallel glide planes. A low energy of intrinsic stacking faults ($\gamma_{isf} < 15$ mJ/m^2) results in stress- or strain-induced solid-solid phase transformations (TRIP-effect), an intermediate range of γ_{isf} (15 mJ/m^2 < γ_{isf} < 45 mJ/m^2) is associated with mechanical twinning, and a high level of γ_{isf} ($\gamma_{isf} > 45$ mJ/m^2) leads to perfect dislocation glide and shear banding. The temperature plays a key role in the relation between γ_{isf}, deformation twinning, and plasticity of TWIP steels, as the magnitude of γ_{isf} increases with

$$\gamma_{isf} = n\cdot\rho\cdot\Delta G_C^{\gamma\to\varepsilon}$$
$$\frac{d\gamma_{isf}}{dT} = n\cdot\rho\cdot\frac{d\left(\Delta H_C^{\gamma\to\varepsilon} - T\cdot\Delta S_C^{\gamma\to\varepsilon}\right)}{dT} = -n\cdot\rho\cdot\Delta S_C^{\gamma\to\varepsilon} = -\frac{8}{\sqrt{3}}\cdot\frac{1}{a_\gamma^2\cdot N_A}\cdot\Delta S_C^{\gamma\to\varepsilon} \quad (22)$$

temperature. This can be shown by considering Hirth's definition of an intrinsic stacking fault as a thin plate of the hcp ε-phase [94]: where a_γ is the lattice parameter of the γ-phase, N_A is Avogadro's number, and $\Delta G_C^{\gamma\to\varepsilon}$, $\Delta H_C^{\gamma\to\varepsilon}$, and $\Delta S_C^{\gamma\to\varepsilon}$ are, respectively, the Gibbs free energy, enthalpy, and entropy changes associated with the $\gamma\to\varepsilon$ transformation. For the case when the γ-phase is the thermodynamically stable phase, the inequalities $\Delta G_C^{\gamma\to\varepsilon} > 0$, $\Delta S_C^{\gamma\to\varepsilon} < 0$, and $d\gamma/dT > 0$ hold. At high temperatures, perfect dislocation glide with frequent cross-slip is expected when γ_{isf} becomes larger than 45 mJ/m^2. At lower temperatures, when 15 mJ/m^2 < γ_{isf} < 45 mJ/m^2, large dislocation dissociation widths lead to the nucleation of twins and their growth by thickening. As the temperature is further reduced, ε-martensite formation gradually replaces deformation twinning. The analysis of data on a low-γ_{isf} single crystal alloy prompted Venables [95] to assume a parabolic relationship between the twinning stress and γ_{isf} - despite a considerable scatter in the available data. Remy and Pineau [96,97] also emphasized the role of γ_{isf} by arguing that the occurrence of deformation twinning required γ_{isf} to be within a specific range: 20 mJ/m^2 < γ_{isf} < 50 mJ/m^2. In the case of high Mn TWIP steels, various γ_{isf}-ranges have been proposed as the ones in which the TWIP mechanism is activated: 12–35 mJ/m^2 [71], 25–60 mJ/m^2 [96], 25–80 mJ/m^2 [97]. The occurrence of strain-induced transformations has also been linked to the magnitude of γ_{isf} [98,99]. Although these observations are largely empirical, they have contributed to the wide acceptance of Venables' opinion on the subject and it is therefore not surprising that major efforts have been made to calculate the temperature and composition dependence of γ_{isf} for TWIP steels in order to predict their mechanical properties. The empirically determined γ_{isf}-ranges in which specific deformation modes are activated, are shown in Fig. 19 [34,82,97,101].

There are two basic computational approaches to determine γ_{isf}: the thermodynamic approach based on the Olson-Cohen model for the intrinsic stacking fault in fcc metals and alloys [102] and the *ab initio* approach based on the determination of key intrinsic energy barriers in the generalized stacking fault energy surface.

3.2.1. Thermodynamic approach

In the thermodynamic approach, the intrinsic stacking fault energy is computed by means of the CALPHAD method used in modeling the equilibrium thermodynamic properties of multicomponent alloys. The CALPHAD method employs experimental and theoretical information to obtain a complete thermodynamic description of the phase equilibria and the thermo-chemical properties of alloy systems. This thermodynamic description is provided in terms of the Gibbs free energy of each phase, expressed

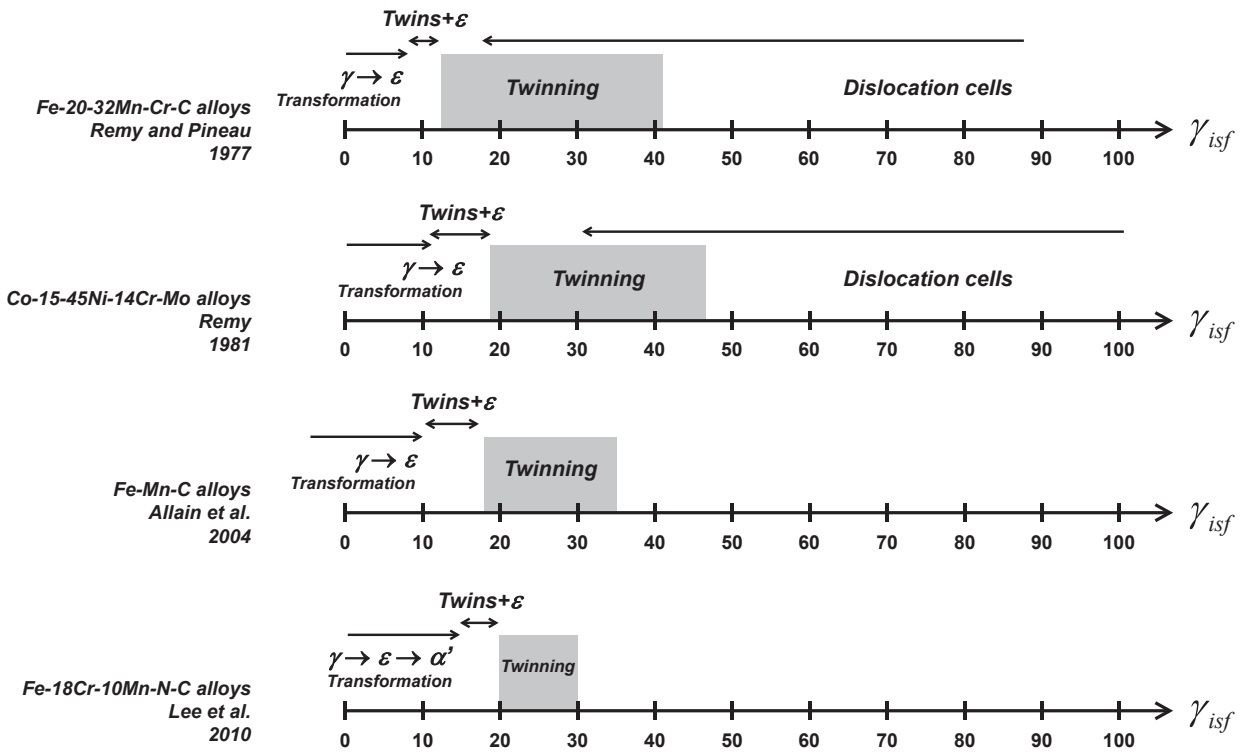

Fig. 19. Ranges of the intrinsic stacking fault energy γ_{isf} for phase transformation, deformation twinning, and dislocation glide in fcc γ-Fe alloys reported in the literature for Fe-(20-32)Mn-Cr-C alloys [96], Co-15-45Ni-14Cr-Mo alloys [82], Fe-Mn-C TWIP steels [34], and Fe-18Cr-10Ni-C-N alloys [101]. The relation between the γ_{isf} axis and $\Delta G^{\gamma\to\varepsilon}$ is also indicated, assuming that $2\times\sigma^{\gamma/\varepsilon} = 15$ mJ/m^2.

as a function of composition and temperature. Extrapolation or interpolation makes it possible to compute thermodynamic properties when no experimental data is available. This approach has been used for all the thermodynamic calculations of γ_{isf} of high Mn TWIP steels by employing the sub-regular solution model approximation. In the thermodynamic approach, γ_{isf} is calculated based on the equilibrium thermodynamic formalism originally proposed by Olson and Cohen [102], which separates the stacking fault formation energy into contributions from the Gibbs free energy difference between the hexagonal close-packed (hcp) and face-centered cubic (fcc) phases, based on Hirth's definition of an intrinsic stacking fault as a thin plate of the hcp ε-phase [94], cf. Eq. (22), as extended by Olson and Cohen [102] to include the γ/ε interface energy:

$$\gamma_{isf} = 2\cdot\frac{4}{\sqrt{3}\cdot a^2\cdot N_A}\cdot \Delta G_C^{\gamma\rightarrow\varepsilon} + 2\cdot\sigma^{\gamma/\varepsilon} \tag{23}$$

Here, $\Delta G_C^{\gamma\rightarrow\varepsilon}$ is the chemical driving force for the γ→ε transformation, i.e the difference between the Gibbs free energy of the γ-phase and the ε-phase. $\sigma^{\gamma/\varepsilon}$ is the γ/ε interface energy. The factor 2 in the first term on the right-hand side of the equation is the number of close-packed planes of the hcp ε-phase. The equation is for an ideal stacking fault, i.e. it does not take into account the effect of partial dislocations, the change in the atomic density in the stacking fault plane and the possible effect of an externally imposed stress on the Gibbs free energy balance. The molar surface density ρ in the {111} plane (in moles per unit area) is taken as

$$\rho = \frac{4}{\sqrt{3}\cdot a_\gamma^2\cdot N_A} \tag{24}$$

The lattice constant a_γ of TWIP steels typically equals about 0.36 nm. The temperature and composition dependence of the Gibbs free energy for the γ-phase can easily be determined using the CALPHAD approach. This is not the case for the ε-phase. For the Fe-Mn system ε-martensite formation data is used, based on the assumption that, above the Néel temperature, the free energies of the γ-phase and the ε-phase are equal at the temperature T_0, which is located midway between the $A_S^{\varepsilon\rightarrow\gamma}$ and $M_S^{\gamma\rightarrow\varepsilon}$ transformation temperatures. The driving force for the γ→ε martensitic transformation is small, approximately 70 J/mol for Fe-17%Mn, and it is not dependent on the Mn content [103]. The addition of C strongly decreases $A_S^{\varepsilon\rightarrow\gamma}$ and $M_S^{\gamma\rightarrow\varepsilon}$. C also increases the driving force to approximately 300 J/mol for a 0.6 mass-% addition of C to Fe-17%Mn, indicating that C is a strong γ-stabilizing alloying addition.

The lattice parameter is influenced by the composition [104–108]. Fig. 20 shows the effect of C, Mn, Al, and Si on the lattice parameter of TWIP steels. Fig. 20 (a) includes room temperature and low alloy content extrapolations for γ-Fe-C and γ-Fe-Mn binary alloys.

Equation (23) was further developed to include magnetism, strain, and grain size effects:

$$\gamma_{isf}^{\infty} = 2\cdot\frac{4}{\sqrt{3}\cdot a^2\cdot N_A}\cdot \Delta G^{\gamma\rightarrow\varepsilon} + 2\cdot\sigma^{\gamma/\varepsilon}$$

$$\gamma_{isf}^{\infty} = 2\cdot\frac{4}{\sqrt{3}\cdot a^2\cdot N_A}\cdot \left(\Delta G_C^{\gamma\rightarrow\varepsilon} + \Delta G_{Mag}^{\gamma\rightarrow\varepsilon} + E_S^{\gamma\rightarrow\varepsilon} + \Delta G_{ex}\right) + 2\cdot\sigma^{\gamma/\varepsilon} \tag{25}$$

Both the γ and the ε phase undergo an anti-ferromagnetic-to-paramagnetic transformation. $\Delta G_{Mag}^{\gamma\rightarrow\varepsilon}$ is the Inden-Hillert-Jarl description of the difference of the magnetic contributions to the Gibbs free energy of the two phases [109,110]. $E_S^{\gamma\rightarrow\varepsilon}$ is the strain energy resulting from the shear deformation and the lattice compression due to the difference in atomic density between the γ and the ε phase. This strain increases the energy of the stacking fault region. This term was analyzed in detail by Olson and Cohen [102], as well as by Cotes et al. [111] and Müllner et al. [112]. Various methods, usually based on the Eshelby inclusion theory, have been proposed to calculate $E_S^{\gamma\rightarrow\varepsilon}$. These are listed in Table 1. The equations generally predict that the strain contribution is small, and independent of the Mn content. Note that the strain energy equations do not take into account the elastic strain associated with the partial dislocations involved in the formation of the stacking fault during plastic deformation.

The grain size is expected to influence dislocation glide, stacking fault formation and deformation twinning, but there are also reports of an unexpected influence of the grain size on γ_{isf}. Volosevich et al. [113] were the first to report an effect of the grain size on the

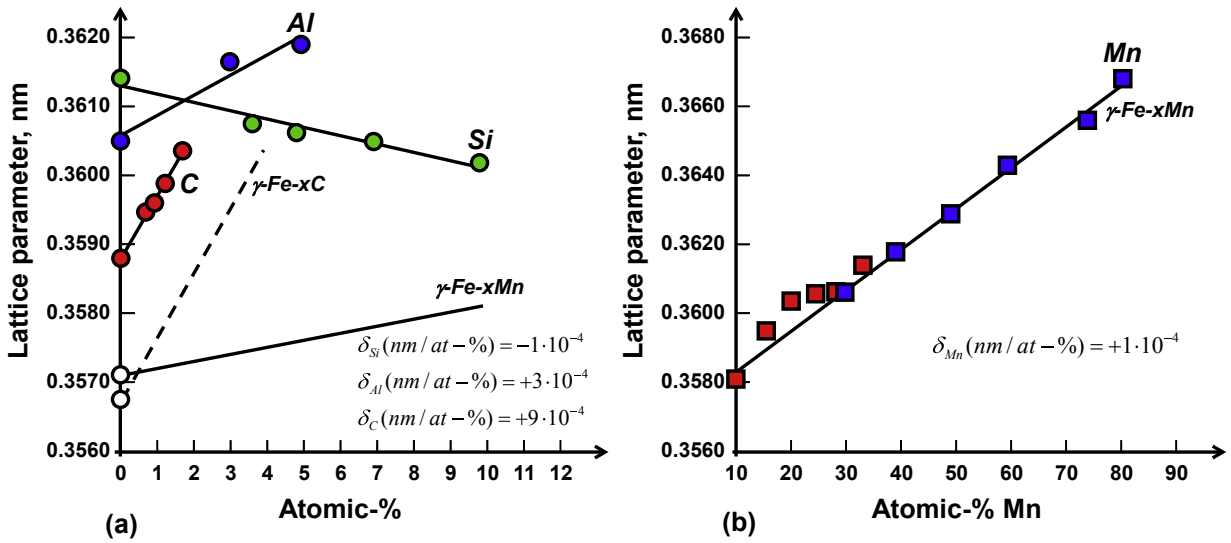

Fig. 20. (a) Effect of solute C [104], Al [105] and Si [106] on the lattice parameter of γ-Fe-Mn alloys at room temperature. The data for the binary γ-Fe-C and γ-Fe-Mn alloys are extrapolations from high temperature and high Mn content, respectively [106]. (b) Effect of the Mn content on the lattice parameter of binary γ-Fe-Mn alloys at room temperature [106,108].

Table 1
Review of the proposed methods for calculating the contribution of the free energy of the $\gamma \rightarrow \varepsilon$ transformation to the stacking fault strain energy. Here V_m^{fcc}, V_m^{hcp} are the molar volumes of the fcc and hcp phases, respectively; the Poisson's ratio ν equals 0.333, and the shear modulus G equals 74 GPa. Lattice contraction normal to the stacking fault plane was estimated as ε_{33}~0.01 [102] and ε_{33}~0.02 [111]. NA is the Avogadro number, and c_{fcc} is the c-axis lattice parameter of the conventional hexagonal unit cell of the fcc crystal structure.

	Shear: $E_{shear}^{\gamma\rightarrow\varepsilon}$	Dilatation: $E_{dilatation}^{\gamma\rightarrow\varepsilon}$
Olson-Cohen Spherical [102]	$E_{shear}^{\gamma\rightarrow\varepsilon} = \frac{7-5\nu}{15\cdot(1-\nu)}\cdot\frac{2}{3}\cdot G\cdot V_m^{fcc}\cdot\varepsilon_{33}^2$	$E_{dilatation}^{\gamma\rightarrow\varepsilon} = \frac{2\cdot(1-\nu)}{9\cdot(1+\nu)}\cdot G\cdot V_m^{fcc}\cdot\left(\frac{V_m^{hcp}-V_m^{fcc}}{V_m^{fcc}}\right)^2$
Cotes et al. Spherical [111]	Olson-Cohen method, with $\varepsilon_{33} = \frac{c^{fcc}-c^{hcp}}{c^{fcc}}$ $c^{fcc} = \frac{2\cdot a_{fcc}}{\sqrt{3}}$	Olson-Cohen method, with $V_m^{hcp} = \frac{\sqrt{3}}{4}(a^{hcp})^2 c^{hcp}\cdot N_A$ $V_m^{fcc} = (a^{fcc})^3\cdot N_A$
Müllner-Ferreira Isotropic theory Platelet [112]	$E_S^{\gamma\rightarrow\varepsilon} = 2\cdot d_{\{111\}}\cdot\frac{G\cdot\varepsilon^2}{4\cdot(1-\nu)}$ $d_{\{111\}} = \frac{a_{fcc}}{\sqrt{3}}$	

stacking fault energy. They explained their observations for the grain size dependence of γ_{isf} of Fe-17.8%Mn-0.47%C steel by (i) a higher solute C content obtained in small grained samples due to the thermal processing of their materials which involved a quenching step, and (ii) the presence of grain size dependent internal stresses which caused a change in the dislocation dissociation width. Takaki et al. [114], and Lee and Choi [115] proposed to take the grain size effect into account by considering the influence of the grain size on the $\gamma \rightarrow \varepsilon$ transformation start temperature through a grain size-dependent excess free energy term:

$$\Delta G_{ex}^{GS}(J/mol) = 170.06\cdot e^{\frac{d(\mu m)}{18.55}} \tag{26}$$

Such an extra term in the Gibbs free energy was introduced originally by Jun and Choi [116] to take into account the effect of the grain size on γ_{isf} for Fe-Mn alloys, and it has been used by others, too [117,118]. The grain size effect on the transformation kinetics can be rationalized as follows. When the kinetics are controlled by the autocatalytic propagation of the transformation from one grain to the next, small grain size will inhibit the transformation in the same way the Hall-Petch effect inhibits propagation of plastic deformation from grain to grain. While this explanation is plausible conceptually, the grain size effect remains poorly understood from a thermodynamic viewpoint.

The interfacial energy $\sigma^{\gamma/\varepsilon}$ is also a poorly defined parameter and it is often adjusted to reach better agreement with the experimental data. Reported $\sigma^{\gamma/\varepsilon}$ values for Fe-Mn alloys are in the range of 5–30 mJ/m^2 [111,113,118]. Pierce et al. reported values for $\sigma^{\gamma/\varepsilon}$ in the range of 15–33 mJm^{-2} for Fe-Mn alloys, and 8–12 mJm^{-2} for TWIP steels [93]. There is no experimental technique to determine $\sigma^{\gamma/\varepsilon}$ directly. Theoretical values from *ab initio* calculations are not yet available either, although the interface energy term $\sigma^{\gamma/\varepsilon}$ should be approximately similar to γ_{twin}, the energy of a coherent twin. This has resulted in a fundamental uncertainty in the value of γ_{isf} based on the thermodynamic approach. A value of 10 mJ/m^2 appears to be a reasonable choice in the case of Fe-Mn-C and Fe-Mn-Al-C TWIP steels [119,120]. Pierce et al. [93] discussed the possibility of determining $\sigma^{\gamma/\varepsilon}$ experimentally, through measurements of γ_{isf} by X-ray diffraction or high resolution electron microscopy techniques. Once the experimental value of γ_{isf} is known, $\sigma^{\gamma/\varepsilon}$ can be calculated by inverting Eq. (25):

$$\sigma^{\gamma/\varepsilon} = \frac{1}{2}\cdot\left(\gamma_{isf} - 2\cdot\left(\Delta G_C^{\gamma\rightarrow\varepsilon} + \Delta G_{Mag}^{\gamma\rightarrow\varepsilon} + E_S^{\gamma\rightarrow\varepsilon} + \Delta G_{ex}^{GS}\right)\right) \tag{27}$$

Fig. 18 shows that, in the Olson-Cohen model for γ_{isf}, the deformation-induced $\gamma \rightarrow \varepsilon$ transformation is possible in metastable austenitic Fe alloys because γ_{isf} can still be positive when $\Delta G^{\gamma\rightarrow\varepsilon}$ is negative, due to the relatively large contribution of the interface energy term $2 \times \sigma^{\gamma/\varepsilon}$.

Geissler et al. [121] have pointed out that ambiguities in the Olson-Cohen formalism produce contradictions. According to them, the inclusion of a major interface energy term in the model is inconsistent with the requirement that the interface energy should be three orders of magnitude smaller than γ_{isf}, i.e. approximately 0.5 mJ/m^2. They conclude that the use of $\sigma^{\gamma/\varepsilon}$ leads to an overestimate of γ_{isf} and that it can only be considered as a correction term without a direct physical meaning. Li et al. [122] also questioned the physical meaning of $\sigma^{\gamma/\varepsilon}$ and regarded it as a correction term. According to them, the contribution of the interface energy to $\sigma^{\gamma/\varepsilon}$ is small, in the range of 1–2 mJ/m^2. In their view, $\sigma^{\gamma/\varepsilon}$ is not interface energy related, but is rather a correction term of a volumetric origin. It stems from the need to calculate the free energy difference $\Delta G^{\gamma\rightarrow\varepsilon}$ for the same interatomic distance in the γ and ε phase and not for the equilibrium interatomic distance for each bulk phase at equilibrium.

The *ab initio* calculations of $\sigma^{\gamma/\varepsilon}$ reported by Lee et al. [123] for pure γ-Fe at zero Kelvin indicate a very large negative value of −241 mJ/m^2. This value is however not inconsistent with the value of γ_{isf} of −380 mJ/m^2 obtained by *ab initio* calculations for pure γ-Fe at 0 K, if one considers the well-known approximations $\gamma_{isf} \approx 2 \times \gamma_{twin}$ and $\sigma^{\gamma/\varepsilon} \approx \gamma_{twin}$.

Talonen and Hänninen [124] made an interesting observation related to the equilibrium width of overlapping stacking faults in stress-free conditions, which also illustrates the importance of the quantity $\sigma^{\gamma/\varepsilon}$ in low γ_{isf} situations. Neglecting the interaction between the partial dislocations, they derive the following equation for the dependence of the equilibrium width w on the number of overlapping intrinsic stacking faults N:

$$w = \frac{N\cdot G\cdot b_p^2}{2\cdot\pi\cdot\left(N\cdot\left(\gamma_{isf} - 2\cdot\sigma^{\gamma/\varepsilon}\right) + 2\cdot\sigma^{\gamma/\varepsilon}\right)}\cdot\left(\frac{3}{4} - \frac{1}{4\cdot(1-\nu)}\right) \tag{28}$$

Here b_P denotes the magnitude of the Burgers vector of partial dislocations. When the volume contribution to γ_{isf} is lower than the surface energy contribution $2 \times \sigma^{\gamma/\varepsilon}$, the overlap of additional fault planes causes w to diverge. Talonen and Hänninen [124] consider that the formation of ε-martensite, i.e. the overlapping of intrinsic stacking faults on every second {111}-type plane is a special case of this situation. They also consider a set of N dissociated dislocations forming overlapping intrinsic stacking faults on successive planes, i.e. a twin, and derive the following equation for the dependence of the twin width w on N in equilibrium:

Please cite this article in press as: B.C. De Cooman, et al., Twinning-induced plasticity (TWIP) steels, Acta Materialia (2017), http://dx.doi.org/10.1016/j.actamat.2017.06.046

$$w = \frac{N \cdot G \cdot b_P^2}{4 \cdot \pi \cdot \sigma^{\gamma/\varepsilon}} \cdot \left(\frac{3}{4} - \frac{1}{4 \cdot (1-\nu)} \right) \quad (29)$$

The equation implies that, if the interaction between the partial dislocations is ignored, the energy of the twin is not twin volume dependent and that it has a constant value of $2 \times \sigma^{\gamma/\varepsilon}$ determined by the surface energy. It also implies that when the volume contribution to γ_{isf} is higher than the surface energy contribution $2 \times \sigma^{\gamma/\varepsilon}$, the overlap of additional fault planes causes w to increase very gradually. Fig. 21 illustrates the fundamental difference in the equilibrium widening behavior in the case of overlapping stacking faults and twin formation.

Two points are worth mentioning. First, it is important to realize that the CALPHAD method relies on the thermodynamic parameters in the databases used. We note specifically that the expression for the excess energy difference between the fcc and hcp phase in the Fe-Mn system in the TCFE7 database differs from that proposed elsewhere in the literature. Second, the Olson and Cohen thermodynamic formalism has been claimed to be ambiguous, especially in relation to the use of large $\sigma^{\gamma/\varepsilon}$ values [121]. Still, this approach has been used to model the composition and temperature dependence of γ_{isf} with considerable success. A few notable examples are as follows. A model developed by Allain et al. gives the composition and temperature dependence of γ_{isf} for Fe-(10–35)%Mn-(0–1.2)%C TWIP steels [71]. The model due to Dumay et al. focusses on the effect of alloying additions of Al, Cr, Cu and Si on the stacking fault energy of the Fe-22%Mn-0.6%C ($\gamma_{isf} = 23$ mJ/m^2) TWIP steel [125]. The model developed by Saeed-Akbari [117] addresses the Fe-Mn-C and Fe-Mn-Al-C TWIP steels. While the previous models were developed explicitly for high Mn TWIP steels, that by Curtze et al. [126] applies to a wide range of complex austenitic Fe-Cr-Ni-Mn-Al-Si-Cu-C-N alloys. Curtze and Kuokkala [127] have also applied their model specifically to low-C, high-Mn Fe-(25–28)%Mn-(1.6–4.1)%Al-0.08%C TWIP steel. Nakano and Jacques [128] proposed an alternative model for the stacking fault energy calculations for Fe-Mn and Fe-Mn-C alloys after a thorough re-evaluation of the available thermodynamic parameters. Using improved parameters for the Mn-C and Fe-Mn-C systems provided by Djurovic et al. [129,130], Pierce et al. evaluated the stacking fault energy for Fe-Mn-Al-Si-C alloys [93]. Their model correctly predicts the experimentally observed influence of Si on the stacking fault energy. They carried out an in-depth determination of the value of the interfacial energy for various high Mn TWIP steels, which they report to be in the range of 8.6–11.8 mJ/m^2 for Fe-18%Mn-0.6%C-(0–1.5)%Al/Si TWIP steel. They also found a strong correlation between the interfacial energy $\sigma^{\gamma/\varepsilon}$ and the difference in free energy between the fcc γ-phase and hcp ε-phase, $2 \times \rho \times (\Delta G_C^{\gamma \to \varepsilon} + \Delta G_{Mag}^{\gamma \to \varepsilon})$.

Table 2 provides a survey of the main aspects of these three key studies, and Fig. 22 compares some of their results. In the figures the line for alloy compositions with $M_s^{\gamma \to \varepsilon} = RT$ (where R is the gas constant and T the absolute temperature) is also indicated [131]. This line delineates the limits for thermal ε-martensite formation. Olson and Cohen have suggested that γ_{isf} is close to zero at the $M_s^{\gamma \to \varepsilon}$ temperature [102]. The composition dependence of $M_s^{\gamma \to \varepsilon}$(K), the temperature of the martensitic $\gamma \to \varepsilon$ transformation, is given by a heuristic relation [131]:

$$\begin{aligned} M_s^{\gamma \to \varepsilon}(\mathrm{K}) = 576 &- 489\%\mathrm{C} - 9.1\%\,\mathrm{Mn} + 21.3\mathrm{Al} - 17.6\%\,\mathrm{Ni} \\ &- 9.2\%\,\mathrm{Cr} + 4.1\%\,\mathrm{Si} - 19.4\,\%\,\mathrm{Mo} - 1\%\,\mathrm{Co} \\ &- 41.3\,\%\mathrm{Cu} - 50\,\%\,\mathrm{Nb} - 86\,\%\mathrm{Ti} - 34\,\%\,\mathrm{V} - 13\%\,\mathrm{W} \end{aligned}$$

Here the concentrations are in mass-%. A comparison between the experimental and the calculated values of γ_{isf} is shown in Fig. 23. The figure demonstrates a reasonable agreement between the measured γ_{isf} and the value predicted by the thermodynamic model of Saeed-Akbari et al. [117], assuming an interfacial energy

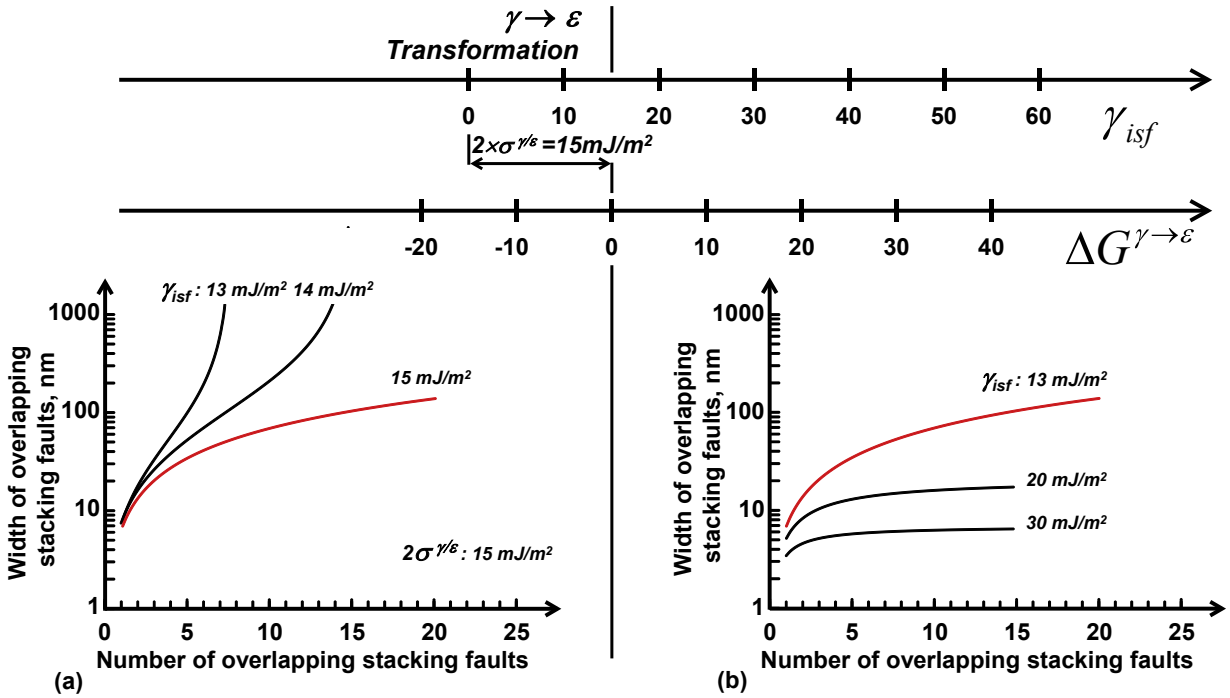

Fig. 21. Effect of the intrinsic stacking fault energy γ_{isf} on the equilibrium width of faults consisting of stacking faults overlapping on every second {111} plane for $2 \cdot \sigma^{\gamma/\varepsilon} = 15$ mJ/m^2 [124]. (a) The width diverges when $\gamma_{isf} < 15$ mJ/m^2. (b) The width increases gradually with N when $\gamma_{isf} > 15$ mJ/m^2. The case of a twin, $\gamma_{isf} = 2 \cdot \sigma^{\gamma/\varepsilon}$, corresponds to the red line in (a) and (b).

Table 2
Comparison of CALPHAD-based models used to determine the magnitude of γ_{isf} of TWIP steels.

Reference	TWIP Steel Alloy System	Strain energy term	Grain size excess term	Surface energy, mJ/m^2	Database employed
Allain et al. [71]	Fe-Mn-C	Not Included	Not Included	9	SGTE
Dumay et al. [125]	Fe-Mn-C-Al-Cr-Cu-Si 0 < mass-% alloying < 8	Not Included	Not included	8	Literature
Saeed-Akbari et al. [117]	Fe-Mn-C-Al Mn: 10–30 mass-% C: 0–1.2 mass-% Al: 0–7 mass-%	Included	Included	15	Literature CALPHAD
Curtze and Kuokkala [127]	Fe-Mn-Al-Si-C	Included	Not included	8	Literature SGTE
Nakano and Jacques [128]	Fe-Mn-C	Included	Not included	16	Literature CALPHAD T_0 data
Pierce et al. [93]	Fe-Mn-Al-Si-C	Included	Not included	8–12	Literature CALPHAD

of 15 mJ/m^2. The figure also shows that the TWIP effect has been observed for various TWIP steels within the measured γ_{isf}-range of 15 mJ/m^2 to 45 mJ/m^2. The data suggests that when $\gamma_{isf} \approx 15$ mJ/m^2, $\Delta G^{\gamma \rightarrow \varepsilon}$ is close to zero, as expected based on the Olson-Cohen work [102].

It is recognized that the magnitude of a single parameter, γ_{isf}, cannot be sufficient to predict the dominant plastic deformation mode of low and medium stacking fault energy metals and alloys. The interpretation of mechanical twinning requires the computation of intrinsic energy barriers which control the twinning process,

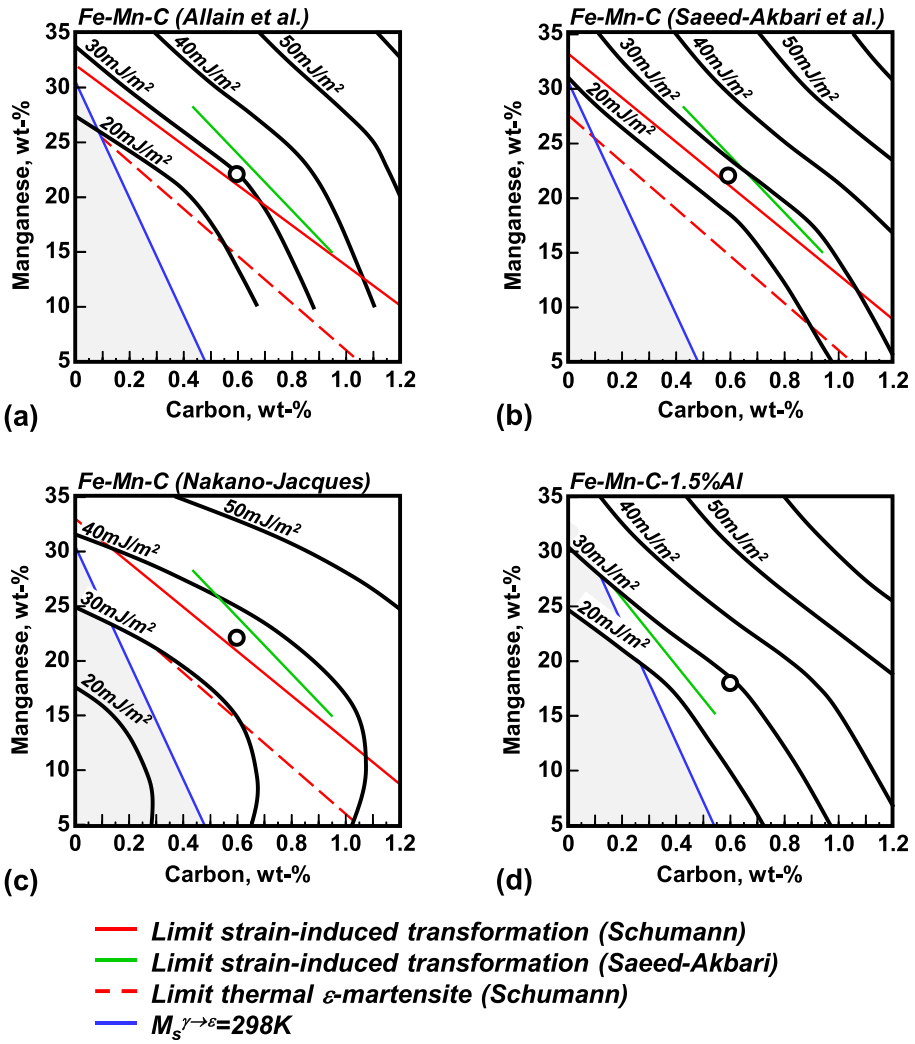

Fig. 22. Comparison of stacking fault energy calculations in C-Mn composition diagrams, as redrawn from (a) Allain et al. for Fe-Mn-C [72], (b) Saeed-Akbari et al. for Fe-Mn-C [26], (c) Nakano and Jacques for Fe-Mn-C [128] and (d) Saeed-Akbari et al. [26] for Fe-x%Mn-y%C-1.5%Al. The limits for the room temperature transformation and the strain-induced transformation to ε-martensite reported by Schumann [132] are also included in the graphs.

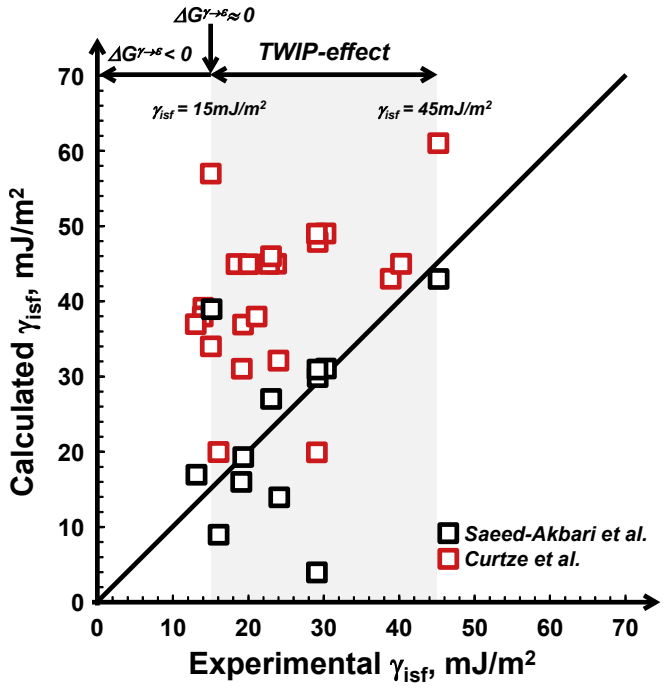

Fig. 23. Comparison between experimentally measured [52,62,73,93,113,170–172] and CALPHAD-based calculated intrinsic stracking fault energy γ_{isf} [117,126,127].

in addition to the computation of γ_{isf} [133]. It is widely accepted that the conditions for the glide of dissociated dislocations or isolated partial dislocations trailing wide stacking faults, as well as deformation twinning occurring during the plastic deformation of low and medium stacking fault energy metals and alloys, are controlled by four stacking fault energy parameters: (a) γ_{isf}, the intrinsic stacking fault energy, (b) γ_{usf}, the unstable stacking fault energy, (c) γ_{esf}, the extrinsic stacking fault energy, and (d) γ_{utf}, the unstable twin fault energy. These four intrinsic energy barriers provide a description of the generalized planar fault energy (GPFE) or γ-surface, *i.e.* the excess free energy when the fcc lattice is sheared on a {111}-type plane. Ratios or differences between these four energy barriers can be used to predict the type of planar fault which is more likely to form.

The concept of a generalized stacking fault energy (GSFE) surface, or γ-surface, and the generalized planar fault energy (GPFE) surface was originally proposed by Vitek [134,135]. The GSFE surface of a TWIP steel represents the energy required to rigidly shear two parts of a supercell with the fcc crystal structure on a {111} glide plane in a ⟨112⟩ direction. It is defined by the difference between the energy of the perfect lattice E_{fcc} and the energy of the sheared crystal E_{sf}, normalized by the sheared area A:

$$GSFE\left(J/m^2\right) = 1.6\cdot 10^{-19}(J/eV)\cdot\frac{\left(E_{sf}-E_{fcc}\right)(eV)}{A(m^2)} \qquad (30)$$

It should be noted that conceptually, twinning should be seen as a result of a combination of shear and shuffle components of atomic movement [136]. However, unlike in *ab initio* simulations, in most thermodynamic studies the shuffle component is disregarded.

3.2.2. Ab initio approach

Ab initio computational methods have made it possible to compute the GSFE surface, which can be used to understand the role of characteristic energy barriers in deformation twinning and predict the ability for twinning of a TWIP steel. Experimental determination of these energy barriers is not possible and *ab initio* calculations are therefore absolutely necessary. A number of codes are available for the *ab initio* computation of the electronic structure of solids, cf., e.g. Gebhardt et al. [137]. When applied to the problem of deformation twinning in TWIP steel, these simulation programs use specific theoretical approaches, such as density functional theory, to compute from first principles the correlation between specific shear displacements of a rigid lattice and the corresponding free energy changes associated with the nucleation of an intrinsic stacking fault, a two-layer twin or a multi-layer twin. In this way the stacking fault energy can be computed explicitly. *Ab initio* methods make it possible to calculate minimum energy pathways to generating intrinsic, extrinsic, and twin faults. The outcomes of these calculations, which will be discussed in the next section, provide the free energy landscapes for TWIP steels. Energy barriers apparent in the GSFE, characterized by an 'unstable fault energy', need to be overcome to produce stable intrinsic stacking faults, extrinsic stacking faults, or twins. GSFE surfaces typically have one of the following characteristic shapes: (i) a single maximum for an undissociated dislocation and (ii) a local minimum corresponding to the formation of an intrinsic stacking fault in the case of a dissociated dislocation. For case (ii) the local minimum on the reaction trajectory is preceded by an energy barrier, which represents the resistance to the nucleation of the leading partial dislocation and the formation of an intrinsic stacking fault. This energy barrier is quantified as the unstable stacking fault energy γ_{usf} [138]. This energy barrier is reduced from γ_{usf} to γ_{usf} - γ_{isf} if nucleation of the trailing partial of a dissociated dislocation is considered.

Expanding on Rice's ideas, the unstable twinning fault energy, γ_{utf}, was introduced by Tadmor and Hai [139]. It corresponds to the resistance to a one-layer intrinsic stacking fault becoming a two-layer stacking fault or twin embryo. Tadmor and Hai assume that the following sequence of events take place during twinning: first, a leading partial dislocation is emitted; then, instead of emission of a trailing partial, a new leading partial dislocation with the same Burgers vector as the first one is emitted, yet on a neighboring glide plane. The energy barriers associated with this sequence of shears is illustrated in the schematic GSFE curve shown in Fig. 24 (c). When the GSFE curve for an intrinsic stacking fault is calculated, the starting configuration is the perfect fcc lattice. The GSFE curve is obtained by calculating the energy difference between the perfect fcc lattice and the sheared lattice. The baseline zero energy of the GSFE curve corresponds to the relaxed perfect crystal with no shift. In the GSFE, the first maximum encountered, for a shear equal to a/12<112>, is the unstable stacking fault energy, γ_{usf}, which corresponds to the energy required to nucleate a partial dislocation at absolute zero temperature. An intrinsic stacking fault is obtained by shifting the top layers by $\frac{a}{6}<\bar{2}11>$ on a {111}-type plane. When this is repeated a second time on an adjacent plane, a two-layer twin or an extrinsic stacking fault is obtained.

Note that once the GSFE surface has been calculated, it can be used to derive the critical resolved stress for slip nucleation from first principles [87]:

$$\tau_{crss} = \frac{1}{b}\cdot\left.\frac{dE}{du}\right|_{\max} \qquad (31)$$

A key parameter for mechanical twinning is the unstable twinning fault energy γ_{utf}, the saddle point energy associated with a rigid {111}⟨112⟩ shift in the presence of an intrinsic stacking fault on an adjacent {111} plane. Whether dislocation activity is dominated by perfect dislocations or partial dislocations is determined by the $\frac{\gamma_{isf}}{\gamma_{usf}}$ ratio. A low $\frac{\gamma_{isf}}{\gamma_{usf}}$ value indicates a greater tendency for

Please cite this article in press as: B.C. De Cooman, et al., Twinning-induced plasticity (TWIP) steels, Acta Materialia (2017), http://dx.doi.org/10.1016/j.actamat.2017.06.046

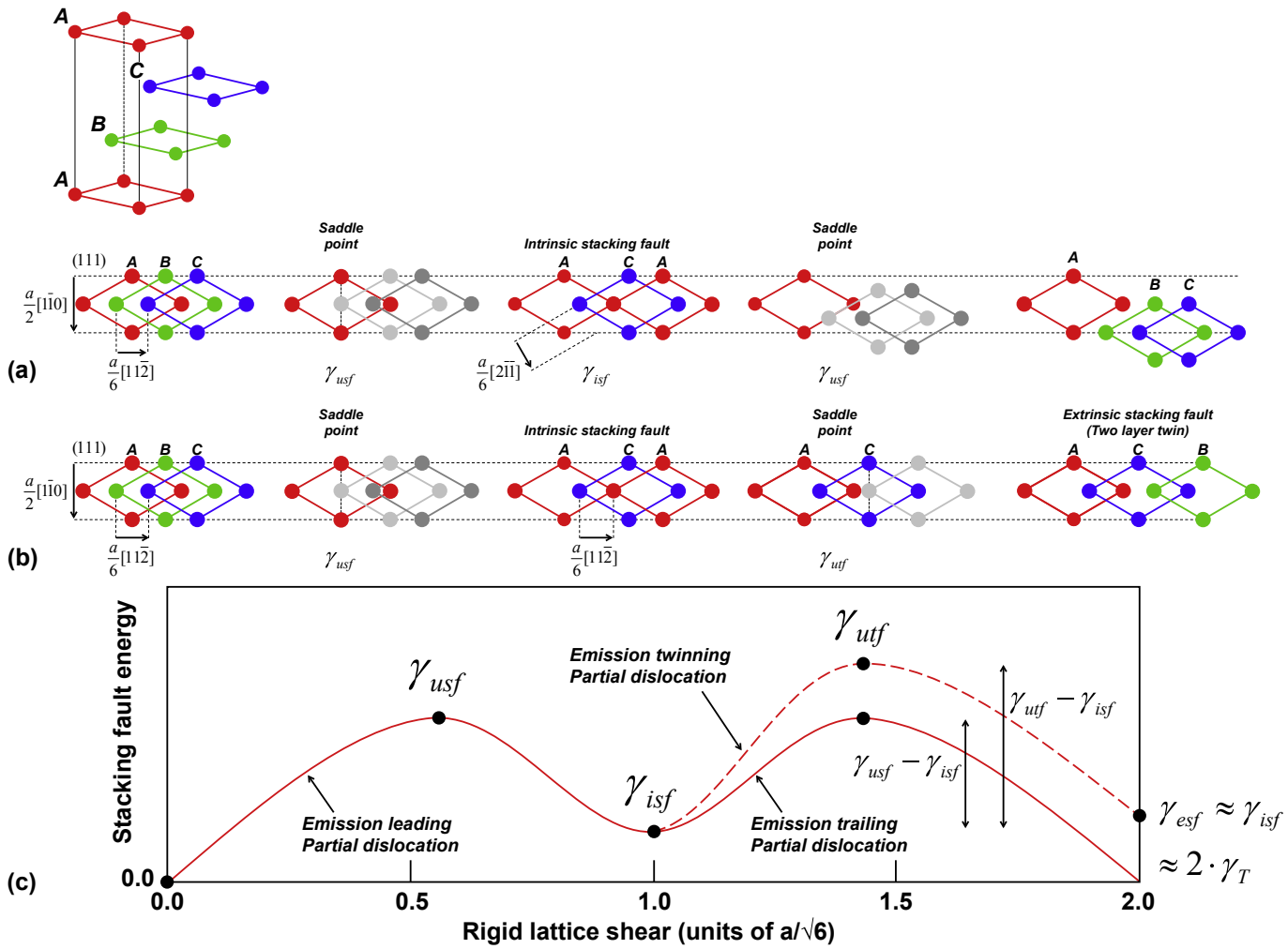

Fig. 24. Schematic of the supercell method, which consists in sliding a part of the supercell by a distance a/6<211>, i.e. by the Burgers vector of a partial dislocation, on a {111} plane, to create an intrinsic stacking fault. A two-layer twin is obtained by shifting the next atomic plane by the same distance. (a) Rigid lattice shear corresponding to the emission of a leading partial dislocation followed by the emission of the trailing partial dislocation, which restores the perfect lattice. (b) Rigid lattice shear corresponding to the passage of a partial dislocation followed by the passage of a twinning partial dislocation, which results in the formation of a two-layer twin. (c) Schematic of the generalized planar fault energy for the shear in (a) and (b). The solid GSFE curve corresponds to the energy landscape for slip by a dissociated dislocation. The dotted line is the energy landscape for the formation of a two-layer twin by shearing on the adjacent plane.

plastic deformation by dissociated dislocations with a large stacking fault. The movement of the leading partial requires overcoming an energy barrier of height γ_{usf}. The trailing partial encounters a lower energy barrier of height $\gamma_{usf}-\gamma_{isf}$. A large difference between γ_{usf} and γ_{isf} will therefore promote the formation of wide stacking faults. The ratio $\frac{\gamma_{isf}}{\gamma_{usf}}$ is a much better parameter to predict the occurrence of deformation twinning than γ_{isf}, deformation twinning being more likely when the $\frac{\gamma_{isf}}{\gamma_{usf}}$ ratio has a low value.

Assuming that a two-layer twin acts as an embryo for a full size deformation twin by thickening, the tendency for twinning by nucleation of a partial dislocation on a slip plane adjacent to a stacking fault is actually better predicted if both the $\frac{\gamma_{isf}}{\gamma_{usf}}$ ratio and the $\frac{\gamma_{utf}}{\gamma_{usf}}$ ratio are considered [140]. The $\frac{\gamma_{isf}}{\gamma_{usf}}$ ratio characterizes the energy barrier for slip only, and the parameters related to the energy barrier for twinning should also be taken into account. The key to twin nucleation is therefore the energy landscape for the nucleation of the trailing partial dislocation as compared to the energy landscape for twin nucleation, *i.e.* the emission of a second leading partial on an adjacent slip plane. When the $\frac{\gamma_{utf}}{\gamma_{usf}}$ ratio is close to one, the barrier for the nucleation of a partial dislocation and the barrier for the nucleation of a two-layer mechanical twin are similar. Twinnability therefore depends on both the $\frac{\gamma_{isf}}{\gamma_{usf}}$ ratio, a measure for the energy barrier for partial dislocation glide, and the $\frac{\gamma_{usf}}{\gamma_{utf}}$ ratio, a measure for the energy barrier for twinning. Twinning will be observed when $\frac{\gamma_{usf}}{\gamma_{utf}}$ is large, *i.e.* the energy barrier for the emission of the twinning partial is low, and, at the same time, $\frac{\gamma_{isf}}{\gamma_{usf}}$ is small. The schematic in Fig. 25 (b) shows the planar stacking fault energy variations for twin nucleation and thickening path.

Jin et al. [141] have proposed the following universal relation between the planar fault energy barriers in fcc metals and Cu-Al alloys based on *ab initio* GSFE computations:

$$\frac{\gamma_{utf}}{\gamma_{usf}} \approx \frac{1}{2} \cdot \frac{\gamma_{isf}}{\gamma_{usf}} + 1 \tag{32}$$

They also confirmed the well-known relation between γ_{isf}, γ_{esf} and γ_T, *viz.* $\gamma_{isf} \approx \gamma_{esf} \approx 2 \cdot \gamma_T$. *Ab initio* computations have also shown that the local composition and the local atomic configuration affected the energy barriers, and confirmed the Suzuki effect, i.e.

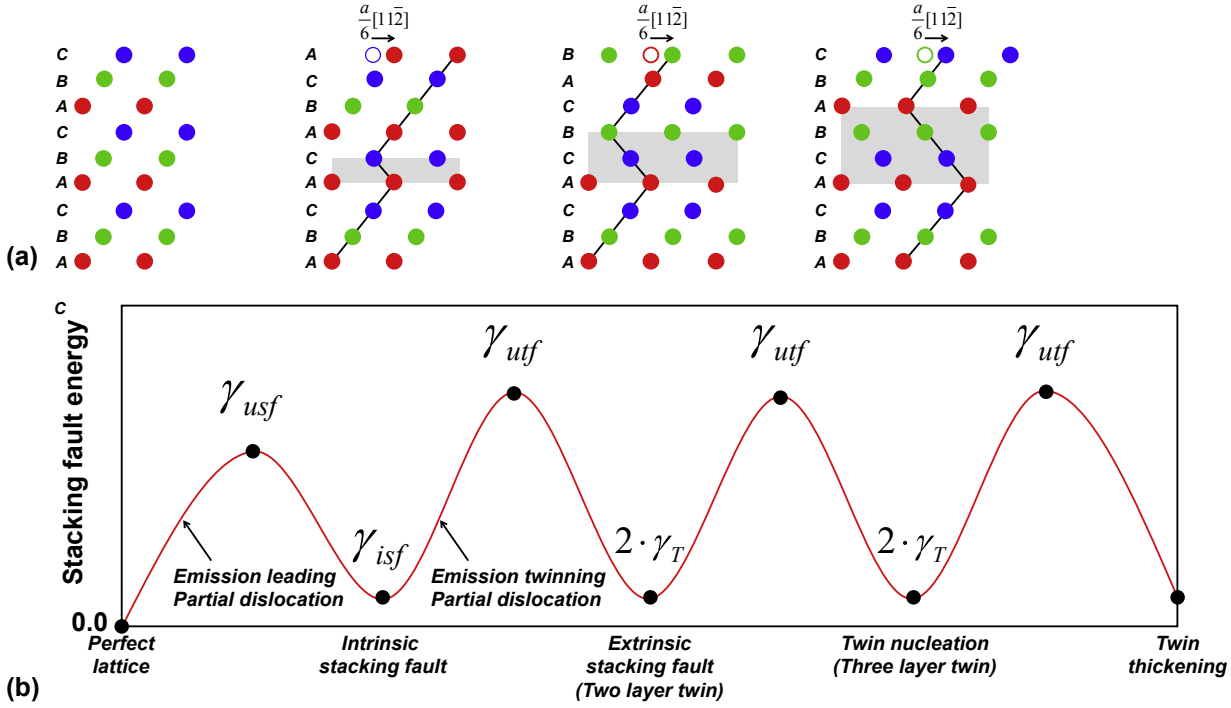

Fig. 25. (a) Rigid lattice shears for the formation and thickening of a twin nucleus. In the first stage, the energy path from a perfect fcc crystal supercell to one with an intrinsic stacking fault is calculated. The saddle point of the transition is γ_{usf}, the unstable stacking fault energy. In the second stage, the energy path is calculated for the transformation of an intrinsic stacking fault to an extrinsic stacking fault, i.e. a two-layer twin. The saddle point is γ_{utf}, the unstable twin energy. In the third stage and the subsequent ones, the saddle point remains equal to γ_{utf} as the twin thickens. (b) Schematic of the corresponding planar stacking fault energy for twin nucleation and thickening.

the influence of solute segregation on γ_{isf} [142]. Li et al. [143] have shown that the above relation is obeyed by Cu-X (X: Al, Ni, Zn, Ga), Pd-X (X: Ag, Au), Ni-X (X: Nb, W, Mn, Fe, Cu) and Al-X (X: Mg, Ga, Zn, Si, Cu) alloys. It is worth mentioning that in the work of Jo et al. [144] another interesting form of the same universal relation between γ_{isf}, γ_{usf} and γ_{utf} was derived:

$$\left(\gamma_{utf}-\gamma_{isf}\right)-\frac{\left(\gamma_{usf}-\gamma_{isf}\right)+\gamma_{usf}}{2}=0\rightarrow\gamma_{utf}-\gamma_{usf}=\frac{\gamma_{isf}}{2} \tag{33}$$

Equation (33) implies that when $\gamma_{isf}=0$, i.e. for $\Delta G^{\gamma\rightarrow\varepsilon}=0$, twinning and stacking fault formation leading to hcp ε-phase formation, are equally likely to occur. As the universal relation expressed by Eq. (33) corresponds to idealized conditions which do not take strain contributions into account, Li et al. [133] revised it as follows:

$$\gamma_{utf}=\gamma_{usf}+\frac{\gamma_{isf}}{2}+\delta \tag{34}$$

Here δ is a deviation parameter. The critical upper limit of γ_{isf}, for the transition from the strain-induced formation of the ε-phase to deformation twinning, denoted $\gamma_{isf,cr}$, is determined by the deviation from the relation expressed by Eq. (33):

$$\gamma_{isf,cr}=2\cdot\delta=\gamma_{utf}-\gamma_{usf} \tag{35}$$

This equation implies that stacking fault formation is preferred over deformation twinning when γ_{isf} is smaller than the difference between the energy barrier for twinning and stacking fault formation. The value of $\gamma_{isf,cr}$ for typical TWIP steels is in the range of 10–20 mJ/m^2.

Various 'twinnability' parameters have been proposed. They are based on the characteristic energy barriers in the GSFE. The twinnability parameter T_{AS} proposed by Asaro and Suresh quantifies the tendency for partial dislocation nucleation at grain boundaries [145]:

$$T_{AS}=\sqrt{\frac{3\cdot\gamma_{usf}-2\cdot\gamma_{isf}}{\gamma_{utf}}} \tag{36}$$

When $T_{AS}>1$, mechanical twinning is favored, while $T_{AS}<1$ signifies the occurrence of dislocation glide. Li et al. [149] have pointed out that, if Jin's relation [141] given by Eq. (32) is, indeed, a universal law as they claim, then the twinnability should only depend on a single parameter, the $\frac{\gamma_{isf}}{\gamma_{usf}}$ ratio:

$$T_{AS}=\sqrt{3\cdot\frac{\gamma_{usf}}{\gamma_{utf}}-2\cdot\frac{\gamma_{isf}}{\gamma_{utf}}}=\sqrt{\frac{3-2\cdot\frac{\gamma_{isf}}{\gamma_{usf}}}{1+\frac{1}{2}\cdot\frac{\gamma_{isf}}{\gamma_{usf}}}} \tag{37}$$

Accordingly, twinning is favored ($T_{AS}>1$) if the ratio $\frac{\gamma_{isf}}{\gamma_{usf}}$ is smaller than 0.8.

Jo et al. [144] have introduced a different parameter, according to which the deformation mechanisms can be classified. This parameter, r_d, again depends only on the $\gamma_{isf}/\gamma_{usf}$ ratio:

$$r_d=\frac{\frac{\gamma_{isf}}{\gamma_{usf}}}{1-\frac{\gamma_{isf}}{\gamma_{usf}}} \tag{38}$$

Low values of r_d favor twinning. If r_d is less than $-1/2$, only stacking faults are formed. If r_d is in the range of $-1/2$ to 0, stacking faults and dislocation glide occur. Although no orientation dependence enters Eq. (38) explicitly, the occurrence of stacking fault or dislocation glide in this range of r_d does depend on the grain orientation. For r_d values ranging between 1 and 2, mechanical

twinning and dislocation glide occur. Finally, for r_d in excess of 2, dislocation glide prevails. This is a useful concept as it allows one to set limits on the magnitude of $\gamma_{isf}/\gamma_{usf}$ leading to twinning and through that determine the alloy compositions which will promote deformation twinning:

$$1 < r_d = \frac{\gamma_{isf}}{\gamma_{usf} - \gamma_{isf}} < 2 \Rightarrow \frac{1}{2} < \frac{\gamma_{isf}}{\gamma_{usf}} < 1 \tag{39}$$

Combining these inequalities with the 'universal' relation proposed by Jin et al. [141] Eq. (32), one arrives at the following condition for the ratio of the saddle point energy values for twinning and stacking fault formation:

$$\frac{1}{4} < \frac{\gamma_{utf}}{\gamma_{usf}} < \frac{1}{2} \tag{40}$$

While it can be considered as established that deformation twinning is controlled by the intrinsic slip barrier, γ_{usf}-γ_{isf}, and the intrinsic stacking fault energy, γ_{isf}, crystallographic orientation is also essential, as shown by Jo et al. for fcc metals by molecular dynamics (MD) simulations [144]. The direction of the externally applied shear is also essential as it can override the intrinsic energy barrier conditions. This implies that twinning also depends on the angle between the externally imposed shear stress and the orientation of the dislocation line. While screw dislocations will readily form twins when the energy barrier conditions for twinning are met, edge dislocations will never form twins. The geometrical reason for this orientation dependence is illustrated in Fig. 26. The edge components of the partial dislocations of a screw dislocation point in opposite direction. This increases their separation and partial dislocation breakaway can occur [146] if the following condition is fulfilled:

$$\tau \cdot b_P = 2 \cdot \gamma_{isf} \tag{41}$$

Here τ is the resolved imposed shear stress, and b_P is the magnitude of the partial dislocation Burgers vector. When the angle between the dislocation line and the dislocation Burgers vector is larger than 30 °, the edge components of the partial dislocations of the dislocation point in same direction, i.e. the trailing partial always follows the leading partial dislocation and eliminates the fault created by the leading partial dislocation. Fig. 26 also shows that this occurs despite an increase of the dissociation width with increasing imposed stress. This also implies that dislocation segments in the screw orientation play a key role in the emergence of deformation twinning.

The twinnability measure introduced by Bernstein and Tadmor [147,148],

$$T_{BT} = \left(1.136 - 0.151 \cdot \frac{\gamma_{isf}}{\gamma_{usf}}\right) \cdot \sqrt{\frac{\gamma_{usf}}{\gamma_{utf}}} \tag{42}$$

indicates the tendency for the occurrence of mechanical twinning during the deformation of a polycrystalline fcc metal or alloy. A T_{BT} value of 0.987 (e.g. for Ni) corresponds to the absence of twinning, a value of 1.05 (e.g. for Cu) indicates that twinning is still not

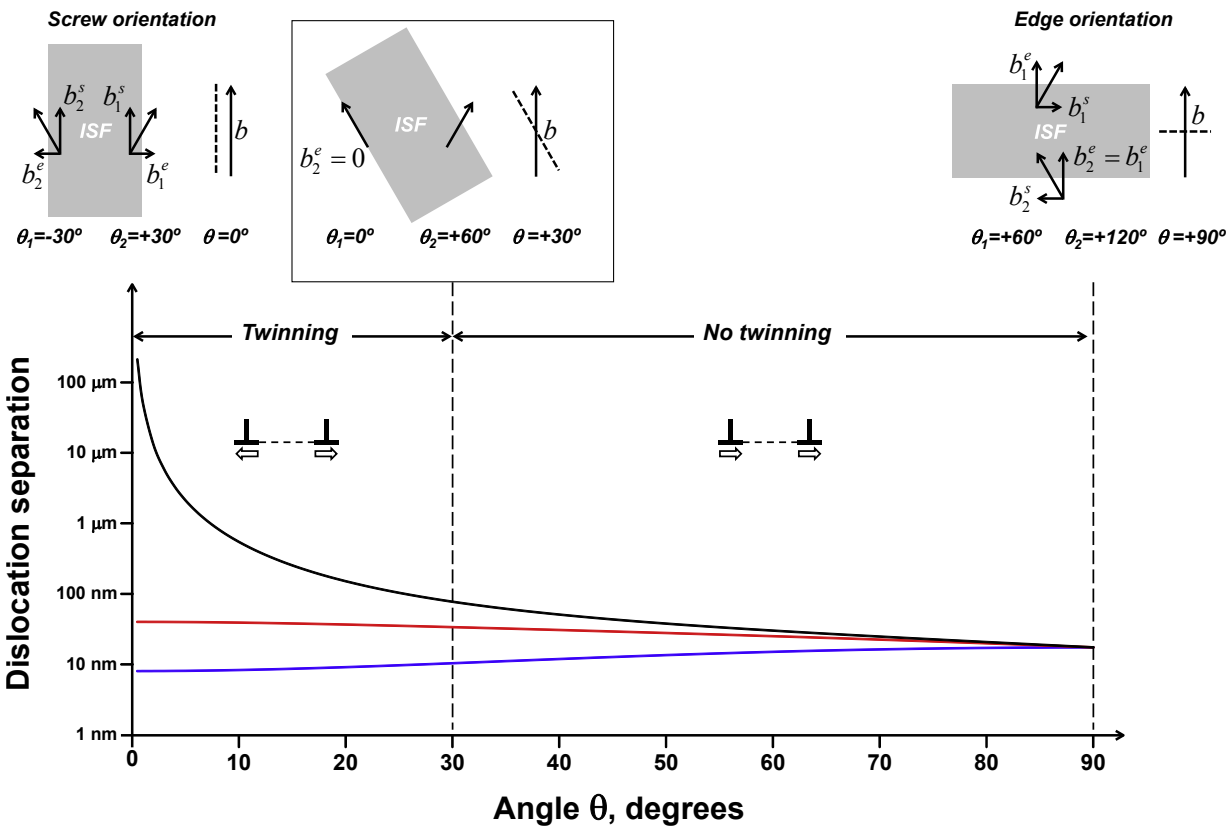

Fig. 26. Stacking fault width as a function of the angle θ between the perfect dislocation line direction and the Burgers vector for different values of the normalized imposed shear stress R = $\frac{\tau \cdot b_P}{2 \cdot \gamma_{isf}}$ [146]. For γ_{isf} = 30 mJ/m^2, R = 1 corresponds to τ = 409 MPa. For $\theta < 30°$, the edge components of the Burgers vectors of the partial dislocations point in opposite directions. The partial dislocations thus move in opposite directions, and the widening of the stacking faults leads to twin formation in areas where intrinsic stacking faults overlap. For $\theta > 30°$, the partial dislocations move in the same direction. In this case the stacking fault trailed by the leading partial will always be removed by the trailing partial, *i.e.* no twinning will ensue. The three curves represent the stress-free, intermediate and breakaway situation.

Please cite this article in press as: B.C. De Cooman, et al., Twinning-induced plasticity (TWIP) steels, Acta Materialia (2017), http://dx.doi.org/10.1016/j.actamat.2017.06.046

Table 3
Twinnability parameters. The twinnability parameter values, assuming γ_{isf} = 20 mJ/m^2, γ_{usf} = 120 mJ/m^2, and γ_{utf} = 140 mJ/m^2, predict that deformation-twinning will occur during straining.

Twinnability Parameter	Parameter Value	Reference
$\delta_{ut/us} = \gamma_{utf} - \gamma_{usf}$	$\delta_{ut/us} = 20$ mJ/m$^2 > 0$	Tadmor-Hai [139]
$T_{BT} = \left(1.136 - 0.151 \cdot \frac{\gamma_{isf}}{\gamma_{usf}}\right) \cdot \sqrt{\frac{\gamma_{usf}}{\gamma_{utf}}}$	$T_{BT} = 1.08$	Bernstein-Tadmor [147,148]
$T_{AS} = \sqrt{\frac{3 \cdot \gamma_{usf} - 2 \cdot \gamma_{isf}}{\gamma_{utf}}}$	$T_{AS} = 1.56$	Asaro-Suresh [145]
$r_d = \frac{\gamma_{isf}}{\gamma_{usf} - \gamma_{isf}}$	$r_d = 0.2$	Jo et al. [144]

predominant, while T_{BT} value of 1.1 or higher points to an easy activation of twinning. It should be noted that, unlike the Jo et al.'s parameter r_d, the Bernstein-Tadmor parameter T_{BT} involves not one, but two energy ratios, $\frac{\gamma_{isf}}{\gamma_{usf}}$ and $\frac{\gamma_{usf}}{\gamma_{utf}}$. In that regard, it is closer to the Asaro-Suresh parameter T_{AS}.

In other publications [131,139] the difference between γ_{utf} and γ_{usf} was considered as an appropriate quantitative measure for the tendency for deformation twinning:

$$\delta_{utf/usf} = \gamma_{utf} - \gamma_{usf} \tag{43}$$

The parameter $\delta_{utf/usf}$ compares the barrier for the nucleation of a second leading partial, when a first one has been emitted, relative to the energy barrier for the emission of the trailing partial. If this parameter is positive, the barrier for the nucleation of a trailing partial is lower than for the formation of a two-layer twin nucleus, and dislocation glide will be predominant. The different twinnability parameters are compiled in Table 3 and Fig. 27, which illustrates the relationship between the twinnability parameters and the shape of the generalized planar stacking fault energy curve.

3.2.3. First principles computations

In the previous paragraphs the GSFE concept was introduced. The GSFE of a TWIP steel can be obtained by first principles computations of the structural stability and the fault energy landscape of fcc γ-Fe, Fe-Mn, Fe-Mn-C, Fe-Mn-Al-C, and other TWIP alloys. Although the results apply to zero absolute temperature, they can provide valuable information about the effect of alloying on the GSFE. The calculation of the GSFE involves complex computations of solid state properties related to the electronic structure. This requires solving the Schrödinger equation self-consistently for electrons in a periodic lattice. This is done by means of *ab initio* methods, which do not require any empirical input. Only a very limited number of inputs, *viz.* the atomic numbers and the crystallographic structure, are required. The *ab initio* electronic structure computations used to determine the GSFE are based on Density Functional Theory (DFT).

Analysis of *ab initio* calculations for γ-Fe-Mn alloys [149,150] and γ-Fe-Mn-C alloys [151,152] shows that Mn has only a minor effect on the GSFE [153,154]. Binary γ-Fe-C and γ-Fe-N have therefore been used to represent the Fe-Mn-C and Fe-Mn-N alloys.

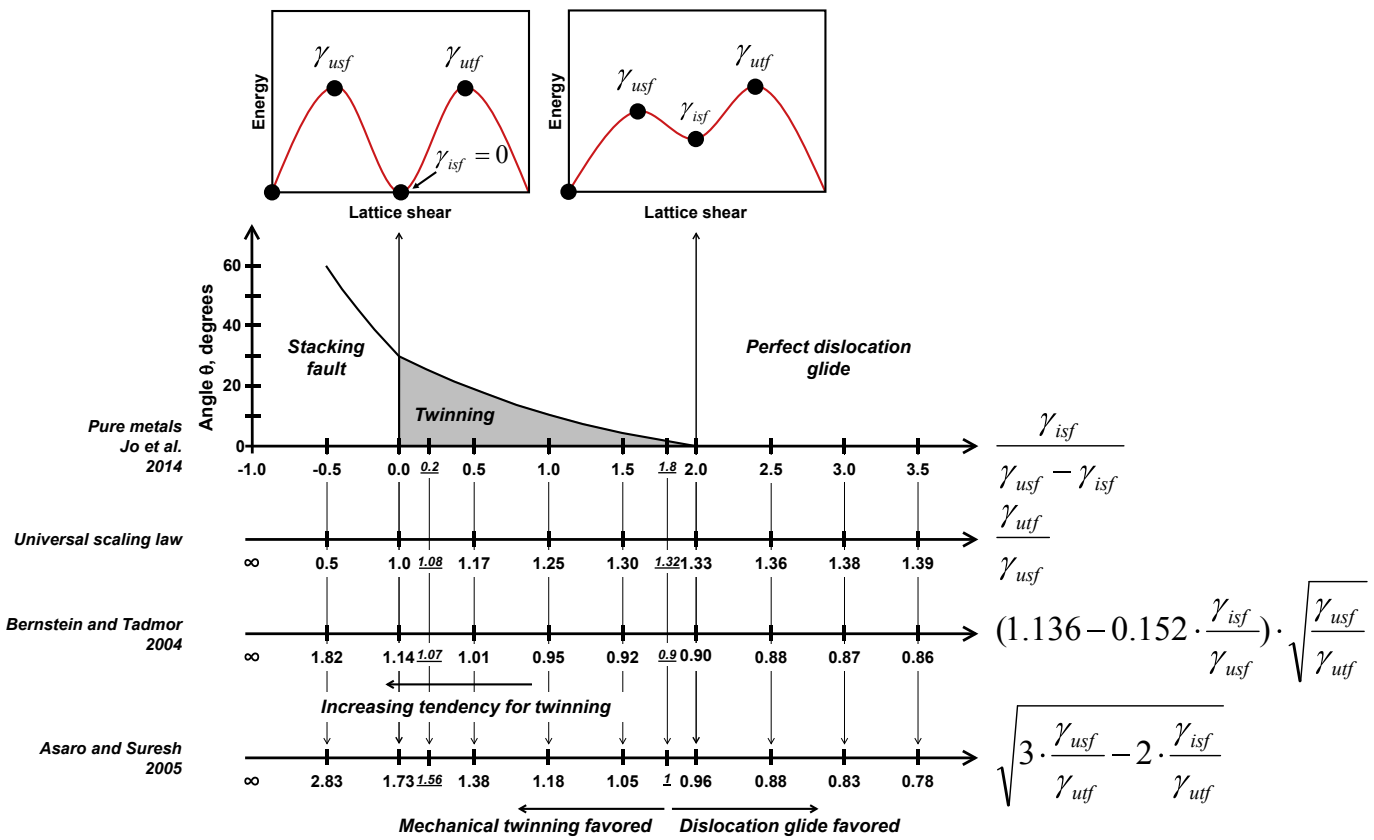

Fig. 27. Schematic illustrating the relationship between proposed twinnability parameters and the shape of the generalized planar stacking fault energy curve [141,145,149,150,155].

The periodic supercell approach mentioned above has been implemented for γ-Fe alloys in the commercial quantum simulation software Vienna *Ab Initio* Software Package (VASP). The periodic supercell method avoids the problem of surfaces and involves the use of a cell which explicitly contains a specific fault. On this basis, zero Kelvin calculations for pure γ-Fe correctly predict large negative values, e.g. −380 mJ/m^2 [155,156] or −347 mJ/m^2 [157] for γ_{isf} of TWIP steels when no spin magnetization is considered. This comes as no surprise, as at 0 K the hcp ε-phase is more stable than the fcc γ-phase, even if different magnetic states (non magnetic, ferromagnetic, and anti-ferromagnetic) are considered for γ-Fe.

Another important group of *ab initio* methods are based on the so called Muffin-Tin Approximation (MTA) [158]. The *ab initio* DFT method can be used to determine the total energy and electronic density of a solid [158,159]. Whereas the use of supercell first principles approach is common in *ab initio* DFT calculations, it is challenging to use it for modeling all possible concentrations and configurations. The exact muffin tin orbital (EMTO) method is considered to be the most powerful technique to obtain the electronic structure of random substitutional alloys with a close packed crystal structure, such as γ-Fe alloys [158]. It replaces the alloy by an ordered effective medium. In this method the solid is subdivided into spherically symmetrized regions around the atomic nuclei and interstitial regions between the atoms. The DFT Kohn-Sham equations are solved using the EMTO method and the full charge density (FCD) technique, which is combined with the coherent-potential approximation (CPA). CPA is a method of performing configurational averaging which replaces a multi-component random alloy with a translationally invariant system with a single component representing an effective medium. It is used in conjunction with a mean-field approximation called the disordered local moment (DLM), which takes into consideration the effects of magnetic disorder on the electronic structure [160]. Results of the combined EMTO-CPA method, which is computationally efficient, have almost the same accuracy as the full potential methods that do not involve approximations. In the EMTO-CPA method the stacking fault energy at 0 K is defined as an excess free energy per unit area [147]:

$$\gamma_{isf} \approx \gamma_{esf} \approx \frac{2\cdot\left(E_{hcp} - E_{fcc}\right)}{A_{SF}} \tag{44}$$

Here E_{hcp} and E_{fcc} are the total energy per atom of the hcp and the fcc phase, respectively. A_{SF} is the area of the stacking fault.

Ab initio methods based on density functional theory are in principle very suitable to support materials design, and the approach has been useful for the calculation of 0 K ground state properties. While this is very valuable at a fundamental level, it is not sufficient for the actual design of γ-Fe alloys, as these can have a variety of magnetic states which will significantly influence the outcome of DFT computations. Despite the popularity of the *ab initio* calculations, a careful approach is required in their implementation and application to high Mn TWIP steels. Ekholm and Abrikosov [161] noted that standard *ab initio* computational approaches do not always describe 3d electron systems, such as γ-Fe-Mn based alloys, sufficiently accurately, Reyes-Huamantinco et al. [162] have shown that magnetism and thermal lattice expansion play a role in the determination of γ_{isf} for a paramagnetic random Fe-22.5%Mn alloy, thereby illustrating that γ_{isf} is sensitive to the magneto-volume coupling at finite temperatures. This is in disagreement with the results by Vitos et al. for Fe-Cr-Ni alloys, who report that the temperature dependence of the γ_{isf} is determined only by the contribution of magnetic fluctuations to the free energy [163].

The fault energy barriers can also be calculated using the energy of crystal structures with periodically repeated stacking faults. The approach requires prior DFT calculation of the total energy of defect-free unit-cells with different stacking sequences. In the axial next-nearest-neighbor Ising (ANNNI) model proposed by Denteneer and van Haeringen [164], the energy of a particular stacking fault γ_{sf} is defined as an excess energy per unit area [165,166]:

$$\gamma_{sf} = \frac{E_{sf} - E_0}{A} \tag{45}$$

Here E_{sf} and E_0 are the energy of the crystal with and without a stacking fault, respectively, and A is the area associated with a single atom in the slip plane, *i.e.*$A = \sqrt{3}\cdot a_\gamma/4$. Using the ANNNI approach, Denteneer and Soler derived the following equations for γ_{isf} and γ_{esf} [167]:

$$\begin{aligned}\gamma_{isf} &\approx \frac{-4\cdot(J_1 + J_2 + J_3)}{A}\\ \gamma_{esf} &\approx \frac{-4\cdot(J_1 + 2\cdot J_2 + 2\cdot J_3)}{A}\end{aligned} \tag{46}$$

Here J_1, J_2, and J_3 are the nearest-neighbor, next nearest-neighbor and next-next nearest-neighbor interaction parameters. In can be shown that the J_i parameters are related to G^{hcp}, the free energy of ε-Fe (… ABAB … -type stacking), G^{dhcp}, the free energy of double hexagonal close packed Fe (dhcp-Fe with … ABACABAC … -type stacking) and G^{fcc}, the free energy of γ-Fe (… ABCABC … -type stacking). The calculation of γ_{isf} requires the computation of the free energy of just these three defect-free structures:

$$\gamma_{isf} \approx \frac{G^{hcp} + 2\cdot G^{dhcp} - 3\cdot G^{fcc}}{A} \tag{47}$$

Local changes in atomic positions or magnetic order resulting from the presence of the stacking fault are not taken into account in the ANNNI approach.

It is important to note that in γ-Fe with low γ_{isf} alloys deformation twins, ε-martensite and α'-martensite are often observed experimentally. At large strains α'-martensite nucleates at intersections of ε-martensite, twins and shear bands. This has also been observed in TWIP steels [168,169]. The formation of ε and α'-martensite have not yet been related to the GSFE surface approach discussed in the previous section, and the energy barriers associated with the formation of ε and α'-martensite have not been studied as yet.

3.3. Effect of alloying elements

In the original work of Schumann [132] on the mechanical properties of Fe-Mn-C alloys, the composition was mainly considered as a means to achieve room temperature phase stability for the fcc crystal structure. The observation of the microstructure formed also enabled the author to draw a characteristic boundary line between two regions in the Mn-C composition plane: one of stable compositions deforming by dislocation glide and twinning and another one of unstable compositions, i.e. those leading to the deformation-induced formation of the ε phase:

$$\%Mn = 32 - 20\cdot\%C \tag{48}$$

Here %C and %Mn denote the weight percentage of C and Mn in the alloy, respectively. In the range of 15–25%Mn and 0.4–0.8%C, this equation corresponds approximately to alloy compositions with an iso-γ_{isf} value of about 20 mJ/m^2, according to Saeed-Akbari et al. [117], and 30 mJ/m^2, according to Nakano and Jacques [128] (Fig. 22).

It is clear that the alloy composition plays a key role in determining the magnitude of γ_{isf}, but the fundamental reasons for this

influence are often more complex than the composition dependence of stability of the γ and ε phases. In what follows, the influence of the most important alloying elements on the properties of TWIP steels is therefore reviewed in detail.

3.3.1. Carbon

Carbon plays a central role in the properties of TWIP steels as: (a) it increases the lattice parameter, (b) it enhances the stability of the austenite relative to ε-martensite (*i.e.* C increases $\Delta G^{\gamma\rightarrow\varepsilon}$), (c) it promotes paramagnetism by reducing the Néel temperature T_N^{γ}, (d) it substantially increases γ_{isf}, with a larger effect for a lower Mn content in Fe-Mn-C TWIP steels, and (e) it leads to a strong solid solution hardening effect. In γ-Fe and alloys, carbon occupies octahedral interstitial sites. The small lattice distortion caused by C is isotropic. The nearest neighbor (NN) and next nearest neighbor (NNN) interactions between carbon atoms in austenite have been studied by Mössbauer Spectroscopy (MS), thermodynamic estimations and Monte Carlo simulations [170,171]. The NN and NNN C-C interactions have been found to be repulsive in γ-Fe-C alloys (Fig. 28). The results imply that the C distribution should be homogeneous. The repulsive character of C-C interactions also leads to a reduction of the probability that an interstitial octahedral site in the vicinity of a C-occupied octahedral site will also be occupied by a C atom. As a result, the C diffusivity will rise with increasing C/Fe-atomic ratio [172,173]. The 0 K first principles analysis of Fe-Mn-Al-C alloys has also shown that there is a pronounced repulsion between interstitial C atoms in TWIP steels [155,157,174–178]. Substitutional solutes, such as Al and Mn, affect the properties of C (Fig. 28). Al has been shown to have a small effect on the C diffusivity in γ-Fe-C-Al alloys, but Shun et al. [179], who studied the temperature dependence of the properties of austenitic Fe-30%Mn-1.0%C ($\gamma_{isf} = 27$ mJ/m^2), report that the apparent activation energy for the onset of DSA-related serrations on the deformation curves was significantly lower than the activation energy for bulk diffusion of carbon. According to Shun et al., this suggests that the serrations are related to the short range diffusion of C in the dislocation core, rather than its bulk diffusion. Addition of 2.7% Al increased the activation energy for the onset of serrations, indicating that Al reduces the C mobility at dislocations.

Carbon also strongly affects the local magnetic interactions in γ-Fe-Mn-C alloys. Various magnetic states have been observed experimentally for γ-Fe (non-magnetic, low-spin ferromagnetic,

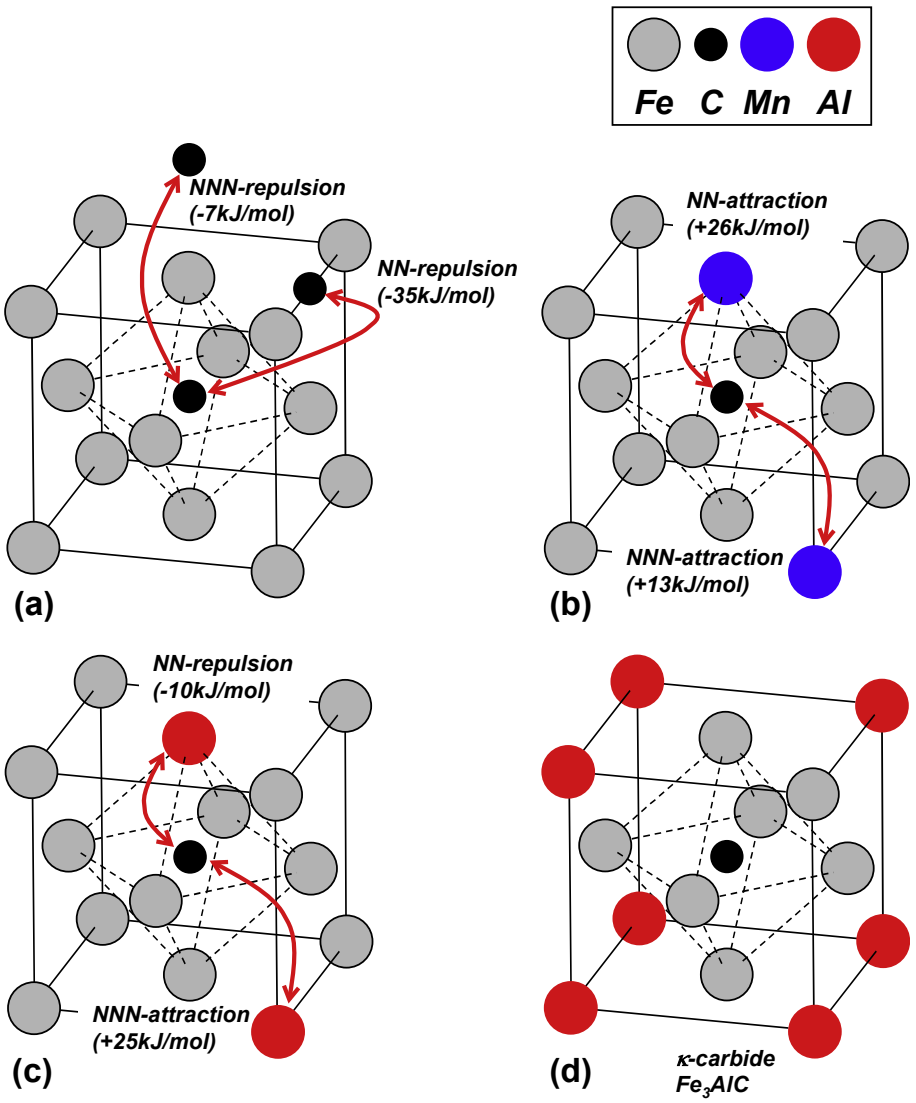

Fig. 28. Schematic for the NN and NNN interactions of solute atoms in fcc γ-Fe alloys. (a) Repulsive NN and NNN C-C interaction. (b) Attractive NN and NNN C-Mn interaction. (c) Repulsive NN and attractive NNN C-Al interaction. (d) Crystal structure of κ-carbide, which is stabilized by the attractive NNN C-Al interaction.

high-spin ferromagnetic, and collinear and non-collinear anti-ferromagnetic) [180–183]. The collinear spin, anti-ferromagnetic double layer (AFMD) state is the lowest energy state in γ-Fe, γ-Fe-C and γ-Fe-Mn-C alloys [151]. In the lowest energy AFMD state the Fe_6-octahedra comprise five Fe atoms which are ferro-magnetically coupled and one Fe atom which has an opposite spin. The presence of C induces the formation of local ferro-magnetic Fe clusters in γ-Fe-C alloys, *i.e.* the ferro-magnetic coupling of the spins of nearest Fe atoms is favored by the presence of C. In γ-Fe-Mn-C alloys there is a strong tendency to form Mn-C pairs. The γ-Fe-Mn-C alloys are magnetically non-homogeneous, because C also affects the local magnetic interactions in this case. C also frustrates the local magnetic ordering in γ-Fe-Mn-C alloys by the re-orientation of the magnetic moments of the nearest Fe and Mn atoms, thereby stabilizing the Fe-Mn ferro-magnetic coupling. The results of the above mentioned studies suggest that the preferred location of C atoms is away from the stacking fault plane. The stacking fault energy is the highest when C atoms are situated in the stacking fault plane. The 0 K value of γ_{isf} is increased by 300 mJ/m^2 by the addition of about 1 mass-% C. The effect is very short range. Thus, the influence of C on the stacking fault energy rapidly decreases when the C atoms are positioned further away from the fault plane. This dependence of γ_{isf} on the distance of the C-atom from the stacking fault plane is shown in Fig. 29 based on the work of Gholizadeh [74]: the further C atoms are from the stacking fault plane, the smaller their influence on γ_{isf}. Only a few atomic hops of the C atom away from the stacking fault are required to obtain a decrease of γ_{isf} to its C-free stacking fault value. Abbasi et al. [155] also reported a significant increase of the stacking fault energy with increasing C content, along with a strong dependence of the stacking fault energy on the position of the C atoms relative to the stacking fault.

Experimental evidence for the short-distance (nano-scale) diffusion of C atoms away from the stacking fault has been provided by Hickel et al. [184], who report a transmission electron microscopy observation of an irreversible increase of the stacking fault width by 40–60%, corresponding to a decrease of the γ_{isf} by approximately 9 mJ/m^2, during *in situ* heating of Fe-22%Mn-0.6%C TWIP steel from −158 °C to +40 °C. They refer to this C 'nano-diffusion' out of the stacking fault plane as an anti-Suziki effect, to highlight the fact that the normal Suzuki effect involves a *reduction* of γ_{isf} resulting from the diffusion of substitutional solutes to the stacking fault plane. The solute C interstitials cause a lattice expansion of γ-Fe by about 0.0041 nm/mass-%, which affects γ_{isf}. In addition, the shear of the atomic layers during the glide of the leading partial dislocation of a dissociated perfect dislocation will cause an iron atom to pass on top of the carbon atoms which are located in the stacking fault plane. This creates an unstable high energy configuration, forcing the C atoms to carry out a diffusional jump to a nearby vacant octahedral interstitial site. Both effects will cause the carbon atoms to diffuse away from the stacking fault, thereby decreasing γ_{isf} and widening the stacking fault. Fig. 29, which is based on the work of Gholizadeh [74] and Limmer [185], illustrates an increase of γ_{isf} when C-atoms are located in the stacking fault plane. Their calculations do not take into account the interaction of carbon atoms with the partial dislocation which may influence the carbon-stacking fault interaction.

The affinity of Fe and Mn for C is related to the Fe-C and Mn-C chemical bond strength in the solid. According to von Appen and Dronskowski [67], the C-Fe and C-Mn bonds are strong local covalent bonds. The formation of Mn-rich octahedra with C in the interstitial positions cannot be explained in terms of bond strength, as the binding energy of the C-Fe bond (−4.43eV) is slightly larger in magnitude than that of the C-Mn bond (−4.31eV). Since there are relatively few C-Fe and C-Mn bonds in the alloy, they are not expected to have a significant influence on its electronic structure and lattice properties which depend on it, such as the elastic constants.

The solid solution strengthening effect of C in TWIP steel, with an increment of approximately 279 MPa/mass-% C [186], is less pronounced than in common stainless steels [187]. Allain [66] and Kusakin et al. [188] reported a similar solid solution strengthening effect of 250 MPa/mass-% C.

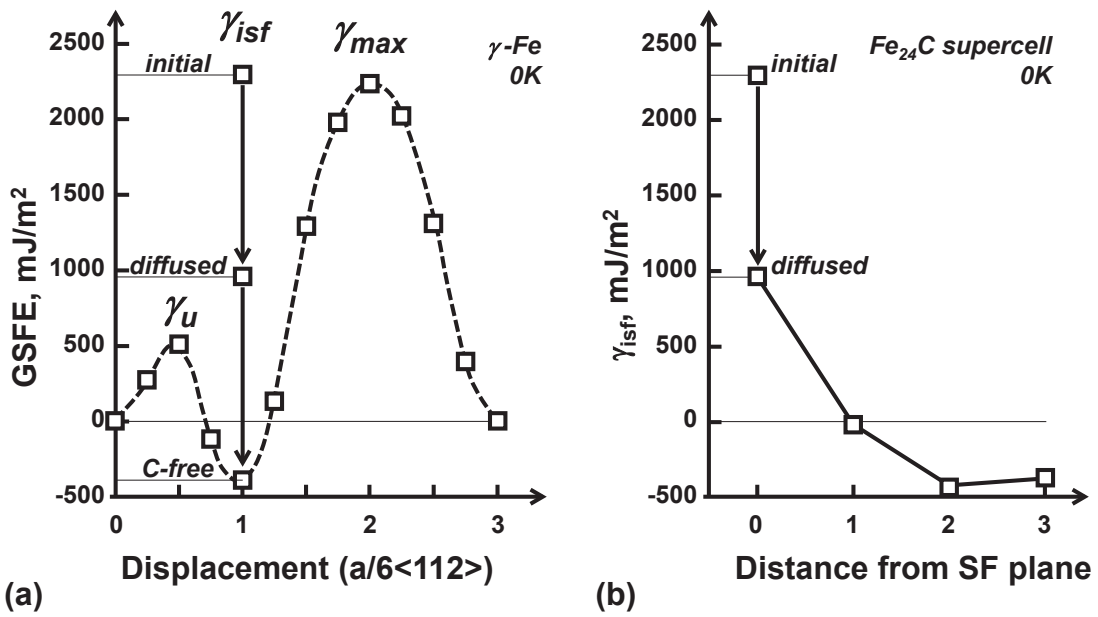

Fig. 29. (a) Generalized stacking fault energy for γ-Fe at 0 K, illustrating the effect of C on the magnitude of γ_{isf}. The value of γ_{isf} is very high when a C atom is in its initial state, i.e. positioned on the stacking fault plane during the passage of a dissociated dislocation. As the C atom diffuses to a more favorable position inside the stacking fault, γ_{isf} is reduced but is still high compared to a C-free stacking fault. (b) Effect of the distance of solute C from the stacking fault plane on γ_{isf}. Data redrawn from the work of Gholizadeh [74] and Limmer [185].

Please cite this article in press as: B.C. De Cooman, et al., Twinning-induced plasticity (TWIP) steels, Acta Materialia (2017), http://dx.doi.org/10.1016/j.actamat.2017.06.046

3.3.2. Manganese

As manganese increases the $\varepsilon \rightarrow \gamma$ transformation temperature, it is expected that addition of Mn results in a decrease of γ_{isf}. This appears to make Mn rather exceptional as all other transition metals increase γ_{isf} [177]. The Mn content dependence of γ_{isf} is non-linear. In binary Fe-Mn alloys, in low concentrations, Mn reduces γ_{isf}.The lowest γ_{isf} value is obtained in the range of 10–16 at.% Mn. At higher Mn content, in the concentration range from 16 at.% to 33 at.%, alloying with Mn increases γ_{isf} by 18 mJ/m2 per 1 at.% Mn. This non-linear dependence of γ_{isf} is due to the effect of Mn on the fcc-hcp energy difference: an increase of the Mn content suppresses the formation of the hcp structure. The experimentally observed non-linear dependence has been confirmed by first principles calculations for disordered Fe-Mn alloys. With regard to the stacking fault formation, first principles computations predict that alloying with Mn should result in a continuous decrease of γ_{usf}. A further prediction is that Mn atoms should have a tendency to segregate to stacking faults.

The strong attractive NN C-Mn (+26 kJ/mol) and NNN C-Mn (+13 kJ/mol) interaction between Mn and C atoms in TWIP steels results in the formation of Mn-C pairs [157,177]. Kang et al. [189] carried out *ab initio* calculations of the energy change related to the addition of manganese atoms to Fe_{6-x}-Mn_x-C ($0 \leq x \leq 6$) octahedra in which a carbon atom occupies the central octahedral interstitial position. They report a free energy decrease by 0.0528eV per Mn atom (or 5.09 kJ/mol), *i.e.* the C-Mn interaction is attractive. The attractive C-Mn interaction leads to an increase of the solubility limit of C in γ-Fe when Mn is added.

Below we consider the effects of Mn on the properties of γ-Fe-C alloys, in addition to the effect on γ_{isf} discussed above, namely, (i) magnetic properties and (ii) diffusivity.

(i) The presence of Mn suppresses ferromagnetism and extends the temperature range in which anti-ferromagnetism occurs by raising the Néel temperature. In the temperature range for which C diffusion has typically been studied, *i.e.* in the high temperature range of 720–1200 °C, dilute fcc γ-Fe-C alloys are paramagnetic, i.e. they are characterized by a random orientation of local magnetic moments. Depending on the composition, fcc γ-Fe-Mn-C alloys and other TWIP steels are either anti-ferromagnetic or paramagnetic at room temperature. Serrated stress-strain curves observed at room temperature suggest the possibility of the occurrence of short-range diffusion of carbon atoms. A*b initio* calculations by Jiang and Carter [75] mentioned above have shown that the activation energy for diffusion of C in γ-Fe strongly depends on its magnetic state. According to that study, the ground state of γ-Fe is the anti-ferromagnetic double layer phase with a bi-layer … ↑↑↓↓ … in the ⟨001⟩ orientation.

(ii) The formation of Mn-C pairs reduces the C diffusivity. Using the nudged elastic band method, Jiang and Carter [75] calculated the activation energy for C diffusion and found a value of 0.99 eV, which is close to the experimental value for very dilute Fe-C alloys [190–192]. The details of carbon diffusion in γ-Fe based alloys are complex, the activation energy being temperature and composition dependent. Thus, the activation energy for C diffusion in γ-Fe in the C concentration range of 0–1.4 mass-% is 1.01–1.19 eV; specifically, at 0.6% mass-% C it amounts to about 1.17 eV [70].

The room temperature dynamic strain aging of TWIP steel, which manifests itself in serrated stress-strain curves, has been linked to the re-orientation of Mn-C pairs in the vicinity of stacking faults during dislocation glide [193].

3.3.3. Aluminium

The role of Al in TWIP steel is complex. *Ab initio* calculations show that Al is a potent stabilizer of the γ-Fe-Mn random alloys below as well as above the Néel temperature, which is consistent with an increase in the γ_{isf} upon alloying with Al. The influence of Al appears to be independent of the magnetic state, and the volume effect outweighs the chemical effect [137]. Jin et al. [62] have studied the influence of Al addition on γ_{isf} for a Fe-18%Mn-0.6%C-x% Al TWIP steel by XRD and TEM. Their findings are expressed by the following linear Al-content dependence of the intrinsic stacking fault energy:

$$\gamma_{isf}\left(mJ\Big/m^2\right) = 20 + 7.8 \cdot \%Al(mass-\%) \tag{49}$$

Using γ_{isf} measurements based on neutron diffraction, Kang et al. demonstrated an increase of γ_{isf} by 10 mJ/m per mass-% Al, *i.e.* from 17 mJ/m^2 for Fe-18%Mn-0.6%C to 37 mJ/m^2 for Fe-18%Mn-0.6% C-2%Al [194]. These results are in reasonable agreement with the increase by approximately 8 mJ/m^2 per mass-% Al predicted by thermodynamic calculation [117].

Alloying with Al inhibits dynamic strain aging in C-alloyed TWIP steels. Based on their study of the temperature dependent properties of austenitic Fe-30%Mn-x%Al-1.0%C alloys, Shun et al. [195] report that Al additions increased the apparent activation energy, as defined by the onset strain for the onset of discontinuous yielding, from 14.4 to 22.3 kcal/mol due to the addition of 2.7 mass-% Al, suggesting that Al-additions reduce the C diffusivity within the dislocation core.

Al promotes short range ordering and carbide formation. This is related to the strong attractive NNN C-Al interaction, which has a binding energy of 25 kJ/mol. It results in an increase of the solubility limit of carbon in γ-Fe when Al is added. As the NN C-Al interaction (−10 kJ/mol, or −0.104 eV/at) is repulsive, the formation of local order resembling the crystal structure of perovskite Fe_3AlC κ-carbide is favored [173]. This compound was experimentally identified by Park et al. in Fe-22%Mn-0.6%C-(0-3-6)%Al TWIP steels [61]. The NN C-Al repulsive interaction was also reported by Kang et al. [189] who carried out *ab initio* calculations of the energy increase associated with the addition of an Al atom to Fe_{6-x}-Al_x-C octahedra, in which a carbon atom occupies the central octahedral interstitial position. An energy increment of +0.382eV per Al atom (+36.86 kJ/mol) means that the interaction is strongly repulsive. As a result of Al-Mn interaction being repulsive, Al atoms avoid Mn atoms as nearest neighbors. Zero Kelvin first principles computations [157,177] also suggest that the Al distribution in TWIP steel is non-uniform.

Ab initio calculations have revealed that alongside the mentioned increase of the intrinsic stacking fault energy γ_{isf}, alloying of TWIP steels with Al leads to a systematic decrease of γ_{usf}. The ensuing reduction in the difference γ_{usf}-γ_{isf} with the growing Al content is expected to facilitate the emission of a trailing partial relative to the emission of a twinning partial dislocation, provided the magnitude of γ_{utf} is unaffected by the Al content or decreases with it.

3.3.4. Silicon

Si is a strong solid solution strengthening element in γ-Fe alloys. Its addition to an alloy reduces the Néel temperature and affects the magnetic order below the Néel temperature. No volume change is observed when Si is added to Fe-Mn alloys, indicating that the effect of Si on the stability of the γ-phase is governed by electron contributions to the interactions between the atoms. In the presence of C, the NN Si-C interaction is strongly repulsive. The NNN Si-C interaction is attractive. In the presence of both C and Mn, which

Please cite this article in press as: B.C. De Cooman, et al., Twinning-induced plasticity (TWIP) steels, Acta Materialia (2017), http://dx.doi.org/10.1016/j.actamat.2017.06.046

is the case for a TWIP steel, there is a repulsive Si-Mn interaction. According to Tian and Zhang [196], an increase in the Si content results in a decrease of γ_{isf} in Fe-Mn-Si-C alloys with up to 8 at-%Si. This was confirmed by Jeong et al. [172] who measured a drop in γ_{isf} at a rate of 4 mJm^{-2} per mass-% of Si for Si concentrations up to 1.5 mass-%. They also reported that the decrease of γ_{isf} in a 1.5% Si-added TWIP steel resulted in a higher strain hardening, which they attributed to enhanced activation of primary and secondary twinning.

There is no consensus about the effect of Si on γ_{isf}, however. Based on calculations, Dumay et al. [125] reported an increase of γ_{isf} for Si concentrations of up to 6 at.-% and a smooth decrease at higher concentrations. This is at variance with the mentioned results of Tian and Zhang [196] and Jeong et al. [172]. The latter group of authors suggested that this discrepancy is due to insufficient accuracy of the Mn-Si and Si-C interaction parameters used in the model calculations.

3.3.5. Nitrogen

Nitrogen has been reported to promote the formation of ε-martensite in Fe-16%Mn-(0.015, 0.05)%N TWIP steel, indicating that its presence reduces γ_{isf} [104]. Using a combination of neutron diffraction, XRD, and TEM Lee et al. [104] have shown, however, that γ_{isf} varies with the concentration of nitrogen at a rate of approximately 100 mJm^{-2}/mass-%N. The authors explained the observed retardation of twinning kinetics and reduction of the thickening of the twins to this increase of γ_{isf} with increasing N content. Huang et al. [197] showed that N increases γ_{isf} in Fe-(20−22)%Mn-0.01%C-(0.7−2.5)%Al-(2−3)%Si-(0−0.05)%N TWIP steel. The observed reduction in the probability of the occurrence of stacking faults with increasing N content in Fe-30%Mn-6%Si-(0−0.047%) N steel also suggests that alloying with N raises γ_{isf} [198].

According to Lua et al. [199], the main effect of interstitials on γ_{isf} is through the variation of the lattice parameter they cause. Their calculations of the effect of N and C additions on of Fe-22%Mn TWIP steel showed the variation of γ_{isf} at a rate of 29 mJm^{-2}/mass-% N and 32 mJm^{-2}/mass-% C, in agreement with the results of thermodynamic modeling [117].

The lowering of γ_{isf} by N has been used to explain the activation of twinning in Hadfield steel (12%Mn-1.2%C). In High Nitrogen Steels (HNS) and in austenitic stainless steels N inhibits twinning in favor of planar slip of dissociated dislocations when N < 0.4 mass-%. For N > 0.7 mass-%, the addition of N promotes extensive twinning. Thus, alloying with 1 mass-% of N (4 at-%) was shown to increase the γ_{isf} of these steels. Lee et al. [104] have studied the effect of nitrogen on γ_{isf} of a Fe-15%Mn-2%Cr-0.6%C-x%N TWIP steel by means of XRD. They established the following phenomenological dependence of the stacking fault energy on the nitrogen concentration:

$$\gamma_{isf}\left(mJ\Big/m^2\right) = 12 + 100\cdot\%N(mass-\%) \tag{50}$$

A similar trend, i.e. a linear increase of γ_{isf} from −404 mJ/m^2 to 179 mJ/m^2 for an increase of the N content by 2.14 mass-% in Fe-12% Mn-x%N alloys was found by means of *ab initio* DFT calculations [156]. This corresponds to the rate of variation of γ_{isf} of 272 mJ/m^2/mass-% N. They also report that the proximity of N to the stacking fault increases γ_{isf}, which implies that N should have a tendency to diffuse away from the stacking fault.

3.3.6. Copper, nickel

Both Cu and Ni stabilize the fcc γ-phase relative to the hcp ε-martensite. Cu atoms also tend to cluster in fcc austenite, as N atoms do as well. That is to say, Cu-Cu or Ni-Ni bonds are favored over Cu-Fe and Ni-Fe bonds. The effect of Cu on the stacking fault energy of TWIP steels was studied by considering the variation of γ_{isf} of Fe-Mn-C-Al TWIP steel from 22.8 mJm^{-2} to 26.0 mJm^{-2} due to an addition of 2% of Cu [104]. Cu additions also retard the kinetics of twin formation [104]. Alloying with copper also has an effect on DSA of Fe-Mn-C-Al TWIP steels, which is similar to the effect of N with respect to the type of serrations on the stress-strain curves and the number of PLC bands. A beneficial role of Cu additions in increasing total elongation without a loss of strength was reported by Lee et al. [200].

At the atomistic scale, an important effect of Cu and Ni on γ_{isf} was established by the *ab initio* calculations of Limmer [185]. It was found that Cu and Ni atoms located in the stacking fault plane increase γ_{isf} and decrease γ_{usf}. Specifically, the following figures for the rate of increase of γ_{isf} were found: 9.9 mJ/m^2 per atom-% Cu and 10.0 mJ/m^2 per atom-% Ni.

3.3.7. Chromium

While Cu and Ni atoms prefer to cluster in fcc austenite, the interaction between Cr atoms appears to point to a preference for their planar segregation, favoring Cr-Fe over Cr-Cr bonds. In the presence of both C and Mn, as is the case for a TWIP steel, the attractive C-Cr bond remains attractive. Due to a weak Cr-Mn repulsion, the preferred atomic arrangement is the 180 °-oriented Cr-C-Mn octahedral complex. *Ab initio* computations for binary γ-Fe-Cr alloys predict that the effect of Cr is similar to that of Mn. Alloying with either of them diminishes γ_{usf} and γ_{isf}. Cr atoms located at a stacking fault reduce γ_{isf} by 1.7 mJ/m^2 per atom-% Cr within the range of Cr concentrations up to 5.6 atom-% Cr [177]. This is consistent with the predictions of thermodynamic stacking fault energy models, which also predict a decrease γ_{isf} upon addition of Cr.

A general observation that refers to the alloying additions considered above (including Mn, Al, Ni, Cu, and Cr) is that their influence on γ_{isf} extends only over a region of two {111} planes adjacent to the stacking fault [185].

4. Mechanical properties of TWIP steel

The yield strength of TWIP steels is relatively low, and a large strain is needed to see the strength benefits associated with strain hardening. This implies that additional strengthening mechanisms have to be introduced to attain a well-balanced property profile. An obvious option is pre-straining, but it results in lower tensile elongation under subsequent loading. Alternative strengthening mechanisms involve grain refinement and precipitation hardening by micro-alloying.

4.1. Elastic properties of TWIP steel: Young's modulus anomaly

The magneto-elastic properties of anti-ferromagnetic high Mn Fe-alloys are associated with a pronounced Young's modulus anomaly. The Young's modulus E is higher in the high-temperature paramagnetic state than in the low-temperature magnetically ordered anti-ferromagnetic state. The origin of this "ΔE"-effect is spontaneous magnetostriction. A volume expansion caused by the anti-ferromagnetic ordering that occurs when the alloy is cooled below the Néel temperature leads to a deviation from the normal temperature dependence of the modulus of elasticity [201,202]. The decrease in the modulus can be rationalized in terms of an increase in the interatomic distances associated with the volume expansion, which leads to a weaker interatomic bonding. That is to say, the attendant lattice softening results in a stiffness reduction. The fundamental reason for this magneto-elastic effect lies in the

Please cite this article in press as: B.C. De Cooman, et al., Twinning-induced plasticity (TWIP) steels, Acta Materialia (2017), http://dx.doi.org/10.1016/j.actamat.2017.06.046

effect of the changing interatomic distances on the electronic structure, i.e. the density of states and the topology of the Fermi surface. This kind of "ΔE"-effect associated with the formation of antiferromagnetic order below the Néel temperature has been observed for TWIP steels.

A systematic study of Young's modulus of relatively highly Mn-alloyed ternary face-centered cubic Fe-(28.0–37.5)at.% Mn-(1.5–3.0)at.% C steels was carried out by Reeh et al. [203] by means of nano-indentation and *ab initio* calculations. According to their findings, within the compositional range studied, the carbon content significantly affected the lattice parameter, whose value was varied in the range of 0.3597–0.3614 nm. The *ab initio* calculations using the VASP code predict that the addition of carbon leads to a slight lattice expansion by 0.4% relative to the binary Fe-Mn alloys. Reech et al. also reported that carbon has no effect on Young's modulus. The measured Young's modulus values were in the range of 185(±12)-220(±20) GPa for bulk samples. Assuming a Poisson ratio value of $\nu = 0.29$, this corresponds to a magnitude of 72–85(±20) GPa for the shear modulus $G = \frac{E}{2(1+\nu)}$ at room temperature. These values are in broad agreement with Jung and De Cooman who measured the temperature and Al-content dependence of the shear modulus for Fe-18%Mn-0.6%C-x%Al TWIP steels (Fig. 30) [105]. The value of the room temperature shear modulus they quote is in the range of 76.5–79.0 GPa. It should be noted that the Néel temperature of Fe-18%Mn-0.6%C-x%Al TWIP steels is below room temperature.

The weak sensitivity of the Young's modulus of TWIP steels to alloying with carbon can be rationalized in terms of the nature of the atomic bonds. According to von Appen and Dronskowski [67], the electronic structure of Fe-Mn-C TWIP steels consists of covalent Fe-C and Mn-C bonds and metallic Fe-Fe, Mn-Mn, and Fe-Mn bonds. Since the number of covalent bonds is small, the addition of C has only a local effect and the electronic structure is not affected by C additions in the concentration range used for TWIP steels. The effect of C on the Young's modulus is therefore also expected to be minimal.

Allain [66] stated that the shear modulus is reduced substantially if the Néel temperature for the anti-ferromagnetic transition happens to be close to room temperature or to exceed it. The Néel temperature of Al-free Fe-22%Mn-0.6%C TWIP steel is 321 K (at 48 °C). The magnitude of the shear modulus is reduced from 72 GPa at 107 °C to as low a value as 60.5 GPa at −74 °C. At room temperature it takes the value of 62 GPa. For the same steel composition, Steinmetz et al. report a shear modulus value of as low as 52.5 GPa [41].

Fig. 30 shows that Al-additions, which increase the lattice parameter, also result in a reduction of the shear modulus of Fe-18% Mn-0.6%C-x%Al TWIP steel. The values of the elastic constants for high Mn Fe-alloys are compiled in Table 4. As the Mn content is reduced from 40 to 5 at. %, C_{44} is unaffected, while C_{11} and C_{12} increase by 25.6% and 39.2%, respectively. This behavior of the elastic constants is due to the magneto-volume effect which softens the lattice.

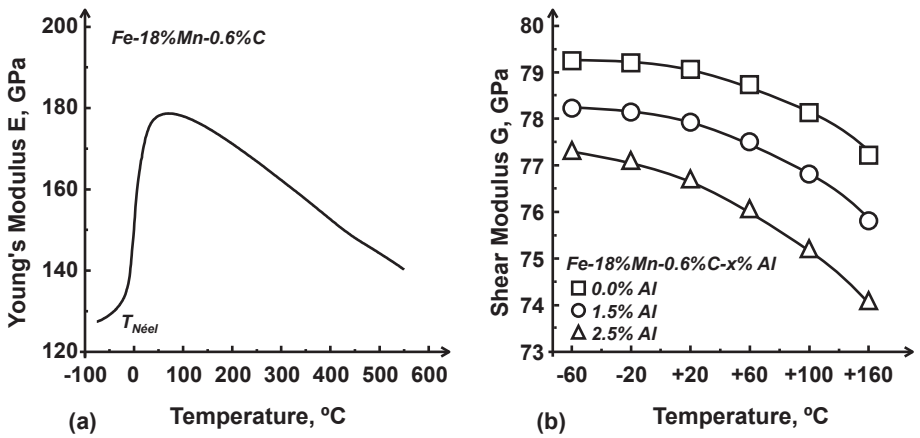

Fig. 30. (a) Temperature dependence of Young's modulus of Fe-18%MMn-0.6%C TWIP steel. The anti-ferromagnetic ordering results in a reduction of the modulus below the Néel temperature. (b) Effect of Al on the shear modulus of Fe-18%Mn-0.6%C-x%Al TWIP steel [210].

Table 4
Single crystal elastic constants for selected high Mn Fe-alloys. Average isotropic shear modulus *G* and bulk modulus *B* (compressive modulus) were computed according to the following equations.

$$G = \frac{G_{Voigt} + G_{Reuss}}{2}, \quad B = \frac{C_{11} + 2C_{12}}{3}$$

$$G_{Voigt} = \frac{C_{11} - C_{12} + 3C_{44}}{5}, \quad G_{Reuss} = \frac{5(C_{11} - C_{12})C_{44}}{3(C_{11} - C_{12}) + 4C_{44}}$$

	C_{11} GPa	C_{12} GPa	C_{44} GPa	$C_{12}-C_{44}$ GPa	G GPa	B GPa	B/G	Reference
Fe-25%Mn-3%Al-3%Si	174	85	45	−14	71.8	114.7	1.60	Pierce et al. [206]
Fe-22%Mn-3%Al-3%Si	175	83	46	−14	71.9	113.7	1.58	Pierce et al. [206]
Fe-20%Mn-1.2%C	236	139	117	+22	82.2	171.3	2.08	Idrissi et al. [91]
Fe-24%Mn-3%Al-2%Si-1%Ni-0.06%C	167	110	140	−30	75.0	128.9	1.72	Saleh et al. [43]

Please cite this article in press as: B.C. De Cooman, et al., Twinning-induced plasticity (TWIP) steels, Acta Materialia (2017), http://dx.doi.org/10.1016/j.actamat.2017.06.046

Table 5
Room temperature shear modulus of selected TWIP steels.

Composition	G GPa	Reference
Fe-24%Mn-0.7%C[a]	62.4	Kang et al. [184]
Fe-22%Mn-0.5%C[a]	63.6	
Fe-18%Mn-0.5%C[a]	73.2	
Fe-22%Mn-0.6%C[a]		Choi et al. [186]
[5 4 22] single crystal	67.0	
[16 6 23] single crystal	77.0	
Fe-22%Mn-0.6%C[a,b]	62.0	Bouaziz et al. [6]
Fe-18%Mn-0.6%C[b]	79.0	Jung and De Cooman [105]
Fe-18%Mn-0.6%C-1.5%Al[b]	78.0	
Fe-18%Mn-0.6%C-2.5%Al[b]	76.7	

[a] Anti-ferromagnetic.
[b] Polycrystal.

Considerable grain to grain stress incompatibilities can be generated in polycrystals deformed in the elastic regime and during the elasto-plastic transition when the elastic anisotropy coefficient, $A = 2C_{44}/(C_{11}-C_{12})$, is large [204]. The *ab initio* single crystal elastic coefficients of C-free Fe-Mn-Al and Fe-Mn-Si TWIP steels determined by Gebhardt et al. [205] give very large A values in the range of 4.6–7.4. In contrast, experimentally determined single crystal elastic coefficients for the Fe-22%Mn-3%Al-3%Si, Fe-25%Mn-3%Al-3%Si and Fe-18%Mn-1.5%Al-0.6%C TWIP steels result in a much lower value for A in the range of 2.11–2.22 [206]. This difference is very likely due to a magneto volume effect [207]: while anti-ferromagnetically ordered TWIP steels have a large elastic anisotropy, the anisotropy is significantly lower for magnetically disordered TWIP steels.

According to Pugh [208], the *B*/*G* ratio, i.e. the ratio of the bulk modulus *B* to the shear modulus *G*, can be used as a guidance to predict the ductility of a solid. The bulk modulus *B* is a measure of the resistance of a material against volume compression. It is related to the metallic bond strength and the resistance to rupture. The shear modulus *G* is a measure of the resistance to a shape change by shear deformation. Materials which deform easily commonly have a lower shear modulus compared to hard brittle materials. A ductile material will therefore have a high *B*/*G* ratio, as the grains at the tip of a crack will deform by having their atomic planes slip rather than being pulled apart. Conversely, a brittle material is characterized by a low *B*/*G* ratio. At the crack tip in a brittle material the atomic planes will be pulled apart instead of slipping. Brittleness in metals and alloys with a cubic crystal structure is characterized by $B/G < 1.75$, ductility is associated with $B/G > 1.75$. The *B*/*G* ratio is mainly determined by the difference $C_{12}-C_{44}$, which is positive for ductile materials [209]. In first-principle calculations of elastic and magnetic properties of Fe-Mn-X alloys, the calculated *B*/*G* ratio can therefore be used as a useful criterion to predict which alloying element might improve the intrinsic ductility of a TWIP steel. In this light, the data shown in Table 5 suggests that high Mn Fe-alloys are more likely to display brittle behavior. Based on the Pugh and Pettifor criteria, only the Fe-15%Mn alloy is expected to have a ductile behavior. Reeh et al. [203] predict that Cu additions, which significantly reduce *G* while only slightly increasing *B*, should give rise to a substantial improvement of ductility of high Mn Fe-alloys, such as TWIP steels. Their calculations, based on the EMTO formalism as implemented in the EMTO5.7 Package, suggest that the addition of Cu increases the valence electron occupancy in the d-bands, which are not fully occupied. This enhances the metallic component of the bonds relative to the covalent component, and leads to a reduction of the shear modulus. A similar trend was observed by Jung [210] in experiments on Fe-18%Mn-0.6%C-x%Al TWIP steels. It was found that an increase in Al content lowers the magnitude of the shear modulus, cf. Fig. 30b.

4.2. The elasto-plastic transition

Fig. 31 compares stress-strain curves for polycrystalline TWIP steel samples tested in tension and single crystals of TWIP steel tested in compression. Using the Taylor factor ($M = 3.06$) to compute the critical resolved shear stress for plastic flow initiation, one obtains the values of 76 MPa and 72 MPa for single crystals with a twinning-suppressing [011]-orientation and a twinning-enhancing [001]-orientation, respectively. Bracke et al. [17] reported very similar values, *viz.* a critical resolved stress for dislocation slip of 89 MPa, and a critical resolved twinning shear stress of 77 MPa. It is unlikely that partial dislocation sources can be activated at such low stresses, since Frank-Read type partial dislocation sources required to generate twins cannot achieve instability and expand at such a low stress level. This suggests that the elasto-plastic transition is controlled by a dislocation slip mechanism which does not involve twinning. The deformation of single crystal TWIP steel micro-pillars was investigated by Choi et al. [186] and Wu et al. [211]. The well-defined testing conditions used enabled a study of plastic deformation in the absence of strain gradients,

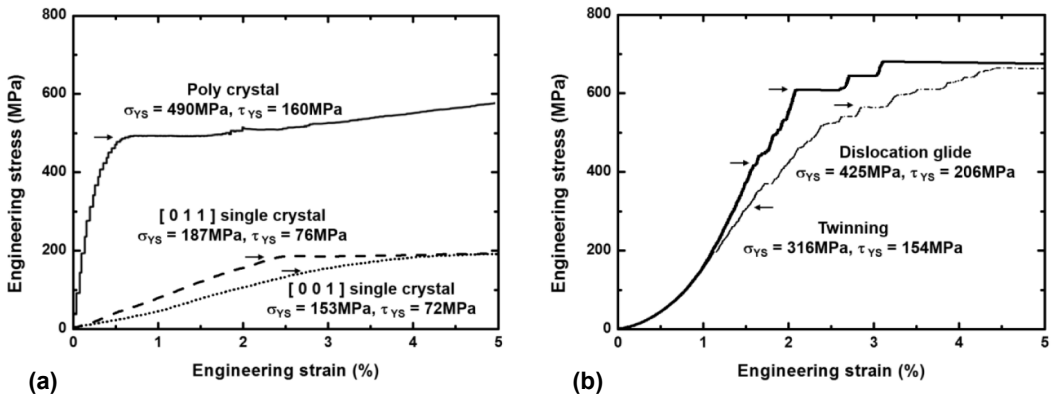

Fig. 31. (a) Stress-strain curves for polycrystalline TWIP steel deformed in tension and single crystals TWIP steel deformed in compression. (b) Stress-strain curves for submicron diameter TWIP steel micropillars deformed in compression. The arrows indicate small strain bursts at low stress levels. σ_{YS}: yield strength, τ_{YS}: yield shear strength [186].

grain boundaries, grain size effects, etc. A complicating issue in micro-pillar measurements is the size effect. A size effect is also of relevance to the critical stress for twinning [212]. In fcc metals and alloys this effect is associated with source starvation, when the pillars "run out of dislocations" and the dislocation-free state requires high strength for commencement of plastic flow. Alternatively, truncation of the dislocation Frank-Read source size may be the reason for a size effect. It is interesting that Wu et al. [211] concluded that twins were nucleated at the surface of the pillars, whereas Choi et al. [186] observed that dislocation–dislocation interactions were needed for twin formation in the bulk. The yield strength of micro-pillars oriented for dislocation glide was 425 MPa, while that associated with an orientation favoring twinning was 316 MPa. Wu et al. measured a critical resolved shear stress of 488 MPa for a Fe-22%Mn-0.6%C micropillar 0.705 μm in diameter with a [001] orientation favoring twinning. The large difference, i.e. 488 MPa in Wu et al. study versus 316 MPa in Choi et al. is due to the fact that Wu et al. report the maximum compression stress, whereas Choi et al. consider the average value of the stress at the first strain burst as a signature of plastic flow initiation due to the activation of a single source. The size-independent critical resolved shear stress measured on a 7.6 μm diameter Fe-22%Mn-0.6%C TWIP steel micro-pillar was 61.1 MPa, i.e. only slightly smaller than the critical resolved shear stress of 76 MPa obtained experimentally for polycrystalline TWIP steel. Table 6 reviews reported values for the critical resolved shear stress and indicates whether a particular orientation favors dislocation glide or deformation twinning.

4.3. Solute solution strengthening

The strengthening effect of solute atoms in austenitic fcc Fe alloys is known to be much less pronounced than in the case of ferritic bcc Fe alloys. Bouaziz et al. have proposed the following heuristic equation for the lattice friction stress, which includes the solid solution strengthening effect of C and Mn in Fe-Mn-C TWIP steel [53]:

$$\sigma_0(MPa) = 228 + 187\cdot\%C - 2.0\cdot\%Mn \tag{51}$$

Using the Taylor orientation factor $M = 3.06$, the critical resolved shear stress and the corresponding yield strength for Fe-22%Mn-0.6%C TWIP steel are given by:

$$\begin{aligned}\tau_{crss}(MPa) &= 74.5 + 61.11\cdot\%C - 0.65\cdot\%Mn = 97\ MPa\\ \sigma_{ys}(MPa) &= 296\ MPa\end{aligned} \tag{52}$$

Choi et al. [186] put forward an alternative equation for composition-dependent solid solution strengthening in terms of the critical resolved shear stress and the lattice friction stress for Fe-Mn-C-Al-Si TWIP steel:

$$\begin{aligned}\tau_{crss}(MPa) &= 31.7 + 91.3\cdot\%C - 0.49\cdot\%Mn + 16.2\cdot\%Si + 6.7\cdot\%Al\\ \sigma_0(MPa) &= 97 + 279\cdot\%C - 1.5\cdot\%Mn + 49.6\cdot\%Si + 20.5\cdot\%Al\end{aligned} \tag{53}$$

Using the equation proposed by Choi et al. [186], one obtains for Fe-15%Mn-0.7%C-2%Al-2%Si TWIP steel:

$$\begin{aligned}\tau_{crss}(MPa) &= 31.7 + 91.3\cdot\%C - 0.49\cdot\%Mn + 16.2\cdot\%Si + 6.7\cdot\%Al = 134MPa\\ \sigma_0(MPa) &= 410MPa\end{aligned} \tag{54}$$

It is recognized that the overall effect of solutes on the characteristics of plastic yielding is quite appreciable. It should be noted that Mn additions provide a negative contribution to this effect regardless of the specific form of the heuristic relation for solute solution strengthening chosen by the different authors.

There are conflicting reports on the solid solution strengthening of Al and further investigation of the effect of Al on the yield strength of TWIP steel are needed. In contrast to Jung and De Cooman who report a hardening effect of 6.7 MPa/mass-%Al [105], Pasakin et al. [188] find a much lower solid solution strengthening effect of 0.8 MPa/mass-% Al.

4.4. Thermally activated plastic flow in TWIP steels

Allain et al. [213] and Jung and De Cooman [105] have investigated the thermally activated plastic flow in austenitic high Mn Fe-Mn-C steels. The Peierls shear stress, τ_P, is the resolved shear stress required to move a straight dislocation from one valley of the Peierls relief to the next one a thermally, at absolute zero. This quantity cannot be measured experimentally, but theoretical equations can be used to calculate the Peierls shear stress at 0 K [214,215]. Using the characteristic parameter values for {111}-a_γ/2<110> dislocation glide in γ-Fe, *viz.* an effective inter-planar spacing equal to $d_{111} = \sqrt{6}\ \frac{a}{3}$, a dislocation Burgers vector of magnitude $b = \sqrt{2}\ \frac{a}{2}$, a lattice parameter a of 0.36 nm, a zero Kelvin shear modulus $G_\gamma(0\ K)$ of 78.24 GPa, and Poisson's ratio $\nu(0\ K) = 0.313$, one obtains the following estimates for the zero Kelvin Peierls stress for an edge and a screw dislocation, respectively:

Table 6
Overview of the reported critical resolved shear stress values for dislocation glide and twinning in TWIP steels.

Steel	Compression axis	Sample type	Deformation	τ_{CRSS} MPa	Reference
Fe-22%Mn-0.6%C	[0 0 1]	Micro-pillar (0.7 μm diameter)	Twinning	488	Wu et al. [211]
Fe-22%Mn-0.6%C	[16 6 23]	Micro-pillar (2.0 μm diameter)	Dislocation glide	206	Choi et al. [186]
Fe-22%Mn-0.6%C	[1 3 6]	Micro-pillar (3.9 μm diameter)	Twinning	188	Wu et al. [211]
Fe-22%Mn-0.6%C	–	Polycrystal (EN10002)	–	160	Choi et al. [186]
Fe-22%Mn-0.6%C	[5 4 22]	Micro-pillar (2.0 μm)	Twinning	154	Choi et al. [186]
Fe-18%Mn-0.6%C	–	Polycrystal (ASTM E8)	–	144	Dumay et al. [125]
Fe-22%Mn-0.6%C	[0 1 1]	Single crystal (4.0 mm)	Dislocation glide	76	Choi et al. [186]
Fe-22%Mn-0.6%C	[0 0 1]	Single crystal (4.0 mm)	Twinning	72	Choi et al. [186]

Please cite this article in press as: B.C. De Cooman, et al., Twinning-induced plasticity (TWIP) steels, Acta Materialia (2017), http://dx.doi.org/10.1016/j.actamat.2017.06.046

$$\tau_{P,edge} = \frac{G}{1-\nu}\cdot\exp\left[-\frac{2\cdot\pi}{1-\nu}\cdot\frac{d}{b}\right] = \frac{78\ GPa}{1-0.313}\cdot\exp\left[-\frac{2\pi}{1-0.313}\cdot 1.1547\right] = 2.9MPa$$
$$\tau_{P,screw} = G\cdot\exp\left[-2\cdot\pi\cdot\frac{d}{b}\right] = 78\ GPa\ \exp[-2\cdot\pi\cdot 1.1547] = 55\ MPa \quad (55)$$

Allain et al. [213] suggested that, in addition to its influence on the TWIP effect, C also affects the dislocation mobility. The temperature dependence of the yield strength of various Fe-Mn, Fe-Mn-C, and Fe-Mn-C-Al steels, modified by subtraction of the yield stress at room temperature, is presented in Fig. 32. The yield stress exhibits a clear temperature dependence below room temperature. By analyzing the data from various literature sources, Allain et al. [213] showed that the temperature dependence of the contribution to the yield stress associated with thermally activated dislocation motion was more pronounced in TWIP steels with a high C content.

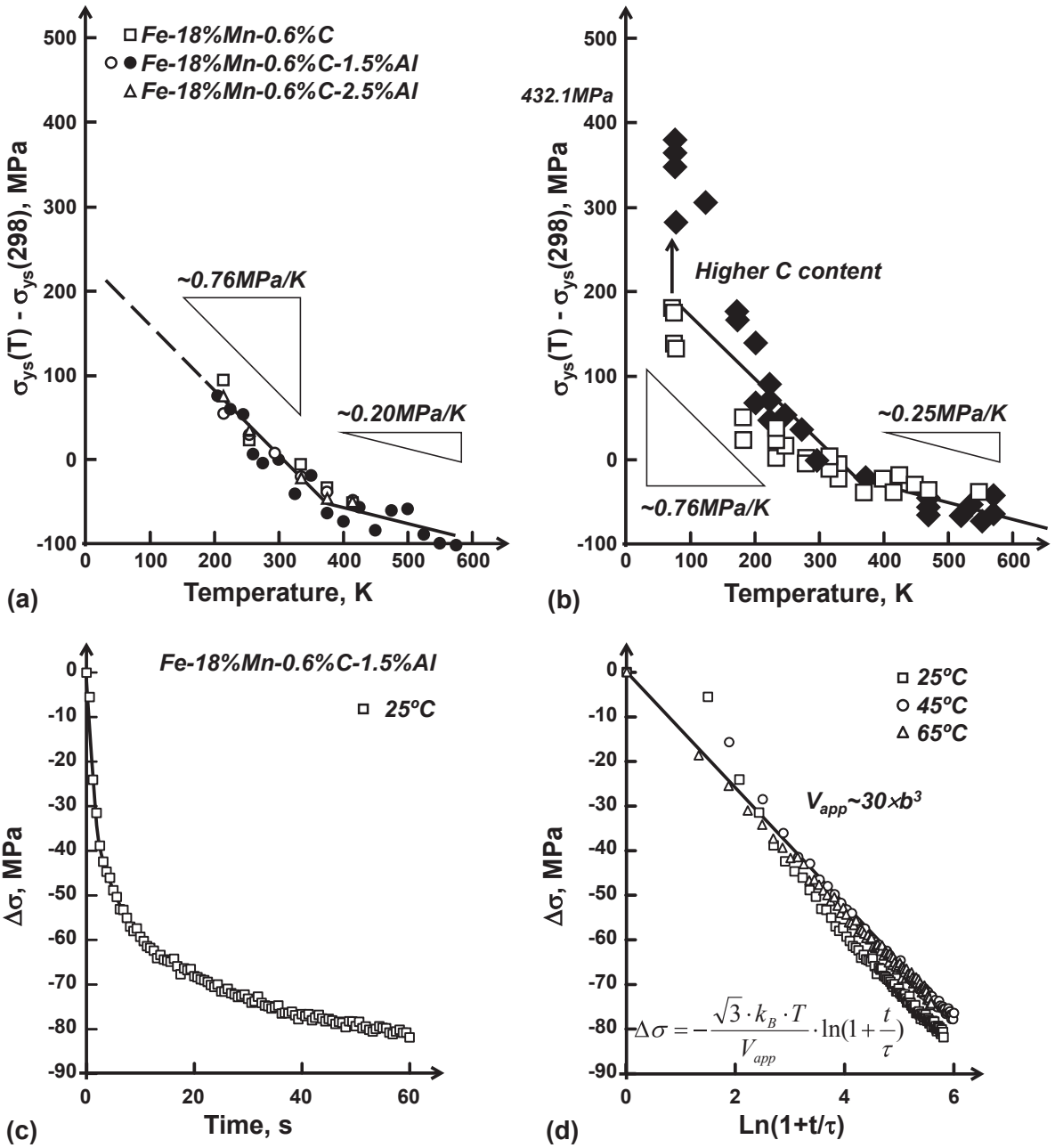

Fig. 32. (a) Temperature dependence of the difference $\sigma_{ys}(T)$- $\sigma_{ys}(298)$ for TWIP steels with 0.6%C. (b) Temperature dependence of the difference $\sigma_{ys}(T)$- $\sigma_{ys}(298)$ for TWIP steels with a higher C content (>0.6%). (c) Isothermal stress relaxation test results for Fe-18%Mn-0.6%C-1.5%Al TWIP steel. (d) $\Delta\sigma$ *vs.* $\ln(1 + t/\tau)$ plot for isothermal relaxation tests carried out at 25 °C, 45 °C and 65 °C to determine the apparent activation volume V_{app} [66,216].

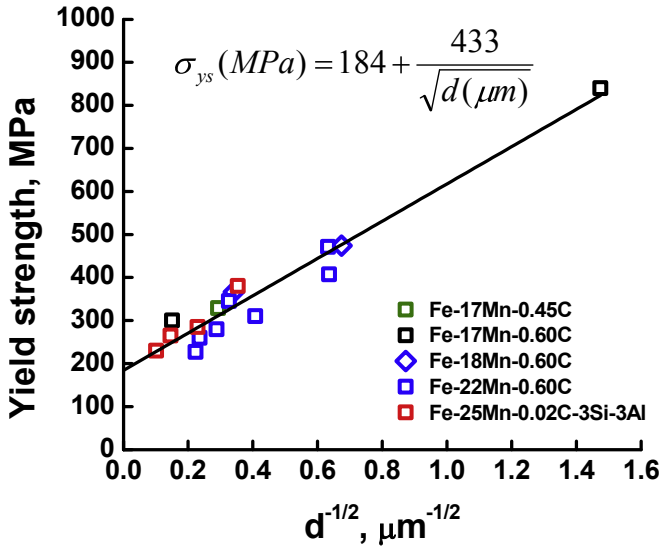

Fig. 33. Verification of the Hall-Petch relation for various TWIP steels (Fe-22%Mn-0.6%C [218], Fe-17%Mn-0.45%C [221], Fe-25%Mn-3%Si-3%Al-0.02%C [225], Fe-17%Mn-0.6%C [228]).

They also determined the attendant activation volume, which was in the range of 14–60 × b_{110}^3, where b_{110} is the atomic spacing in the close-packed direction ⟨110⟩. Majidi et al. [216] carried out careful isothermal measurements of the apparent activation energy of Fe-18%Mn-0.6%C-1.5%Al TWIP steel using stress relaxation experiments. The results are shown in Fig. 32. The time dependence of the stress decrement $\Delta\sigma$ was found to roughly follow a logarithmic dependence and be linear in $\ln(1 + t/\tau)$. Here t is the time, and τ is a characteristic relaxation time, whose temperature dependence presented in an Arrhenius form can be used to determine the activation energy of the process. Such a logarithmic dependence, in the form

$$-\Delta\sigma = \sqrt{3}\cdot\frac{k_B\cdot T}{V_{app}}\cdot\ln\left(1+\frac{t}{\tau}\right) \tag{56}$$

would, indeed, follow for a stress relaxation curve under the assumption of a constant apparent activation volume, V_{app}, in the Arrhenius relation for the plastic strain rate (or individual dislocation velocity). The activation volume is an informative footprint of the rate-controlling mechanism of plastic deformation, which can be used to identify the mechanism. While dislocation dynamics controlled by thermally activated breakaway from forest dislocation junctions is characterized by a large activation volume of the order of 1000 × b_{110}^3, a very small activation volume, of the order of the atomic volume, or ~ b_{110}^3, is indicative of dislocation climb control. An activation volume in the intermediate range of 10–100 × b_{110}^3 is likely to be associated with the lattice resistance (Peierls mechanism) or dislocation-point defect interaction. Allain reported that while the activation energy for TWIP steels (~0.5eV) was independent of the C content, the activation volume did depend on it, decreasing with the carbon concentration [71]. This suggests that the low temperature dislocation dynamics are controlled by a strong interaction of mobile dislocations with carbon atoms facilitated by a low activation energy for C diffusion in the vicinity of the dislocation core. However, in the observed range of the apparent activation volume there may be an overlap of solute-controlled and Peierls relief-controlled mechanisms of thermally activated dislocation dynamics [217,218]. To untangle these effects, a detailed analysis of the temperature, stress, and solute concentration dependence of the plastic strain rate would be required.

In the cited studies by Allain [213] and Majidi et al. [216], the magnetic state of the alloys (anti-ferromagnetic or paramagnetic), the Mn content, and the Al content did not appear to influence the activation volume. Above the room temperature, the yield stress of all the TWIP steels studied showed a reduced temperature sensitivity of approximately −0.20 to −0.25 MPa/K, cf. Fig. 32, which may be associated with the temperature dependence of the shear modulus, rather than a thermally activated character of plastic flow.

4.5. Grain size strengthening in TWIP steels

In numerous publications, the yield stress, σ_{YS}, of polycrystalline TWIP steels was shown to follow the Hall-Petch relation:

$$\sigma_{ys}(MPa) = \sigma_{ys}^0 + \frac{k_{ys}^{HP}}{\sqrt{d}} \tag{57}$$

Here the parameter σ_{YS}^0 includes the lattice friction stress, the solid solution strengthening contribution of the alloying elements, and the strain hardening contribution of the initial dislocation density, k_{YS}^{HP} is a material parameter, and d is the average grain size. Fig. 33 compiling some data for TWIP steels demonstrates that they obey the Hall-Petch relation. Available literature data on the parameters σ_{ys}^0 and k_{ys}^{HP} for a number of TWIP steels are reviewed in Table 7 [6,49,217–221]. For polycrystalline Fe-22%Mn-0.6%C TWIP steel, the reported values of σ_{YS}^0 and k_{YS}^{HP} are 132 MPa and 449 MPa μm$^{1/2}$ (14.2 MPa mm$^{1/2}$), respectively. However, the σ_{YS}^0 value given by Bouaziz et al. [6] in their original manuscript seems to have been misprinted since the yield stress level is significantly lower than the value calculated using the parameters from the same reference. Therefore, the value of σ_{YS}^0 for polycrystalline Fe-22%Mn-0.6%C TWIP steel was re-evaluated. The corrected

Table 7
Parameters of the Hall-Petch relation for TWIP steels.

Alloy	σ_{ys}^0, MPa	k_{ys}^{HP}, MPa.μm$^{1/2}$	Reference
Fe-31%Mn-3%Al-3%Si	53	764	Dini et al. [217]
Fe-22%Mn-0.6%C	137	449	Bouaziz et al. [6]
	170	428	Scott et al. [218]
Fe-22%Mn-0.6%C	157	357	Gil Sevillano-Cuevas [49]
Fe-22%Mn-0.5%C-0.08%N	219	478	Lee-De Cooman [214]
Fe-20%Mn-0.6%C	158	485	Shen et al. [220]
Fe-17%Mn-0.45%C-1.5%Al-1%Si[a]	208	445	Gwon [221]
Fe-17%Mn-0.45%C-1.5%Al-1%Si[b]	403	445	
Fe-15%Mn-0.7%C-2%Al-2%Si	305	330	Rahman et al. [20]

[a] Hot rolled.
[b] Hot rolled and recrystallization annealed.

magnitude for σ_{YS}^{0} is 242 MPa, rather than 132 MPa, the value reported by Bouaziz et al., and the corresponding critical resolved shear stress is 79 MPa, assuming a Taylor factor of 3.06 [6]. Lee and De Cooman [214] have derived the following Hall-Petch equations for the yield strength and the ultimate tensile strength for Fe-22% Mn-0.5%C-0.08%N:

$$\sigma_{ys}(MPa) = 219 + \frac{15.1MPa\cdot mm^{1/2}}{\sqrt{d(mm)}} = 219 + \frac{477.5MPa\cdot \mu m^{1/2}}{\sqrt{d(\mu m)}}$$
$$\sigma_{UTS}(MPa) = 754 + \frac{18.8MPa\cdot mm^{1/2}}{\sqrt{d(mm)}} = 754 + \frac{594.5MPa\cdot \mu m^{1/2}}{\sqrt{d(\mu m)}} \quad (58)$$

Kang et al. [222] analyzed the influence of the C content on the Hall-Petch coefficient k_{ys}^{HP} using a slow cooling procedure to ensure equilibrium C segregation to the available grain boundary sites. Kang et al. reported that k_{ys}^{HP} increased from 218 MPa $\mu m^{1/2}$ to 344 MPa $\mu m^{1/2}$ when the C content was doubled from 0.3 mass-% to 0.6 mass-%. They offered two possible explanations for this pronounced increase of k_{ys}^{HP}. The effect may be associated either with an increased stress for the activation of dislocation sources in the bulk of a grain when the C content is increased or with an increased density of grain boundary ledges acting as dislocation sources [223]. The second explanation is erroneous as the mechanism would result in a decrease of k_{ys}^{HP} upon an increase in C.

The Hall-Petch diagram can be affected by alloying additions, as demonstrated in Fig. 34 for the case of alloying TWIP steels with Ti, V, and Ni. It also depends on the pre-strain at which the measurements are taken for a particular material. While the slope k_{ys}^{HP} of the Hall-Petch diagram decreases with increasing strain for α-Fe and ferritic steels, it increases with strain for austenitic steels. The latter trend is also observed for TWIP steels. Gil Sevillano et al. [44] and de las Cuevas [224] reported a Hall-Petch slope of about 350 MPa $\mu m^{1/2}$ for the yield strength, and a Hall-Petch slope of 630 MPa $\mu m^{1/2}$ for the ultimate tensile strength. The data of Wang et al. [225] for Fe-24.8%Mn-0.022%C-3.17%Si-3.12%Al confirms that the Hall-Petch slope is higher for the ultimate tensile strength, amounting to 638 MPa $\mu m^{1/2}$ vs. 568 MPa $\mu m^{1/2}$ for the yield strength.

The yield strength of TWIP steels is generally rather low, and relatively large deformations are required to achieve a high flow stress. This limits the use of TWIP steels to complex press-formed parts whose manufacturing involves large amounts of plastic strain. Micro-alloying of TWIP steels was therefore considered as a way to increase the yield strength by grain size reduction and precipitation hardening. Results are available for low carbon Fe-25% Mn-3%Si-3%Al-0.02%C TWIP steel [225], and high carbon Fe-17% Mn-0.6%C [226] and Fe-22%Mn-0.6%C TWIP steel [218]. The observed strengthening was accounted for in terms of the Orowan precipitate bypassing mechanism. Unfortunately, no information on the equilibrium solute solubility and precipitation kinetics for nitrides, carbides or carbo-nitrides in TWIP steels is currently available in relation to micro-alloying additions of Ti, Nb or V. It can therefore not be ruled out that some of the observed improvements of strength were due to solid solution strengthening by the micro-alloying additions.

Vanadium appears to be the most efficient micro-alloying element, as it both reduces the grain size and leads to the formation of very small precipitates, which can be 3.4 nm in size, according to Scott et al. [218]. The solid solution strengthening effect of V is approximately 17 MPa/mass-% V. Vanadium also inhibits the recrystallization kinetics. According to Chateau et al. [227], who studied the effect of V micro-alloying additions on the properties of Fe-22%Mn-0.6%C TWIP steel, the VC particles do no change the strain hardening behavior. Based on their TEM analysis, Chateau et al. concluded that VC precipitates do not act as strong obstacles to the propagation of microtwins. They report that the addition of 0.21 mass-% V was found to bring about a strengthening effect of 140 MPa. Yen et al. [228] associated the strengthening effect of V in Fe-21.6%Mn-0.63%C-0.87%V TWIP steel with precipitation. Indeed, a high density of V_4C_3 carbide precipitates with the average diameter of 13 ± 7.7 nm were formed during a recrystallization annealing treatment (60 s at 850 °C). A stress increment of 198 MPa by precipitate strengthening was attributed to the Orowan bypassing mechanism. This is a rather modest strengthening effect considering the high V content in the steel studied. A reduction of the precipitate size to below 5 nm, as observed by Scott et al. [218] enables a more pronounced strengthening effect due to the Orowan bypassing mechanism. To quantify the effect for the case of VC

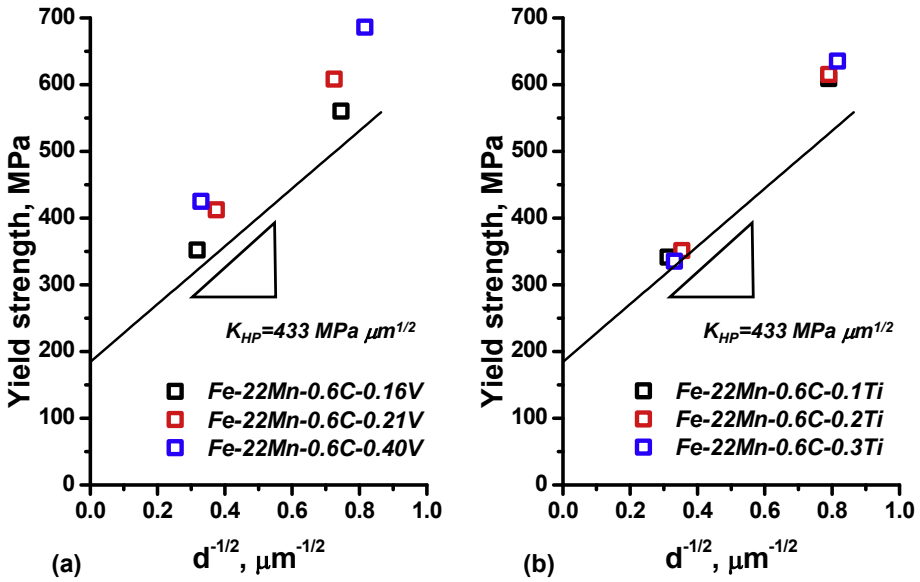

Fig. 34. Influence of micro-alloying additions of (a) V and (b) Ti on the Hall-Petch diagram for TWIP steel [218,221].

precipitates, the Ashby-Orowan equation

$$\Delta\sigma_{ys} = 0.847 \cdot M \cdot \frac{1.2}{2 \cdot \pi} \cdot G \cdot b \sqrt{\frac{3}{2 \cdot \pi}} \cdot \frac{\sqrt{f_{VC}}}{r_p} \cdot \ln\left(\frac{r_p}{b}\right) \quad (59)$$

can be used. Here f_{VC} is the volume fraction of vanadium carbides and r_p is their mean radius. The least-square fitting of the data shown in Fig. 35 to Eq. (56) yields $r_p = 10$ nm for $M = 3.06$. This is in excellent agreement with the precipitate radius range of 7–12 nm reported by Chateau et al. [227].

It is generally accepted that grain refinement down to the submicron grain size, 100 nm < d < 1 μm, results, with a few exceptions, in a reduction of strain hardening and hence lowered uniform tensile elongation [229,230]. Plasticity as such is not suppressed, as the ultrafine grained (UFG) materials sustain a large post-uniform elongation in the necking region. TWIP steel does not appear to be susceptible to a negative influence of small grain size on the uniform elongation. Grain growth after recrystallization annealing makes it possible to obtain a broad grain size range for a high Mn TWIP steel. Ueji et al. [231,232] reported that grain size reduction in C-free Fe-31%Mn-3%Al-3%Si TWIP steel (with the intrinsic stacking fault energy γ_{isf} ~42 mJ/m^2) resulted in a strong inhibition of deformation twinning and a significant drop in ductility. In fine grained TWIP steel twinning was still prevalent in grains oriented with a ⟨111⟩ direction close to the tensile axis. Gutierrez-Urrutia et al. [233] report that grain refinement did not suppress deformation twinning in a Fe-22%Mn-0.6%C TWIP steel (γ_{isf} ~23 mJ/m^2) altogether, but made it more difficult. They also associated the smaller grain size obtained to a reduction of the twin volume fraction. Lee et al. [226] compared the tensile deformation behavior of UFG C-free Fe-17%Mn and Fe-17%Mn-0.6%C TWIP steel with that of the C-added TWIP steel and concluded that the grain refinement induced reduction in elongation was smaller for the latter. It should be noted that TWIP steel with the grain size down to about 2 μm still retained a large uniform elongation of approximately 50% engineering strain. In a recent work [234] the properties of a Fe-22.3Mn-0.19Si-0.14Ni-0.27Cr-0.61C TWIP steel deformed by equal channel angular pressing (ECAP) were investigated. It was shown that a good balance between strength (1702 MPa) and tensile elongation (24%) in the steel with a resulting UFG structure can be achieved by a suitable choice of the processing schedule. This was associated with the formation of deformation microbands and twins (including nano-twins) in the microstructure during the ECAP processing.

5. Twinning mechanisms in TWIP steels

As deformation twinning is at the core of the mechanical properties of TWIP steels, a detailed exposé on this subject will be given in this section.

5.1. Mechanisms of deformation twinning

Deformation twinning results from a homogeneous shearing of the matrix by a highly coordinated glide of partial dislocations with the same Burgers vector, with exactly one dislocation gliding on each successive {111}-type twinning plane. In polycrystalline materials twin formation by {111}⟨112⟩ slip results in a volume orientation change of a certain fraction of the twinned grains which affects the crystallographic texture. {111}⟨112⟩ slip requires complete separation of partial dislocations, or the existence of partial dislocation sources. The spontaneous formation of twins is very unlikely as it would require very high stresses. The model originally proposed by Fontaine [235] for deformation twinning is generally accepted. In this model wide stacking faults are first formed, overlapping stacking faults then generate twin embryos, and twin growth occurs by the addition of a stacking fault on the twin plane. The wide stacking faults that form twin embryos can either be a result of suitable dislocation reactions or they can be emitted from interfaces such as grain boundaries. The conditions for twin nucleation from stacking faults emitted from grain boundaries are not well established. Grain boundaries containing interfacial

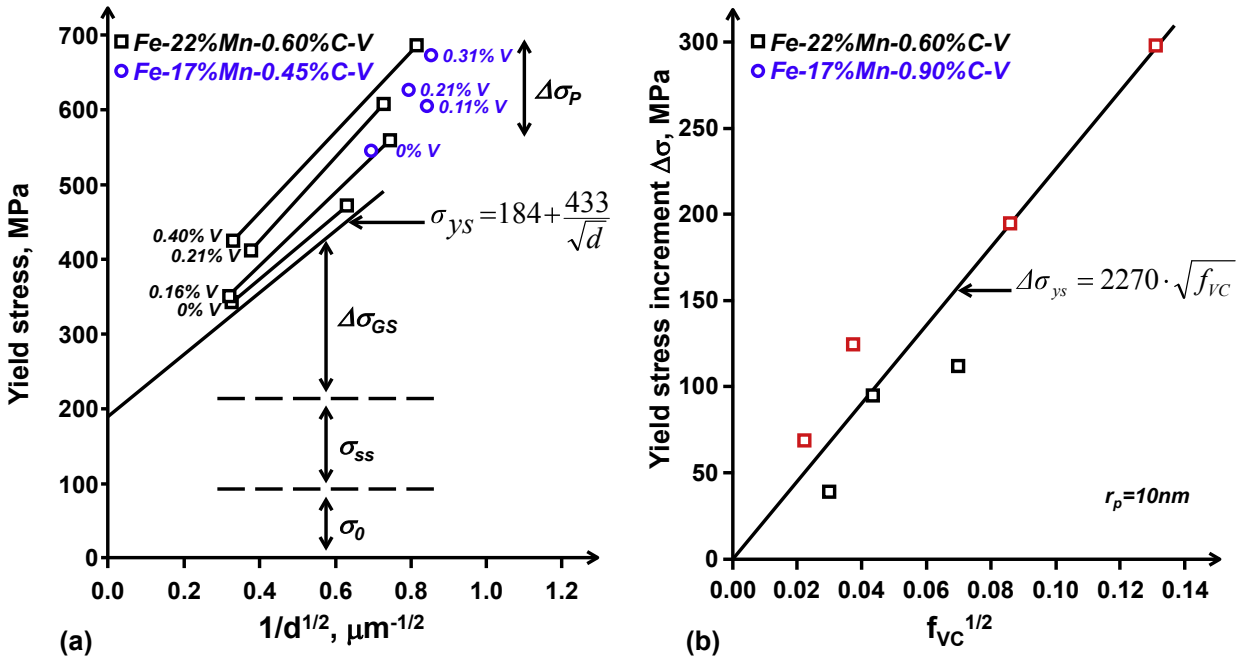

Fig. 35. (a) Analysis of the grain size dependence of the yield strength of V-added Fe-22%Mn-0.6%C and Fe-17%Mn-0.45%C TWIP steels, indicating the various contributions to strength. (b) Analysis of the contribution of the VC precipitates through the Orowan bypassing mechanism [218,221].

dislocations which can emit a twinning partial dislocation with a Burgers vector out of the boundary plane, e.g. dissociated screw-type misfit dislocations in a twist boundary, could act as areas where twin embryos are formed. Random grain boundaries could also contain pre-existing multi-layer twin nuclei which can easily be activated at low strains.

Models for deformation twinning should be compatible with the basic feature of the deformation in TWIP steel, which is generally considered to be initially by dislocation slip. During this early stage secondary slip systems are already activated, and long stacking faults and secondary slip systems are visible in TEM. Deformation twins are formed soon after yielding and at low strains in areas where two slip systems are activated. Twins are mainly formed on the primary twin system and the contribution of secondary twins systems to deformation twinning is limited. A twinned region consists of very thin twin plates. Twinning is sensitive to the crystal orientation. It is easy when a grain has a ⟨111⟩ direction or a direction on the ⟨111>–<100⟩ tie line close to the tensile axis.

Reviews offering an in-depth description of classical models for deformation twinning are available in the literature [236,237], but it should be mentioned that several new twinning mechanisms have recently been proposed due to the importance of deformation twinning in imparting enhanced plasticity to UFG and nano-crystalline materials with high γ_{isf} [238–241]. The present section will review only those deformation twinning models which have been reported to be compatible with the TEM analysis of twins in TWIP steels. Six twinning mechanisms which have been discussed in relation to deformation twinning in TWIP steel are as follows:

(1) the Venables pole mechanism [95].
(2) the Cohen-Weertman Frank cross-slip mechanism [242].
(3) the Fujita-Mori stair-rod cross-slip mechanism [243].
(4) the Mahajan-Chin extrinsic fault mechanism [244].
(5) the Miura-Takamura-Narita Frank primary slip mechanism [245].
(6) the Copley-Kear-Byun partial dislocation breakaway mechanism [146,246].

These models have in common that deformation twinning requires achieving a high enough dislocation density and a high local stress to trigger the twin nucleation and growth. The schematics in Fig. 36 illustrate the key aspects of the deformation twinning mechanisms which have been reported in relation to TWIP steels in literature. In the figure, the Thompson tetrahedron is used to describe the twinning mechanisms. Perfect and partial dislocations

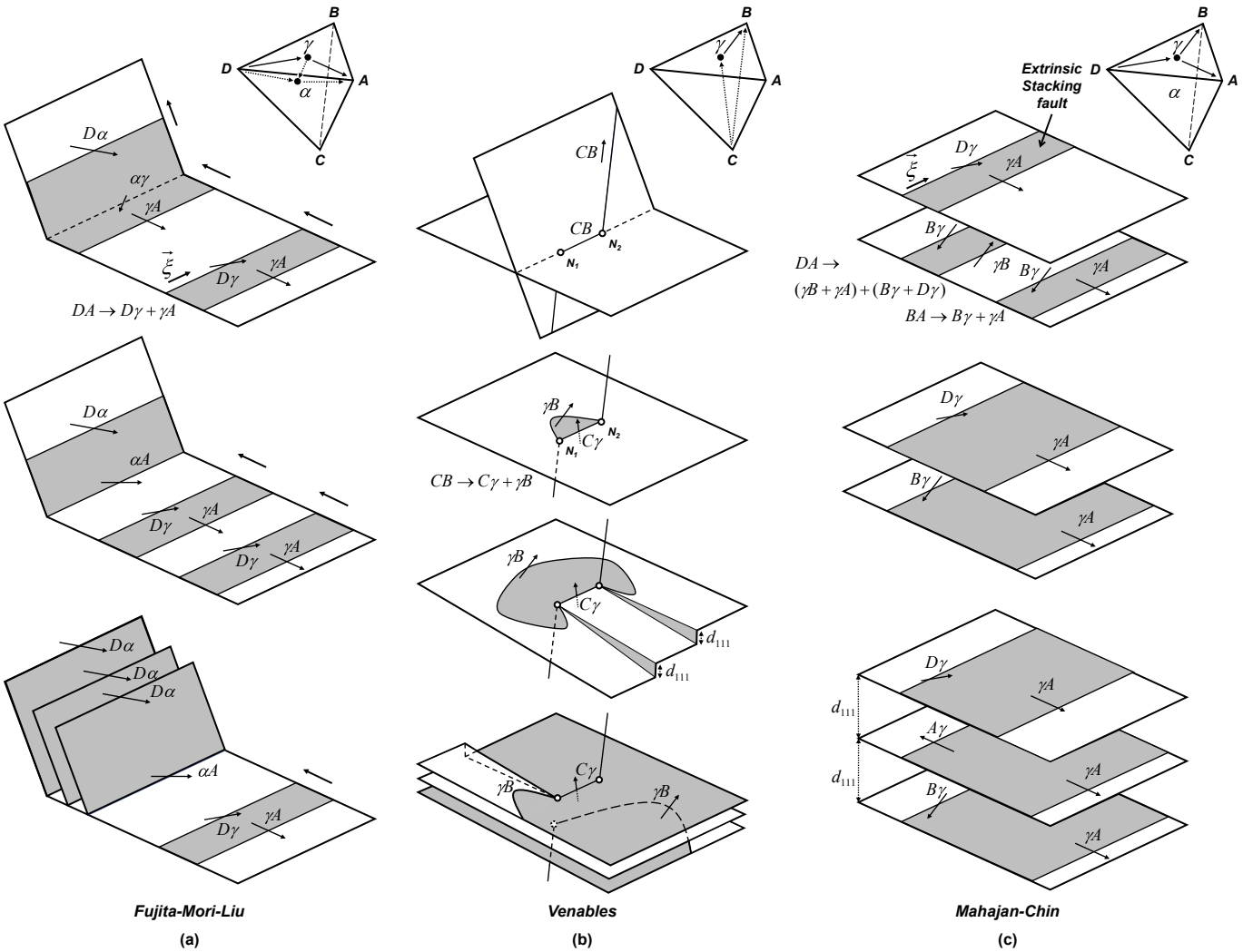

Fig. 36. Schematics of (a) the Fujita-Mori-Liu stair-rod cross slip twinning model [243], (b) the Venables pole dislocation mechanism model [95], and (c) the Mahajan-Chin three layer twin nucleus [244].

slip on {111}-type slip planes only. There are four {111} slip planes in total. Adjacent {111} slip planes intersect at an angle of 70.53 °. The edges of the tetrahedron are a/2<110>-type perfect dislocation Burgers vectors [247]. Much of the early work on deformation twinning was done on single crystals of metals or alloys strained beyond stage II and into stage III strain hardening range, i.e. in relatively strongly deformed material subjected to high stresses. In the case of TWIP steels, deformation twinning is believed to start in early stages of the deformation. It is generally accepted that twinning requires the presence of dissociated dislocations, i.e. a low γ_{isf}, and that the nucleation of the twins requires dislocation reactions leading to the formation of twinning partial dislocations trailing an intrinsic stacking fault, and a process which suppresses the formation or the movement of the corresponding trailing partial dislocation. The twinning partial dislocations involved in the process of twin thickening must all have the same Burgers vector and move on consecutive {111} slip planes.

In the Venables model [95,248,249], a twinning partial, formed on a long jog on the primary slip plane, rotates around a specific pole dislocation. The model requires the formation of a large enough jog, which implies that multiple intersections must have taken place in multi-slip conditions. The obvious advantage of the Venables pole mechanism is that a perfect twin can be formed, without the need to create new overlapping twinning partials, as the twin gradually thickens with strain. The mechanism requires that a long jog is first formed on a dislocation of the secondary slip system plane by intersection of primary slip dislocations. The jog then dissociates into an a/6<112>-type twinning partial and an a/3<111>-type sessile Frank partial dislocation. The Venables mechanism implies that a certain amount of plastic strain must precede twin formation. An alternative process has been proposed by Niewczas and Saada [250]. They assumed conditions of high stress and large dislocation density and envisaged that a primary dislocation reacts with one arm of a faulted Frank dipole, forming a twinning partial dislocation that is free to move on the conjugate slip plane. In the case of the Venables mechanism, the jog, which lies on the primary slip plane, should be large enough, i.e. result from about 20 intersections of the dislocation by primary dislocations (~5 nm in length) and subjected to a considerable stress concentration in order to operate as a source. Accordingly, high passing stresses must be overcome for the operation of the twin source. The poles of the source should be on opposite sides of the twinning partial. The Venables pole model [95] offers an elegant explanation for how a perfect mirror twin, which implies that exactly one partial dislocation glides on each consecutive slip plane, is formed. Whereas there is no direct experimental evidence for the Venables mechanism, Niewczas and Saada have published weak-beam dark field transmission electron micrographs of twin sources in high deformed Cu-8%Al which support their model. While the Venables and Niewczas-Saada models have been used to explain the observation made by Choi et al. [186] for TWIP micropillars, no convincing experimental evidence is available, to the best of the authors' knowledge, for the operation of Venables or Niewczas-Saada twin sources in TWIP steel.

Glide-type twin nuclei models are attractive due to their simplicity. Pure glide type models for twin formation do not require multi-slip conditions. The simplest glide-type twin nuclei model is based on the Copley-Kear-Buyn's dislocation break-away mechanism. The Mahajan-Chin model for the formation of a three-layer twin nucleus, formed by two dissociated co-planar dislocations, is also a glide-type source. It requires the cross-slip of partial dislocations. In the Copley-Kear-Byun model twinning is assumed to be initiated by partial dislocation breakaway, solely based on straightforward application of the Peach-Koehler equation for the partial dislocation on either side of a dissociated primary dislocation, taking into account γ_{isf} and the drag force. The twin thickening mechanism is based on a chance overlap of wide stacking fault generated by the breakaway process.

In the Mahajan-Chin model two dislocations with coplanar Burgers vectors form a set of three Shockley partials on three consecutive slip planes, resulting in an extrinsic fault configuration. This three-layer extrinsic stacking fault is considered to act as a twin nucleus. The mechanism requires the cross-slip of a partial dislocation, and twin thickening requires the chance overlap of similar three-layer twin nuclei [244]. Bracke et al. [17] report that their TEM observations agree with the Mahajan-Chin twinning model. Steinmetz et al. [41] considers a strongly pinned segment of a pre-existing three-layer Mahajan-Chin stacking fault as the twin nucleus in their model for the TWIP effect. Mahato et al. [19] observed extrinsic stacking faults by TEM of TWIP steel. Taking the viewpoint that extrinsic stacking faults serve as precursors to the formation of twin nuclei, they conclude that the Mahajan-Chin mechanism operates in their case. Kibey et al. [156] also favor the Mahajan-Chin model for the deformation twinning in Hadfield steel.

Based on the direct observation of twin formation, Liu et al. [251] concluded that a slightly revised version of the Fujita-Mori model [243] was compatible with their *in situ* observations made in a Fe-24%Mn-0.5%C TWIP steel. The Fujita-Mori-Liu model implies prior activation of slip on two slip systems. In the model, the leading partial dislocation of a primary slip dislocation splits into a stair-rod dislocation and a twinning partial dislocation on the conjugate slip plane.

A key feature of the Fujita-Mori model [243] involves the “stair-rod cross slip” mechanism, which enables cross-slip of partial dislocations. The model requires that slip is activated on at least two slip systems. A a/6<112>-type partial dislocation on the primary slip plane dissociates into a sessile a/6<110>-type stair-rod dislocation and a glissile a/6<112>-type partial dislocation on the conjugate slip plane. The model is based on a dislocation reaction originally proposed by Cohen and Weertman: a perfect a/2<1110>-type dislocation at the head of a dislocation pileup in front of a strong barrier, e.g. a Lomer-Cottrell lock or dislocation dipole, can dissociate in a sessile a/3<111>-type Frank dislocation and a a/6<112>-type partial dislocation. The partial dislocation can glide away from the Frank dislocation on the conjugate slip plane trailing a wide stacking fault. In the Cohen-Weertman deformation twinning mechanism additional partials have to be emitted for a twin to thicken, but this would require a highly ordered arrangement of stacking faults to be produced by chance. In the Fujita-Mori model, the cross-slip of the partial dislocations occurs in an orderly manner.

In the Miura-Takamura-Narita mechanism (Fig. 37) primary dislocations first form a dislocation pileup at a Lomer-Cottrell dislocation barrier located at the junction of the primary slip plane and a cross-slip plane. A two-layer twin nucleus, consisting of two twinning partial dislocations and a sessile Frank partial dislocation, is formed. Karaman et al. [252] used a modified version of the Miura-Takamura-Narita model to compute the critical twinning stress for Fe-12%Mn-1.2%C steel.

Idrissi et al. [91] studied the twin nucleation mechanism in Fe-20%Mn-1.2%C TWIP steel by TEM. Their results appear to support the Cohen-Weertman (Fig. 38) or the Miura-Takamura-Narita nucleation mechanisms, whereas twin thickening appears to be due to the pole mechanism as proposed by Venables [95].

Considering the large variety of possible mechanisms and in the absence of clear microscopic evidence for the previous models in many other reports, it remains very plausible that grain boundaries may be playing a key role in the nucleation of deformation twins as sites for emission of twinning partials. This is the position of de las

Please cite this article in press as: B.C. De Cooman, et al., Twinning-induced plasticity (TWIP) steels, Acta Materialia (2017), http://dx.doi.org/10.1016/j.actamat.2017.06.046

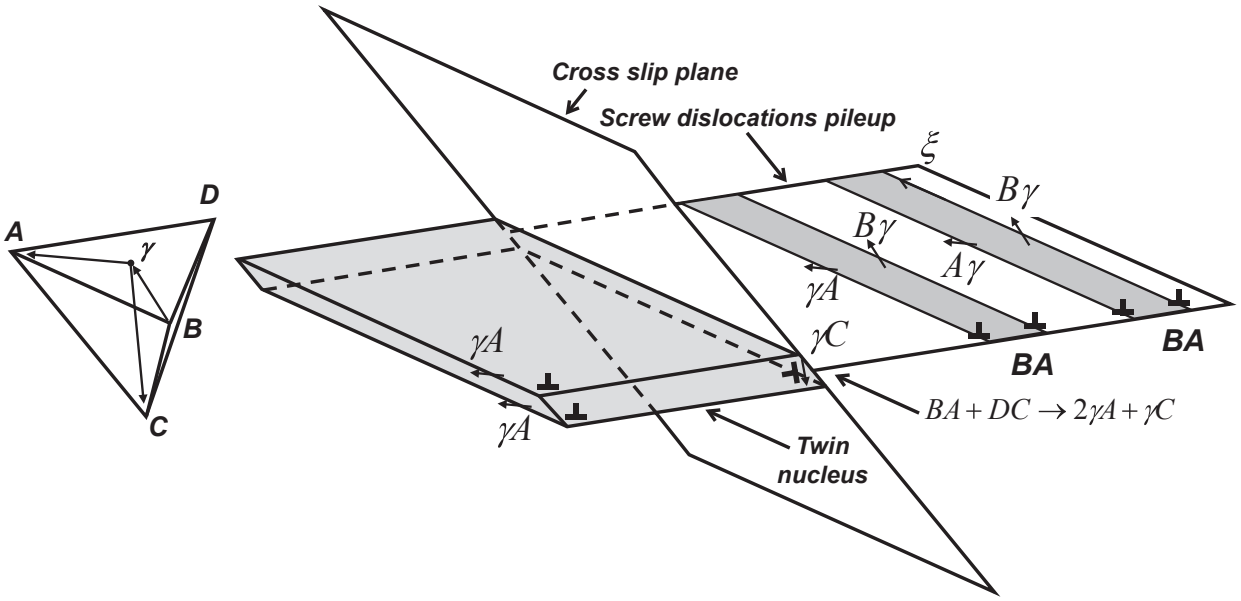

Fig. 37. The Miura-Takamura-Narita twinning mechanism [245]. Primary dissociated screw dislocations *BA* form a pileup against a Lomer dislocation *DC*. The reaction between the leading dislocation of the pileup and the Lomer dislocation results in the formation of a sessile Frank partial dislocation and a two-layer twin nucleus.

Cuevas et al. [224] who assert that the deformation twins are nucleated at high-angle boundaries. In their scenario, the emitted twins have a sub-micrometer or nanometer thickness and they traverse a grain until they run into a grain boundary, another twin, or some strong obstacle.

The variety of reported microstructural constituents in deformed TWIP steel, i.e. faulted austenite, ε-martensite, and twinned austenite may be a result of apparent occurrence of ε-martensite and twins in the electron and X-ray diffraction patterns that stem from clustering of stacking faults [253].

Indeed, deformation twins are often identified on the basis of electron diffraction in transmission electron microscopy. The effect of overlapping stacking faults causes diffuse scattering, and the coincidental overlapping of wide stacking faults can result in the formation of thin twins and ε-martensite plates even if the process of fault formation is entirely controlled by random events in TWIP steel with an initially perfect fcc crystal structure with an … ABCABC … stacking sequence in the cubic [111] direction. Electron diffraction patterns of the perfect γ-phase observed along ⟨110⟩-type zone axes show only the sharp Bragg reflections of the cubic structure. When a number of random stacking faults is created in this crystal structure, the volume fraction of the regions with the hcp stacking sequence will initially be extremely low, but the volume fraction of regions with a twin stacking sequence will statistically be greater. This results in the appearance of Bragg reflections corresponding to the twin orientation. There will also be diffuse streaks connecting the Bragg reflections of the matrix and the twins. With a higher stacking fault density the probability of hexagonal stacking increases. The random stacking of cubic and hexagonal sequences will result in a presence of continuous diffuse

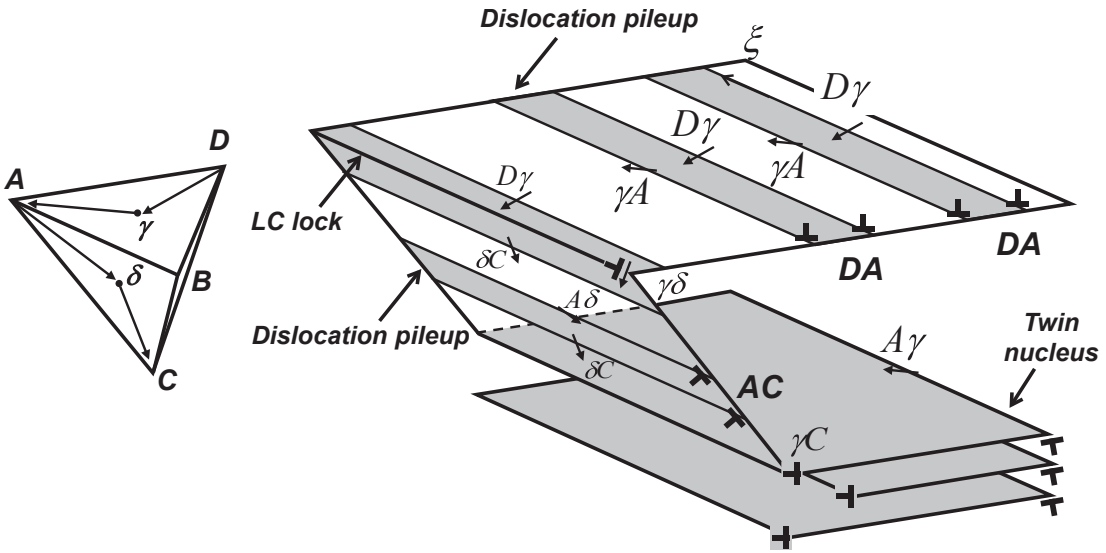

Fig. 38. The Cohen-Weertman twinning mechanism [242]. In one of the two dislocation pileups forming a Lomer-Cottrell (LC) lock a primary dislocation at the head of the pileup dissociates into a Shockley partial dislocation and a sessile Frank partial dislocation. The Shockley partial dislocation moves away from the Frank partial dislocation trailing a stacking fault. The chance overlap of stacking faults formed in a similar manner results in the formation of a twin.

Please cite this article in press as: B.C. De Cooman, et al., Twinning-induced plasticity (TWIP) steels, Acta Materialia (2017), http://dx.doi.org/10.1016/j.actamat.2017.06.046

streaks in the electron diffraction pattern. These gradually develop maxima at positions corresponding to Bragg reflections for the hexagonal crystal structure with an … ABAB … stacking sequence in the hexagonal [0001] direction. The interpretation of the electron diffraction patterns taken from thin foils of strained TWIP steels is therefore subject to ambiguity. These considerations also suggest that deformation twins may be nucleated at pre-existing multi-layer defects, and that the increase to the volume fraction of twins is due to the activation of more and more pre-existing twin nuclei as the applied stress is increased with strain. The chance overlap of similar twins will result in an apparent twin thickening. The saturation of the winning process would then occur when all the pre-existing twin nuclei have been activated. These observations are consistent with the model for deformation twinning due to Beyerlein and Tomé [254]. These authors proposed a probabilistic theory for twin nucleation in hcp metals, which relies on the dissociation of pre-existing multilayer grain boundary defects under stress. The model emphasises the importance of twin nucleation, rather than twin growth in deformation twinning. Their mechanism has the following features, which could in principle also explain the salient features of deformation twinning in TWIP steel: (a) the number of twin nuclei is related to the grain boundary structure, rather than the dislocation density, (b) twin nucleation does not require a large amount of pre-deformation, (c) the twinning kinetics are nucleation-controlled, rather than growth-controlled, and (c) the twin volume fraction at saturation is governed by the initial density of grain boundary twin sources. Similar to the model by Beyerlein and Tomé [254], the phenomenological model proposed by Vinogradov et al. [255] is based on the idea that deformation twinning is stress-driven, rather than strain-driven. The model provides a closed-form constitutive description for materials exhibiting twinning-induced plasticity and is considered suitable for TWIP steels.

5.2. Critical stress for twinning

The formation of deformation twins is generally considered to be preceded by dislocation activity which creates the conditions for dislocation-mediated twin nucleating processes, such as the Venables' pole mechanism [95], the Cohen-Weertman deviation process [242], or the Mahajan-Chin stacking fault process [244]. While various equations are available to determine the twinning stress theoretically for specific deformation twinning models, the experimental determination of the twinning stress of TWIP steels is notoriously difficult. Experimentally measured values of the critical stress for the onset of deformation twinning are listed in Table 8. Under tensile deformation, twinning tends to be initiated in grains with the ⟨111⟩ orientation in tensile direction. At room temperature, deformation twinning in TWIP steels is initiated at the flow stress corresponding to the onset of stage B of strain hardening introduced in Section 2.1. A review of the literature shows that there is a small difference between the yield stress and the twinning stress of TWIP steels.

Bouaziz et al. [35] reported that for Fe-22%Mn-0.6%C TWIP steel the twin nucleation stress was independent of the grain size, at least in the grain size range of 1.3–25 μm. The magnitude of this stress, approximately 550 MPa, corresponds to the critical twinning shear stress of $\tau_T \approx 180$ MPa. Rahman et al. [20] evaluated the twinning stress and its grain size dependence in cyclic loading with the stress amplitude below the yield strength. They reported a critical twinning stress of 67 MPa for a single crystal. This value is close to the critical resolved shear stress of 72 MPa reported by Choi et al. [186] for a Fe-22%Mn-0.6%C single crystal oriented to favor deformation twinning, i.e. in compression along the [001]-axis.

Classical twinning theories generally predict that the critical resolved shear stress for twinning is proportional to γ_{isf}:

$$\tau_T \cdot b_{112} \sim \gamma_{isf} \tag{60}$$

Specifically, Narita and Takamura [256] report the following equation for the twinning stress:

$$\tau_T = \frac{\gamma_{isf}}{2 \cdot b_P} \tag{61}$$

where b_P is the Burgers vector of a partial dislocation. Application of Eq. (58) to Fe-22%Mn-0.6%C ($\gamma_{isf} = 23$ mJ/m^2, $b_P = 0.147 \times 10^{-9}$ m) and Fe-18%Mn-0.6%C-1.5%Al ($\gamma_{isf} = 30$ mJ/m^2, $b_P = 0.147 \times 10^{-9}$ m) yields 78 MPa and 102 MPa, respectively. Suzuki and Barrett [257] assumed that a small segment of dislocation consisting of a sessile partial and a twinning partial pinned at two points act as a twin nucleus. They defined the twinning stress as the critical stress for the loss of stability of the twinning partial bowing out under the shear stress:

$$\tau_T = \frac{\gamma_{isf}}{2 \cdot b_P} + \frac{G \cdot b_P}{L_0} \tag{62}$$

Here L_0 is the length of the sessile partial dislocation engaged in the twin nucleus. Assuming a pole mechanism is operating, Mahato et al. [19] also used the Suzuki-Barrett equation to calculate the twinning shear stress, but they omitted the factor 2 in the denominator of the first term in Eq. (62).

Grain size reduction is generally believed to make deformation twinning more difficult. Meyers et al. [258] quantified that trend in terms of a grain-size dependent twinning stress equation:

Table 8
Reported values of the critical twinning stress for TWIP steels.

Alloy	Twinning stress MPa σ_T (τ_T)[a]	Grain size μm	γ_{isf} mJ/m^2	Reference
Fe-27%Mn-2.5%Si-3.5%Al	272 (89)	–	18	Mahato et al. [19]
Fe-22%Mn-0.5%C	272 (89)	-	–	Bracke et al. [17]
Fe-22%Mn-0.6%C	220 (72)[b]	–	23	Choi et al. [186]
Fe-22%Mn-0.6%C	550 (180)	1.3–25	23	Bouaziz et al. [6]
Fe-22%Mn-0.1%C-1.2Al	251 (82)	15	16	Present work
Fe-17%Mn-0.4%C-1.3%Al	312 (102)	15	17	id.
Fe-18%Mn-0.6%C-1.5%Al	422 (138)	5	25	id.
Fe-15%Mn-0.7%C-2%Al-2%Si	190 (62)	84	30	Rahman et al. [20]
Fe-15%Mn-0.7%C-2%Al-2%Si	352 (115)	10	30	id.
Fe-15%Mn-0.7%C-2%Al-2%Si	563 (184)	4.3	30	id.

[a] Assuming $\sigma_T = 3.06 \cdot \tau_T$.

[b] [001] single crystal in compression (twinning favored).M

$$\tau_T = \frac{\gamma_{isf}}{b_P} + \frac{K_T}{\sqrt{D}} \tag{63}$$

where D is the grain diameter. The influence of the grain size on the critical shear stress for twinning in TWIP steel is not entirely clear. While according to Phiu-on [259] the grain size has no effect on τ_T, Mohammed et al. reported an increase in the critical shear stress for deformation twinning with decreasing grain size [260]. Gutierrez-Urrutia et al. [27] also observed that, in the grain size range of 3–50 μm, a grain size reduction resulted in an increase of the twinning stress for a Fe-22%Mn-0.6%C TWIP steel. They proposed the following grain size dependent twinning stress equation:

$$\tau_T = \frac{\gamma_{isf}}{b_p} + \frac{G \cdot b_p}{D} \tag{64}$$

The first term in the equation is the stress required to achieve partial dislocation separation to create a twin and the second term is the stress it takes to nucleate a twin at a grain boundary. Using $\tau_T = 0.447 \times \sigma_T$, $\gamma_{isf} = 22 mJ/m^2$, $G = 62$ MPa and $b_P = 0.147$ nm, the twinning stress for Fe-22%Mn-0.6%C according to Eq. (64) due to Gutierrez-Urrutia et al. [27] is given by:

$$\tau_T = \frac{\gamma_{isf}}{b_p} + \frac{G \cdot b_p}{D} = \frac{22 \cdot 10^{-3} Nm/m^2}{0.147 \cdot 10^{-9} m} + \frac{62 \cdot 10^9 Pa \cdot 0.147 \cdot 10^{-9} m}{2 \cdot 10^{-6} m} = 154.3\ MPa$$
$$\sigma_T = 2.238 \cdot \tau_T = 345.3\ MPa \tag{65}$$

It is reasonable to assume that Mahajan-Chin three-layer twin nuclei are preexisting multi-layer defects, residing, for instance, at grain boundaries, which are activated when the stress reaches a critical value. Steinmetz et al. [41] assumed that a small segment of a Mahajan-Chin three-layer twin between two pinning points acts as twin nucleus. The twinning stress, defined as the critical stress for the formation of an unstable bow-out of the three twinning partials, is expressed by the following equation:

$$\tau_T = \frac{\gamma_{isf}}{3 \cdot b_P} + \frac{3 \cdot G \cdot b_P}{L_0} \tag{66}$$

This equation yields very reasonable values for the critical twinning stress for Fe-22%Mn-0.6%C TWIP steel, suggesting that twins are initiated in the early stages of deformation. The reported values for the critical twinning stress based on Eq. (66) are compiled in Table 9.

According to Venables, the twinning stress τ_T is comprised by a twin nucleation stress and a twin growth stress [248,249]. It can be calculated by solving the following equation:

$$\left(1 - \frac{2 \cdot \theta}{3 \cdot \lambda} + \frac{(1-\nu) \cdot L}{1.84 \cdot G \cdot b} \cdot \theta^2 \cdot \tau_T\right) \cdot \tau_T = \frac{\gamma_{isf}}{b_P} \tag{67}$$

Here θ is an orientation-dependent term. It is the ratio of the Schmid factors for slip and twinning. b_P is the Burgers vector of a partial a/6<112>-type dislocation, and b is the Burgers vector of an un-dissociated a/2<110>-type dislocation. λ is a parameter governed by the forest dislocation density and the critical resolved shear stress for slip. In practice, $\theta \approx \lambda \approx 1$. A simplified version of the (parabolic) Venables equation for the γ_{isf}-dependence of the critical resolved shear stress for twinning has been derived by Remy [82]:

$$\frac{1}{\sqrt{3}} \cdot \left(\frac{1}{3} + K \cdot \frac{\tau}{G}\right) = \frac{\gamma_{isf}}{Gb} \tag{68}$$

where K is a numerical constant. The results for a Fe-18%Mn-0.6%C-1.5%Al TWIP steel are compared to Eq. (65) in Fig. 39. The symbols represent the measured twinning stress at 25 °C, 50 °C and 75 °C plotted against the calculated values of γ_{isf}. The twinning stress is defined as the stress at the onset of stage B strain hardening. The twinning shear stress was calculated by using the average Schmid factor of 2.238 for fcc crystals. The data agree well with the Venables equation for $K = 200$. Note that the parameter K was calculated to be 900 by Venables, and that Remy and Pineau gave a value of 600 and 700 [96]. According to Bouaziz et al. [35] the twinning initiation stress of a Fe-18%Mn-0.6%C-1.5%Al TWIP steel is in the range of 501–574 MPa, i.e. τ_T is in the range of 164–188 MPa. That is to say, for $G = 65$ GPa the ratio τ_T/G is in the range of 2.5×10^{-3}-2.9×10^{-3} - in excellent agreement with an estimate in terms of the Venables model. As mentioned in Section 3.2.2, according to Buyn [146] twinning is activated when the applied stress is high enough to initiate breakaway of partial dislocations into which a straight screw dislocation segment is split. The twinning stress is defined as the critical stress at which the distance between the partial dislocations diverges. It is given by Eq. (41).

Fig. 40 illustrates the effect of an externally imposed shear stress on the separation of two partial dislocations in a TWIP steel with $\gamma_{isf} = 30$ mJ/m^2 based on Buyn's equation for the distance d between the partials:

$$d = \frac{(2 - 3 \cdot \nu)}{8 \cdot \pi \cdot (1 - \nu)} \cdot \frac{G \cdot b_P^2}{\left(\gamma_{isf} - \frac{\tau \cdot b_P}{2}\right)} \tag{69}$$

Table 9
Reported values of the twinning shear stress of TWIP steels based on Eq. (63).

	τ_T MPa	σ_T $2.24 \times \tau_T$ MPa	σ_T $3.06 \times \tau_T$ MPa	γ_{isfe} mJ/m2	G GPa	L_0 nm	Ref
Fe-22%Mn-0.5%C	160	358	490	23	63.6	260	Kang et al. [189]
Fe-18%Mn-0.5%C	160	358	490	16	73.2		
Fe-24%Mn-0.7%C	183	410	560	24	62.4		
Fe-22%Mn-0.6%C	192	430	588	29	52.5	260	Steinmetz et al. [41]
Fe-27Mn–2.5Si–3.5Al	201	450	615	18.8	66.0	200	Mahato et al. [19]

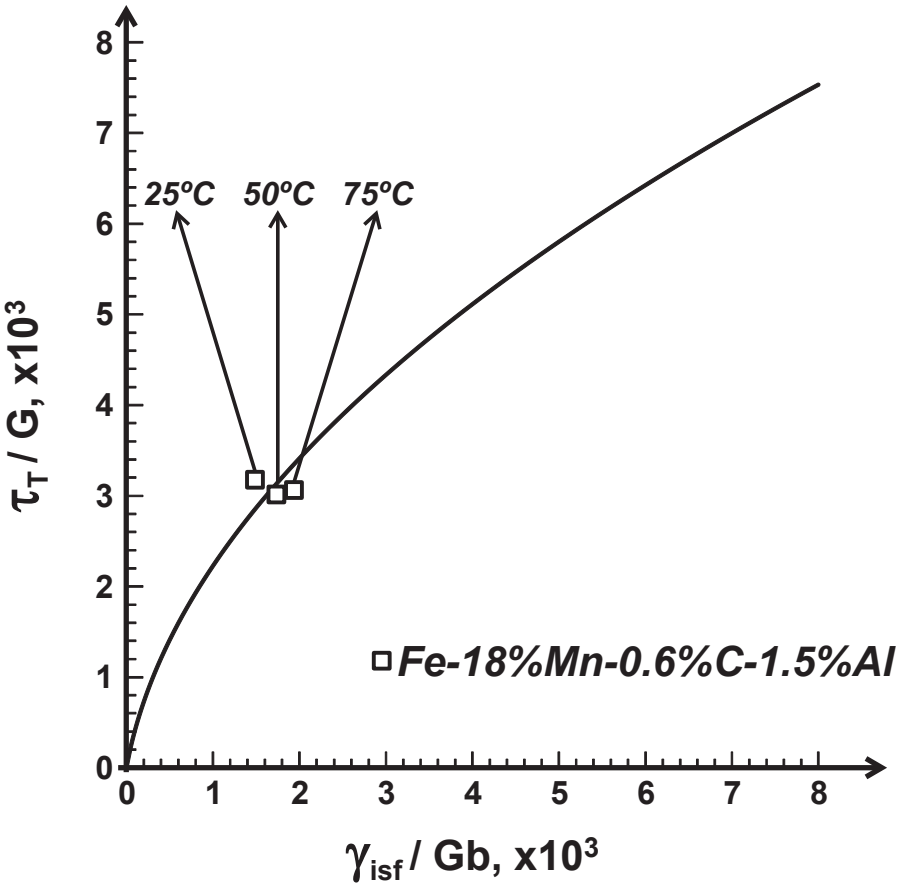

Fig. 39. Graphical representation of the Venables equation for the γ_{isf}-dependence of the critical resolved shear stress for deformation twinning in a Fe-18%Mn-0.6%C-1.5%Al TWIP steel (solid line). The following parameter values were used: $\gamma_{isf} = 31$ mJ/m^2, $G = 79$ GPa, $\nu = 0.312$, a/6<112>-type Burgers vector $b_P = 0.147$ nm, based on the lattice parameter equation a(nm) $= 0.3575 + 2.89 \cdot 10^{-5} \cdot$%Mn $+ 8.44 \cdot 10^{-5} \cdot$%C, dislocation pileup length $L = 134$ nm, and K $= 200$.

from which Eq. (41) follows when the denominator vanishes. The figure shows that the twinning stress predicted by Byun's model is much larger than the experimentally measured critical twinning stresses. The Steinmetz et al. [41] model is closest to the experimentally determined values. This is an important observation as it implies that (a) the critical dislocation density required for twin-nucleating dislocation-dislocation interactions is achieved after small amounts of strain and that (b) twinning is very easily initiated in TWIP steel. Alternatively, the result can also be interpreted as an indication that there are pre-existing multi-layer twin nuclei in the recrystallized microstructure. An obvious likely location for these pre-existing nuclei are grain boundaries where Mahajan-Chin type three-layer twin nuclei may be part of the grain boundary defect structure, as suggested by Steinmetz et al. [41].

More recent deformation twinning theories have proposed that it is γ_{usf}, the unstable twinning fault energy, rather than γ_{isf}, which governs twinning nucleation:

$$\tau_T \cdot b_{112} \sim \gamma_{utf} \tag{70}$$

This relation has been verified for pure metals [142] and for Cu-Al alloys [261] by *ab initio* simulations using the VASP–PAW-GGA software. Such analysis has not been applied to TWIP steels as yet. The 'ideal' twining stress associated with the homogeneous nucleation of a deformation twin in a defect-free crystal, not involving a heterogeneous twin nucleus such as a three-layer twin nucleus, can be computed using calculated generalized planar fault energy (GPFE) curves [140,142]. The relevant equation reads

$$\tau_T = \frac{\pi}{b_P} \cdot \left(\gamma_{utf} - 2 \cdot \gamma_{tsf} \right) \approx \frac{\pi}{b_P} \cdot \left(\gamma_{usf} - \frac{\gamma_{isf}}{2} \right) \tag{71}$$

where γ_{utf} is the unstable and $2\gamma_{tsf}$ the stable twin fault energy. As $\gamma_{isf} = 2\gamma_{tsf}$, and assuming the universal scaling law expressed by Eq. (32), one has $\gamma_{utf} = \gamma_{usf} + \frac{\gamma_{isf}}{2}$. Using the zero Kelvin values available for critical energy barriers in TWIP steels listed in Table 10, one obtains an estimate $\tau_T = 14$ GPa for homogeneous nucleation of twins. This figure is excessively large compared with the experimental value for the critical twin nucleation stress. It is thus obvious that twin formation requires a *heterogeneous* twin nucleation at pre-existing lattice defects.

A quantitative equation for the onset stress for twinning, which incorporates the barriers to twinning obtained from *ab initio* calculations of the GPFE surface by Kibey et al. [261] reads

$$\begin{aligned} \tau_T = & \frac{2}{3 \cdot N \cdot b_P} \cdot \left(\frac{3 \cdot N}{4} - 1 \right) \cdot \left(\gamma_{utf} + \frac{2 \cdot \gamma_{tsf} + \gamma_{isf}}{2} \right) \\ & - \frac{2}{3 \cdot N \cdot b_P} \cdot \left(\gamma_{usf} + \gamma_{isf} \right) \end{aligned} \tag{72}$$

Here N denotes the number of planes involved in a nascent twin. Taking into account that for a three-layer Mahajan-Chin twin nucleus N = 3 holds, and assuming that $\gamma_{isf} = 2\gamma_{tsf}$ applies, Eq. (72) can be simplified to

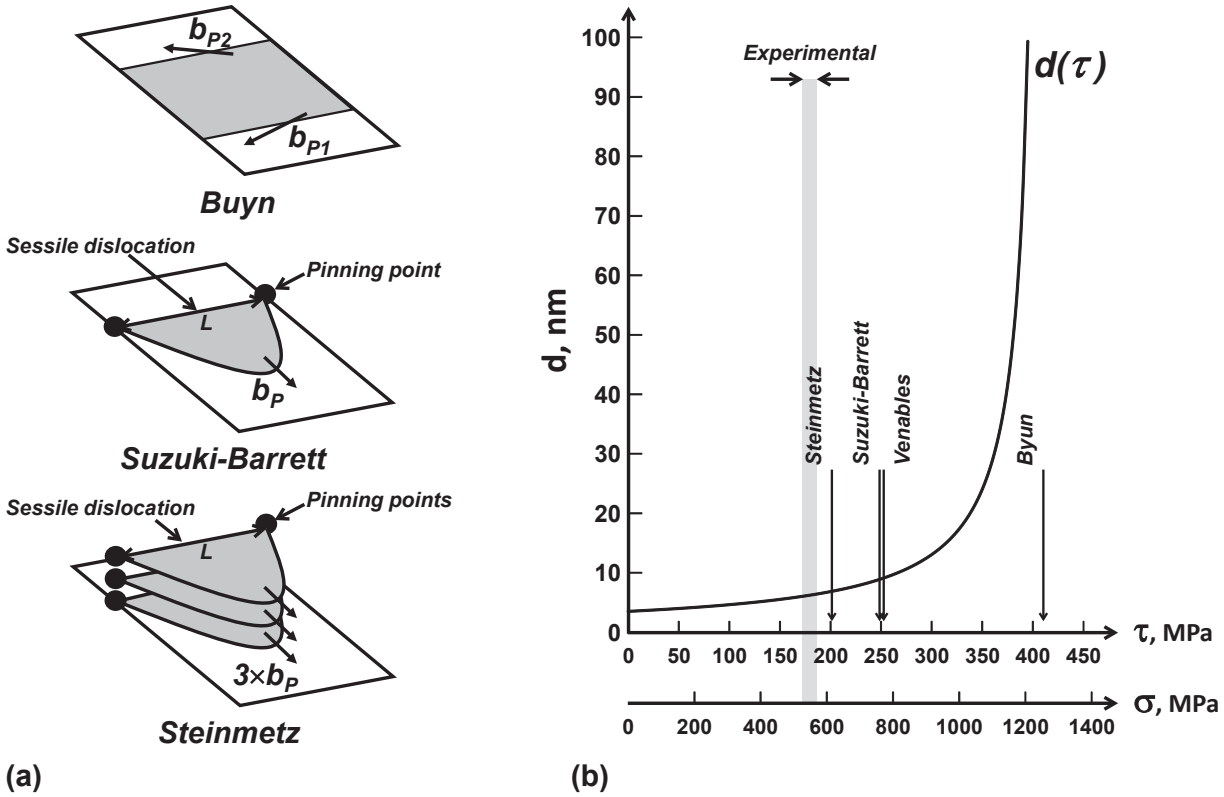

Fig. 40. (a) Schematics of twin nucleation models due to Buyn [146], Suzuki and Barrett [257], and Steinmetz et al. [41]. (b) Stress dependence of the partial dislocation separation d according to Buyn, cf. Eq. (41). The values for the twinning stress according to the Buyn, Suzuki-Barrett, Venables and Steinmetz models are compared with the experimentally measured value for a Fe-18%Mn-0.6%C-1.5%Al TWIP steel. The following parameter values were used for the calculated twinning shear stress: $\gamma_{isf} = 30$ mJ/m^2, $G = 79$ GPa, $b_P = 0.147$ nm, $\nu = 0.312$, $L = 261$ nm [41], and $L = 135$ nm [95].

$$\tau_T = \frac{5}{18 \cdot b_P} \cdot \left(\gamma_{utf} + \gamma_{isf}\right) - \frac{4}{18 \cdot b_P} \cdot \left(\gamma_{usf} + \gamma_{isf}\right) \tag{73}$$

The first term in Eq. (73) describes the stress it takes to overcome the twin nucleation barrier. The second term accounts for cross-slip effects, as increasing γ_{usf} results in the inhibition of cross-slip, thus promoting twinning through a decrease of τ_T. Eq. (73) also implies that τ_T increases with increasing γ_{utf}, so that twinning becomes less favorable.

Using first principle calculations, Medvedeva et al. [157] showed that Al short-range order strongly reduces the unstable stacking fault energy γ_{usf}, *i.e.* it facilitates the formation of partials trailing a stacking fault, while inhibiting an increase of γ_{isf}, as discussed in Section 3.3. Medvedeva et al. therefore conclude that Al additions should promote planar slip prior to twinning, as observed experimentally. Progress in the calculation of the non-0K critical energy barriers for TWIP steel should make it possible to determine an *ab initio*-value for τ_T.

5.3. Twinning kinetics and twinning saturation

The paramount role of twinning in the deformation of TWIP steels is unquestionable. However, the direct contribution of deformation twins to plastic strain is not a significant factor responsible for their exceptional mechanical properties. Understanding the exact nature of the twinning-related phenomena in the microstructure and texture development and the attendant mechanical properties is therefore a formidable task. Part of it is understanding the evolution of the volume fraction of twins in the course of plastic deformation. This evolution is known to terminate in saturation. While there are a few cases in which high saturation volume fractions of deformation twins [217,262,263] were reported, most researchers agree that deformation twinning in TWIP steels saturates at relatively low volume fractions. In early work on TWIP steels it was not uncommon for authors to report that deformation twinning was the primary deformation mechanism in low γ_{isf} austenitic TWIP steels. Vercammen et al. [88] argued that the superior mechanical properties were due to the formation of a

Table 10
Generalized stacking fault energy (GSFE) parameters for pure fcc Fe: γ_{usf}, unstable stacking fault energy at $b_{112}/2$; γ_{isf}, intrinsic stacking fault energy at b_{112}; γ_{tsf}, unstable twin fault energy at $1.5b_{112}$; $2\gamma_{tsf}$, stable twin fault energy at $2b_{112}$. It was assumed that the relation $2\gamma_{tsf} = \gamma_{isf}$ applies.

γ_{isf} mJ/m^2	γ_{isf} mJ/m^2	γ_{max} mJ/m^2	$2\gamma_{tsf}$ mJ/m^2	Reference
−393				Kibey et al. [156]
−464<γ_{isf} < −452				Abbassi et al. [155]
−350				Gholizadeh [74]
−359	+490	+3191	−359	Limmer [185]
−347				Medvedeva et al. [157]

layered nano-scale microstructure. Early TWIP effect models by Bouaziz et al. [33] also led to the conclusion that of all possible deformation mechanisms in TWIP steel, deformation twinning had the most beneficial effect on strain hardening. In their original model, the evolution of the twin volume fraction with strain is described by the equation$F(\varepsilon) = 1 - e^{-m\cdot\varepsilon}$, m being a phenomenological parameter. The twin saturation volume fraction was found to be 0.69, based on the substitution of $m = 1.95$ (their published value) and the uniform elongation $\varepsilon_u = 0.6$ in the equation$F(\varepsilon_u) = 1 - e^{-m\cdot\varepsilon_u}$. The above saturation value was, however, revised downward to 0.2 in later work [35]. In reality, the volume fraction of deformation twins in TWIP steels remains small and ε_T, the contribution of the twins to the macroscopic strain, is very small. Indeed, assuming a twin volume fraction $f_T \approx 0.1$ and a twinning strain of$\sqrt{2}/2$, it can be estimated as

$$\varepsilon_T = \frac{1}{M}\cdot\frac{\sqrt{2}}{2}\cdot f_T \approx 0.023 \tag{74}$$

Similarly, deformation twinning does not appear to contribute directly to the evolution of the crystallographic texture during deformation. The contribution of deformation twinning to strain hardening is therefore chiefly due to its influence on the dislocation density evolution through the reduction of both the dislocation mean free path and the dislocation annihilation rate. The latter effect is associated with planar glide promoted by twinning.

Three major factors have been reported to affect deformation twinning: the stacking fault energy, the grain size, and the crystallographic orientation of a grain. The role of these factors is a subject of intense experimental and theoretical research. Karaman et al. [264] proposed a model for the deformation of Fe-12%Mn-1.2% C Hadfield steel using a viscoplastic self-consistent approach. Their constitutive model incorporates the twin lamellae spacing and the grain size. In the spirit of the Kocks-Mecking-Estrin model [11], theirs employs the dislocation density as a state variable within a self-consistent approach and on this basis predicts the flow stress as a function of strain. The predicted saturation twin volume fraction for coarse grained polycrystals with a grain size of 100 μm was approximately 0.3. The self-consistent approach used is potentially suited for the prediction of polycrystalline plasticity, particularly texture evolution. Although the authors reported good agreement between experimental measurements and the model predictions with regard to the variation of the twin volume fraction, it may have been overestimated in the experimental measurements by light microscopy, since bundles of very thin twins formed may have been identified as thicker twins.

Other literature data suggests saturation volume fraction of deformation twins of lower magnitude, about 10% [71,265–267], while Haase et al. report a saturation volume fraction of twins in a cold rolled TWIP steel as low as 5% [268].

It should be stressed that not all grains undergo twinning even under the conditions when deformation twinning is possible in principle. Thus, according to Kim et al. 20% of the grains do not twin during deformation in uni-axial tensile tests [18]. The twinning kinetics in the grains which do exhibit deformation twinning saturates at a volume fraction of approximately 15%. This saturation of the twinning activity is very likely due to an increase of the dislocations density.

The strain-dependent kinetics of the evolution of the twin volume fraction inside the grains which do undergo deformation twinning, $F_T(\varepsilon)$, has a characteristic S-shape dependence on the applied strain. $F_T(\varepsilon)$ has usually been described by means of the following empirical equation:

$$F_T(\varepsilon) = F_{T,sat}\cdot\left(1 - e^{-\beta\cdot(\varepsilon-\varepsilon_i)}\right)^{m_T} \tag{75}$$

Here $F_{T,sat}$ is the saturation twin volume fraction. Reported saturation values, $F_{T,sat}$, are usually less than 0.20, and typically about 0.15. Obviously, these values are higher than the overall volume fraction of twins, which is calculated by considering the entire population of grains, including those that do not twin. A larger grain size, which promotes twinning, may result in greater twin volume fractions inside twinned grains. ε_i is a critical strain for the nucleation of deformation twins. Reported values for ε_i are usually small. For example, Bracke et al. [17] observed micro-twins already at a true strain of 0.02. β and m_T are adjustable parameters which need to be determined experimentally. Table 11 lists typical parameter values for Fe-18%Mn-0.6%C-x%Al TWIP steel at 293 K [266]. Fig. 41 shows twinning kinetics data reported in the literature for various TWIP steels. While Eq. (73) is used in models for the mechanical properties of TWIP steel, it is difficult to apply it to experimental data, as the twins are commonly very small in size. Instead, the fraction of twinned grains is often used to describe the twinning kinetics.

As discussed above, deformation twins are often nucleated preferentially at grain boundaries, which are known to act as sources for overlapping stacking faults. Most grains tend to develop one main twinning system in addition to the dislocation glide. Often in a TWIP steel long primary twins occur, which span a grain from one grain boundary to another. Secondary twins may be nucleated within the twins of the primary system, where they remain confined. The deformation twins in TWIP steels are usually very thin, typically 20–30 nm in thickness. When observed in transmission electron microscope, most primary twins appear to have propagated easily across entire grains without encountering many obstacles. It is therefore rather surprising that the deformation twins in TWIP steels do not thicken appreciably once they are formed. TEM observations have revealed that what appears to be wide deformation twins in optical metallography are in fact bundles of nanometer thick twins. The relation between n_P, the number of partial dislocations, and t_T, the thickness of the twin they form is given by:

$$n_P = \sqrt{3}\cdot\frac{t_T}{a_\gamma} \approx 4.37\cdot t_T \tag{76}$$

The twins do not thicken to any sizeable degree and retain their mean thickness of 20–30 nm. The formation of twins with a thickness of this order of magnitude involves glide of a/6<112>-type twinning partial dislocations on approximately 100 successive {111} planes each. This value is surprisingly close to the number of dislocations emitted by Frank-Read sources in the avalanches predicted by the Fisher-Hart-Pry model for slip band formation [269]. In this model the avalanches are terminated by their own back stress.

Transmission electron microscopy observations show that deformation twining does not result in perfect twins with straight coherent twin boundaries. Usually, the twins are faulted and they often have a variable thickness. Their formation appears to be a result of a disorderly overlapping of stacking faults. Although no pronounced strain dependence of the twin thickness was found in the carbon-free Fe-31%Mn-3%Al-3%Si TWIP steel [262], close inspection by means of TEM reveals some variation of thickness. Still,

Table 11
Typical parameter values for the strain dependence of the twin volume fraction in TWIP steels at 293 K.

Parameter	Fe-18%Mn-0.6%C [266]	Fe-18%Mn-0.6%C-1.5%Al [266]	Fe-22%Mn-0.6%C [35]
$F_{T,sat}$	0.15	0.14	0.15
β	7.50	8.00	3.00
ε_i	0.04	0.03	0.06–0.12
m_T	1	1	2

Please cite this article in press as: B.C. De Cooman, et al., Twinning-induced plasticity (TWIP) steels, Acta Materialia (2017), http://dx.doi.org/10.1016/j.actamat.2017.06.046

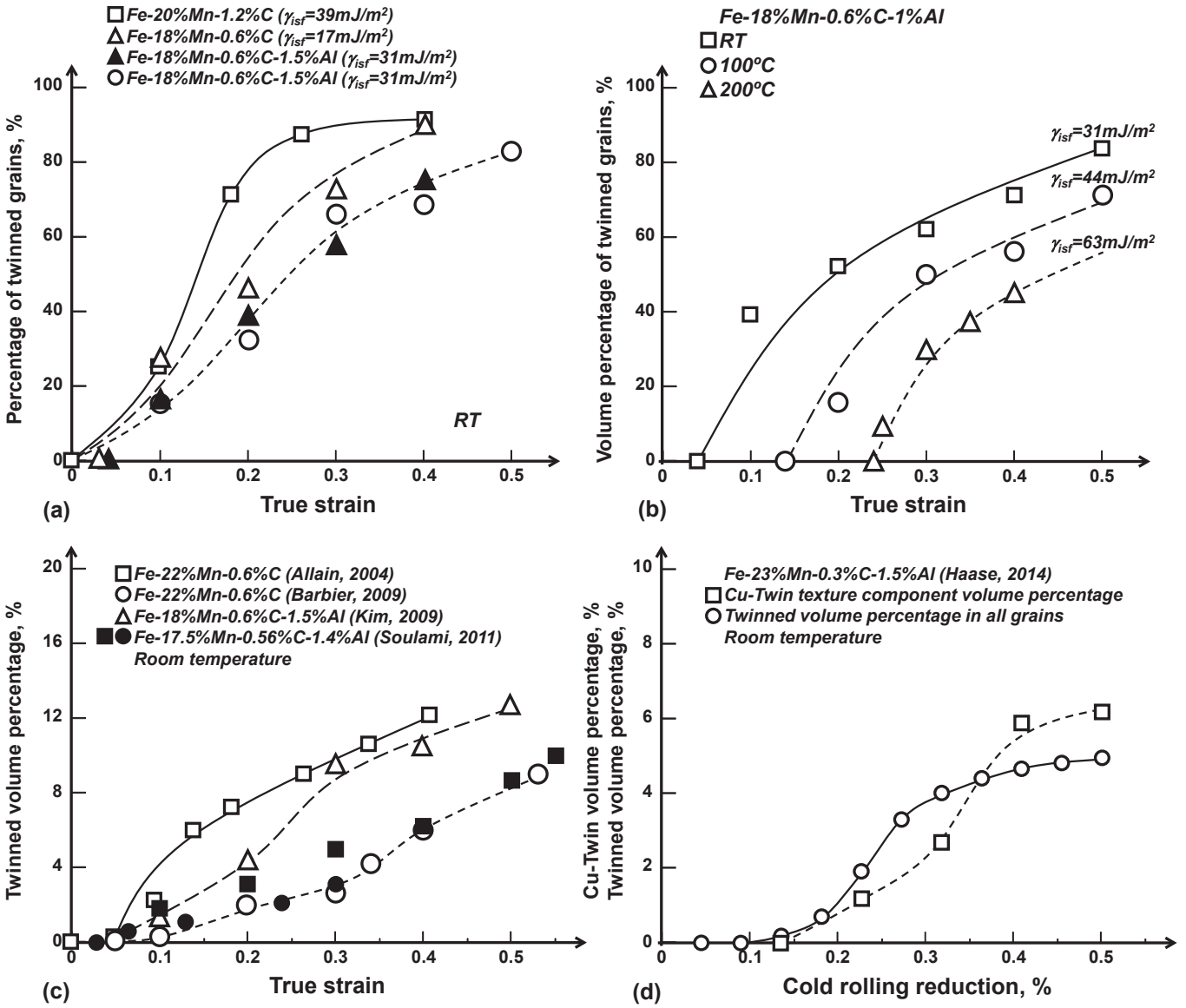

Fig. 41. (a) Strain dependence of the number fraction of twinned grains in TWIP steels based on data by Renard et al. [23], Beladi et al. [78], and Kim [266]. (b) Strain dependence of the volume fraction of twinned grains in TWIP steels at different temperatures based on data by Shterner et al. [270]. (c) Strain dependence of the volume fraction of twins in TWIP steels based on data by Allain [71], Kim [266] and Soulami et al. [267]. (d) Effect of the thickness reduction by cold rolling on the measured volume fraction of the Cu-Twin texture component (cf. Section 5.4) and the calculated value of the corresponding deformation twin volume fraction [268].

the twin thickness typically does not exceed 50 nm, its mean value staying within the range of 20–30 nm. An increase in the twin volume fraction with strain should therefore be associated with the formation of new twins. Continual nucleation of new deformation twins results in an increasing fragmentation of the grains by twin lamellae in the process of straining.

The temperature has a significant influence on the stress required for deformation twinning. According to Shterner et al., an increase in temperature from room temperature to 100 °C results in an increase of the strain at which deformation twinning is initiated from 4% to 20%, a lower density of deformation twins, as well as a decrease of the fraction of twinned grains [270].

5.4. Influence of dislocation slip and twinning on texture development

The texture development during uniaxial tensile deformation and cold rolling of TWIP steels has been studied extensively. Although the development of the Brass-type texture is relatively well documented, there is still some uncertainty about the exact contribution of dislocation glide, deformation twinning and shear banding to the development of this specific texture in TWIP steels. Since TWIP steels are low-to-medium γ_{isf} fcc alloys, there has been a considerable interest in analyzing whether the material underwent the well-known texture transition between the two main types of fcc rolling textures, *i.e.* the Cu-type and the Brass-type textures, and how the texture development was affected by the steel composition, the initial texture, the rolling conditions, and the recrystallization processes. A Cu-texture typically develops during rolling in high γ_{isf} metals and alloys which deform by octahedral {111}⟨110⟩ slip and cross-slip. The Cu-texture is a combination of several texture components: a relatively high fraction of S-{123}⟨634⟩ component, and equal amounts of the Cu-{112}⟨111⟩ and the Brass-{110}⟨112⟩ components. Deformation twinning in

TWIP steels appears to transforms a Cu-type texture into a Brass-type one. Analysis of this transition provides insights into the influence of deformation twinning on the development of texture and mechanical properties. The Brass-texture is the stable end rolling deformation texture when both octahedral slip and deformation twinning are active deformation mechanisms. It develops in low γ_{isf} fcc metals and alloys and consists mostly of the Brass-{110}⟨112⟩ and Goss-{110}⟨001⟩ texture components, with a minor, almost negligible, fraction of Cu-{112}⟨111⟩ and S-{123}⟨634⟩ texture components. The Cu-type to Brass-type texture transition can therefore be evaluated on the basis of the presence vs. absence of these two texture components.

Most reports on the development of crystallographic texture of TWIP steels focus on texture evolution during uniaxial tensile testing and, to a lesser extent, plane-strain cold rolling. As discussed in the previous section, microstructural observations of TWIP steels have clearly shown that the volume fraction of deformation twins is relatively small. As the accumulation of the volume fraction occurs through the addition of nano-twins of almost non variable thickness, the contribution of twinning to crystallographic texture development is therefore not expected to be a volume effect, but rather to stem from an indirect effect of the twins on the conventional {111}⟨110⟩-type slip. Models for the crystallographic texture development in TWIP steel, for example in rolling, should not rely on a large volume fraction of deformation twins to capture the observed evolution to a predominantly Brass-type texture during deformation [16].

Most authors agree that under uniaxial tensile deformation TWIP steels with a weak initial texture typically develop a double, ⟨111⟩//td and ⟨100⟩//td, fiber orientation and that a pronounced mechanical twinning takes place in grains oriented close to the ⟨111⟩//td fiber [21,25,232]. Usually the ⟨111⟩//td fiber is strong as compared to the ⟨100⟩//td fiber (Fig. 42).

The grains with a ⟨111⟩//td orientation develop a high density of deformation twins. By contrast, only a small fraction of the grains with the ⟨100⟩//td undergo deformation twinning [78,270]. An intermediate twinning behavior is observed for the ⟨110⟩//td oriented grains. In contrast to ⟨111⟩//td and ⟨100⟩//td grains, those with the ⟨110⟩//td orientation are less stable and characterized by a considerable re-orientation during straining. The grains rotate towards orientations with a low and a high Taylor factor.

In the classical picture of the response of single crystals of high γ_{isf} metals and alloys with an fcc crystal structure, the tensile axis rotates to the primary slip direction during tensile deformation. Slip occurs on one primary slip system until the crystal orientation reaches the [100]- [111] symmetry line, after which both the primary and the conjugate slip system should be equally activated. The simultaneous slip results in a crystal rotation towards the [211]-direction. In the [211]-orientation the two rotations cancel each other and the rotation stops, *i.e.* [211] is a stable final orientation. In low γ_{isf} fcc materials the tensile axis often continues to rotate into the conjugate triangle for a while before the conjugate slip starts, a phenomenon usually referred to as "overshooting". Normally softening should occur due to crystal rotation, but overshooting causes latent hardening, *i.e.* it appears as if the slip on the primary system had hardened the conjugate system. This latent hardening persists when the conjugate slip system is activated with further deformation, as the dislocation mean free path of the primary dislocations remains larger than for dislocations of the conjugate slip system. The secondary slip and twinning systems therefore require higher stresses for their activation and they are expected to occur at higher strains. In low γ_{isf} TWIP steels, the grains develop a set of deformation twins which belong to the primary twinning system. The active primary dislocations and the primary twins act as barriers to the dislocations of the conjugate slip system which is non-coplanar with the primary slip and twinning systems. Deformation twins thus control the texture evolution at low strains by suppressing multiple slip owing to the inhibition of the conjugate slip system. The suppression of multiple slip favors the Cu-texture generated by standard {111}⟨110⟩ slip. Hence, deformation twins

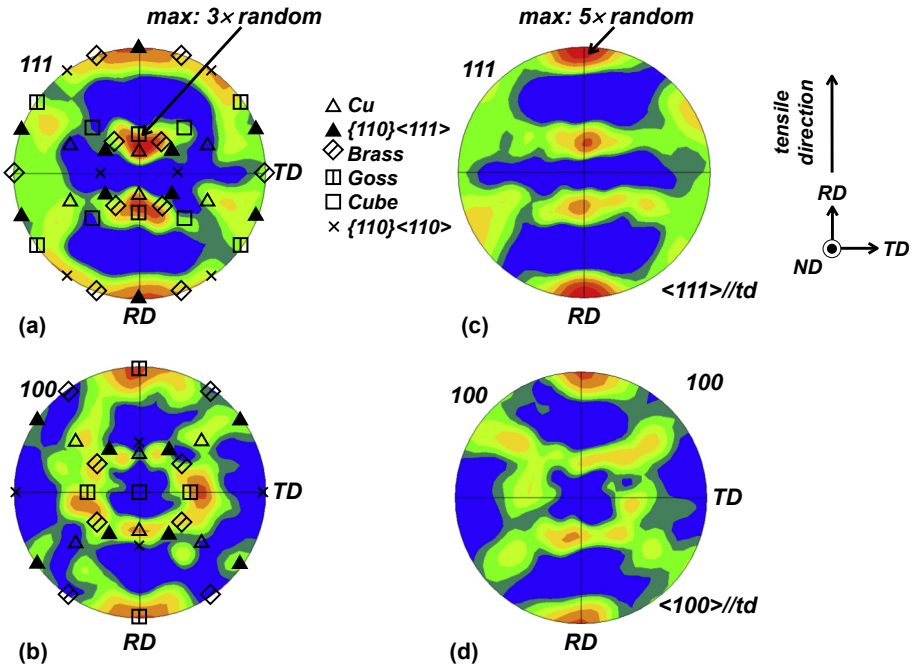

Fig. 42. (a) {111} and (b) {100} pole figures for cold rolled and recrystallization annealed Fe-18%Mn-0.6%C-1.5%Al TWIP steel. The texture is weak and consists of the Cu orientation and α-fiber ⟨110⟩//ND orientations. (c) {111}and (d) {100} pole figures for the same steel tested in tension parallel to the rolling direction to an engineering strain of 20%. The grain re-orientation caused by uniaxial tensile deformation results in the formation of the double fiber texture typical of fcc materials, consisting of a strong ⟨111⟩//td fiber and a weaker ⟨100⟩//td fiber (td: tensile direction).

promote overshooting. Piercy et al. showed that a reduction of γ_{isf} enhances the latent hardening and the overshooting effect [271]. Leffers also argued that the texture transition from Cu-type to Brass-type is delayed by pronounced planar slip brought about by the occurrence of twinning due to the mentioned suppression of multiple slip by deformation twins [272,273].

The initial grain orientation has been reported to have a pronounced influence on twinning and the development of the crystallographic texture. The effect of grain orientation on twinning has been given three different explanations, which are outlined schematically in Fig. 43. According to Gutierrez-Urrutia et al. [27] and Sato et al. [274] the effect of the grain orientation observed at low strain is governed entirely by the relative value of the Schmid factor, as twinning occurs when the resolved shear stress for twinning is smaller than the critical resolved shear stress for dislocation glide:

$$\tau_T = \tau_{crss} = m_T \cdot \sigma_A < \tau_G = \tau_{crss} = m_G \cdot \sigma_A \rightarrow m_T < m_G \quad (77)$$

Here the Schmid factor has a conventional definition as the product of the cosines of the angles between the direction of the applied tensile stress σ_A and the slip plane normal and the direction of shear for a perfect dislocation (m_G) or a partial dislocation (m_T). This view is mainly based on the mentioned observation that during uniaxial tensile deformation of TWIP steels a strong ⟨111⟩// td and a weak ⟨100⟩//td fiber orientations develop. Fig. 44 shows that while ⟨111⟩//td-oriented grains are profusely twinned, ⟨100⟩// td-oriented ones are mostly twin-free. Using the electron channeling contrast imaging (ECCI) technique to analyze Fe-22%Mn-0.6%C TWIP steel (with γ_{isf} = 22 mJ/m^2), Gutierrez-Urrutia and

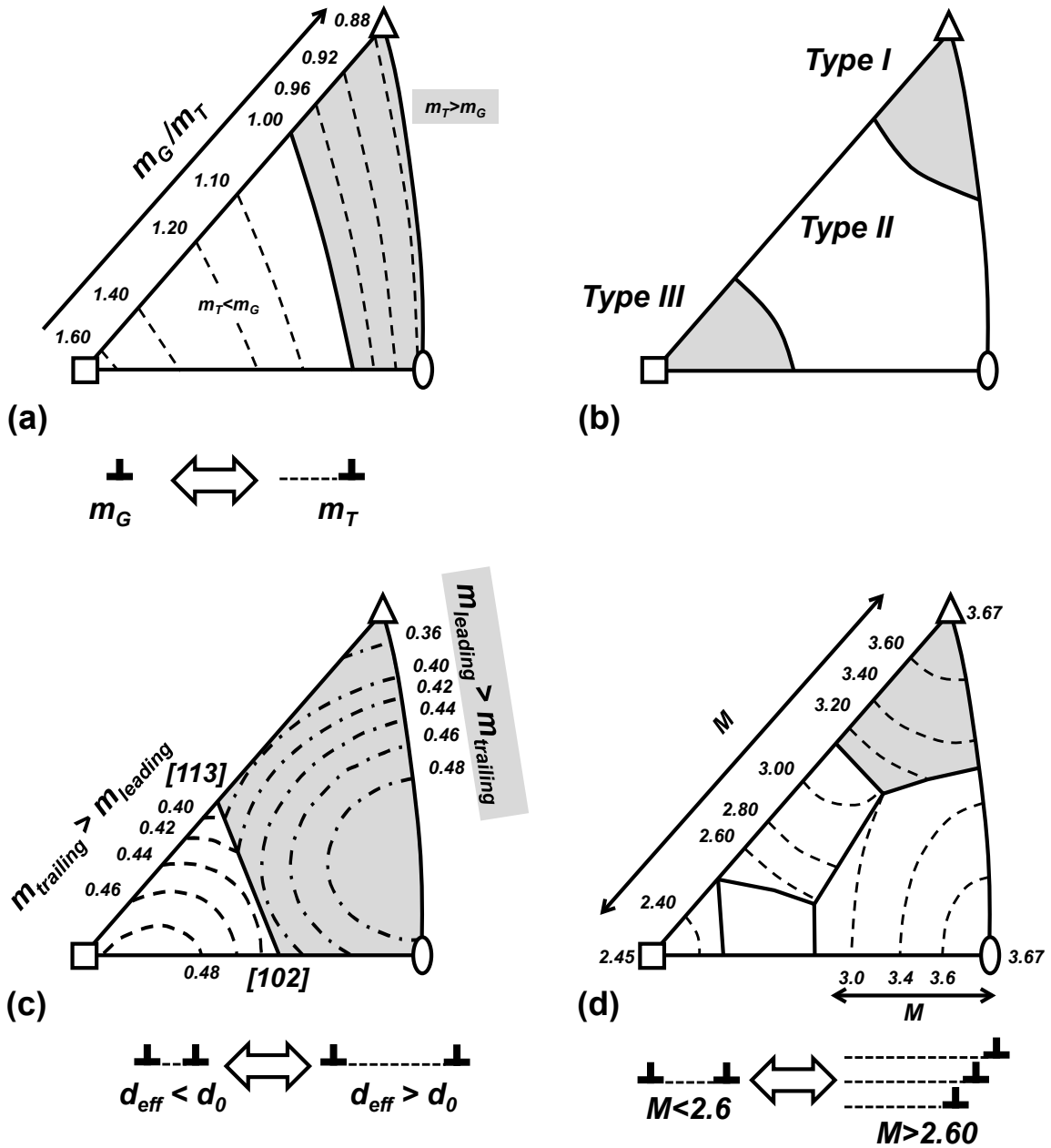

Fig. 43. (a) Schematic illustrating the effect of grain orientation on deformation twinning according to Gutierrez-Urrutia et al. [25] and Sato et al. [274]. (b) Orientation range of Type I and Type II grains, which behave as expected on the basis of their Schmid factor. (c) Schematic illustrating the effect of grain orientation on deformation twinning according to Geissler et al. [276] and Kuprekova et al. [277]. (d) Schematic illustrating the effect of grain orientation on deformation twinning according to Beladi et al. [78].

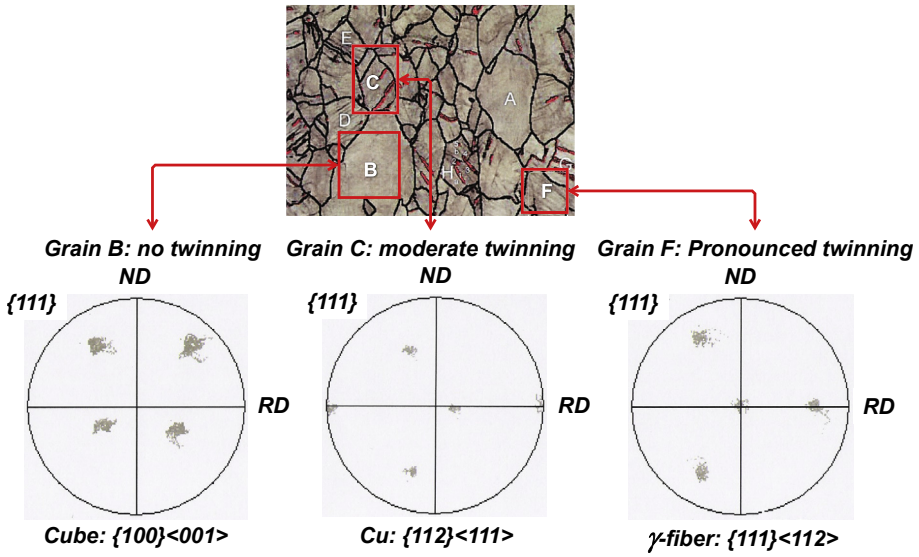

Fig. 44. Illustration of the influence of the grain orientation on twinning in a tensile sample of TWIP steel strained to 50% engineering strain. The pole figures of the individual grains reveal that the C-grain, which has a Cube {100}⟨001⟩-orientation, does not contain deformation twins, the B-grain, which has a Cu {112}⟨111⟩-orientation, exhibits an intermediate twinning behavior, and the F-grain, which has a {111}⟨112⟩ (γ-fiber) orientation, is heavily twinned. Here RD and ND denote the rolling direction and the normal direction, respectively.

Raabe [275] evaluated this mechanism experimentally. They showed that this strict Schmid law orientation dependence of slip and twinning in a tensile test does not apply in practice. Only type I grains, which were favorably oriented for twinning due to their orientation very close to ⟨111⟩//td, and type III grains, which were favorably oriented for dislocation glide with an orientation very close to ⟨100⟩//td, behaved in a manner expected solely on the basis of their Schmid factor. Indeed, micrometer long twins nucleated at grain boundaries in the type III grains were also observed. Furthermore, type II grains, which cover a wide range of orientations unfavorable for twinning based on their Schmid factor, were also found to contain deformation twins. Gutierrez-Urrutia and Raabe associated the deformation twinning in these unfavorably oriented grains with stress concentrations and strain gradients at grain boundaries.

Other authors, e.g. Geissler et al. [276] and Kuprekova et al. [277], considered the Schmid factor for the individual partial dislocations. They noted that for specific grain orientations the force on the leading partial dislocation is larger than that on the trailing partial dislocation of a dissociated perfect dislocation. When this happens, the effective stacking fault width d_{eff} is larger than d_0, the equilibrium stacking fault width in the absence of an applied stress. This can result in breakaway of the leading partial dislocation of a dissociated screw dislocation [146] when the applied stress σ_A exceeds the level of

$$\sigma_A = 6.14 \cdot \frac{\gamma}{b_p} \tag{78}$$

Beladi et al. [78] observed that whereas grains with an orientation close to the Goss and Cube orientations, i.e. low Taylor factor grains, were free of mechanical twins, those having an orientation close to the Brass, S, or Cu, orientations i.e. high Taylor factor grains, were twinned. They therefore correlated the tendency for twinning of individual grains with the magnitude of the Taylor factor for their orientation. According to Beladi et al. [78] the nucleation and growth of twins requires the activation of multiple slip systems and the presence of a high stress resulting from dislocation pile-ups. They report that deformation twinning is initiated at a strain of 0.04. The Taylor factor M, the ratio of the axial flow stress and the shear stress, τ, for a grain with a specific orientation and subjected to a specific deformation is defined as the ratio of the sum of the shear increments over the active slip systems and the axial strain increment:

$$M = \frac{\sigma_A}{\tau} = \frac{\sum_i d\gamma_i}{d\varepsilon} \tag{79}$$

Here σ_A is the applied uniaxial tensile stress. The larger the Taylor factor for a particular grain, the higher is the stress for its plastic deformation. Grains with larger Taylor factors experience a faster evolution of the dislocation density and strain harden more than grains with a low Taylor factor. For Fe-18%Mn-0.6%C-1%Al TWIP steel, Beladi et al. [78] report that, under uniaxial tensile testing, grains that had rotated towards ⟨111⟩//td had a high Taylor factor, $M \approx 3.67$. These grains twinned in the early stages of straining. An example of this behavior is shown in Fig. 44. Grains with a ⟨100⟩//td orientation having a low Taylor factor, $M < 2.6$, remained twin-free up to fracture.

Another confirmation of the thesis that multiple slip precedes twinning is the paper by Yang et al. [278] on texture development in a Fe-33%Mn-3%Al-3%Si TWIP steel during uniaxial tensile deformation. The very thin deformation twins formed did not contribute to texture evolution. The twinned volume was reoriented to CuT-{552}⟨115⟩, Fig. 45, which is an orientation favoring slip. Yang et al. also reported that uniaxial tensile deformation resulted in a strong ⟨111⟩//td and a weak ⟨100⟩//td fiber orientation. Slip caused grain rotation towards the ⟨111⟩−⟨100⟩ line. They also noticed that tension along a ⟨111⟩// td-type direction promoted twinning, in contrast to tension along ⟨100⟩//td, which did not favor twinning. They report that orientations near those with the highest Schmid factor for twinning did not twin. Grains with ⟨110⟩//td orientations were seldom observed to contain twins even after an engineering strain as high as 20%, despite their high Schmid factors for twinning. Yang et al. suggested that there were two contributions of the TWIP effect to strain hardening: (a) the interaction between twin variants in the ⟨111⟩-oriented grains, and (b) the dislocation-dislocation interactions within the deformation

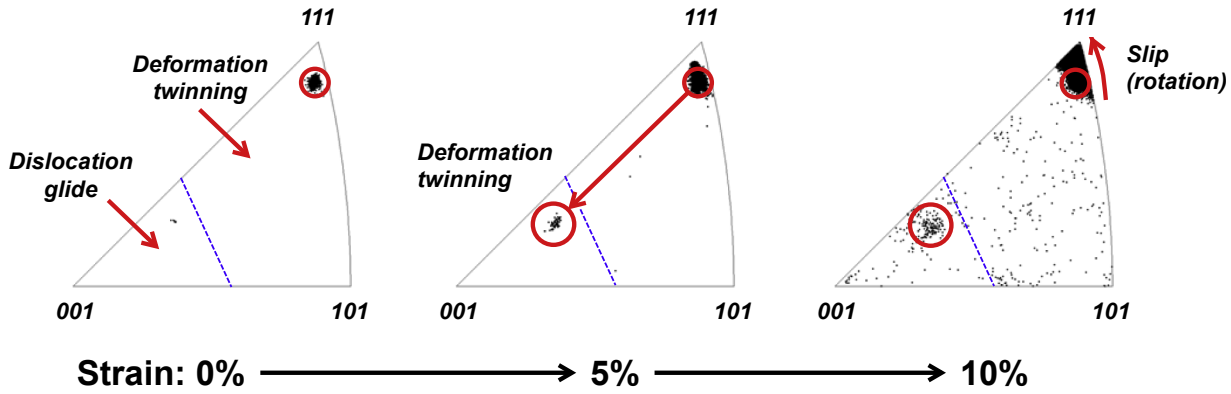

Fig. 45. Orientation changes within a single grain with an orientation close to ⟨111⟩//td. Twinning is clearly seen to give rise to a volume reorientation. The initially Cu-{112}⟨111⟩-oriented grain twins easily to a CuT-{552}⟨115⟩ orientation. In this new orientation, slip is preferred relative to deformation twinning. {111}⟨110⟩ dislocation slip results in a gradual rotation of the grain towards the ⟨001⟩–⟨111⟩ line in the basic stereographic triangle. The dotted line separates the orientations for which twinning and dislocation glide are the preferred deformation modes under uniaxial tension.

twins, whose orientation favors dislocation glide.

Barbier et al. [21] studied the texture development in Fe-22% Mn-0.6%C TWIP sheet steel with 2.6 μm grain size during uniaxial straining along the transverse direction (TD) of rolling that preceded the tensile test. The initial texture of their material was weak. Similar to Yang et al. [278], they observed the development of a pronounced ⟨111⟩//td fiber and a weaker ⟨100⟩//td fiber texture. Twinning started at a true strain of 0.02 (corresponding to a stress of 550 MPa). In accord with the results of other authors cited above, twinning resulted in the formation of bundles of very thin nano-twins, with a thickness in the range of 10–40 nm. Again, the thickness of the twins remained essentially unchanged, whilst the bundles thickened by adding on more new twins in the course of straining. The maximum thickness of the bundles was 250 nm. Barbier et al. estimated that the twinned volume fraction was 9% at a true strain of 0.55, again supporting the observation that saturation levels of the twin volume fraction is typically of the order of 10%, see Section 5.3. Four texture components dominated the texture development during straining: Brass-{110}⟨112⟩, Rotated Cu-{112}⟨110⟩, Rotated Goss-{110}⟨110⟩ and Cube-{001}⟨100⟩. At high strain, the Brass-{110}⟨112⟩ component had the highest intensity. An important conclusion was that deformation twinning in their steel did not generate new orientations, but that it increased the intensity of existing orientations to various degree. According to Barbier et al., deformation twinning affects the texture development in the following ways:

1. The grain rotation resulting from {111}⟨110⟩ slip during uniaxial tensile deformation generates a pronounced ⟨111⟩//td-fiber. The Brass-{110}⟨112⟩ and the Rotated Cu-{112}⟨110⟩ belong to this fiber.
2. The initial recrystallization texture affects the slip activity prior to twinning that sets in when the critical stress for twinning is attained. Deformation twinning is influenced by this prior slip activity and the initial grain orientation.
3. The Cu-{112}⟨111⟩ and Goss {110}⟨100⟩ grains have an orientation favorable for twinning, and the development of the ⟨111⟩// td-fiber orientations continues to favor twinning.
4. Eventually most grains are oriented with ⟨111⟩//td at a strain of 0.3. This promotes twinning at higher strains.
5. Twinning also influences the texture development through the generation of new orientations and the modification of the texture evolution by dislocation glide.
6. New orientations are formed when twins form inside ⟨111⟩//td or ⟨110⟩//td oriented grains. These new orientations are close to the ⟨100⟩//td fiber orientation (Fig. 46). In grains with this orientation, dislocation glide is favored relative to twinning as the Schmid factors for twinning and glide are 0.23 and 0.41, respectively.
7. As most twins are oriented close to ⟨100⟩//td, the increase in the intensity of this fiber orientation during straining is directly related to the evolution of the twin density.

The results by Prakash et al. are slightly different from the previous reports reviewed above [279]. The initial texture of their TWIP steel sheet material had mainly Brass and Goss orientations, and the S texture component was not a major one. Tensile deformation with the loading direction along the rolling direction raised the intensity of the {110}⟨111⟩ texture component and decreased the intensity of the Brass orientation. Goss continued to be a principal component. Uniaxial deformation along the transverse direction (TD) resulted predominantly in the Goss and Brass texture components, with the Brass texture spreading towards {110}⟨111⟩.

It has been pointed out that some of the texture analysis was carried out on TWIP steels which are susceptible to room temperature dynamic strain aging (DSA), such as Fe-22%Mn-0.6%C [280]. The increased temperature in the localized deformation bands due to heat dissipation causes γ_{isf} to increase, which is expected to enhance the Cu-type texture. Al additions also increase γ_{isf}, and this results in a slightly more pronounced Cu-texture. It is believed that these effects and the pronounced planarity of slip may explain the persistence of the Cu-{112}⟨111⟩ texture component in tensile straining, as illustrated by Figs. 47 and 48.

5.5. Rolling texture

The orientation changes in rolling deformation are more complex than those occurring under uniaxial tensile deformation. All high γ_{isf} fcc metals and alloys are similar in that they deform by homogeneous {111}⟨110⟩-type dislocation slip and easy dislocation cross-slip. The {111}⟨110⟩ slip and the grain rotations during rolling result in the development of a β-fiber orientation. The β-fiber is an ODF-skeleton line going from the Cu-{112}⟨111⟩ component, via the S-{123}⟨634⟩ component to the Brass-{110}⟨112⟩ component. It usually consists of a relatively large fraction of the S-{123}⟨634⟩ component.

A Brass-{110}⟨112⟩-type texture is expected as the stable rolling texture in low-to-medium γ_{isf} TWIP steel, since both octahedral slip and mechanical twinning are active deformation mechanisms (Fig. 49). Deformation twinning and the attendant limited cross-

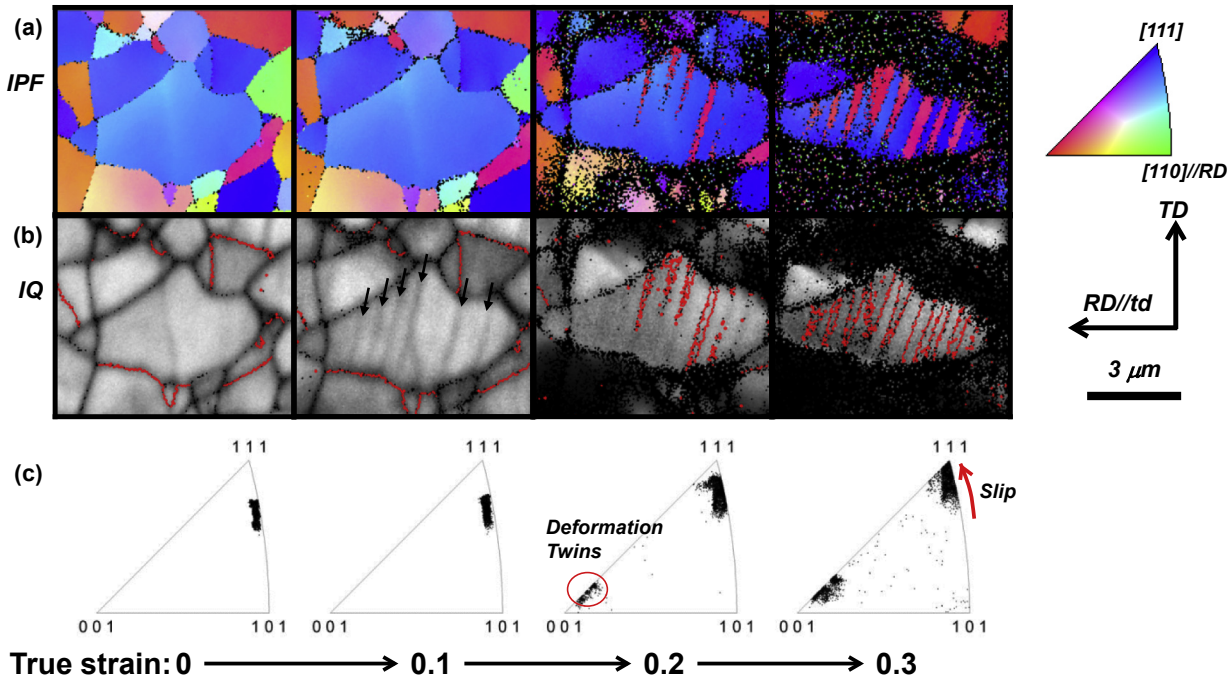

Fig. 46. *In situ* EBSD analysis of twinning in a grain close to the ⟨111⟩//td-orientation for a true strain in the range of 0.0–0.3. (a) Inverse pole figure evolution. (b) Image quality (IQ) contrast of the same region as in (a). Note that the deformation twins are already visible in the IQ image at a strain of 0.1 (Arrows). (c) The pole figures taken at different strain reveal the grain rotation and the formation of CuT-{552}⟨115⟩-oriented twinned regions at a strain of 0.2 and 0.3.

slip result in a texture characterized by α-fiber orientations spreading form the Brass-{110}⟨112⟩ to the Goss-{110}⟨100⟩ orientation. When the Brass-texture is pronounced, the volume fraction of the Cu-{112}⟨111⟩ and S-{123}⟨634⟩ texture components is negligible. According to the classical model for the emergence of the Brass-texture in low γ_{isf} alloys, deformation twinning plays a key role in the texture development. During straining, grains with the Cu-{112}⟨111⟩ orientation first twin into the CuT-{552}⟨115⟩ orientation. Dislocation glide then causes the CuT-{552}⟨115⟩-oriented grains to rotate around ⟨110⟩//TD towards the Goss-{110}⟨001⟩ orientation and the stable Brass-{110}⟨112⟩ final orientation. Hirsch et al. [281,282] proposed that the CuT-{552}⟨115⟩ oriented lamellae formed by twinning first rotate to an intermediate Brass-R-{111}⟨112⟩ orientation, and then to the Goss orientation during the shear band formation. Smallman and Green [283] and Dillamore [284] associate the texture transition to Brass-{110}⟨112⟩ with the limited cross-slip in low γ_{isf} metals and alloys.

At large strains a lamellar microstructure of the matrix and the twins parallel to the rolling plane develops. According to Morii et al. [285], slip cannot continue when the slip planes are almost parallel to the surface, and this leads to the formation of shear bands. However, this alignment of the lamellar microstructure of matrix and twins parallel to the rolling plane does not appear to be necessary to form shear bands, and there is evidence for shear bands forming early on when the rotation of the lamellae is initiated. Vercammen et al. [88] studied the evolution of microstructure and texture of a Fe-30%Mn-3%Al-3%Si TWIP steel during cold rolling. According to that study, a Brass-type texture was already present at small rolling strains. The Brass orientation {110}⟨112⟩ was predominant at every strain level, whilst the Cu-orientation

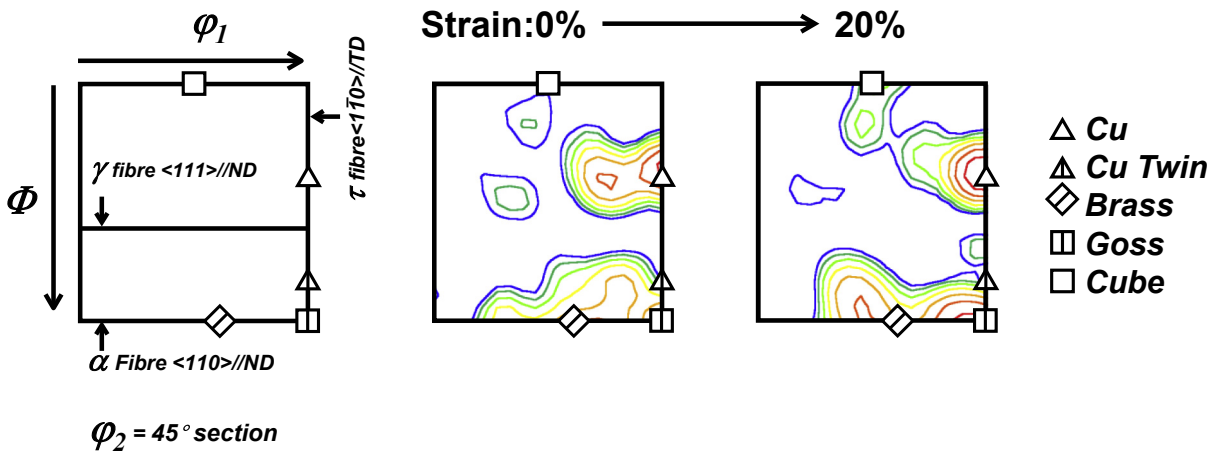

Fig. 47. Evolution of the orientation distribution function (ODF) during tensile straining of a Fe-18%Mn-0.6%C-1.5Al TWIP steel to an engineering strain of 20%, which results in an enhancement of the Cu texture and S components. A schematic $\phi_2 = 45^\circ$ section of the ODF in the Euler angle space with the main texture components and fibers. Note the α-fiber texture from Brass-{110}⟨112⟩ to Goss-{110}⟨100⟩.

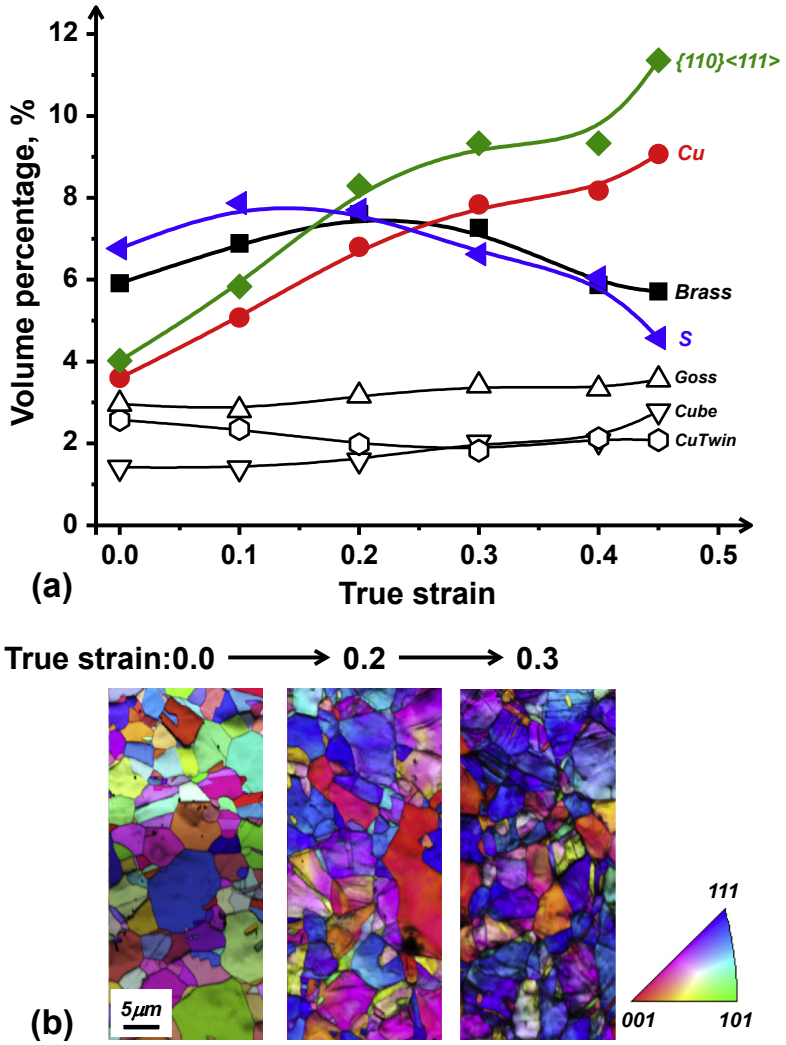

Fig. 48. (a) Evolution of the volume fractions of the various texture components during tensile straining of a Fe-18%Mn-0.6%C-1.5Al TWIP steel. (b) Corresponding RD-inverse pole figure map at different strains. Note the α-fiber texture ranging from Brass-{110}⟨112⟩ to Goss-{110}⟨100⟩. The volume fraction of a texture component is obtained by assuming a 10° orientation tolerance around the exact component.

intensity remained low. The absence of a pronounced Cu-orientation texture was related to the early formation of deformation twins, as supported by their TEM micrographs. The Goss and Cu-Twin orientations developed due to an increase of the twin volume fraction with strain. Most of the grains were twinned at larger values of sheet thickness reduction, the twinning planes being reoriented so as to be parallel to the rolling plane, making homogeneous deformation difficult. Shear banding was initiated because crystallographic slip was inhibited. At a thickness reduction corresponding to an engineering strain of 65%, non-homogeneous shear band formation became the preponderant deformation mechanism. The deformation microstructure consisted of bands oriented at approximately +35° and −35° to the RD. γ-fiber {111}//ND texture components, i.e. {111}⟨110⟩ and {111}⟨112⟩, were formed due to the alignment of twin lamellae parallel to the rolling plane.

The rolling texture development in TWIP steels is akin to that in the austenitic stainless steel grade AISI 316L ($\gamma_{isf} = 64$ mJ/m^2) [286].

5.6. Texture evolution modeling

In Section 2.2, crystal plasticity modeling for TWIP steels deforming by dislocation glide and deformation twinning has been described as a potent way to predict their microstructure evolution and deformation behavior. Crystal plasticity models are also an equally powerful computational tool for describing and predicting the crystallographic texture evolution for technologically important processing operations, such as rolling [31,279,287]. In a polycrystal plasticity model, the interaction of the grains with their surroundings have to be accounted for. The classical Taylor assumption that strain and strain rate are the same in every grain is commonly used, but this full Taylor constraint can be relaxed in more sophisticated models. A challenging part of the modeling is that in the case of TWIP steel the models need to take into account sudden changes in orientation, and make assumptions about the behavior of the twinned volume. One possibility is to consider that the grain population is subdivided in twinned and non-twinned parts and assume that the twinned regions do not contribute to plasticity.

Barbier et al. [288] modeled the texture evolution and microstructure changes in Fe-22%Mn-0.6%C TWIP steel (γ_{isf} ~20 mJ/m^2) during uniaxial tensile and shear deformation. They considered a representative volume element (RVE) of 3000 grain orientations. The texture evolution was found to be mainly controlled by crystallographic {111}⟨110⟩ slip, dislocation slip on multiple slip systems governing the plasticity and strain hardening. Tensile

deformation along RD and TD induced twinning in most grains. As the texture developed, more and more grains assumed an orientation favorable for twinning, while twin-twin interactions made it more difficult to produce more twins.

Dancette et al. [32] used idealized truncated octahedron-shaped grains as representative volume elements (RVE) used in their calculations. By considering the effect of the twin thickness on the dislocation mean free path, and with the aid of a heuristic equation for the twinning kinetics in the parent grains, they were able to calculate the texture evolution. One finding was that a simple Schmid factor analysis does not predict the correct amount of twinning in the grains. Furthermore it was found that for the full constraint Taylor model the calculated texture is too sharp in the Brass and Goss region. The results obtained by Dancette et al. at the grain level are very informative. Whereas a single slip Sachs-type behavior model predicts a Brass-type texture [289], a multi-slip Taylor-type model predicts Cu-type textures [290].

An important issue with the crystal plasticity modeling of C-added TWIP steels is dynamic strain aging, which makes the macroscopic deformation nonhomogeneous, see Section 6 below. The associated serrations in the stress-strain curves are often ignored or simply filtered out [32]. These effects, which are expected to influence the twinning kinetics in the deformation bands, have not yet been implemented in crystal plasticity models. It is therefore not known how DSA-related strain localizations influence the texture evolution in TWIP steels that deform at room temperature by the propagation of deformation bands causing discontinuous yielding, such as e.g. the Fe-22%Mn-0.6%C TWIP steel.

5.7. Recrystallization texture

Y.Lü et al. [291] studied the texture development in Fe-21.6%C-0.38%C TWIP steel cold rolled to a 50% rolling reduction and recrystallization annealed in the temperature range of 560 °C to 700 °C. They report that the nucleation of new grains was site saturated, *i.e.* all nuclei were generated at the start of the recrystallization anneal. The nucleation sites were shear bands, grain boundaries and triple junctions. The growth rate of the nuclei decreased with increasing annealing time, which the authors associated with recovery by pipe-diffusion controlled dislocation climb and a decrease of the driving force for grain boundary migration. The grain structure after annealing was inhomogeneous due to a non-random distribution of nucleation sites. In the initial

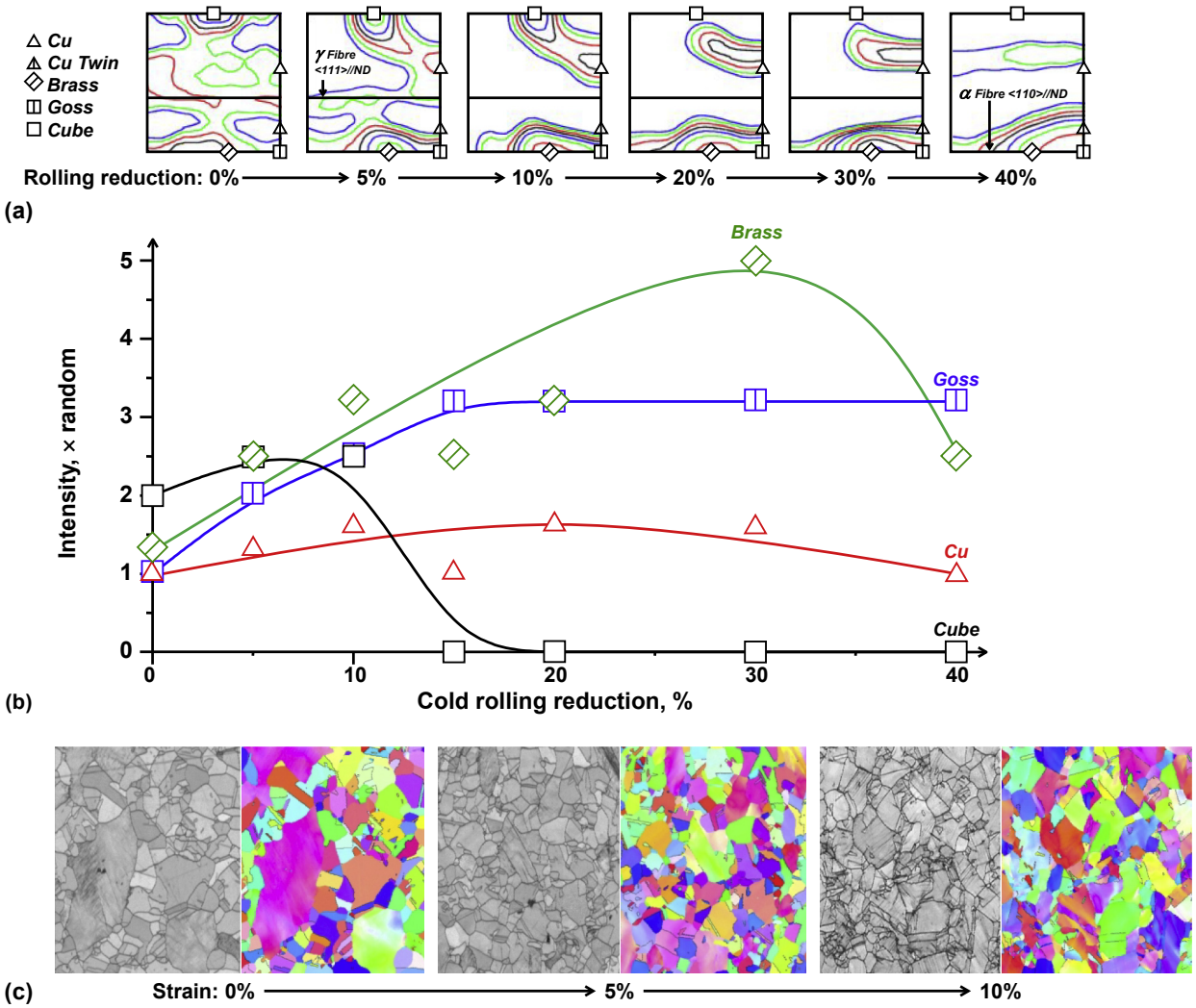

Fig. 49. (a) Evolution of the ODF during cold rolling of a Fe-22%Mn-0.6%C-0.08%N TWIP steel. (b) Evolution of the volume fraction of the main texture components presented in (a). (c) IQ and IPF maps showing that the main twinning activity occurred in the deformation range of 5–10%. Note the α-fiber texture spreading from Brass-{110}⟨112⟩ to Goss-{110}⟨100⟩ and the weakening of the Cu-{112}⟨111⟩ component at large strains. The rolling texture can be described as a Brass-type {110}⟨112⟩-texture with a spread towards the Goss-type texture {110}⟨001⟩.

stages of annealing, *i.e.* prior to the onset of recrystallization, the S-{123}⟨634⟩ texture component increased in intensity for a short period of time due to the transformation of the strain-induced ε-martensite to austenite [292]. The intensity of the dominant texture components developed as a result of cold rolling, *i.e.* the S-{123}⟨634⟩, Brass-{110}⟨112⟩, and Goss-{110}⟨100⟩ components, gradually dropped off during annealing. The texture after full recrystallization was similar to the deformation texture, but was very weak. Texture was also weak after annealing above 630 °C in not fully recrystallized state. Un-recrystallized domains had a Goss-{110}⟨100⟩ orientation. These grains are known to have a low stored energy after cold work [293]. The texture was more pronounced after annealing at lower temperatures. For example, after annealing at 560 °C the intensity of the α-fiber ⟨110⟩//RD and the ⟨100⟩-fiber increased due to selective growth of grains with these orientations.

Bracke et al. [294,295] studied the recrystallization texture of annealed cold rolled Fe-22%Mn-0.6%C, an alloy with a low stacking-fault energy ($\gamma_{isf} = 15$ mJ/m^2). They contrasted it with the texture in a hot rolled strip, which was weak with a low intensity Cube-100<100> component, which is actually a recrystallization texture typical for *high* γ_{isf} fcc alloys. For cold rolling, the TWIP steel investigated showed a deformation texture evolution behavior characteristic of *low* γ_{isf} alloy. This assessment is based on two observed features: (a) a decrease of the intensity of the β-fiber component, and (b) the development of an α-fiber with a high intensity between the Brass and Goss component. The presence of the CuT-552<115> texture component was also considered as a direct proof for twinning and an evidence that twin formation leaves a footprint in the texture. Bracke et al. [294,295] also observed a new texture component they refer to as the "X-component", which is twin related to the Brass component. In their annealing experiments on cold rolled steel, a slightly higher temperature (725 °C) than in the work by Y.Lü et al. [291] (700 °C) was used. They found a recrystallization texture which was almost identical with the cold rolled texture, except for a marginal increase of the Goss-{110}⟨100⟩ component in the recrystallized steel. The texture did not depend on the reheating rate. The high nucleation density observed at the start of the recrystallization was associated with site-saturation nucleation. The nucleation was homogeneous throughout the microstructure. At high rolling strains, the recrystallization was first initiated within the shear bands. Accordingly, no strong orientation selection occurred during nucleation and growth of the recrystallized grains. Once recrystallized grains nucleated, their growth was sluggish, due to the impingement of the growing grains soon after their formation. This process resulted in a small grain size. The results imply that the stored energy of deformation was distributed homogeneously. Grain growth and the formation of recrystallization twins must have occurred in a random way, too. As the nucleation process involved a random sampling of the orientations in the deformed microstructure, the recrystallization texture replicated the initial deformation texture.

The observations of a small grain size and a pronounced cold rolled texture made by Bracke et al. [294,295] are not supported by Barrales et al. [296]. The latter authors found a coarser hot rolled grain structure, which they believe may have resulted in texture randomization and a coarser grain size after recrystallization annealing that followed cold rolling.

6. Dynamic strain aging and strain rate sensitivity in carbon-alloyed TWIP steel

Plasticity controlled by thermally activated dislocation motion discussed in Section 4.4 is normally associated with a positive strain rate sensitivity of the flow stress defined as $S = d\sigma/dln\dot{\varepsilon}$. The strain rate sensitivity parameter, $m = \frac{d \ln \sigma}{d \ln \dot{\varepsilon}} = \frac{S}{\sigma}$, is related to the activation volume of the underlying mechanism governing dislocation glide, which may be associated with thermally activated overcoming of dislocation forest junctions, stationary solute atoms or their clusters, or the Peierls barriers. In all these cases m is positive. However, under certain conditions, mobile solutes segregating to mobile dislocations temporarily arrested at localized obstacles may additionally pin them. This pinning effect, known as dynamic strain aging (DSA), is greater for lower dislocation velocities or plastic strain rates, which means that its contribution to stress has a negative strain rate sensitivity. Indeed, the contribution to stress due to this pinning effect increases with solute concentration c_s on the dislocation, which in turn increases with the waiting time t_w it takes the dislocation to overcome the obstacle it is arrested at. As t_w is inversely proportional to the dislocation velocity, an increase in the velocity brings about a drop in the DSA contribution to stress. The competition between the two contributions to stress having different signs of the strain rate sensitivity may result in an overall negative one. The schematic in Fig. 50 illustrates how a negative strain rate sensitivity component gives rise to an N-shaped $\sigma - \ln\dot{\varepsilon}$ curve. According to the model proposed by Kubin and Estrin [37], the dislocations move slowly dragging along a Cottrell cloud of solute atoms in the low strain rate branch of the curve, *i.e.* in the solute drag region. In the high strain rate branch of the curve, *i.e.* in the lattice friction region, the diffusivity of solutes is insufficient for them to catch up with the rapidly moving dislocations, which thus experience only the effect of the lattice friction and the stationary solutes. In the intermediate strain rate range, represented by the descending part of the curve in Fig. 50, plastic deformation is inherently unstable. In this regime, propagating localized deformation bands are formed [297]. A large volume fraction of the material deforms at a low strain rate whilst a small one, *viz.* the material within the localized deformation bands, deforms at a high strain rate. This extreme manifestation of dynamic strain aging in the negative strain rate sensitivity of the flow stress, referred to as the Portevin-Le Chatelier effect, also occurs in C-alloyed TWIP steels. Propagation of localized deformation bands accompanied with serrations on the stress-strain curve was observed in specific ranges of temperature and strain rate where the strain rate sensitivity of the flow stress is negative, *i.e.* $S < 0$ holds. When a strain rate from within this range, $\dot{\varepsilon}_1 < \dot{\varepsilon} < \dot{\varepsilon}_2$, is imposed, the system will follow the A-B-C-D stress-strain rate cycle shown in Fig. 50, thus avoiding the interval $(\dot{\varepsilon}_1, \dot{\varepsilon}_2)$, while maintaining an average strain rate equal to the externally imposed one. In TWIP steels, the strain rate within a localized band is typically one order of magnitude larger, while that outside the band is one order of magnitude lower, than the applied strain rate.

The strain rate sensitivity being slightly negative is one of the few disadvantageous mechanical properties of C-alloyed TWIP steels. In other fcc metals and alloys micro-twins and nano-twins were shown to increase the strain rate sensitivity considerably. For instance, for ultra-fine grained nano-twinned Cu, with a grain size in the range of 400 nm−500 nm, the strain-rate sensitivity parameter m is significantly higher as compared to ultra-fine grained Cu without nano-sized twins, 0.037 compared to 0.005, respectively. The strain rate sensitivity parameter was also reported to increase with decreasing twin spacing [298].

The main macroscopic manifestations of the Portevin-Le Châtelier (PLC) effect are as follows: (a) the strain rate sensitivity of the flow stress is negative, (b) the stress-strain curve is serrated, (c) plastic strain is localized in PLC deformation bands, and (d) the post-uniform elongation, as measured in a uniaxial tensile test, is very limited.

The jerky flow associated with the serrated stress-strain curves

Please cite this article in press as: B.C. De Cooman, et al., Twinning-induced plasticity (TWIP) steels, Acta Materialia (2017), http://dx.doi.org/10.1016/j.actamat.2017.06.046

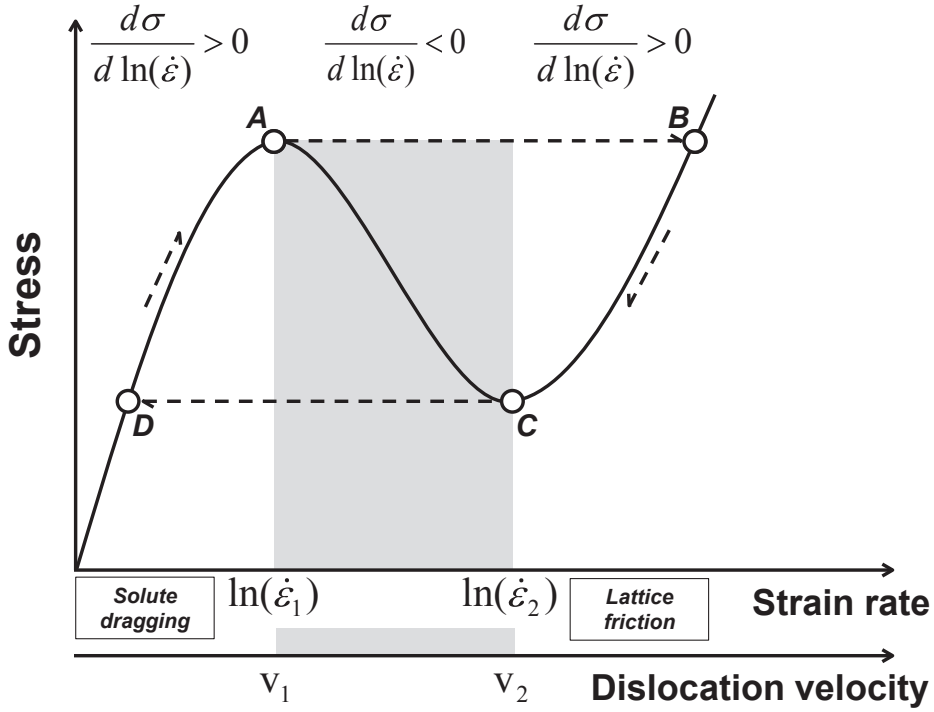

Fig. 50. Schematic $\sigma - \ln\dot{\varepsilon}$ curve with a region of negative strain rate sensitivity, $d\sigma/d\ln\dot{\varepsilon} < 0$. In the strain rate interval between $\dot{\varepsilon}_1$ and $\dot{\varepsilon}_2$, uniform deformation is unstable. In the low strain rate condition, $\dot{\varepsilon} < \dot{\varepsilon}_1$, the dislocations drag along an atmosphere of solute atoms. In the high strain rate condition, $\dot{\varepsilon} > \dot{\varepsilon}_2$, the dislocations move without a solute atmosphere, and experience only a resistance from the lattice friction and the stationary solutes. A regime characterized by localization of strain in deformation bands corresponds to an imposed strain rate falling in the interval $(\dot{\varepsilon}_1, \dot{\varepsilon}_2)$.

in uniaxial tension is an indication of non-uniformity of deformation. Strain localization takes place in propagating or static deformation bands. From a technological point of view, it is important to avoid DSA, in order to ensure stable material flow during sheet forming processes. Strain non-uniformities also give rise to visible surface defects on press-formed parts. DSA also leads to the inability of C-alloyed TWIP steels to sustain large post-uniform strains after the initiation of necking. It has also been linked to premature ductile fracture occurring during stretch-flanging of TWIP steels, as DSA leads to rapid edge cracking during hole expansion [299,300]. It is therefore important to suppress the occurrence of DSA- or PLC-related instabilities of plastic flow by defining suitable strain rate and temperatures for processing. In particular, the temperature dependence of the critical strain for the onset of serrations on the stress-strain curve needs to be known. The temperature dependence of the critical strain for Fe-18%Mn-0.6%C-1.5%Al steel for a particular level of the imposed strain rate is shown in Fig. 51.

Several types of PLC bands are considered, according to their appearance, character of propagation, and statistics [297]. Three major types observed during uniaxial tensile tests are labeled A, B, and C. Type A bands appear as successive solitary bands which, in the case of TWIP steels, are usually nucleated at or close to one of the ends of the tensile sample and propagate across the entire sample length, as illustrated by results on Fe-18%Mn-0.6%C TWIP steel in Fig. 52a. Type A bands are observed at relatively high strain rates (typically $\geq 10^{-3}s^{-1}$). They are approximately 2 mm wide, with a wider IR-thermography image of about 4 mm, and are inclined to the tensile axis at an angle of about 53° [311]. The local strain within a type A band, as well as the band velocity, were strain dependent. At low strains, the initial strain within a band was ~0.005 and the band velocity was ~36 mm/s. Local measurements of the characteristics of type A PLC bands showed that the strain rate in the deformation band velocity was ten to twenty times the imposed strain rate [301]. Accordingly, the temperature was higher inside the bands than outside of them. Close to fracture the strain within a band increased to ~0.090, whilst the band velocity dropped to ~4 mm/s. The band displacement became progressively smaller as the strain rate decreased and eventually type B bands occurred in a correlated manner.

Type B bands are stationary, but as a new band emerges ahead of a previously formed one in a 'relay-race' fashion, they appear to have a hopping behavior. Whereas the propagation velocity of type A bands can be up to hundreds mm/s, the effective propagation velocity of a B band pattern is very low, of the order of tens mm/s. Mainly type A and type B bands have been observed for TWIP steel. Type C bands are static bands nucleated at random, in a non-correlated way, over the entire sample. They are characterized by sharp stress drops. Type C bands are usually formed at very low strain rates (typically $\leq 10^{-5}s^{-1}$). Qian et al. [302] observed type C serrations on the flow curves of Fe-22%Mn-0.6%C TWIP steel tested in the strain rate range of $6 \times 10^{-6}s^{-1}$-$10^{-4}s^{-1}$.

DSA in Fe-24%Mn-0.6%C ($\gamma_{isf} = 31$ mJ/m^2) and Fe-27%Mn-0.6%C-3.5%Al ($\gamma_{isf} = 50$ mJ/m^2) was studied by Saeed-Akbari et al. [303]. They detected persistent presence of instabilities even in apparently smooth stress-strain curves. As TWIP steels have a relatively low thermal conductivity, Bäumer and Bleck suggested that adiabatic heating plays a significant role during straining at higher strain rates [304]. They stress the importance of the effect of adiabatic heating on the magnitude of γ_{isf} and the deformation mechanism. Their work also indicates that the serrations occurred earlier in the fine grain size state, and that the largest changes in the flow stress occurred for the finest grain structure of TWIP steel.

A common scenario for the emergence of PLC related plastic instabilities suggests that an initially stable uniform strain regime prevailing when plastic deformation commences becomes unstable once a specific critical strain ε_c is reached. For identifying deformation conditions which are less conducive for the occurrence of

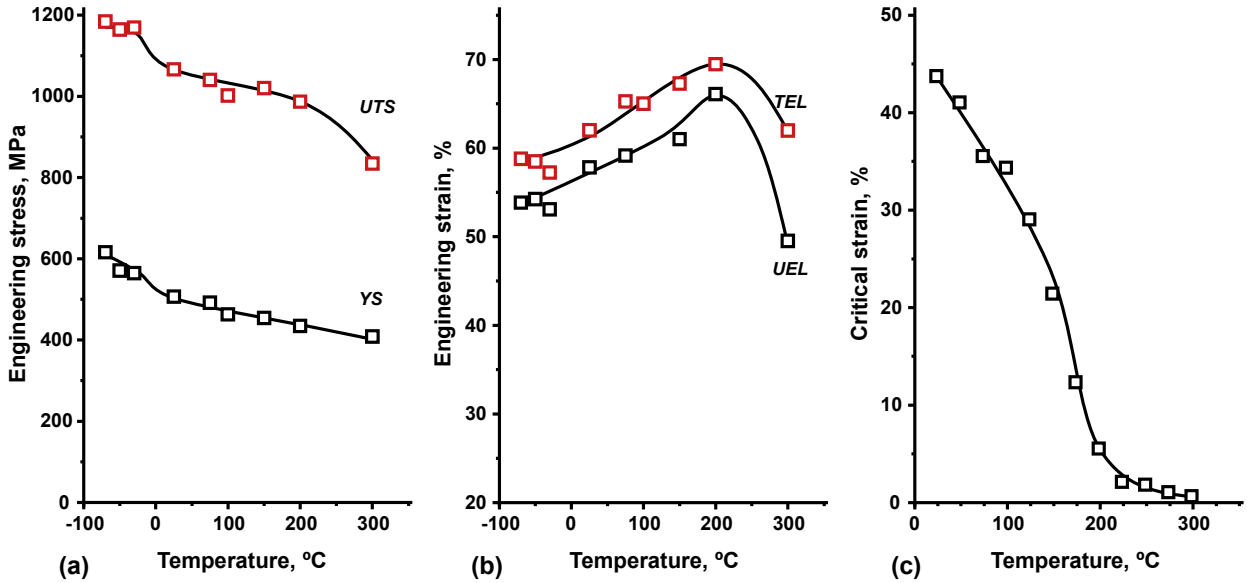

Fig. 51. Temperature dependence of (a) the yield stress and the ultimate tensile stress, (b) the uniform (UEL) and the total (TEL) elongation, and (c) the critical onset strain for serrations on the stress-strain curve of Fe-18%Mn-0.6%C-1.5%Al steel. (Imposed strain rate: $10^{-3}s^{-1}$).

undesired PLC instabilities, it is important to know the strain rate dependence of the critical strain ε_c for the onset of serrated yielding. Commonly accepted models of the PLC effect [297] predict a non-monotonic, V-shaped ε_c vs. $\dot{\varepsilon}$ curve. Experiments by Qian et al. [302], who studied PLC instabilities in Fe-22%Mn-0.6%C TWIP steel in the strain rate interval of $6 \times 10^{-6}s^{-1}$-$6 \times 10^{-3}s^{-1}$, confirm this dependence, Fig. 53. At high strain rates (10^{-4}-$10^{-2}s^{-1}$, type A regime), ε_c increased with strain rate ('normal' behavior). In the lower part of the strain rate range considered (10^{-6}-$10^{-4}s^{-1}$, type C regime), ε_c exhibited a negative strain rate dependence, referred to as inverse, or 'anomalous'. Grain size was shown to have an effect on the critical strain, as well, grain refinement leading to an increase of ε_c. This grain size effect is also seen in Fig. 53. In certain cases, though, no critical strain can be identified. This is the case with Fe-20%Mn-1.2%C TWIP steel investigated by Renard et al. [305] at room temperature. In their material, stress serrations always appeared right from the start, as soon as plastic deformation commenced. Their material had a slightly negative strain rate sensitivity of the flow stress right from the start of plastic deformation.

The entirety of the mentioned work suggests that plastic instabilities exhibited by TWIP steels are consistent with the idea that they are of the PLC type, i.e. take their origin in the dynamic strain aging effect. However, Lebedkina et al. [22] indicated that the

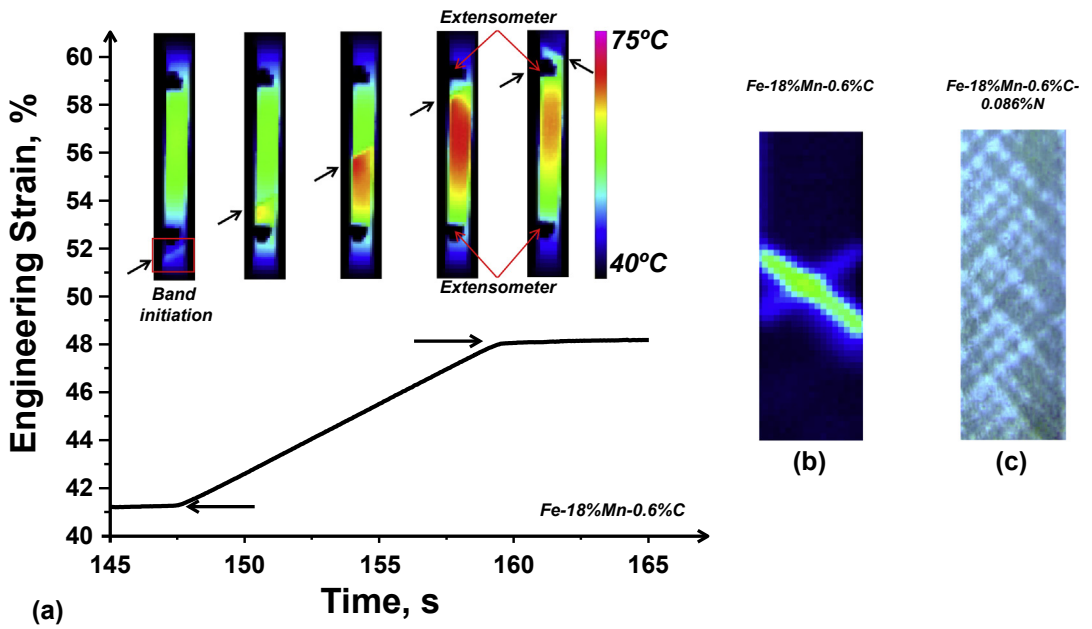

Fig. 52. (a) Example of a type A band in Fe-18%Mn-0.6%C TWIP steel which nucleates at one end of the tensile specimen and propagates across the entire sample length. The passage of the band is only detected when it is moving within the extensometer range. This gives rise to characteristic type A serrations on the stress-strain curves. (b) High resolution infrared image of a type A band; a secondary band is also visible. (c) Traces of multiple deformation bands which give rise to type B serrations on the stress-strain curve of Fe-18%Mn-0.6%C-0.086%N TWIP steel.

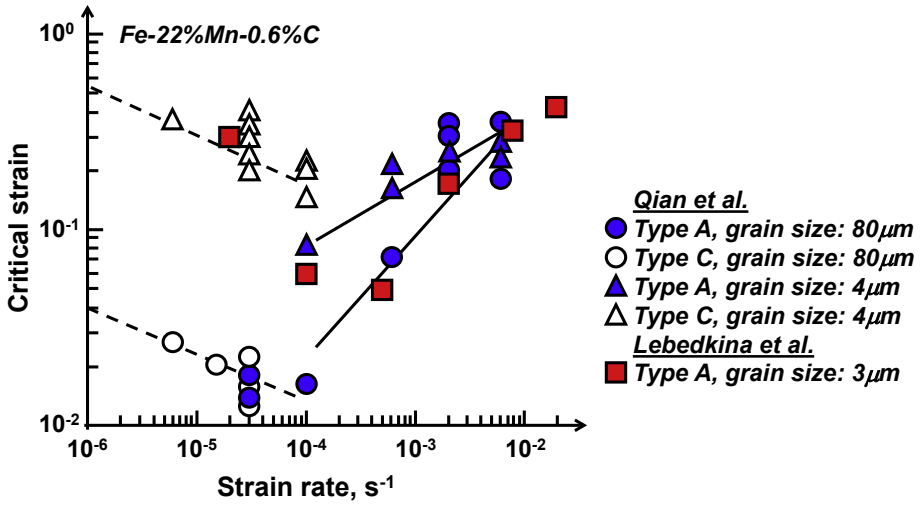

Fig. 53. Strain rate dependence of the critical strain for Fe-22%Mn-0.6%C TWIP steel, which exhibits an inverse behavior at low strain rates and a normal behavior at high strain rate [22,302].

plastic instabilities observed in the case of TWIP steels are not due to a standard DSA effect because propagation of type A bands prevails over an unusually wide strain rate range ($2.1 \times 10^{-5}s^{-1}$-$10^{-1}s^{-1}$). They argued that deformation twins will locally cause a hardening and generate internal stresses which drive the persistent propagation of localized deformation bands having the appearance of type A bands. It should also be noted that the pseudo-PLC effect discussed in Section 2.2.5 cannot be ruled out as a mechanism for unstable, discontinuous plastic flow observed in TWIP steels.

The salient features of type A bands (Fig. 54) [301,306] can be summarized as follows:

(a) The deformation bands are observed over a wide range of strain rates (10^{-6}-$10^{-1}s^{-1}$) in C-alloyed TWIP steels, characterized by a negative strain rate sensitivity of the flow stress, $m < 0$.
(b) Type A bands cause plateaus or steps in the strain *vs.* time curves, which are due to the low deformation rate in the gauge length of the sample when type A bands are nucleated and propagating outside of the measurement range of the strain gauge.
(c) The deformation band velocity decreases with increasing strain.
(d) The deformation band velocity increases with increasing imposed strain rate.
(e) The localized strain inside a band increases in the course of straining.
(f) The strain rate within the deformation bands is typically at least 10–20 times larger than the imposed strain rate.
(g) A deformation band is inclined at an angle of 53°-55° to the tensile direction.

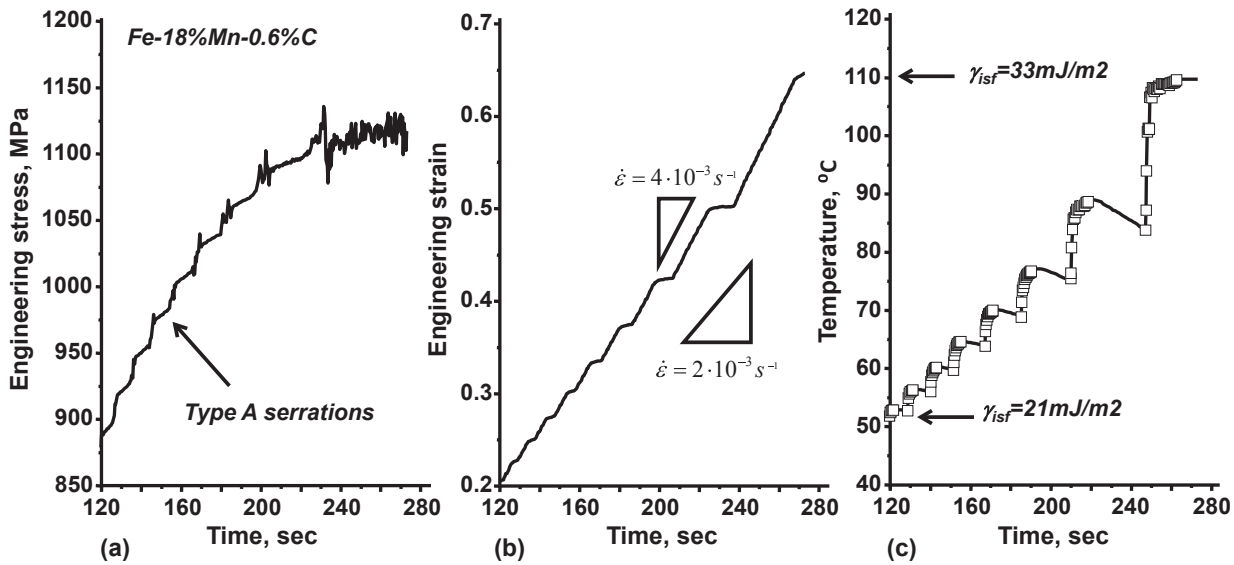

Fig. 54. Characteristics of type A serrations in the stress-strain curve of C-alloyed TWIP steel Fe-18%Mn-0.6%C. (a) Serrated stress *vs.* time curve. (b) Strain *vs.* time curve with typical strain plateaus and steps, which illustrates that the strain rate in the deformation band is higher than the externally imposed strain rate. (c) Temperature *vs.* time curve for a location near the center of a tensile specimen. The rapid temperature increases are due to the passage of successive deformation bands through the point of measurement. The increase of the stacking fault energy associated with the temperature rise is also indicated [306].

(h) A temperature increment caused by the passage of an individual deformation band is typically in the range of 5°C-30 °C. Combined heating by the deformation band and the background adiabatic heating of the overall tensile sample can result in a temperature rise of ~100 °C. (Test conditions: strain rate of ~$10^{-3}s^{-1}$, temperature ~25 °C, sample thickness 1–2 mm)

(i) A localized deformation band is accompanied by a weaker secondary band which compensates for the axial misalignment of the two parts of the tensile specimen on either side of the main deformation band.

There is reasonable consistency between the data reported in literature, and most of the deviations from the properties presented above are likely due to differences in composition and grain size of the TWIP steels considered.

DSA is influenced by the temperature, the strain rate, the microstructure and the composition. It is also influenced by the grain size. Several metallurgical variable may affect DSA in TWIP steels. Thus, alloying with Al [179,195] and V [307]. Alloying with nitrogen was also found to increase the critical strain for the onset of the PLC effect and modify the initiation of the deformation bands. Lee et al. [200] in particular showed that the addition of 0.09% N to a Fe-18%Mn-0.6%C TWIP steel alters the appearance of the serrated flow curves and the properties of type A bands considerably. This is illustrated in Fig. 55. Instead of a step-like pattern, stress discontinuities appear as spikes. The reason is the location of the deformation bands, which are initiated in the gauge, rather than the grip part of the sample [200]. The band initiation stress therein is higher than the stress required for band propagation, which explains the spike-like appearance of the curve.

Fig. 56 shows that the *instantaneous* strain rate sensitivity, as measured by various strain rate jump tests, is always positive. The quantity appearing in the PLC instability condition, Eq. (78), is a steady state strain rate sensitivity attained after a transient associated with a strain rate jump [308]. This steady-state strain rate sensitivity may have a very small positive value or be negative. It typically varies in the range of +0.002 to −0.010. According to Chung et al. [9] the strain rate sensitivity parameter m for Fe-18% Mn-0.5%C-1.5%Al TWIP steel is −0.007. Shen et al. found larger negative values, e.g. −0.021, for the strain rate sensitivity of Fe-20% Mn-0.6%C TWIP steel [220] with a grain size of 3.5 μm, and −0.029 for a steel with a grain size of 25 μm. Note that the strain rate sensitivity of low C ferritic steel, interstitial-free steel and austenitic stainless steel is typically about 0.015.

As the strain rate sensitivity measurements by strain rate jumps are made when the stress-strain curve appears smooth, the results presented in Fig. 56 also indicate that a TWIP steel can have a negative strain rate sensitivity even when there are no visible deformation bands. It should be noted in this connection that the necessary condition for PLC-type instabilities reads as follows [308]:

$$S < -\Omega \cdot \sigma \tag{80}$$

Here Ω denotes an increment in strain (typically of the order of 10^{-4}) that would be produced if all mobile dislocations experienced a collective jump in strain rate corresponding to the A-B transition in the diagram in Fig. 50. The condition expressed by equation (80) means that it is not enough for the strain rate sensitivity to be negative: it has to have a sufficiently large negative value for a PLC instability to occur. The strain dependence of Ω stems from the variation of the mobile and forest dislocation density with strain. Along with the variability in behavior and the types of deformation bands, this strain dependence adds to the complexity of the DSA related plastic instabilities in TWIP steels.

Fig. 57 compares the occurrence of DSA-related serrations on the stress-strain curve of a ferritic steel and a TWIP steel. The serrations on the room temperature stress-strain curve of the TWIP steel are unexpected. The activation energy for the interstitial diffusion of carbon in γ-Fe and austenitic Fe-alloys is high, (Q = 112.5 kJ/mol), implying that long range C diffusion is very unlikely at room temperature: the time required for a carbon atom to diffuse from one interstitial site to the next covering a distance of 0.4 nm at room temperature is estimated at 1495 h (setting the pre-exponential function in the diffusion coefficient at $D_0 = 0.0156\ cm^2/$

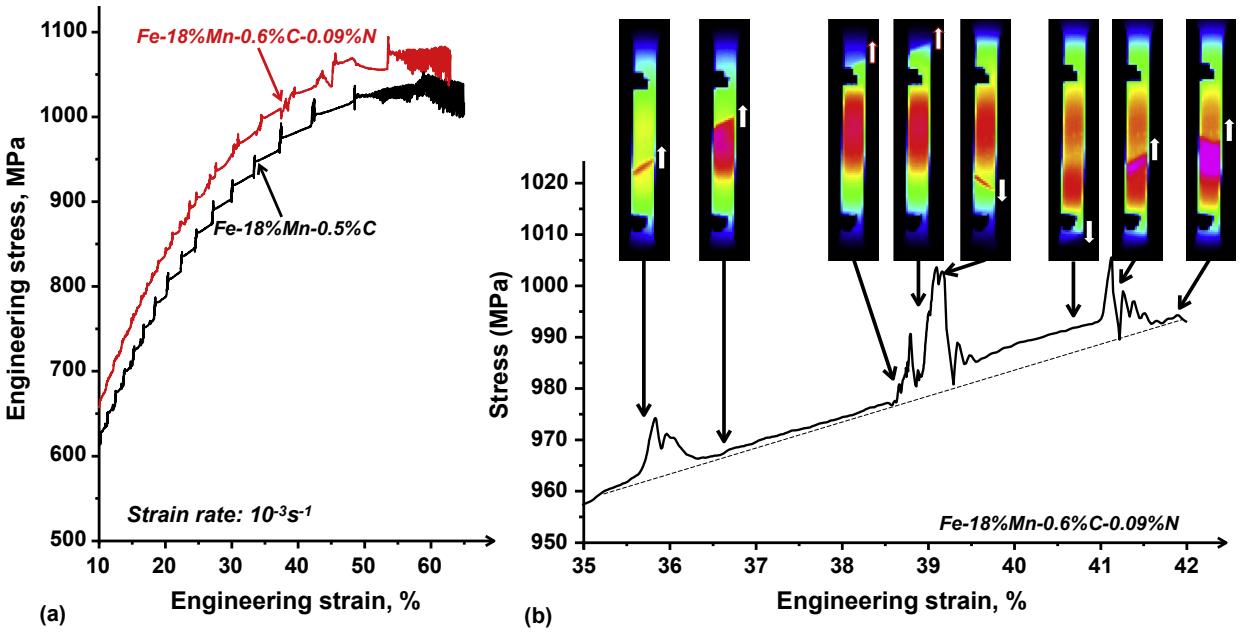

Fig. 55. (a) Effect of alloying with N on the appearance of the serrations on the stress-strain curve of TWIP steel. (b) Relation between the stress discontinuities and the events of nucleation and propagation of three type A deformation bands. The bands are nucleated inside the strain gauge length. Note the absence of plateaus between the stress spikes.

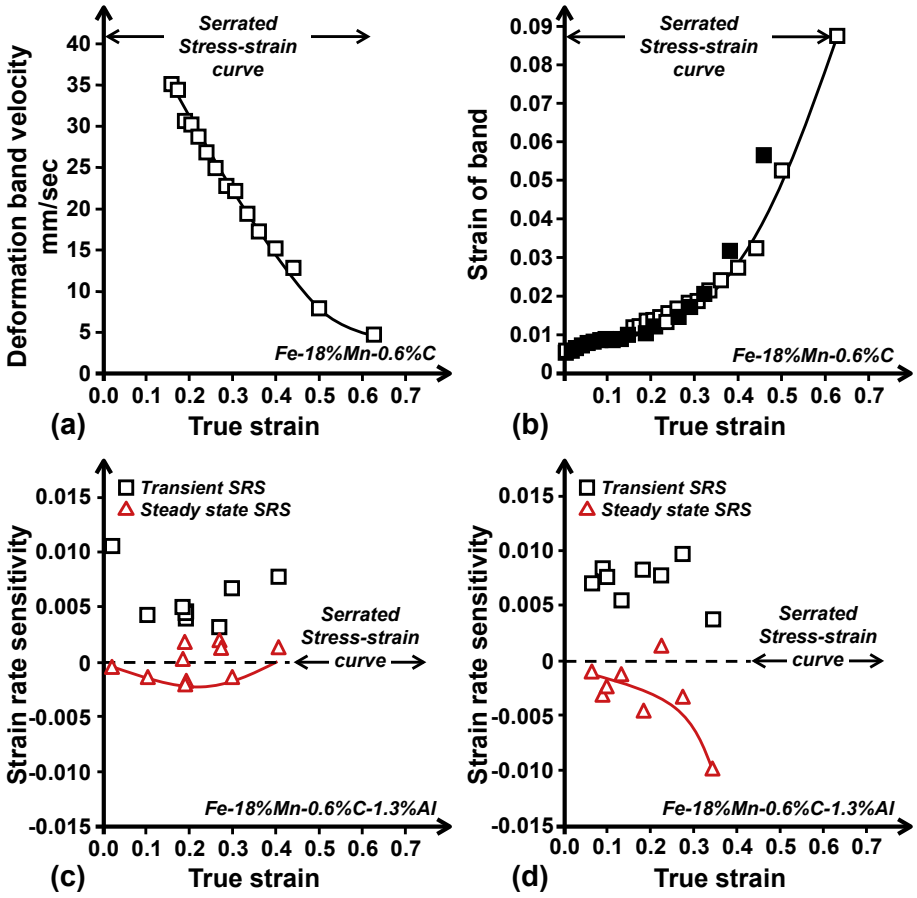

Fig. 56. Main features of the room temperature DSA in various TWIP steels. Strain dependence of (a) the velocity and (b) the strain of type A deformation bands in Fe-18%Mn-0.6%C. Strain dependence of the strain rate sensitivity (SRS) measured in (c) *upwards* and (d) *downwards* jumps in strain rate in Fe-18%Mn-0.6%C-1.3% Al. Note that the instantaneous (transient) strain rate sensitivity is always positive [301].

s). Several micro-mechanical models for DSA have therefore been proposed to relate DSA to accelerated diffusion of solute C in the presence of twinning. These models are collated in Fig. 58. Lee et al. [64] suggested that the immobile C-Mn point defect complexes interact with the stacking faults of gliding dislocations. They argue that C atoms located on the stacking fault plane will be re-located to a high energy tetrahedral position by the shear from the leading partial dislocation. The C atoms then reorient themselves by a single diffusive hop to an octahedral interstitial site out of the stacking fault plane. This process, which is associated with a local reduction of the stacking fault energy, enhances planar glide. This leads to larger dislocation pile-ups and a reduction of the critical stress for deformation twinning, as implied by the Venables [95] equation, cf. Section 5.1. Allain [66] suggested that the plastic flow instabilities and the negative strain rate sensitivity observed for C-alloyed TWIP steel were due to a dynamic interaction between solute C atoms and dislocations, which interact with deformation twins to stabilize type A deformation bands. He proposed that the C-related DSA may have an important effect on the strain hardening mechanisms, including deformation twinning. Based on earlier work by Andrews et al. [309], Allain suggested that carbon, despite an increase of γ_{isf} it causes, may still raise the rate of deformation twinning. As C increases the lattice friction, it inhibits dislocations glide and promotes the activation of deformation twinning as an alternative plasticity mechanism at higher stresses. Allain argued that the presence of solute C atoms at the core of partial dislocations also hinders the formation of constrictions on screw dislocations, thus inhibiting cross-slip and favoring slip planarity. Koyama et al. [310] observed that deformation twinning in ⟨114⟩-oriented grains was not influenced by an increase of the C content, despite an increase in γ_{isf} carbon causes. They also noted that deformation twins were formed in high-γ_{isf} Fe-18%Mn-1.2%C TWIP steel (γ_{isf} = 55 mJ/m^2), which had a serrated stress-strain curve. Both effects were explained by trapping of the trailing partial dislocations by solute C atoms when the velocities of the leading and trailing partial dislocations were significantly different. Their point was that when this occurs, an infinite separation of the partials, and hence deformation twinning, can be effected.

Short range ordering discussed in Section 2.2.5 occurs when the number of unlike atom pairs in an alloy is larger than in the random solution. Using the McLellan model [191] for the distribution of interstitial solutes in a binary substitutional alloy, Kang et al. [189] have calculated the effect of SRO on the yield strength of TWIP steel. They proposed the following equation for the yield stress:

$$\sigma_{ys}(MPa) = \sigma_i + \frac{11.3}{\sqrt{d(mm)}} + \sigma_{SRO} = 90 + \frac{11.3}{\sqrt{d(mm)}} + M \cdot \frac{E_r - E_{SRO}}{b^3} \tag{81}$$

Here σ_i is the Peierls lattice friction stress, d the average grain size, and b the magnitude of the dislocation Burgers vector. The SRO contribution to stress, σ_{SRO}, was expressed in terms of E_r and E_{SRO} - the energy per atom in the alloy with a fully random C distribution and with short range order, respectively. *Ab initio* values for E_r and E_{SRO} were obtained by computing the binding energy of C to three types of ternary octahedral cell configurations, *i.e.* $Fe_{6-x}Mn_xC_1$, Fe_{6-}

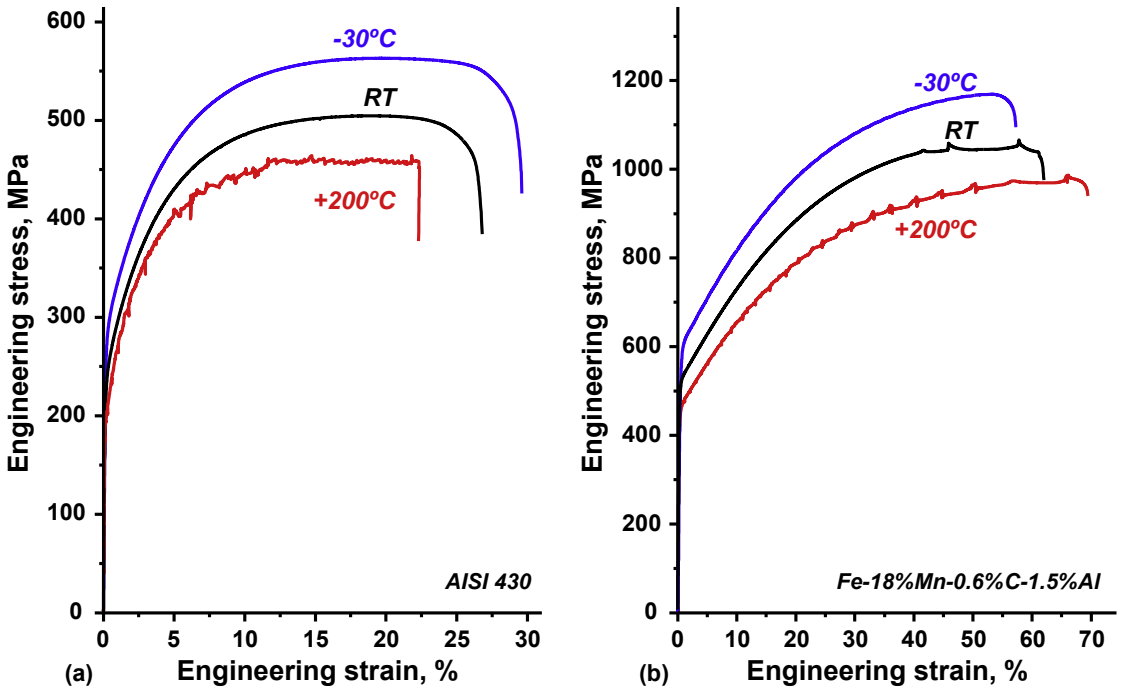

Fig. 57. Illustration of the difference of the effect of DSA on the deformation curves of (a) C-alloyed ferritic stainless steel AISI 430 and (b) C-alloyed TWIP steel Fe-18%Mn-0.6%C-1.5%Al.

$_xAl_xC_1$ and $Mn_{6-x}Al_xC_1$, in which the C atom occupies the center position. The contribution of SRO to the yield strength calculated in this way was considerable: approximately 100 MPa and 200 MPa for Fe-(15–25)%Al-0.6%C and Fe-(15–25)%Al-0.6%C-3%Al TWIP steel, respectively.

The effect of DSA on the mechanical performance, notably strength and ductility, is of primary interest in the context of the present treatise. A fortunate property that distinguishes TWIP steels from non-TWIP alloys is that the occurrence of DSA in TWIP steels does not lead to a reduction of their ductility [22,305]. This unusual feature is also illustrated in Fig. 57 which compares the temperature dependence of the flow stress of a ferritic steel and a TWIP steel. Whereas there is a reduction of tensile elongation associated with the occurrence of serrations on the stress-strain curve in the case of the ferritic steel, the elongation is significantly larger for the serrated stress-strain curve of the TWIP steel.

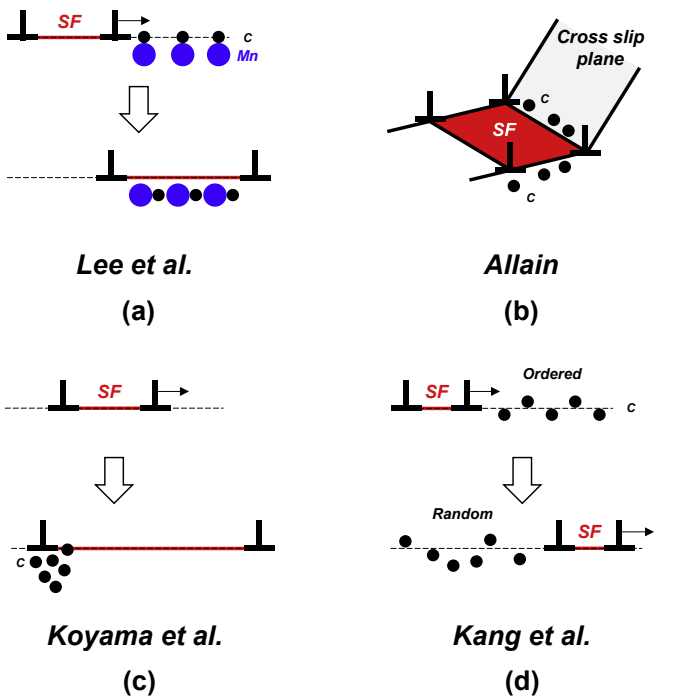

Fig. 58. Schematics of the micro-mechanical mechanism of DSA in C-alloyed TWIP steel according to (a) Lee et al. [64], (b) Allain [72], (c) Koyama et al. [310], and (d) Kang et al. [189].

Similar to common alloys exhibiting DSA, an increase in mechanical strength due to dynamic strain aging can also be expected for TWIP steels [311]. Kim et al. [18] showed, however, that this strength increase is rather small, approximately 20 MPa. The relation between DSA and strain hardening is complex. Renard et al. [305] reported such a correlation. They observed a pronounced increase in strain hardening when testing a TWIP steel at 170 °C, which they relate to an observed reduction of the number of serrations on the stress-strain curve. This report appears to be in disagreement with the deformation curves shown in Fig. 59. Indeed, the room temperature data presented therein indicates that the addition of Al to a Fe-18%Mn-0.6%C TWIP steel results in a decrease of the strain hardening and a pronounced delay with the onset of serrations. Both features are related to an increase of γ_{isf} by alloying with Al, which has two effects: (a) inhibition of deformation twinning, and (b) a weakening of interaction between carbon atoms and dislocations temporarily arrested at localized obstacles. The latter is associated with a decrease of the stacking fault width resulting in a reduced interaction, if this interaction involves reorientation of C-Mn complexes in the stacking fault plane.

While dynamic strain aging has been the subject of numerous publications, little is know about the static strain aging of TWIP steel. Allain et al. [312] carried out room temperature stress relaxation tests on a Fe-22%Mn-0.6%C TWIP steel micro-alloyed with V. They observed a yield point phenomenon and an associated yield plateau upon reloading and ascribed these effects to

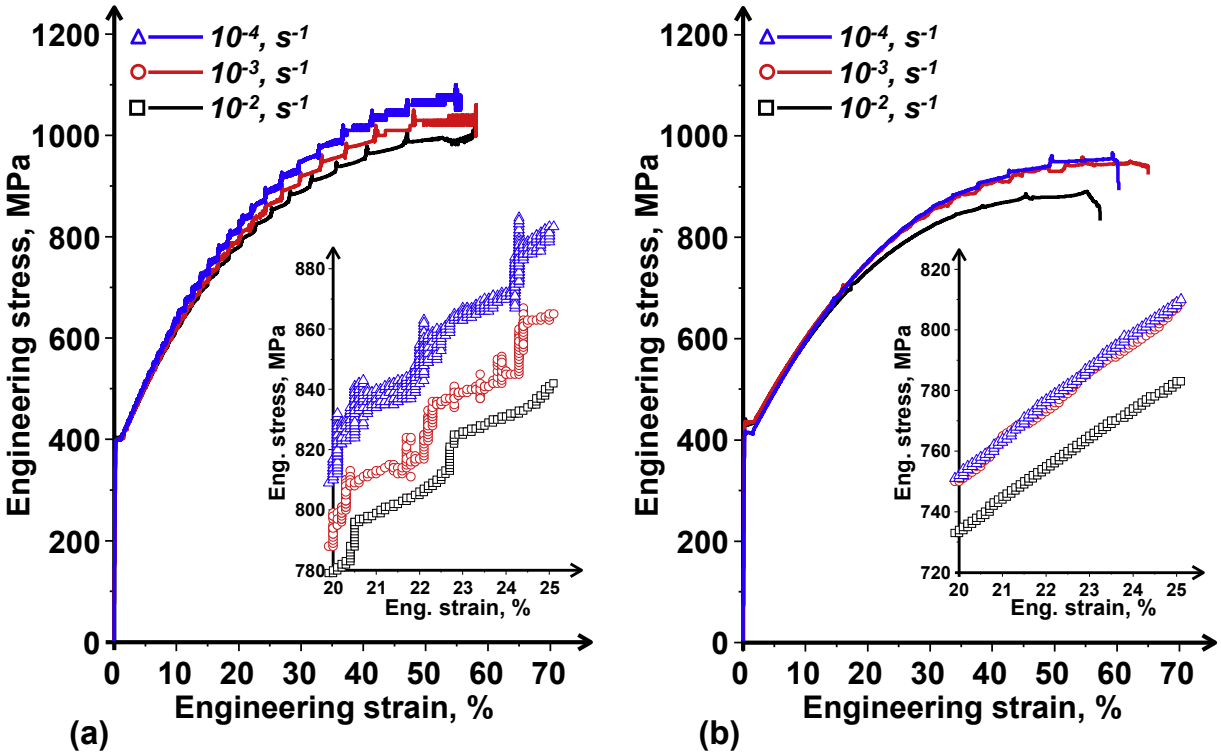

Fig. 59. Stress-strain curves for (a) Al-free Fe-18%Mn-0.6%C TWIP steel, and (b) Al-added Fe-18%Mn-0.6%C-1.5% Al TWIP steel. Both steels exhibit a negative strain rate sensitivity of the flow stress.Type A serrations, characterized by sharp spikes in flow stress followed by stress plateaus, are present on deformation curves of both steels. Whereas type A serrations appear on the stress-strain curve of the Al-free TWIP steel from the start of the plastic deformation, a large latent strain is required for serrations to set in for the case of the Al-added TWIP steel.

aging by segregation of C atoms to dislocations during the stress relaxation test. In addition, stress relaxation triggers the occurrence of serrations on the deformation curve. Based on an analysis of these experiments, Allain et al. argue that not only may twins be responsible for the high strain hardening rate observed for TWIP steels, but they could also be responsible for pronounced plastic instabilities. They base their view on the consideration that deformation twins act as stress concentrators able to emit dislocations which hinder the propagation of localized deformation bands. The presence of twins may, however, be not as important as envisaged by Allain et al. Fig. 60 provides clear evidence for static strain aging at room temperature in both Al-free and Al-alloyed Fe-18%Mn-0.6%C TWIP. Since the yield drop phenomenon was observed in conditions where twinning did not occur, it is likely that the static strain aging is due to an interaction between dislocations and solutes in the initial as-annealed microstructure. Tsuji et al. [313] also reported that TWIP steel with a grain size less than 2 μm exhibited a yield phenomenon, similar to ultra-fine grained (grain size <1 μm) fcc and bcc metals, but they did not provide an explanation for their observation.

Kang et al. [189] suggested that the observed yield phenomenon can be rationalized in terms of SRO. The idea was that yielding is caused by the disruption of the SRO by the passage of dislocations, and that this would result in a softening effect manifesting itself in a yield drop. The data shown in Fig. 60 also proves that static aging occurs during stress relaxation test, as reflected in the stress overshoots and yield drops observed upon reloading. Very often the strain rate, as observed in strain *vs.* time plots, is temporarily lower than the imposed strain rate upon reloading. This is evidence for local deformation band formation in the part of the sample outside the range of the strain gauge.

7. Recovery annealing

Recovery annealing is an unusual microstructure optimization process, consisting in a partial recrystallization annealing treatment in the temperature range of 575–625 °C. It is effective for the production of TWIP steels with a wide range of strength-ductility combinations. The retention of the deformation twins in cold deformed TWIP steel during recovery annealing is utilized to obtain a microstructure that provides a high yield strength and an appreciable tensile elongation. Through a suitable combination of cold rolling and annealing conditions (temperature and time) it is possible to tailor the mechanical properties of recovery annealed TWIP steel over a wide range. The retained twin boundaries result in a higher yield strength after recovery annealing as compared to fully recrystallized TWIP steel. The recovery process also significantly improves the ductility over that of the cold-rolled state. According to Dao et al. [298] the introduction of a large number of nanoscale twin boundaries leads to a high strength, while retaining ductility.

Kang et al. [314] studied the recrystallization of 60% cold rolled Fe-18%Mn-0.6%C-1.5%Al TWIP steel in the temperature range of 550°C-1100 °C. While the dislocation density was reduced during a recovery annealing at 550 °C, deformation twins were thermally stable. The static recrystallization set in at 600 °C and was complete at 700 °C. The recrystallized grains had an average size of 2.38 μm. The increase of the yield strength and tensile strength observed after annealing in the temperature range of 700°C-800 °C was due to M_3C carbide precipitation. At 840 °C, grain coarsening occurred as a result of the dissolution of the M_3C carbides. During recovery annealing of a cold rolled TWIP steel below 600 °C a low dislocation density microstructure was obtained which still contained

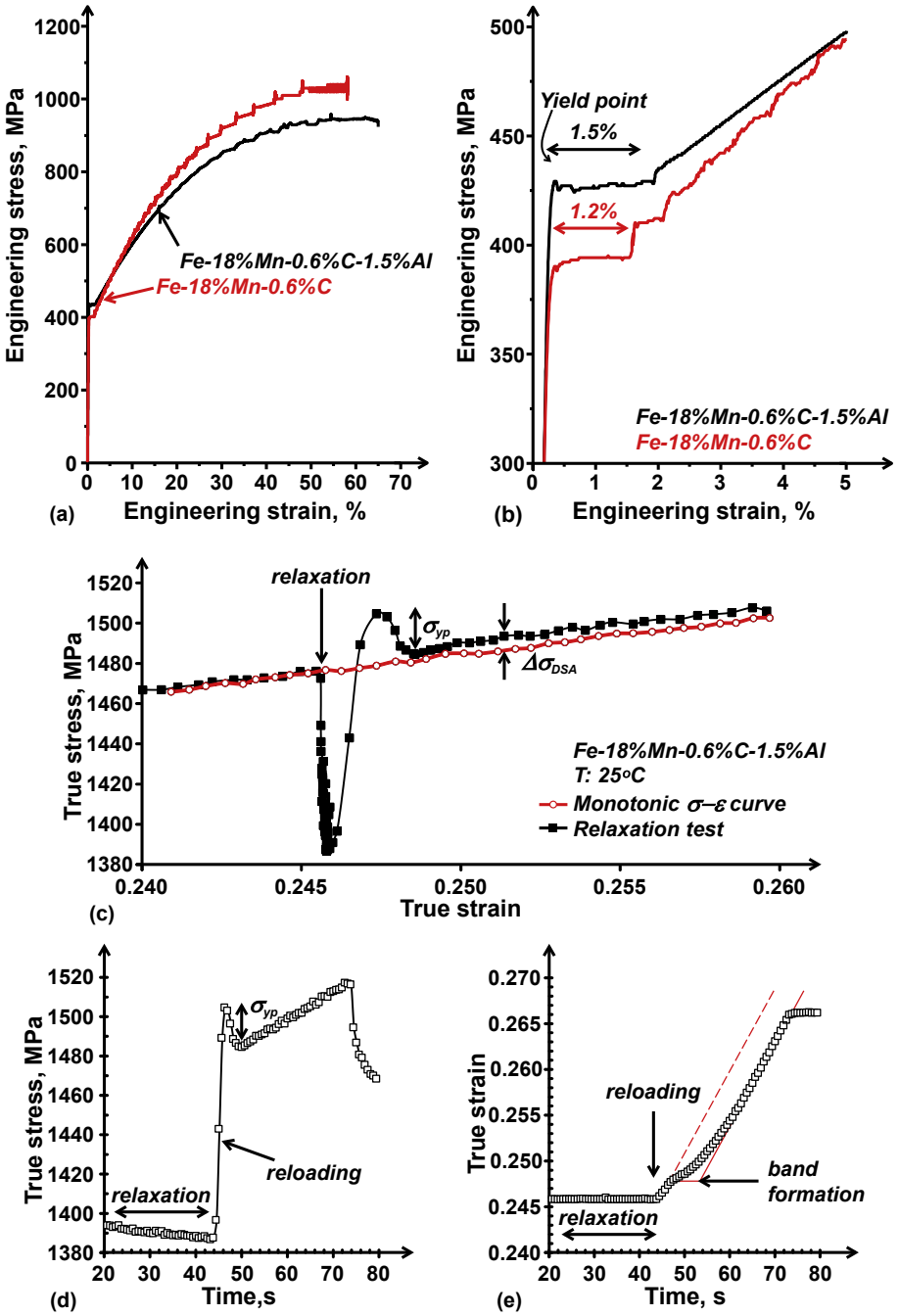

Fig. 60. (a) Engineering stress-strain curves for Al-free and Al-alloyed Fe-18%Mn-0.6%C TWIP steel aged at room temperature under stress relaxation conditions. (b) Magnification of the elasto-plastic transition region of (a), showing that both steels are susceptible to static strain aging. A yield drop phenomenon is seen on the stress-strain curves for both steels. A distinct stress overshoot and a yield drop are visible on the curve for the Al-alloyed Fe-18%Mn-0.6%C TWIP steel. (c) Comparison of a monotonic tensile tes and a stress relaxation test. A stress overshoot followed by a yield drop appears upon reloading after the stress relaxation test, and dynamic strain aging results in a small increment, $\Delta\sigma_{DSA}$, in the flow stress. (c) True stress *vs.* time plot for the reloading between two stress relaxation episodes showing the yield point resulting from aging during stress relaxation. (d) Corresponding true strain *vs.* time plot showing evidence for localization at the start of the reloading. As the localized deformation band is formed outside of the strain gauge range, the measured strain rate is initially lower than the imposed strain rate [216].

nanoscale deformation twins.

Dini et al. [315] produced a sub-micron grained microstructure in Fe-31%Mn-3%Al-3%Si TWIP steel by a partial recrystallization annealing treatment in the temperature range of 575–625 °C. Their work provided a demonstration that an excellent tensile strength-ductility balance can be achieved through grain refinement. The partially recrystallized 80%-cold rolled TWIP steel annealed at 575 °C had a yield strength of about 1 GPa and a total elongation close to 30%. Similarly, Bouaziz et al. [316] obtained a nano-twinned Fe-22%Mn-0.6%C TWIP steel by recovery annealing for 3600 s at 500 °C aimed at reducing the dislocation density without changing the nano-twinned structure induced by prior cold rolling. Their recovery annealed TWIP steel had a yield strength of 1200 MPa, a tensile strength of approximately 1700 MPa and a uniform elongation of 8%.

Haase et al. [268,317–319] used the evolution of the crystallographic texture during recovery annealing of cold worked Fe-23%Mn-0.3%C-1.5%Al TWIP steel at 550 °C and 630 °C. Their work

was aimed at optimizing the thermomechanical processing of the steel. Texture analysis revealed that the highest twin density was obtained after a 50% thickness reduction. They observed a slight texture sharpening during recovery, which was indicated by an increased intensity of the deformation texture component. This was followed by randomization of texture during primary recrystallization, as indicated by an increase of the volume fraction of randomly oriented grains and a decrease of the intensity of the main texture components induced by cold rolling. The optimal annealing time was at the transition between the texture sharpening due to recovery and texture randomization during recrystallization. The recrystallized volume fraction after recovery annealing was found to be less than 10%. In a separate study by the same research group the mechanical properties of the recovery annealed Fe-17%Mn-0.6%C-1.5%Al steel were studied in addition to those of Fe-23%Mn-0.3%C-1.5%Al [319]. They reported that the high yield strength retained after recovery annealing resulted in a significant increase of the energy absorption capacity of the steel and its superior crashworthiness as compared to the fully recrystallized state. They also demonstrated by means of cross-shaped cup drawing experiments that a considerable ductility was regained after a recovery annealing treatment.

8. TWIP effect during cyclic deformation

The fatigue performance of TWIP steels is generally considered to be excellent, and superior to the fatigue performance of austenitic stainless steels such as AISI 301 and 316 [320]. Three specific characteristics of TWIP steel, *viz.* a low magnitude of γ_{isf}, which inhibits cross slip, a pronounced glide planarity, and the occurrence of deformation twinning, are known to influence the fatigue properties in both high cycle and low cycle fatigue of fcc alloys in general. A low γ_{isf} generally results in a larger number of cycles to fracture, *i.e.* in an improvement of fatigue life over that of high γ_{isf} materials that deform by dislocation glide only. The effect of γ_{isf} comes to bearing in stage I of fatigue, during crack initiation and growth. Crack growth in stage II is unaffected by γ_{isf}. Crack growth in stage I is transgranular, probably along twins which act as easy paths for crack propagation, similar to persistent slip bands.

Although fatigue testing involves very large accumulated strains as compared to conventional tensile testing, the influence of deformation twinning on the high cycle fatigue (HCF) properties appears to be minor. Niendorf et al. [320] studied the low cycle fatigue (LCF) properties of pre-strained Fe-22%Mn-0.52%C-0.25%V-0.25%Si-0.20%Cr TWIP steel. The effect of pre-straining on the fatigue life of TWIP steels is shown in Fig. 61. The fatigue limit defined as the stress amplitude corresponding to a fatigue life in excess of 2×10^6 cycles is seen to be increased considerably by pre-straining prior to the fatigue test. The cyclic stress hardening behaviour of a Fe-22%Mn-0.6%C-0.3%V reported by Hamada et al. is also illustrated in Fig. 61 [321]. Similar to the commonly observed correlation between the fatigue limit and the tensile strength of metallic materials [322], the ratio of the fatigue limit to the tensile strength of the TWIP steels investigated was typically in the range of 0.4–0.6. Independently of the composition, the fatigue limit of these steels was approximately 400 MPa [321]. The deformation twins formed during pre-straining and the nucleation of new twins during cyclic deformation provided a strength increase which is favorable in LCF conditions, as the extra hardening reduces fatigue damage. In the absence of pre-strain, no cyclic deformation-induced twins were observed, while existing twins were found to grow. A drop in the dislocation density below the level measured in the as-received material was observed in the fatigued one. This resulted in plastic instability and cyclic softening. Hamada et al. also reported a pronounced Bauschinger effect during fatigue testing. This is tantamount to a distinct tension-compression asymmetry and a build-

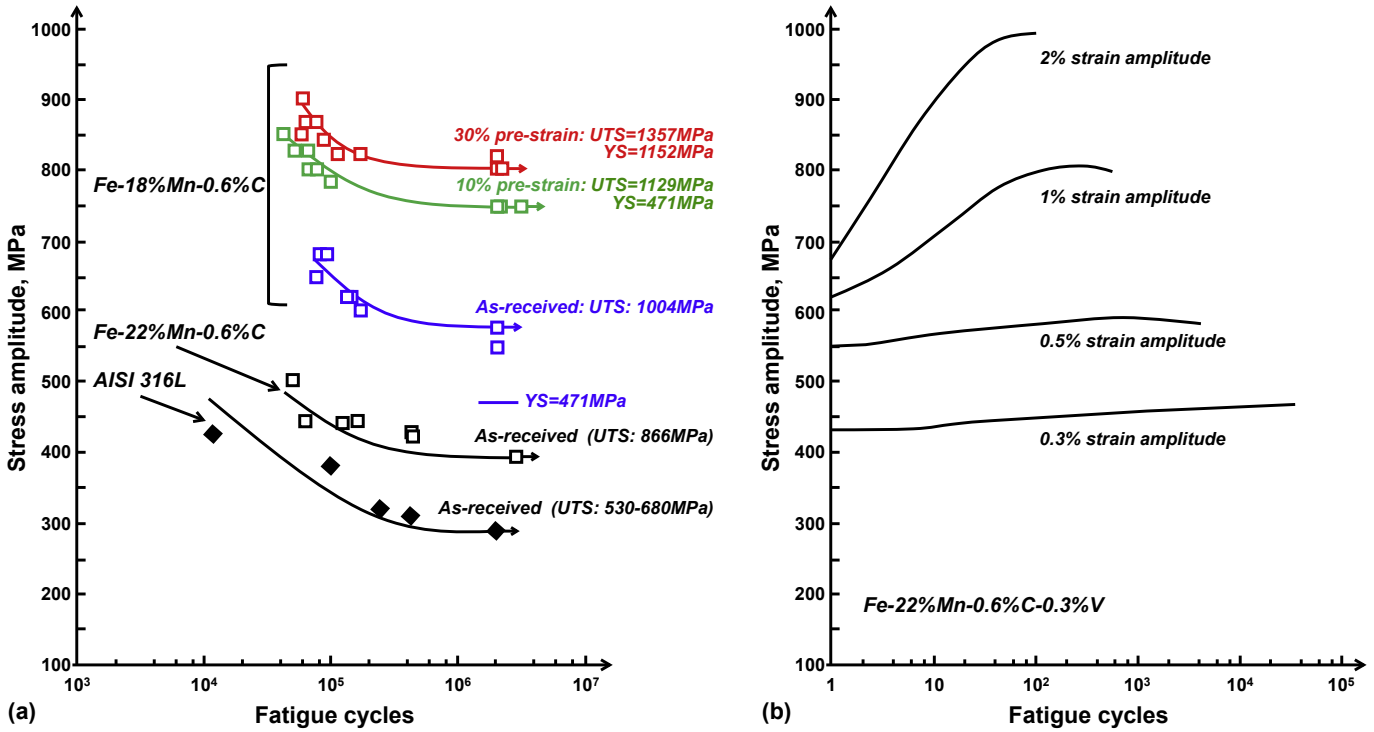

Fig. 61. (a) High cycle fatigue curves for TWIP steel, illustrating the positive effect of pre-strain on fatigue endurance. Data for AISI 316L and Fe-22%Mn-0.6%C TWIP steel is from Hamada et al. [333], for Fe-18%Mn-0.6%C TWIP steel is from Kim et al. [326]. (b) Strain amplitude dependence of the stress amplitude versus number of cycles for a V-microalloyed Fe-22%Mn-0.6%C-0.3%V TWIP steel, illustrating the cyclic hardening behavior of TWIP steel. Data taken from Hamada et al. [327]. The fatigue test conditions are R = −1 (symmetrical tension-compression loading) and a frequency of 1 Hz.

up of a positive mean stress.

Hamada et al. [323] studied the HCF properties, the fatigue strength, the crack initiation sites and the crack propagation paths in three TWIP steels with γ_{isf} of 19, 23 and 26 mJ/m^2. No deformation twins were formed in the three steels during the cyclic loading. They concluded therefore that the TWIP effect had no effect on the HCF properties. The stress amplitude vs. the number of cycles curves are independent of γ_{isf}. As mentioned above, the fatigue limit of the three TWIP steels, approximately 400 MPa, is considerably higher than that of austenitic stainless steels. The ratio of the fatigue limit to tensile strength is, however, similar to that for austenitic stainless steels, i.e. in the range of 0.42–0.48. In the HCF regime fatigue cracks were predominantly initiated at or near grain boundaries due to the local elastic strain incompatibilities there and the intrinsic weakness of the grain boundaries in Mn-alloyed steels. Although the cracks are nucleated at grain boundaries, their propagation is mainly transgranular. The nature of the crack propagation path was determined as 61% transgranular, 18% intergranular, 11% along twins and 9% along slip bands.

Grain refinement results in a significant improvement of the fatigue strength. This was demonstrated by Karjalainen et al. [324] who showed that the fatigue limit of a Fe-16.4%Mn-0.29%C-1.54%Al TWIP steel rose from 400 MPa to 560 MPa upon grain size reduction from 35 μm to 4.5 μm. The fatigue limit of TWIP steels was also typically higher than the yield stress. Using atomic force microscopy, Hamada et al. [323] were able to demonstrate that surface features of fatigued samples were not associated with deformation twins, but are rather extrusion-intrusion profiles due to bands of intense dislocation slip. This confirmed the already mentioned absence of deformation twinning during cyclic loading reported by Niendorf et al. [320] and Hamada et al. [323]. However, the observation that deformation twinning does not take place during fatigue testing and the conclusion that deformation twinning does not influence the fatigue properties of TWIP steels was questioned by Karjalainen et al. [324] who did observe 150–200 nm wide deformation twins in fatigued Fe-16.4%Mn-0.29%C-1.54%Al TWIP steel with a 35 μm grain size by TEM. They noted that cracks were initiated early in the fatigue life, and that the crack growth rate was low. These observations were supported by the results of Niendorf et al. [325] on the effect of twinning on the crack grow behavior of Fe-22%Mn-0.52%C-0.25%V-0.25%Si-0.20%Cr TWIP steel in miniature compact tension specimens. According to Niendorf et al., twinning was observed in the plastic zone, even though their density was low. They report a low crack growth rate, *da/dN*, in the Paris-law regime:

$$\frac{da}{dN}(mm/cycle) = C \cdot \Delta K^m = 2 \cdot 10^{-8} \cdot \Delta K^{2.7} \qquad (82)$$

Here ΔK is the stress intensity, in MPa$\sqrt{\text{m}}$ and C is a constant coefficient in the Paris law. The parameter values in Eq. (82) are given for $R = \sigma_{min}/\sigma_{max} = 0.1$, *i.e.* cyclic deformation in the tension range.

The effect of pre-straining on the fatigue performance of Fe-18%Mn-0.6%C-0.2%Si TWIP steel was studied by Kim et al. [326]. Pre-straining was effected by cold rolling with a thickness reduction of 10% and 30%. This resulted in a considerable increase of tensile strength and a decrease of the total elongation, from 78% in the unformed condition to 20% after a cold rolling to 30% thickness reduction. Both strain-controlled LCF tests and stress-controlled HCF tests were carried out. A significant reduction of the LCF life with increasing pre-strain was found. The authors argued that deformation twins generated during pre-straining reduce the number of twins formed in the course of cyclic deformation. They also suggested that the twin boundaries generated during pre-straining can act as early crack nucleation sites under cyclic loading. These conclusions are in accord with the above mentioned principal observations by other authors indicating that no deformation twins are formed under fatigue loading and that TWIP steels have superior LCF properties. Since, in the spirit of the mentioned correlation, the HCF properties are controlled by the tensile strength, the HCF life of pre-strained TWIP steels is improved with increasing amount of pre-straining.

The effect of *cyclic* pre-straining on the mechanical properties of a Fe-22%Mn-0.6%C-0.3%V TWIP steel were investigated by Hamada et al. [327]. Their original aim was to use cyclic plastic deformation as a way to increase the yield strength. The cyclic pre-straining consisted in fully reversed strain-controlled cycling at different strain amplitudes until the saturation stage was reached. By that, the yield strength was increased without much loss in elongation. The cyclic pre-straining resulted in the formation of a dislocation cell structure with very few mechanical twins. The dislocation arrangement is mainly determined by the prevalent slip mode, *viz.* planar versus wavy dislocation glide. In the case of planar glide, glide plane softening causes dislocations to follow the leading dislocation on its glide plane. This planar glide behavior has been related to a low stacking fault energy, γ_{isf}, short range ordering, and lattice friction effects. A characteristic dislocation pattern consists of regions containing a high density of parallel edge dislocations, separated by low dislocation density regions in which screw dislocation segments glide. The frequent, uncorrelated cross-slip events are the cause of wavy glide, and the typical dislocation arrangement has a cell structure. Karjalainen et al. [324] report the formation of a rough labyrinth or a vein-like dislocation structure in Fe-16.4%Mn-0.29%C-1.54%Al TWIP steel tested in high cycle bending fatigue.

9. High strain rate behavior of TWIP steels

High strain rate properties are of considerable technical interest, especially for automotive applications for passenger safety-related parts where high impact energy absorption is at a premium. Fig. 62 illustrates the results of axial crush tests carried out on various advanced high strength steel grades. The TWIP steel evidently stands out as the material with a superior crashworthiness.

Using a split Hopkinson pressure bar, Ha et al. studied the microstructure of Fe-22%Mn-0.4%C TWIP steel after high strain rate deformation at 10^3 s^{-1} [328], while Curtze and Kuokkala [127] employed the same method to investigate Fe-(25–28)%Mn-1.6%Al-0.08%C TWIP steel. Both groups observed an appreciable increase of tensile strength at high strain rates, e.g. to 2.265 GPa in the study by Ha et al., and an increasing strain hardening up to a true strain of approximately 0.19. Ha et al. report that the dynamic loading leads to the formation of nanostructured austenite which appears random at low magnification. At high magnification the microstructure exhibits nano scale features, such as 20–30 nm sized grains which are twin-related to the neighboring grains in their orientation. According to Ha et al. [328] the formation of twin-matrix lamellae within the grains occurs only in the early stages of the high strain rate deformation. The adiabatic heating of the sample at larger strains has two consequences: an increase of γ_{isf}, which inhibits twin formation, and dynamic recovery. The grain fragmentation resulting from interactions of twins with grain boundaries and concurrent dynamic recovery is believed to generate the nano-structured austenite observed.

10. Fracture of TWIP steels

Due to their low yield strength and large ductility, the failure mode of TWIP steel is usually ductile. The negative strain rate sensitivity makes diffuse necking strain small, and fast fracture is

Please cite this article in press as: B.C. De Cooman, et al., Twinning-induced plasticity (TWIP) steels, Acta Materialia (2017), http://dx.doi.org/10.1016/j.actamat.2017.06.046

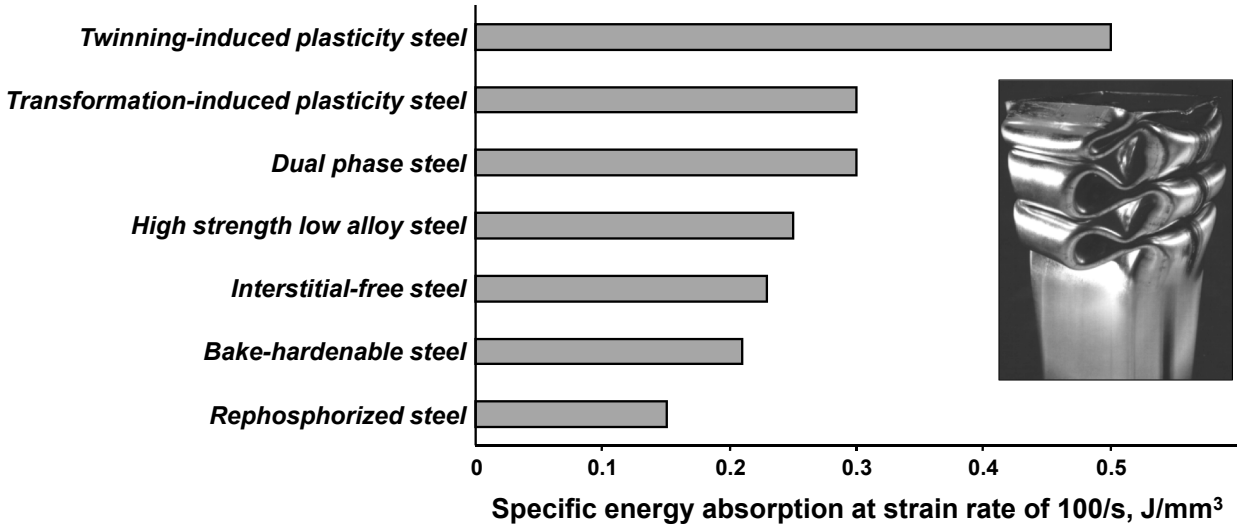

Fig. 62. A qualitative comparison of the crash performance properties of various high strength automotive steel grades obtained in axial crush tests.

observed once necking is initiated. Although not much work has been done in this area, fracture of TWIP steel has been given considerable attention in connection to three phenomena (a) edge fracture in hole expansion, (b) liquid metal-induced embrittlement and (c) the hydrogen-related delayed fracture.

In the cited work by Hamada et al. [329] the fracture surface of Fe-25%Mn and Fe-25%Mn-3%Al TWIP steel after room temperature tensile deformation was analyzed. Despite the presence of strain-induced martensite, the appearance of the fracture surfaces of these steels was consistent with a ductile fracture by microvoid coalescence. Specifically, dimpled fracture surfaces with inclusions visible inside some of the dimples were observed. The SEM-EDS analysis revealed that these were nonmetallic inclusions such as (Fe,Mn)O, Al_2O_3 and MnS, in agreement with the observation of endogenous inclusions in Fe-Mn alloys by Tomota et al. [330], and in TWIP steel by Allain [71] and Gigacher et al. [331]. These inclusions are less deformable than austenite. They are therefore prone to fracture. Alternatively, strain gradients which develop at the matrix/inclusion interface can result in interfacial decohesion. The coalescence of cavities formed by these processes can result in fracture prior to necking. Fig. 63 shows the appearance of a fracture surface for Fe-18%Mn-0.6%C-1.5%Al TWIP steel after tensile straining. The image shows equiaxed dimples associated with a small particle, which plays a key role as a microvoid initiation site in the course of ductile fracture. SEM-EDS analysis results showed that the inclusions could also be AlN or TiN precipitates. The appearance of the fracture surface is identical to that observed by Hamada et al. [329]. Premature ductile fracture of TWIP steels, with little or no post-uniform necking, was originally attributed to large inclusions or smaller precipitates. However, the prevalent current view is that it is a negative strain rate sensitivity of the flow stress, found in certain TWIP steels, which is a key factor determining their fracture behavior.

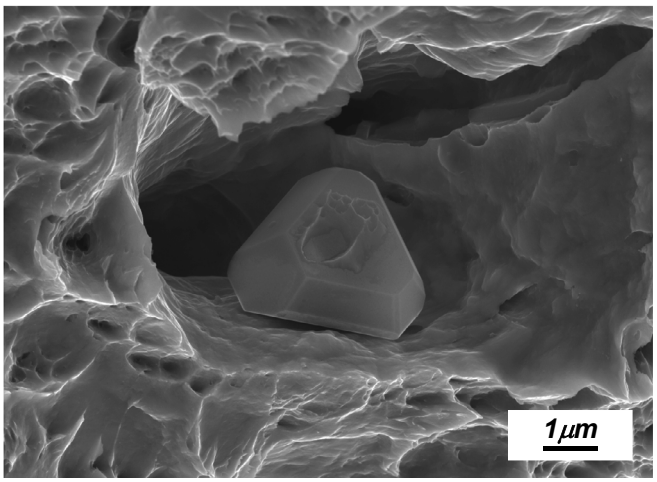

Fig. 63. Fracture surface of Fe-18%Mn-0.6%C-1.5%Al TWIP steel after tensile straining. The dimples seen in the micrograph are indicative of ductile fracture by micro-void coalescence. Note an AlN single crystal precipitate at which a larger void is believed to have nucleated.

11. Fracture in hole expansion

Cut edge stretchability is an important aspect of sheet formability. Whereas the press forming performance of TWIP steels is excellent due to its high strain hardening capability, the lower normal anisotropy, represented by the r-value ($r_{0°} = 0.79$, $r_{45°} = 1.13$, $r_{90°} = 1.28$), and the negative strain rate sensitivity of the flow stress of TWIP steels are detrimental to stretchability. Collectively, these factors result in premature ductile fracture during stretch-flanging (*i.e.* hole expansion) when the initial hole is made using a technique that leads to a considerable prior deformation of the hole edge, such as hole punching [300]. This behavior was analyzed in detail using an advanced *in situ* method that permits local measurement of the principal strains and the temperature. The strain distribution analysis revealed that the hole edge deformation in the deep drawing mode was similar to uniaxial tensile deformation. Fig. 64 compares the hole expansion performance of an interstitial free (IF) steel and a TWIP steel. Edge cracking was ductile in both cases. Outspokenly ductile fracture at the hole edge occurred after appreciable edge thinning and localized necking in the case of the IF steel. By contrast, in the case of the TWIP steel a single crack leading to catastrophic failure occurred. In both cases the fracture surface exhibited shallow dimples, which are indicative of ductile fracture by micro-void coalescence.

12. Hydrogen-delayed fracture

Hydrogen has been reported to reduce the stacking fault energy

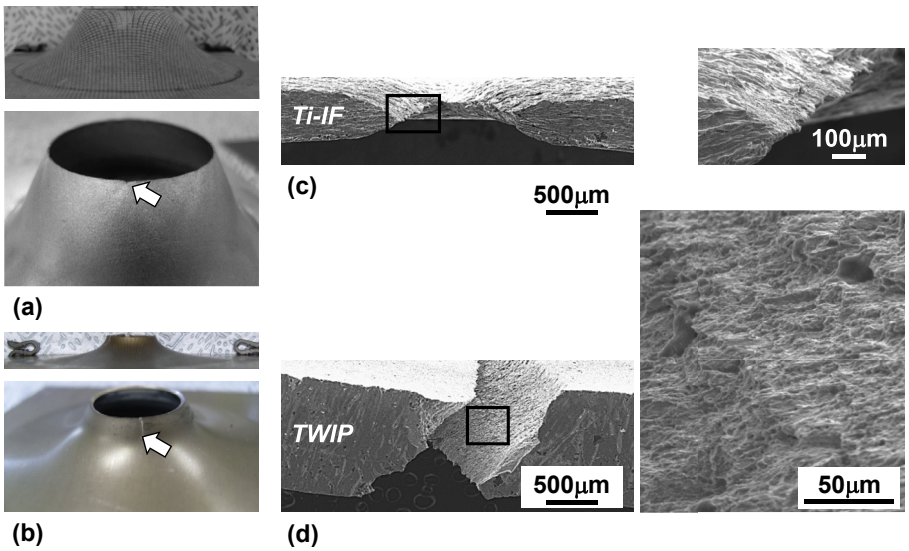

Fig. 64. Hole expansion tests for (a) IF steel and (b) TWIP steel. The arrows indicate the sites of crack initiation. (c) Edge crack appearance for IF steel, showing extensive thinning prior to rupture. (d) Edge crack appearance for TWIP steel, showing the absence of diffuse necking prior to shear rupture. The dimpled appearance of the fracture surface provides evidence for ductile fracture by micro-void coalescence.

of austenitic steels [332,333]. This effect promotes the deformation-induced ε-martensitic transformation [334,335] and deformation twinning [336,337], resulting in a marked change in stress-strain response. When captured by a dislocation in an fcc metal or alloy, a hydrogen atom affects the dislocation mobility by decreasing the activation barrier to dislocation motion. At temperatures slightly below room temperature, H atoms can also form atmospheres around dislocations. Hydrogen has been reported to enhance planar glide in fcc metals and alloys. Two reasons have been put forward to explain this effect: (a) H has an effect on the character of a dislocation and (b) H reduces γ_{isf}. Due to these mechanisms, H stabilizes edge dislocation segments and inhibits cross-slip, thus promoting planar glide. The reduction of γ_{isf} caused by H appears to be considerable, in the range of 20–40%. It is related to a change in the local electronic structure of the stacking fault in the presence of H. As a result of the H-Fe interaction via the Fe 4s and H 1s orbitals, the Fe-Fe bond strength is reduced by about 30%, making the crystal structure more deformable locally. The mentioned effects of low γ_{isf}, i.e. limited cross-slip and enhanced planar glide, are essential for obtaining an increase in strain hardening by reducing the dislocation recovery rate. It is still unclear whether the effect of H is due to the presence of hydrogen atoms in the stress field of a dislocation or through a decrease of the shear modulus they induce in fcc alloys. The modulus effect should reduce the shear stress for dislocation nucleation and motion. H also contributes to the nucleation of martensite by stabilizing the bcc and the hcp martensitic phases in fcc austenitic steel. Both the hydrostatic lattice distortion and the formation of H-H pairs by H charging have been reported to cause the stress-induced martensitic transformation. The formation of H-H pairs has been reported to stabilize the hcp lattice, because the hcp crystal structure allows for the formation of H-H pairs by H atoms located in opposite octahedral sites.

Fig. 65 illustrates the cracking of a deep drawn cup of Fe-22%

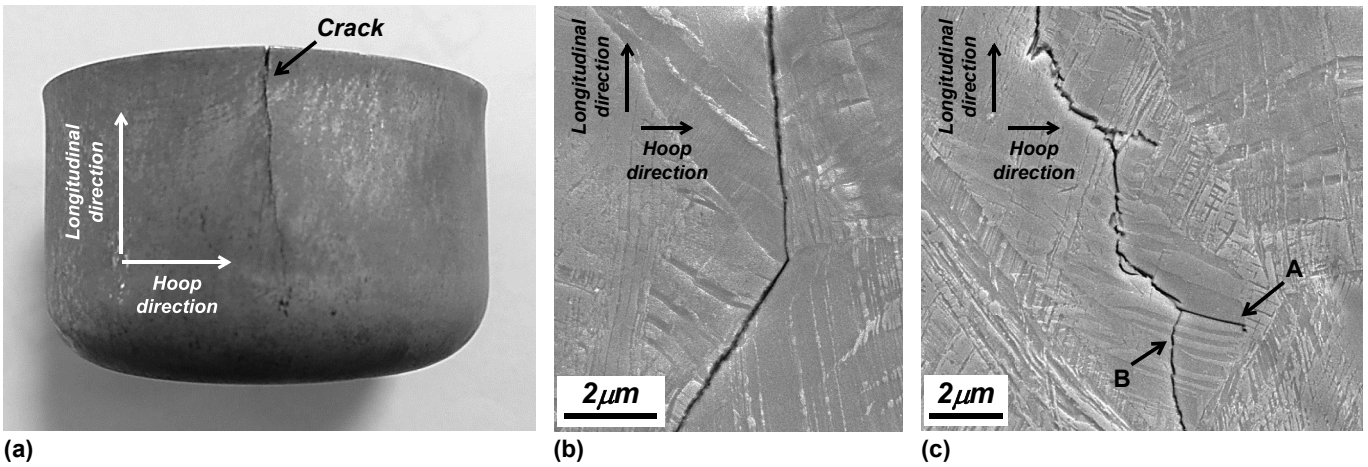

Fig. 65. (a) Large longitudinal crack on a deep drawn cup made from Fe-17%Mn-0.4%C-1.3%Al TWIP steel (grain size = 15 μm; γ_{isf} = 17 mJ/m^2) H-charged for 32 h at room temperature. (b) Intergranular crack. (c) Complex transgranular crack showing crack propagation (A) parallel to the twin/matrix interface and (B) across deformation twins. Note that the cracks shown in (b) and (c) are two examples of the much finer cracks present on the outer side of the sample shown in (a). TEM analysis of samples taken from within the cup wall reveal the presence of ε-martensite; magnetic measurements also showed the presence of 0.5–1.5 vol percent of α'-martensite.

Please cite this article in press as: B.C. De Cooman, et al., Twinning-induced plasticity (TWIP) steels, Acta Materialia (2017), http://dx.doi.org/10.1016/j.actamat.2017.06.046

Mn-0.6%C TWIP steel shortly after it broke spontaneously during a hydrogen-charging test. Both intergranular and transgranular cracks are present on the outer surface in addition to a singular major crack. The transgranular cracks propagate through deformation twins and along twin/matrix interface boundaries. Although the H-delayed fracture of deep drawn cups is quite dramatic, the effect of H pre-charging on the tensile properties of TWIP steels is generally insignificant, because the hydrogen diffusion in the bulk of the material at room temperature is almost negligible. H diffusion in fcc γ-Fe is considerably slower than in bcc Fe, by a factor of approximately 10^6 [338]. This low H diffusivity implies that the testing of the sensitivity of a TWIP steel to H-delayed fracture using H pre-charged tensile specimens results in an inhomogeneous fracture surface, with a brittle fracture close to the sample surface, within the region of solute hydrogen penetration, and a ductile fracture in the bulk of the sample. This is illustrated in Fig. 66, which shows that only the near-surface regions of H-charged TWIP steel experience a predominantly intergranular brittle fracture. The bulk remains very ductile. The surface of the grains in the intergranular fracture zone also shows clear evidence of planar slip. This suggests that hydrogen does have an effect on the dislocations, but due to a limited penetration length, it does not embrittle the bulk of the sample.

The resistance to H-induced embrittlement can be enhanced by Al additions to TWIP steels. The concept was demonstrated for Fe-(15–18)%Mn-1.5%Al-(0.15–0.60%)C TWIP steel, which proved to be resistant to H-delayed fracture, as first reported by Jung et al. [339]. It is usually considered that, through an increase of the SFE, the addition of Al will result in a slowdown of the kinetics of deformation-induced twinning and martensite transformation. The effect may be more subtle, involving the interaction between Al and H atoms in, or close to, the stacking fault plane. H may increase the stacking fault width as it segregates on the stacking fault plane. This phenomenon, known as the Suzuki effect makes it easier to pull the partials apart, thus leading to a decrease of the twinning stress.

It is now recognized that the delayed cracking phenomenon, which occurs in air or during the immersion in water, shares many similarities with stress corrosion cracking. The mechanisms favorable for delayed cracking include (a) the uptake of H in the material during steel production and processing, (b) the high tensile stresses at the edge of the deep drawn cup, and (c) crack-initiating features such as the intersection of twins, strain-induced ε or α' martensite, and the presence of grain boundaries with an intrinsically low cohesion strength.

Possible influence of the H content on the fracture stress, fracture strain and time to fracture of smooth and notched samples of Fe-18%Mn-0.6%C-1.5%Al TWIP steel was tested by Soo et al. [340]. It was found that the specimens were immune to H-induced cracking, the fatigue properties being practically insensitive to the amount of H with which they were pre-charged. Thermal desorption analysis (TDA) of H introduced during cathodic charging revealed that most of H is weakly bound inside the material and gradually diffuses out of the specimen with time. There are two kinds of hydrogen trapping sites, having a low binding energy of 35 mJ/mol and a high one of 62 mJ/mol. These trapping sites were identified as dislocations (or grain boundaries), and twin boundaries, respectively [340]. According to these authors, dislocations and grain boundaries are considered to be shallow or “diffusible” H trap sites. Twin

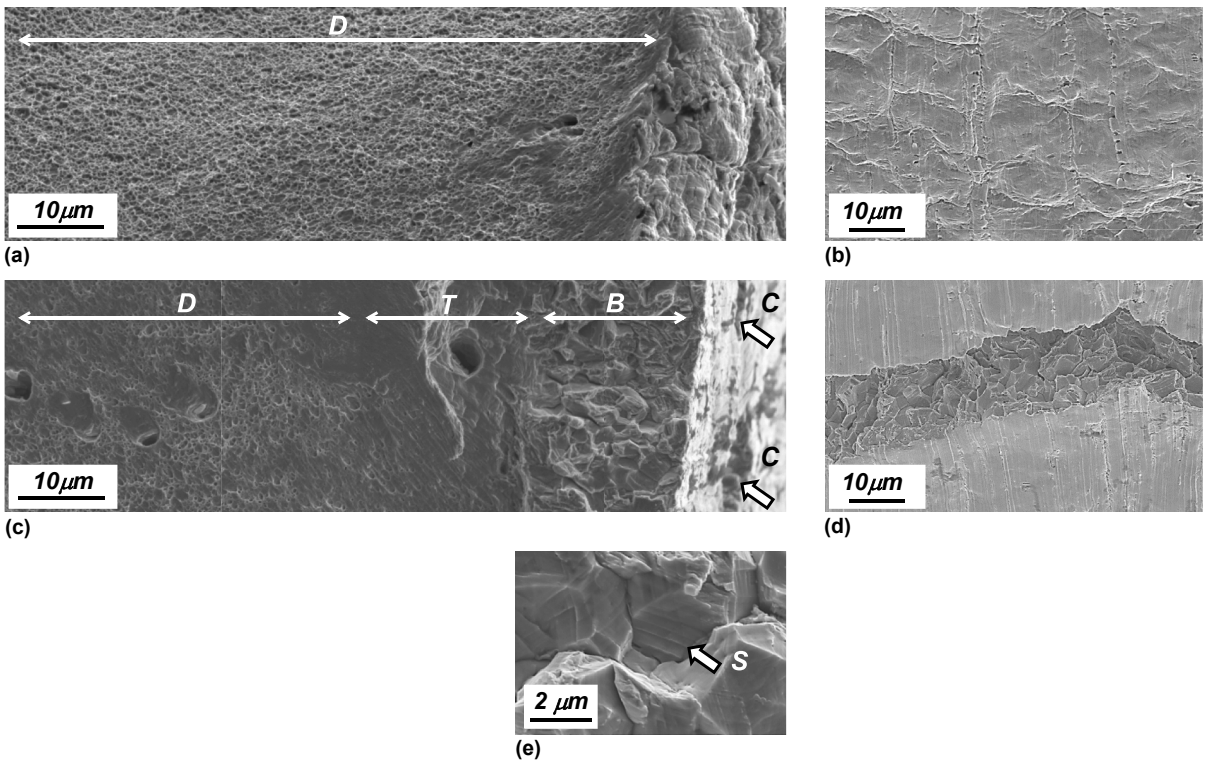

Fig. 66. (a) Fracture surface and (b) sample surface of a Fe-18%Mn-0.6%C-1.5%Al TWIP steel. The appearance of the fracture surface indicates fully ductile fracture. It is entirely covered with dimples, and no cracks are visible on the surface. (c) Fracture surface and (d) sample surface of the same steel pre-strained by 20% at 150 °C, hydrogen-charged to 4.9 ppm of solute H, and tested to fracture at room temperature. The choice of the higher pre-straining temperature is to avoid formation of martensite. The fracture comprises a brittle intergranular fracture zone near the surface (B), a fracture-mode transition zone (T), and a large area of ductile fracture. The sample surface exhibits a high density of wide cracks (C) due to intergranular de-cohesion. (d) Magnification of the brittle fracture surface showing slip traces (S) at the surface of the grains in the zone where intergranular fracture has occurred.

boundaries act as deep or "non-diffusible" H trap sites. The diffusible H is considered to be responsible for H-delayed fracture, whilst non-diffusing hydrogen atoms, strongly bound at deep traps, do not contribute to this phenomenon.

The role of strain-induced ε-martensite in H-delayed fracture was studied by Chun et al. [341]. They made the point that ε-martensite in Fe-15%Mn-0.6%C-2%Cr TWIP steel offers additional H trap sites, and that ε-martensite laths act both as crack initiation sites and as a crack propagation path. H-delayed fracture of cold deformed Fe-18%Mn-0.6%C-1.5%Al TWIP steel exhibited different features. As γ_{isf} in that steel was high enough, no ε-martensite was formed during deformation. Although the cold deformation resulted in a considerable increase of the tensile strength, the notch fracture stress of H-charged samples was only very slightly reduced. This was attributed to increased density of deformation twins, which acted as strong hydrogen traps. The same research group also studied the influence of Al additions on the properties of notched tensile samples pre-charged with hydrogen [342,343]. The addition of Al was found to be a very effective way to suppress the susceptibility of TWIP steel to H-delayed cracking. They argued that a decrease of the solute H trapped at dislocations due to addition of Al should also result in a decrease of the dislocation density. As the authors did not measure the dislocation density, this conjecture is yet to be proven. Park et al. [344] also observed a decrease of solute H at shallow trapping sites. They proposed an alternative mechanism for the suppression of H-delayed fracture of TWIP steel by Al addition by arguing that the improvement was due to the formation of a double oxide layer at the sample surface. This $(Fe_{0.8}Mn_{0.2})O$ surface layer, together with an α-Al_2O_3 interface layer, was considered to act as a diffusion barrier preventing the uptake of H during hydrogen charging.

There also several studies on the influence of Cu and Si additions on the hydrogen embrittling of TWIP steels. According to Kwon et al. [345] Cu additions (0–2 mass-%) to Fe-17%Mn-0.8%C TWIP steel improve its resistance to hydrogen embrittlement. A favorable effect of Si additions (0.01–2.95 mass-%) to Fe-18%Mn-0.6%C TWIP steel was explained in terms of the formation of a double oxide layer on its surface [346]. This layer consisted of a surface layer, an oxide mixture of (Fe,Mn)O and $(Fe,Mn)_2SiO_4$, and a pure $(Fe,Mn)_2SiO_4$ interface layer. The diffusion barrier they formed reduced the hydrogen uptake during H charging of the TWIP steel. The $(Fe,Mn)_2SiO_4$ layer in the Si-added TWIP steel was, however, less efficient than the α-Al_2O_3 layer on the Al-added steel in reducing the H uptake. The addition of 3% of Si also resulted in the strain-induced formation of ε-martensite. According to Lee et al. [346], the binding energy of solute hydrogen to γ/ε interfaces is approximately 22 kJ/mol. Based on H desorption spectra, Lee et al. claim that the enhanced embrittlement observed for the 3% Si-added TWIP steel was due to the higher sensitivity of ε-martensite to H embrittlement.

Ryu et al. [347] looked into the effect of hydrogen on the character of fracture. In their view, when solute H is present, intergranular and transgranular fracture of a TWIP steel is associated with the accumulation of dislocations at grain boundaries and twin boundaries, respectively. In the presence of strain-induced ε-martensite formed in H-charged TWIP steel, ε-martensite plates fracture in a brittle manner and the crack path is transgranular.

In general, most authors agree that the flow stress and the strain hardening behavior of tensile specimens are not affected by the *ex situ* H pre-charging of recrystallization annealed TWIP steels. The tensile elongation is decreased, however [348,349]. Pre-straining prior to H-charging does not influence the flow stress and the strain hardening of TWIP steels, but does have a minor effect on the ductility.

In contrast to other workers, Koyama et al. [350,351] observed a change in mechanical properties during *in situ* H-charging, typically in a 3% NaCl solution containing 3 g/L NH_4SCN at a current density in the range of 1–10 A/m^2. In tensile tests at low strain rates (5×10^{-5} s^{-1}) they observed a clear reduction in ductility in Fe-22% Mn-0.6%C TWIP steel. They also observed that fracture occurred during stress relaxation tests. These effects are illustrated in Fig. 67. The detailed fractography they conducted revealed that the crack path was mostly intergranular. Transgranular fracture was associated with crack propagation along twin boundaries. According to Koyama et al. [352] cracks started at intersections between primary and secondary twins and propagated trans-granularly along twin/matrix interfaces in a zigzag manner. The same authors reported that hydrogen-assisted cracking in Fe-18%Mn–1.2%C TWIP steel initiated at both grain boundaries and deformation twins, with crack propagation occurring along both types of interfaces. According to these authors, the deformation twins assist the formation of intergranular cracks and their propagation, by stress concentration at the tip of the twins [353].

Van Tol et al. [168,169,354] suggested that the nucleation of the delayed H-fracture cracks in the wall of deep drawn cups may be due to the presence of a small volume fraction of strain-induced α'-martensite formed at intersections of shear band or twins. Longitudinal cracks in the wall of H-delayed fractured deep drawn cups were mostly intergranular, but could become transgranular and propagate along twin boundaries. The longitudinal cracks propagated mainly along the grain boundaries. Some cracks were also found to propagate perpendicular to twin boundaries. The H-induced delayed fracture of deep drawn TWIP steel was related to the magnitude of the residual hoop and longitudinal stresses.

The emerging picture of the delayed H-fracture thus relates this phenomenon to the effect of hydrogen on the planarity of dislocation glide and the magnitude of the stacking fault energy. More subtle effects of pre-straining, mainly through deformation-induced twinning and formation of ε- or α'-martensite, and alloying with Al, Cu, and Si on the delayed H-fracture and hydrogen embrittlement are beginning to find rational explanations.

13. Liquid metal-induced embrittlement

Liquid metal induced embrittlement (LMIE) is an undesired phenomenon that occurs due to transgranular or intergranular decohesion of a metal or an alloy by rapid penetration of another liquid metal or alloy into its microstructure. The penetration is usually along grain boundaries in a polycrystalline material, or along sub-grain boundaries in a single crystal. When tensile stresses are present, a liquid film appears to cause grain boundary decohesion, as the boundary within a solid is replaced by a liquid film. This results in a brittle fracture due to the rapid intergranular propagation of one or more cracks formed in the region where the liquid metal has penetrated. The permeation by the liquid may be preceded by rapid solid state diffusion of the embrittling atoms along grain boundaries. In this case it is not known whether the loss of grain boundary cohesion is due to the presence of the diffusing solutes at the grain boundary or the penetration of a liquid phase. When the sensitivity of a combination of materials to LMIE is tested in laboratory conditions, *i.e.* by carrying out a tensile test in conditions in which the embrittling metal or alloy is in the liquid state, a pronounced decrease in both the fracture strength and the amount of plastic deformation prior to fracture is observed. As TWIP steels are considered as prospective materials for structural applications in the automotive industry, they need to be able to be galvanized to protect them from perforation and cosmetic corrosion. Coating of a TWIP steel with Zn or Zn-alloy at high temperatures may result in Zn liquid metal embrittlement (Zn-LMIE), Fig. 68. The issue of Zn-LMIE of TWIP steels is mainly

Please cite this article in press as: B.C. De Cooman, et al., Twinning-induced plasticity (TWIP) steels, Acta Materialia (2017), http://dx.doi.org/10.1016/j.actamat.2017.06.046

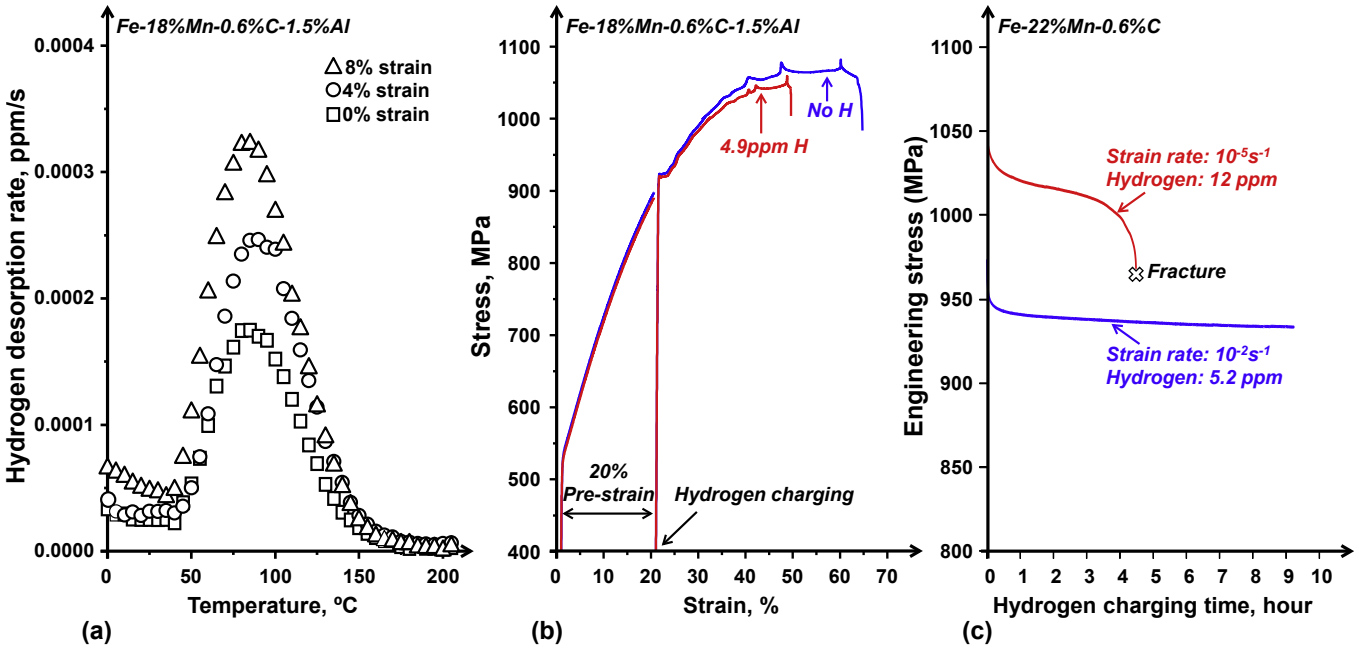

Fig. 67. (a) H-desorption rate curves for Fe-18%Mn0-0.6%C-1.5%Al TWIP steel for three different pre-strain levels: undeformed, 4% pre-strained and 8% pre-strained. The samples were H-charged for 24 h [359]. (b) Influence of pre-straining on the mechanical properties of H-charged Fe-18%Mn0-0.6%C-1.5%Al TWIP steel [349]. (c) Stress relaxation during the *in-situ* charging of Fe-22%Mn-0.6%C TWIP steel [352].

relevant to resistance spot welding, a key process in automotive body assembly. The sensitivity of TWIP steels to Zn-LMIE was studied in detail by Béal and co-workers [355–357]. Zn-LMIE of TWIP steels involves the presence of liquid Zn, Zn_{liq}, or a Zn-rich liquid alloy, combined with a high, uniformly distributed or locally concentrated, tensile stress. The Zn-LMIE of TWIP steels was assessed by Kang et al. [358] by means of microstructural analysis of sub-critical LMIE cracks in Zn-coated TWIP steel deformed in uniaxial tension at high temperature. Zn was found to penetrate into steel along the grain boundaries. Both Zn grain boundary diffusion and Zn_{liq} percolation along grain boundaries was observed. Evidence of Zn_{liq} percolation was inferred from the presence of the Γ-$(Fe,Mn)_3Zn_{10}$ phase along the Zn penetration region. The Γ-$(Fe,Mn)_3Zn_{10}$ phase was also observed at the tip of the Zn penetration zone deep below the surface. Kang et al. [358] proposed two mechanisms for the Zn-LMIE of Zn-coated TWIP steel, which are consistent with the features of the Zn penetration observed by micro characterization: (a) the Krishtal-Gordon-An model [359,360] for LMIE crack formation initiated by rapid intergranular solid state diffusion of Zn, and (b) the Stoloff-Johnson-Westwood-Kamdar model [361,362] for LMIE crack formation due to intergranular liquid metal percolation.

14. Hot ductility

Numerous production difficulties have been reported for

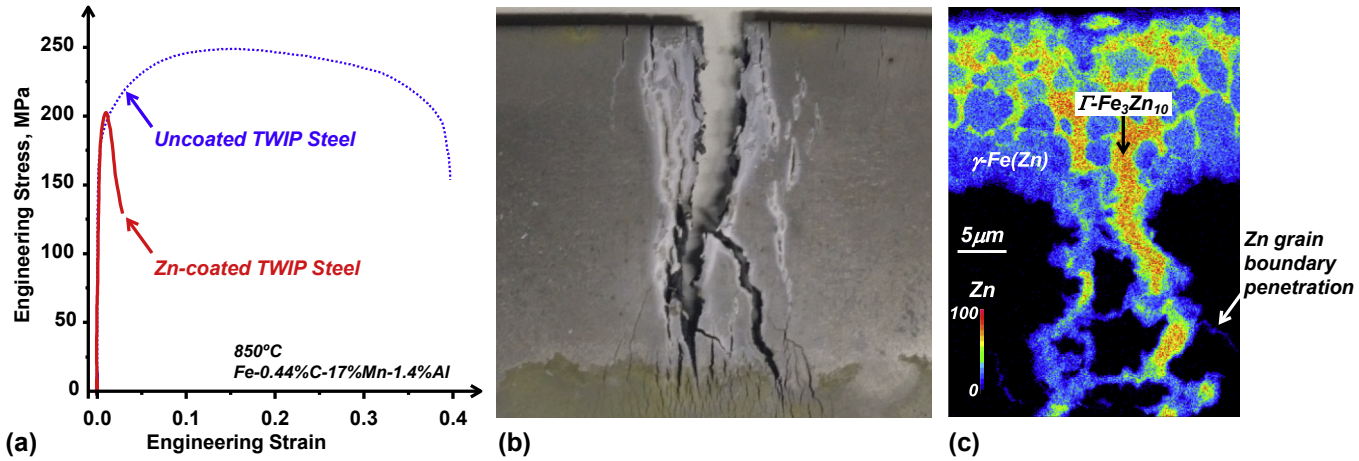

Fig. 68. (a) Engineering stress-strain curves of Zn-coated TWIP steel tested at 850 °C. (b) Fracture of a Zn-coated TWIP steel specimen at the end of a tensile test at 850 °C. The LMIE fracture is associated with a main crack with multiple secondary branches. (c) Electron-probe microanalysis of the Zn distribution in an area of Zn penetration. Γ-$(Fe,Mn)_3Zn_{10}$ is present in the crack opening area of the Zn penetration. The Zn content at the tip of the Zn penetration zone is lower than the maximum solubility of Zn in γ-(Fe,Mn) at the test temperature [357].

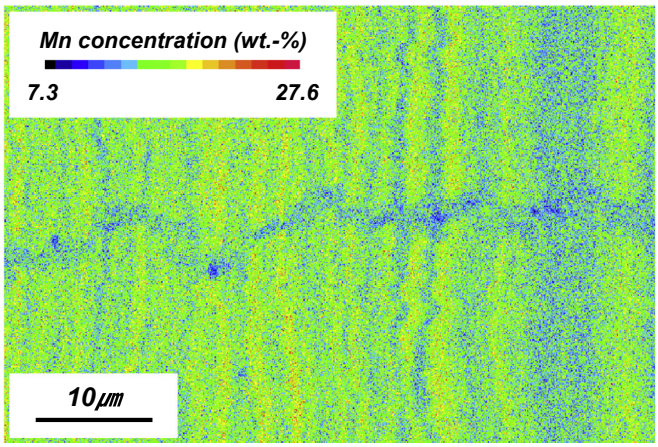

Fig. 69. Electron probe micro-analysis of the Mn distribution in a hot rolled TWIP steel illustrating the inhomogeneous Mn distribution resulting from the interdendritic segregation during casting.

casting, hot rolling, and cold rolling of high Mn steels. Mn loss occurs due to a high Mn vapour pressure reducing the Mn yield during steelmaking. The casting microstructure of TWIP steels is coarse with well-developed dendrites and coarse equiaxed grains. This is due to the wide solidification range and the low thermal conductivity of TWIP steels. According to Scott et al. [363], the solidification range of Fe-22%Mn-0.6%C is 120 °C, from 1407 °C to 1287 °C. The solidification range of Fe-18%Mn-0.6%C-1.5%Al is 110 °C, i.e. from 1380 °C to 1270 °C. The hot ductility of austenitic steels with a Mn content in the range of 9–23 mass-% and C content in the range of 0.6-0.9 mass-% was studied by Bleck et al. [364]. They observed that a reduction of the Mn content resulted in an improvement of the hot ductility. The steels investigated solidified in a relatively wide temperature range. The fracture surfaces of Fe-16%Mn-0.8%C TWIP steel tested at 1201 °C and 1000 °C show dendrite branches, micro-shrinkage leading to the formation of interdendritic micro-porosity and interdendritic segregation, cf. Lan et al. [365]. This interdendritic segregation is associated with an inhomogeneous Mn distribution in the steel (Fig. 69).

The grain boundary oxidation of continuously cast TWIP steel is known to result in the formation of microscabs during hot rolling. Direct strip casting was proposed as a possible solution to this problem, as it avoids the formation of bending-unbending cracks [366]. In rolling, edge cracks, poor surface quality and rolling instabilities are typically reported [367,368].

15. Conclusions

The understanding of the mechanical properties of TWIP steels has greatly improved in the recent years, yet some fundamental questions still remain unanswered. There is a general agreement on the most likely strain hardening mechanisms operating in TWIP steel individually or collectively. These include deformation twinning, nano-twin hardening, buildup of back-stress, pronounced planar glide of dislocations, and dynamic strain aging. The relative magnitude of the individual contributions of these mechanisms is still a matter of debate, however. In certain cases the quantitative evaluation of the contributions of the various mechanisms to strain hardening remains uncertain. This is also the case for deformation twinning. It is now well established that the volume fraction of deformation twins is relatively small, but no precise determination of the evolution of the twin volume fraction by means of a direct experimental method has been reported as yet. It is expected that the use of high resolution diffraction techniques will be required to avoid the limitations of standard electron backscattering diffraction or conventional X-ray diffraction methods.

It is now clear that the activation of the TWIP effect is governed not solely by the value of the intrinsic stacking fault energy. Other energy barriers, which describe the generalized stacking fault energy landscape, play an essential role as well. Progress in this area will require a more systematic use of currently available *ab initio* methods and the development of techniques to compute the generalized stacking fault energy of multi-component alloys such as TWIP steels at non-zero temperatures.

The role of carbon in TWIP steels remains unclear. Although the room temperature diffusion data for C suggest that its influence should be very limited, there are definite indications that solute C is directly involved in many fundamental processes, from static and dynamic strain aging to deformation twinning. It also has an effect on the temperature and strain rate dependence of the mechanical properties of TWIP steels. As with all point defect-related properties in metals and alloys, progress in this research area will require the use of a range of advanced methods of microstructure analysis, including internal friction measurements, and a much more systematic study of the low temperature dependence of the mechanical properties of model TWIP steels in a wide strain rate domain.

The fundamentals of TWIP steels and the developments highlighted in this review should help devising more refined micromechanical models which can predict the role of isotropic hardening and kinematic hardening for complex deformation paths. The importance of dynamic strain aging and the manner in which certain types of TWIP steels deform, characterized by a transition from uniform to localized deformation, by propagating or stationary localized strain bands, highlight the complexity of the strain hardening in TWIP steels. It encompasses an intricate interaction between dislocation glide and deformation twinning, and involves solute effects, which have yet to be accounted for on a solid basis of physical metallurgy.

While the main thrust of the present review has been on the strain hardening mechanisms and the role of deformation twinning in the mechanical performance of TWIP steels, other aspects of this important group of advanced steels relevant for their processing and properties under service conditions have been covered. It is hoped that the information compiled in the review and the critical assessment of the various contributions to this area will provide a starting help for a novice and also in-depth information for an expert in the burgeoning field of TWIP steels.

Acknowledgements

The authors gratefully acknowledge the support and contributions form the following persons: Dr Gwan Keun Chin (POSLAB), Dr Jin Kyung Kim (POSTECH), Professor Wolfgang Bleck (RWTH Aachen), Professor Young-Kook Lee (Yonsei University), Dr Stephanie Sandlöbes (Max-Planck-Institut für Eisenforschung, Düsseldorf), Professor Dierk Raabe (Max-Planck-Institut für Eisenforschung, Düsseldorf), Professor Se Kyun Kwon (POSTECH), and Mr Hojun Gwon (POSTECH). YE also acknowledges support from the Russian Ministry of Education and Science under grant #14.A12.31.0001 and the Increased Competitiveness Program of NUST « MISiS», grant #K2-2016-062.

On-line information on TWIP steel

On-line information on TWIP steel is made available by the German Sonderforschungsbereich SFB 761 Project “Stahl - *ab initio*; Quantum Mechanics Guided Design of New Fe-based Materials”.

The site (http://abinitio.iehk.rwth-aachen.de/) has a wealth of information on TWIP steels.

References

[1] O. Grassel, G. Frommeyer, C. Derder, H. Hofmann, Phase transformations and mechanical properties of Fe-Mn-Si-Al TRIP-steels, J. Phys. IV 7 (1997) 383–388.
[2] O. Grässel, G. Frommeyer, Effect of martensitic phase transformation and deformation twinning on mechanical properties of Fe-Mn-Si-Al steels, Mater. Sci. Tech. 14 (1998) 1213–1217.
[3] O. Grässel, L. Krüger, G. Frommeyer, L. Meyer, High strength Fe-Mn-(Al, Si) TRIP/TWIP steels development—properties—application, Int. J. Plast. 16 (2000) 1391–1409.
[4] O. Grässel, G. Frommeyer, High-strength and ultra-ductile FeMn (Al, Si) TRIP/TWIP light-weight steels for structural components in automotive engineering, Stahl Eisen 122 (2002) 65–69.
[5] G. Frommeyer, U. Brüx, P. Neumann, Supra-ductile and high-strength manganese-TRIP/TWIP steels for high energy absorption purposes, ISIJ Int. 43 (2003) 438–446.
[6] O. Bouaziz, S. Allain, C. Scott, P. Cugy, D. Barbier, High manganese austenitic twinning induced plasticity steels: a review of the microstructure properties relationships, Curr. Opin. Solid. St. M. 15 (2011) 141–168.
[7] B.C. De Cooman, O. Kwon, K.-G. Chin, State-of-the-knowledge on TWIP steel, Mater Sci. Tech. 28 (2012) 513–527.
[8] R. Neu, Performance and characterization of TWIP steels for automotive applications, Mater. Perform. Charact. 2 (2013) 244–284.
[9] K. Chung, K. Ahn, D.-H. Yoo, K.-H. Chung, M.-H. Seo, S.-H. Park, Formability of TWIP (twinning induced plasticity) automotive sheets, Int. J. Plast. 27 (2011) 52–81.
[10] B. Qin, Crystallography of TWIP Steel, MS Thesis, Pohang University of Science and Technology, 2007.
[11] Y. Estrin, H. Mecking, A unified phenomenological description of work hardening and creep based on one-parameter models, Acta Metall. Mater 32 (1984) 57–70.
[12] H. Mecking, B. Nicklas, N. Zarubova, U. Kocks, A "universal" temperature scale for plastic flow, Acta. Metall. Mater 34 (1986) 527–535.
[13] E. Nes, Modelling of work hardening and stress saturation in FCC metals, Prog. Mater. Sci. 41 (1997) 129–193.
[14] U. Kocks, H. Mecking, Physics and phenomenology of strain hardening: the FCC case, Prog. Mater. Sci. 48 (2003) 171–273.
[15] S. Asgari, E. El-Danaf, S.R. Kalidindi, R.D. Doherty, Strain hardening regimes and microstructural evolution during large strain compression of low stacking fault energy fcc alloys that form deformation twins, Metall. Mater. Trans. A 28 (1997) 1781–1795.
[16] S.R. Kalidindi, Modeling the strain hardening response of low SFE FCC alloys, Int. J. Plast. 14 (1998) 1265–1277.
[17] L. Bracke, L. Kestens, J. Penning, Direct observation of the twinning mechanism in an austenitic Fe-Mn-C steel, Scr. Mater 61 (2009) 220–222.
[18] J. Kim, Y. Estrin, B.C. De Cooman, Application of a dislocation density-based constitutive model to Al-alloyed TWIP steel, Metall, Mater. Trans. A 44 (2013) 4168–4182.
[19] B. Mahato, S. Shee, T. Sahu, S.G. Chowdhury, P. Sahu, D. Porter, L. Karjalainen, An effective stacking fault energy viewpoint on the formation of extended defects and their contribution to strain hardening in a Fe-Mn-Si-Al twinning-induced plasticity steel, Acta Mater 86 (2015) 69–79.
[20] K. Rahman, V. Vorontsov, D. Dye, The effect of grain size on the twin initiation stress in a TWIP steel, Acta Mater 89 (2015) 247–257.
[21] D. Barbier, N. Gey, S. Allain, N. Bozzolo, M. Humbert, Analysis of the tensile behavior of a TWIP steel based on the texture and microstructure evolutions, Mater. Sci. Eng. A 500 (2009) 196–206.
[22] T. Lebedkina, M. Lebyodkin, J.-P. Chateau, A. Jacques, S. Allain, On the mechanism of unstable plastic flow in an austenitic FeMnC TWIP steel, Mater. Sci. Eng. A 519 (2009) 147–154.
[23] K. Renard, P. Jacques, On the relationship between work hardening and twinning rate in TWIP steels, Mater. Sci. Eng. A 542 (2012) 8–14.
[24] D. Barbier, N. Gey, N. Bozzolo, S. Allain, M. Humbert, EBSD for analysing the twinning microstructure in fine-grained TWIP steels and its influence on work hardening, J. Microsc. 235 (2009) 67–78.
[25] I. Gutierrez-Urrutia, D. Raabe, Dislocation and twin substructure evolution during strain hardening of an Fe-22wt.% Mn-0.6 wt.% C TWIP steel observed by electron channeling contrast imaging, Acta Mater 59 (2011) 6449–6462.
[26] A. Saeed-Akbari, L. Mosecker, A. Schwedt, W. Bleck, Characterization and prediction of flow behavior in high-manganese twinning induced plasticity steels: Part I. Mechanism maps and work-hardening behavior, Metall. Mater. Trans. A 43 (2012) 1688–1704.
[27] I. Gutierrez-Urrutia, S. Zaefferer, D. Raabe, The effect of grain size and grain orientation on deformation twinning in a Fe-22wt.% Mn-0.6 wt.% C TWIP steel, Mater. Sci. Eng. A 527 (2010) 3552–3560.
[28] A.A. Saleh, A.A. Gazder, A re-evaluation of "The micromechanics of twinning in a TWIP steel", Mater. Sci. Eng. A 649 (2016) 184–189.
[29] S. Zaefferer, N.-N. Elhami, Theory and application of electron channelling contrast imaging under controlled diffraction conditions, Acta Mater 75 (2014) 20–50.
[30] D. Kuhlmann-Wilsdorf, Theory of plastic deformation: properties of low energy dislocation structures, Mater. Sci. Eng. A 113 (1989) 1–41.
[31] M. Shiekhelsouk, V. Favier, K. Inal, M. Cherkaoui, Modelling the behaviour of polycrystalline austenitic steel with twinning-induced plasticity effect, Int. J. Plast. 25 (2009) 105–133.
[32] S. Dancette, L. Delannay, K. Renard, M. Melchior, P. Jacques, Crystal plasticity modeling of texture development and hardening in TWIP steels, Acta Mater 60 (2012) 2135–2145.
[33] O. Bouaziz, N. Guelton, Modelling of TWIP effect on work-hardening, Mater. Sci. Eng. A 319 (2001) 246–249.
[34] S. Allain, J.-P. Chateau, O. Bouaziz, A physical model of the twinning-induced plasticity effect in a high manganese austenitic steel, Mater. Sci. Eng. A 387 (2004) 143–147.
[35] O. Bouaziz, S. Allain, C. Scott, Effect of grain and twin boundaries on the hardening mechanisms of twinning-induced plasticity steels, Scr. Mater 58 (2008) 484–487.
[36] J. Kim, Y. Estrin, H. Beladi, I. Timokhina, K.-G. Chin, S.-K. Kim, B.C. De Cooman, Constitutive modeling of the tensile behavior of Al-TWIP steel, Metall. Mater. Trans. A 43 (2012) 479–490.
[37] Y. Estrin, L. Kubin, Local strain hardening and nonuniformity of plastic deformation, Acta Metall. Mater 34 (1986) 2455–2464.
[38] G.I. Taylor, The mechanism of plastic deformation of crystals, Proc. R. Soc. A 145 (1934) 362–387.
[39] R.L. Fullman, Measurement of approximately cylindrical particles in opaque samples, Trans. Metall. AIME 197 (1953) 1267–1268.
[40] F. Roters, D. Raabe, G. Gottstein, Work hardening in heterogeneous alloys-a microstructural approach based on three internal state variables, Acta Mater 48 (2000) 4181–4189.
[41] D.R. Steinmetz, T. Jäpel, B. Wietbrock, P. Eisenlohr, I. Gutierrez-Urrutia, A. Saeed-Akbari, T. Hickel, F. Roters, D. Raabe, Revealing the strain-hardening behavior of twinning-induced plasticity steels: theory, simulations, experiments, Acta Mater 61 (2013) 494–510.
[42] U.F. Kocks, A.S. Argon, M.F. Ashby, Thermodynamics and kinetics of slip, in: Progress in Materials Science, vol. 19, Pergamon Press, 1975.
[43] A.A. Saleh, E.V. Pereloma, B. Clausen, D.W. Brown, C.N. Tomé, A.A. Gazder, On the evolution and modelling of lattice strains during the cyclic loading of TWIP steel, Acta Mater 61 (2013) 5247–5262.
[44] J.G. Sevillano, An alternative model for the strain hardening of FCC alloys that twin, validated for twinning-induced plasticity steel, Scr. Mater 60 (2009) 336–339.
[45] I. Gutierrez-Urrutia, J. Del Valle, S. Zaefferer, D. Raabe, Study of internal stresses in a TWIP steel analyzing transient and permanent softening during reverse shear tests, J. Mater. Sci. 45 (2010) 6604–6610.
[46] J.-L. Collet, Les Mécanismes de Déformation d'un Acier TWIP FeMnC: une Étude par Diffraction des Rayons X, Institut National Polytechnique de Grenoble-INPG, 2009.
[47] I. Karaman, H. Sehitoglu, Y.I. Chumlyakov, H.J. Maier, I. Kireeva, The effect of twinning and slip on the Bauschinger effect of Hadfield steel single crystals, Metall. Mater. Trans. A 32 (2001) 695–706.
[48] L. Brown, D. Clarke, Work hardening due to internal stresses in composite materials, Acta Metall. 23 (1975) 821–830.
[49] J.G. Sevillano, F. de Las Cuevas, Internal stresses and the mechanism of work hardening in twinning-induced plasticity steels, Scr. Mater 66 (2012) 978–981.
[50] H. Mughrabi, Dislocation wall and cell structures and long-range internal stresses in deformed metal crystals, Acta Metall. Mater 31 (1983) 1367–1379.
[51] H. Mughrabi, Dislocation clustering and long-range internal stresses in monotonically and cyclically deformed metal crystals, Rev. Phys. Appl. 23 (1988) 367–379.
[52] H. Idrissi, K. Renard, D. Schryvers, P. Jacques, On the relationship between the twin internal structure and the work-hardening rate of TWIP steels, Scr. Mater 63 (2010) 961–964.
[53] O. Bouaziz, H. Zurob, B. Chehab, J. Embury, S. Allain, M. Huang, Effect of chemical composition on work hardening of Fe—Mn—C TWIP steels, Mater. Sci. Tech. 27 (2011) 707–709.
[54] J. Nakano, A thermo-mechanical correlation with driving forces for hcp martensite and twin formations in the Fe-Mn-C system exhibiting multi-composition sets, Sci. Technol. Adv. Mater 14 (2013) 014207.
[55] Y. Dastur, W. Leslie, Mechanism of work hardening in Hadfield manganese steel, Metall. Mater. Trans. A 12 (1981) 749–759.
[56] P. Adler, G. Olson, W. Owen, Strain hardening of Hadfield manganese steel, Metall. Mater. Trans. A 17 (1986) 1725–1737.
[57] V. Gerold, H. Karnthaler, On the origin of planar slip in fcc alloys, Acta Metall. Mater 37 (1989) 2177–2183.
[58] J. Fisher, On the strength of solid solution alloys, Acta Metall. Mater 2 (1954) 9–10.
[59] Y. Brechet, Y. Estrin, Pseudo-portevin-le chatelier effect in ordered alloys, Scr. Mater 35 (1996) 217–223.
[60] K.K. Choi, C.H. Seo, H.C. Lee, K.T. Park, N.J. Kim, in: Proceeding of the 9th International Conference on Asia Steels, Busan, Korea, 2009, p. 203.
[61] K.-T. Park, K.G. Jin, S.H. Han, S.W. Hwang, K. Choi, C.S. Lee, Stacking fault energy and plastic deformation of fully austenitic high manganese steels: effect of Al addition, Mater. Sci. Eng. A 527 (2010) 3651–3661.

Please cite this article in press as: B.C. De Cooman, et al., Twinning-induced plasticity (TWIP) steels, Acta Materialia (2017), http://dx.doi.org/10.1016/j.actamat.2017.06.046

[62] J.-E. Jin, Y.-K. Lee, Effects of Al on microstructure and tensile properties of C-bearing high Mn TWIP steel, Acta Mater 60 (2012) 1680–1688.
[63] K. Rose, S. Gloverj, A study of strain-aging in austenite, Acta Metall. 14 (1966) 1505–1516.
[64] S.-J. Lee, J. Kim, S.N. Kane, B.C. De Cooman, On the origin of dynamic strain aging in twinning-induced plasticity steels, Acta Mater 59 (2011) 6809–6819.
[65] I. Jung, S.-J. Lee, B.C. De Cooman, Influence of Al on internal friction spectrum of Fe-18Mn-0.6 C twinning-induced plasticity steel, Scr. Mater 66 (2012) 729–732.
[66] S. Allain, Université de Lorraine, These d'Habilitation, INPL, Grenoble, 2012.
[67] J. von Appen, R. Dronskowski, Carbon-induced ordering in manganese-rich austenite—a density-functional total-energy and chemical-bonding study, Steel Res. Int. 82 (2011) 101–107.
[68] M. Grujicic, W. Owen, A Chemical interstitial order—based model for nitrogen strengthening of Fe-Ni-Cr austenite, Calphad 16 (1992) 291–299.
[69] W. Owen, M. Grujicic, Strain aging of austenitic Hadfield manganese steel, Acta Mater 47 (1998) 111–126.
[70] J. Gegner, Linearisierte Darstellung des Diffusionskoeffizienten von Kohlenstoff in austenitischem Eisen, Mater. Werkst 36 (2005) 56–61.
[71] S. Allain, Institute National Polytechnique de Lorraine, Nancy, Doctoral Thesis, 2002.
[72] S. Vercammen, Doctoral Thesis, Katholieke Universiteit Leuven, 2004.
[73] B. Huang, X. Wang, Y. Rong, L. Wang, L. Jin, Mechanical behavior and martensitic transformation of an Fe-Mn-Si-Al-Nb alloy, Mater. Sci. Eng. A 438 (2006) 306–311.
[74] H.Gholizadeh, Doctoral Thesis, 2013, Montan Universität, Leoben, Austria.
[75] D. Jiang, E.A. Carter, Carbon dissolution and diffusion in ferrite and austenite from first principles, Phys. Rev. B 67 (2003) 214103.
[76] Y. Tian, L. Zhao, S. Chen, A. Shibata, Z. Zhang, N. Tsuji, Significant contribution of stacking faults to the strain hardening behavior of Cu-15% Al alloy with different grain sizes, Sci. Rep. 5 (2015).
[77] M. Meyers, M. Schneider, H. Jarmakani, B. Kad, B. Remington, D. Kalantar, J. McNaney, B. Cao, J. Wark, Deformation substructures and their transitions in laser shock-compressed copper-aluminum alloys, Metall. Mater. Trans. A 39 (2008) 304–321.
[78] H. Beladi, I. Timokhina, Y. Estrin, J. Kim, B. De Cooman, S. Kim, Orientation dependence of twinning and strain hardening behaviour of a high manganese twinning induced plasticity steel with polycrystalline structure, Acta Mater 59 (2011) 7787–7799.
[79] J. Bailey, P. Hirsch, The dislocation distribution, flow stress, and stored energy in cold-worked polycrystalline silver, Philos. Mag. 5 (1960) 485–497.
[80] J.-H. Kang, T. Ingendahl, W. Bleck, A constitutive model for the tensile behaviour of TWIP steels: composition and temperature dependencies, Mater. Des. 90 (2016) 340–349.
[81] D. Kuhlmann-Wilsdorf, Advancing towards constitutive equations for the metal industry via the LEDS theory, Metall. Mater. Trans. A 35 (2004) 369.
[82] L. Remy, The interaction between slip and twinning systems and the influence of twinning on the mechanical behavior of fcc metals and alloys, Metall. Mater. Trans. A 12 (1981) 387–408.
[83] Z.-H. Jin, P. Gumbsch, K. Albe, E. Ma, K. Lu, H. Gleiter, H. Hahn, Interactions between non-screw lattice dislocations and coherent twin boundaries in face-centered cubic metals, Acta Mater 56 (2008) 1126–1135.
[84] T. Ezaz, M.D. Sangid, H. Sehitoglu, Energy barriers associated with slip-twin interactions, Philos. Mag. 91 (2011) 1464–1488.
[85] M.D. Sangid, T. Ezaz, H. Sehitoglu, I.M. Robertson, Energy of slip transmission and nucleation at grain boundaries, Acta Mater 59 (2011) 283–296.
[86] H. Idrissi, D.Schryvers, Current microscopy contributions to advances in science and technology, Microscopy Book Series No. 5, vol. 1, Edited by A.Méndez-Vilas, 1213–1224.
[87] J.P. Hirth, J. Lothe, Theory of Dislocations, second ed., John Willey & Sons, 1982.
[88] S. Vercammen, B. Blanpain, B. De Cooman, P. Wollants, Cold rolling behaviour of an austenitic Fe-30Mn-3Al-3Si TWIP-steel: the importance of deformation twinning, Acta Mater 52 (2004) 2005–2012.
[89] H. Idrissi, L. Ryelandt, M. Veron, D. Schryvers, P. Jacques, Is there a relationship between the stacking fault character and the activated mode of plasticity of Fe-Mn-based austenitic steels? Scr. Mater 60 (2009) 941–944.
[90] T. Tisone, The concentration and temperature dependence of the stacking fault energy in face-centered cubic Co-Fe alloys, Acta Metall. 21 (1973) 229–236.
[91] H. Idrissi, K. Renard, L. Ryelandt, D. Schryvers, P.J. Jacques, On the mechanism of twin formation in Fe-Mn-C TWIP steels, Acta Mater (2010) 2464–2476.
[92] I. Karaman, H. Sehitoglu, Y.I. Chumlyakov, H. Maier, I. Kireeva, Extrinsic stacking faults and twinning in Hadfield manganese steel single crystals, Scr. Mater 44 (2001) 337–343.
[93] D.T. Pierce, J.A. Jiménez, J. Bentley, D. Raabe, C. Oskay, J. Wittig, The influence of manganese content on the stacking fault and austenite/ε-martensite interfacial energies in Fe-Mn-(Al-Si) steels investigated by experiment and theory, Acta Mater 68 (2014) 238–253.
[94] J. Hirth, Thermodynamics of stacking faults, Metall. Trans. 1 (1970) 2367.
[95] R. Reed-Hill, Deformation Twinning, in: TMS-AIME Conference, Am. Inst. Min. Metall. Pet. Eng., 1964. Gainesville Fla.
[96] L. Remy, A. Pineau, Twinning and strain-induced fcc→ hcp transformation on the mechanical properties of Co-Ni-Cr-Mo alloys, Mater. Sci. Eng. 26 (1976) 123–132.
[97] L. Remy, A. Pineau, Twinning and strain-induced FCC→ HCP transformation in the Fe- Mn-Cr-C system, Mater. Sci. Eng. 28 (1977) 99–107.
[98] A.S.Hamada, Doctoral Thesis, University of Oulu, Linnanmaa, Finland, 2007.
[99] S. Vercammen, B.C. De Cooman, N. Akdut, B. Blanpain, P. Wollants, Microstructural evolution and crystallographic texture formation of cold rolled austenitic Fe-30Mn-3Al-3Si TWIP-steel, Steel Res. Int. 74 (2003) 370–375.
[100] B. Oh, S. Cho, Y. Kim, Y. Kim, W. Kim, S. Hong, Effect of aluminium on deformation mode and mechanical properties of austenitic Fe-Mn-Cr-Al-C alloys, Mater. Sci. Eng. A 197 (1995) 147–156.
[101] T.-H. Lee, E. Shin, C.-S. Oh, H.-Y. Ha, S.-J. Kim, Correlation between stacking fault energy and deformation microstructure in high-interstitial-alloyed austenitic steels, Acta Mater 58 (2010) 3173–3186.
[102] G. Olson, M. Cohen, A general mechanism of martensitic nucleation: Part I. General concepts and the FCC→ HCP transformation, Metall. Trans. A 7 (1976) 1897–1904.
[103] B.Hallstedt, Proceedings of the 2nd international Conference on high Mn steel HMnS2014, W.Bleck and D.Raabe Editors, Aachen, Germany, August 31st-September 4th 2014, 113–116.
[104] S.-J. Lee, Y.-S. Jung, S.-I. Baik, Y.-W. Kim, M. Kang, W. Woo, Y.-K. Lee, The effect of nitrogen on the stacking fault energy in Fe-15Mn-2Cr-0.6 C-xN twinning-induced plasticity steels, Scr. Mater 92 (2014) 23–26.
[105] I.-C. Jung, B.C. De Cooman, Temperature dependence of the flow stress of Fe-18Mn-0.6 C-xAl twinning-induced plasticity steel, Acta Mater 61 (2013) 6724–6735.
[106] X. Lu, Z. Qin, X. Tian, Y. Zhang, B. Ding, Z. Hu, Relations between the lattice parameter and the stability of austenite against ε martensite for the Fe-Mn based alloys, J. Mater. Sci. Technol. 19 (2003) 443–446.
[107] M. Onink, C. Brakman, F. Tichelaar, E. Mittemeijer, S. Van der Zwaag, J. Root, N. Konyer, The lattice parameters of austenite and ferrite in Fe-C alloys as functions of carbon concentration and temperature, Scr. Metall. Mater 29 (1993) 1011–1016.
[108] Y. Endoh, Y. Ishikawa, Antiferromagnetism of γ iron manganes alloys, J. Phys. Soc. Jpn. 30 (1971) 1614–1627.
[109] G. Inden, The role of magnetism in the calculation of phase diagrams, Phys. B+ C 103 (1981) 82–100.
[110] M. Hillert, M. Jarl, A model for alloying in ferromagnetic metals, Calphad 2 (1978) 227–238.
[111] S. Cotes, A.F. Guillermet, M. Sade, Fcc/Hcp martensitic transformation in the Fe-Mn system: Part II. Driving force and thermodynamics of the nucleation process, Metall. Mater. Trans. A 35 (2004) 83–91.
[112] P. Müllner, P.J. Ferreira, On the energy of terminated stacking faults, Philos. Mag. Lett. 73 (1996) 289–298.
[113] P. Volosevich, V. Gridnev, Y. Petrov, Influence of Mn and the stacking fault energy of Fe-Mn alloys, Phys. Met. Metallogr. 42 (1976) 126–130.
[114] S. Takaki, H. Nakatsu, Y. Tokunaga, Effects of austenite grain size on ε martensitic transformation in Fe-15mass% Mn alloy, Mater. Trans. JIM 34 (1993) 489–495.
[115] Y.-K. Lee, C. Choi, Driving force for γ→ ε martensitic transformation and stacking fault energy of γ in Fe-Mn binary system, Metall. Mater. Trans. A 31 (2000) 355–360.
[116] J.-H. Jun, C.-S. Choi, Variation of stacking fault energy with austenite grain size and its effect on the M S temperature of γ→ ε martensitic transformation in Fe-Mn alloy, Mater. Sci. Eng. A 257 (1998) 353–356.
[117] A. Saeed-Akbari, J. Imlau, U. Prahl, W. Bleck, Derivation and variation in composition-dependent stacking fault energy maps based on subregular solution model in high-manganese steels, Metall. Mater. Trans. A 40 (2009) 3076–3090.
[118] Y.-K. Lee, Relationship between austenite dislocation density introduced during thermal cycling and M s temperature in an Fe-17 wt pct Mn alloy, Metall. Mater. Trans. A 33 (2002) 1913–1917.
[119] S. Allain, J.-P. Chateau, O. Bouaziz, S. Migot, N. Guelton, Correlations between the calculated stacking fault energy and the plasticity mechanisms in Fe-Mn-C alloys, Mater. Sci. Eng. A 387 (2004) 158–162.
[120] W.S. Wang, C.M. Wan, The influence of aluminium content to the stacking fault energy in Fe-Mn-Al-C alloy system, J. Mater. Sci. 25 (1990) 1821–1823.
[121] D. Geissler, J. Freudenberger, A. Kauffmann, S. Martin, D. Rafaja, Assessment of the thermodynamic dimension of the stacking fault energy, Philos. Mag. 94 (2014) 2967–2979.
[122] W. Li, S. Lu, D. Kim, K. Kokko, S. Hertzman, S.K. Kwon, L. Vitos, First-principles prediction of the deformation modes in austenitic Fe-Cr-Ni alloys, Appl. Phys. Lett. 108 (2016) 081903.
[123] S.-J. Lee, Y.-K. Lee, A. Soon, The austenite/ε martensite interface: a first-principles investigation of the fcc Fe (111)/hcp Fe (0001) system, Appl. Surf. Sci. 258 (2012) 9977–9981.
[124] J. Talonen, H. Hänninen, Formation of shear bands and strain-induced martensite during plastic deformation of metastable austenitic stainless steels, Acta Mater 55 (2007) 6108–6118.
[125] A. Dumay, J.-P. Chateau, S. Allain, S. Migot, O. Bouaziz, Influence of addition elements on the stacking-fault energy and mechanical properties of an austenitic Fe-Mn-C steel, Mater. Sci. Eng. A 483 (2008) 184–187.
[126] S. Curtze, V.-T. Kuokkala, A. Oikari, J. Talonen, H. Hänninen, Thermodynamic modeling of the stacking fault energy of austenitic steels, Acta Mater 59 (2011) 1068–1076.
[127] S. Curtze, V.-T. Kuokkala, Dependence of tensile deformation behavior of

Please cite this article in press as: B.C. De Cooman, et al., Twinning-induced plasticity (TWIP) steels, Acta Materialia (2017), http://dx.doi.org/10.1016/j.actamat.2017.06.046

TWIP steels on stacking fault energy, temperature and strain rate, Acta Mater 58 (2010) 5129–5141.
[128] J. Nakano, P.J. Jacques, Effects of the thermodynamic parameters of the hcp phase on the stacking fault energy calculations in the Fe-Mn and Fe-Mn-C systems, Calphad 34 (2010) 167–175.
[129] D. Djurovic, B. Hallstedt, J. Von Appen, R. Dronskowski, Thermodynamic assessment of the Mn-C system, Calphad 34 (2010) 279–285.
[130] D. Djurovic, B. Hallstedt, J. von Appen, R. Dronskowski, Thermodynamic assessment of the Fe-Mn-C system, Calphad 35 (2011) 479–491.
[131] H.-S. Yang, J. Jang, H. Bhadeshia, D. Suh, Critical assessment: martensite-start temperature for the $\gamma \rightarrow \varepsilon$ transformation, Calphad 36 (2012) 16–22.
[132] V. Schumann, Martensitische Umwandlung in austenitischen mangan-kohlenstoff-stählen, Neue Hütte 17 (1972) 605–609.
[133] H. Van Swygenhoven, P. Derlet, A. Frøseth, Stacking fault energies and slip in nanocrystalline metals, Nat. Mater 3 (2004) 399–403.
[134] V. Vitek, Intrinsic stacking faults in body-centred cubic crystals, Philos. Mag. 18 (1968) 773–786.
[135] V. Vitek, Multilayer stacking faults and twins on {211} planes in bcc metals, Scr. Metall. 4 (1970) 725–732.
[136] R.C. Pond, J. Hirth, A. Serra, D. Bacon, Atomic displacements accompanying deformation twinning: shears and shuffles, Mater. Res. Lett. 4 (2016) 185–190.
[137] T. Gebhardt, D. Music, M. Ekholm, I.A. Abrikosov, L. Vitos, A. Dick, T. Hickel, J. Neugebauer, J.M. Schneider, The influence of additions of Al and Si on the lattice stability of fcc and hcp Fe-Mn random alloys, J. Phys.-Condens. Mat. 23 (2011) 246003.
[138] J.R. Rice, Dislocation nucleation from a crack tip: an analysis based on the Peierls concept, J. Mech. Phys. Solids 40 (1992) 239–271.
[139] E. Tadmor, S. Hai, A peierls criterion for the onset of deformation twinning at a crack tip, J. Mech. Phys. Solids 51 (2003) 765–793.
[140] S. Ogata, J. Li, S. Yip, Energy landscape of deformation twinning in bcc and fcc metals, Phys. Rev. B 71 (2005) 224102.
[141] Z. Jin, S. Dunham, H. Gleiter, H. Hahn, P. Gumbsch, A universal scaling of planar fault energy barriers in face-centered cubic metals, Scr. Mater 64 (2011) 605–608.
[142] S. Kibey, J. Liu, D. Johnson, H. Sehitoglu, Predicting twinning stress in fcc metals: linking twin-energy pathways to twin nucleation, Acta Mater 55 (2007) 6843–6851.
[143] W. Li, S. Lu, Q.-M. Hu, S.K. Kwon, B. Johansson, L. Vitos, Generalized stacking fault energies of alloys, J. Phys. -Condens. Mat 26 (2014) 265005.
[144] M. Jo, Y.M. Koo, B.-J. Lee, B. Johansson, L. Vitos, S.K. Kwon, Theory for plasticity of face-centered cubic metals, P. Natl. Acad. Sci. 111 (2014) 6560–6565.
[145] R.J. Asaro, S. Suresh, Mechanistic models for the activation volume and rate sensitivity in metals with nanocrystalline grains and nano-scale twins, Acta Mater 53 (2005) 3369–3382.
[146] T. Byun, On the stress dependence of partial dislocation separation and deformation microstructure in austenitic stainless steels, Acta Mater 51 (2003) 3063–3071.
[147] N. Bernstein, E. Tadmor, Tight-binding calculations of stacking energies and twinnability in fcc metals, Phys. Rev. B 69 (2004) 094116.
[148] E. Tadmor, N. Bernstein, A first-principles measure for the twinnability of FCC metals, J. Mech. Phys. Solids 52 (2004) 2507–2519.
[149] V. García-Suárez, C. Newman, C.J. Lambert, J. Pruneda, J. Ferrer, First principles simulations of the magnetic and structural properties of Iron, Eur. Phys. J. B 40 (2004) 371–377.
[150] T. Gebhardt, D. Music, B. Hallstedt, M. Ekholm, I.A. Abrikosov, L. Vitos, J. Schneider, Ab initio lattice stability of fcc and hcp Fe-Mn random alloys, J. Phys.-Condens. Mat. 22 (2010) 295402.
[151] N. Medvedeva, D. Van Aken, J.E. Medvedeva, Magnetism in bcc and fcc Fe with carbon and manganese, J. Phys.-Condens. Mat. 22 (2010) 316002.
[152] N. Medvedeva, D.C. Van Aken, J.E. Medvedeva, The effect of carbon distribution on the manganese magnetic moment in bcc Fe-Mn alloy, J. Phys.-Condens. Mat. 23 (2011) 326003.
[153] N.G. Kioussis, N.M. Ghoniem, Modeling of dislocation interaction with solutes, nano-precipitates and interfaces: a multiscale challenge, J. Comput. Theor. Nanosci. 7 (2010) 1317–1346.
[154] D. Boukhvalov, Y.N. Gornostyrev, M. Katsnelson, A. Lichtenstein, Magnetism and local distortions near carbon impurity in γ-iron, Phys. Rev. Lett. 99 (2007) 247205.
[155] A. Abbasi, A. Dick, T. Hickel, J. Neugebauer, First-principles investigation of the effect of carbon on the stacking fault energy of Fe-C alloys, Acta Mater 59 (2011) 3041–3048.
[156] S. Kibey, J. Liu, M. Curtis, D. Johnson, H. Sehitoglu, Effect of nitrogen on generalized stacking fault energy and stacking fault widths in high nitrogen steels, Acta Mater 54 (2006) 2991–3001.
[157] N. Medvedeva, M. Park, D.C. Van Aken, J.E. Medvedeva, First-principles study of Mn, Al and C distribution and their effect on stacking fault energies in fcc Fe, J. Alloy. Compd. 582 (2014) 475–482.
[158] L. Vitos, Computational Quantum Mechanics for Materials Engineers: the EMTO Method and Applications, Springer Science & Business Media, 2007.
[159] M. Petersilka, U. Gossmann, E. Gross, Time-dependent Optimized Effective Potential in the Linear Response Regime, Electronic Density Functional Theory, Springer, 1998, pp. 177–197.
[160] J.P. Perdew, K. Burke, M. Ernzerhof, Generalized gradient approximation made simple, Phys. Rev. Lett. 77 (1996) 3865.
[161] M. Ekholm, I. Abrikosov, Structural and magnetic ground-state properties of γ-FeMn alloys from ab initio calculations, Phys. Rev. B 84 (2011) 104423.
[162] A. Reyes-Huamantinco, P. Puschnig, C. Ambrosch-Draxl, O.E. Peil, A.V. Ruban, Stacking-fault energy and anti-Invar effect in Fe-Mn alloy from first principles, Phys. Rev. B 86 (2012) 060201.
[163] L. Vitos, P.A. Korzhavyi, B. Johansson, Evidence of large magnetostructural effects in austenitic stainless steels, Phys. Rev. Lett. 96 (2006) 117210.
[164] P. Denteneer, W. van Haeringen, Stacking-fault energies in semiconductors from first-principles calculations, J. Phys. C. Solid State Phys. 20 (1987) L883.
[165] L. Vitos, J.-O. Nilsson, B. Johansson, Alloying effects on the stacking fault energy in austenitic stainless steels from first-principles theory, Acta Mater 54 (2006) 3821–3826.
[166] A. Dick, T. Hickel, J. Neugebauer, The effect of disorder on the concentration-dependence of stacking fault energies in Fe1-xMnx-a first principles study, Steel Res. Int. 80 (2009) 603–608.
[167] P. Denteneer, J. Soler, Energetics of point and planar defects in aluminium from first-principles calculations, Solid. State. Commun. 78 (1991) 857–861.
[168] R. Van Tol, J. Kim, L. Zhao, J. Sietsma, B. De Cooman, α'-Martensite formation in deep-drawn Mn-based TWIP steel, J. Mater. Sci. 47 (2012) 4845–4850.
[169] R. Van Tol, Microstructural Evolution in Deformed Austenitic TWinning Induced Plasticity Steels, TU Delft, Delft University of Technology, 2014.
[170] J. Kim, S.-J. Lee, B.C. De Cooman, Effect of Al on the stacking fault energy of Fe-18Mn-0.6 C twinning-induced plasticity, Scr. Mater 65 (2011) 363–366.
[171] J. Jeong, W. Woo, K. Oh, S. Kwon, Y. Koo, In situ neutron diffraction study of the microstructure and tensile deformation behavior in Al-added high manganese austenitic steels, Acta Mater 60 (2012) 2290–2299.
[172] K. Jeong, J.-E. Jin, Y.-S. Jung, S. Kang, Y.-K. Lee, The effects of Si on the mechanical twinning and strain hardening of Fe-18Mn-0.6 C twinning-induced plasticity steel, Acta Mater 61 (2013) 3399–3410.
[173] K. Oda, H. Fujimura, H. Ino, Local interactions in carbon-carbon and carbon-M (M: Al, Mn, Ni) atomic pairs in FCC gamma-iron, J. Phys.-Condens. Mat. 6 (1994) 679.
[174] H. Bhadeshia, Carbon-carbon interactions in iron, J. Mater. Sci. 39 (2004) 3949–3955.
[175] R. McLellan, C. Ko, The diffusion of carbon in austenite, Acta. Metall. Mater 36 (1988) 531–537.
[176] S. Babu, H. Bhadeshia, Diffusion of carbon in substitutionally alloyed austenite, J. Mater. Sci. Lett. 14 (1995) 314–316.
[177] K. Limmer, J.E. Medvedeva, D.C. Van Aken, N. Medvedeva, Ab initio simulation of alloying effect on stacking fault energy in fcc Fe, Comp. Mater. Sci. 99 (2015) 253–255.
[178] D. Hepburn, D. Ferguson, S. Gardner, G. Ackland, First-principles study of helium, carbon, and nitrogen in austenite, dilute austenitic iron alloys, and nickel, Phys. Rev. B 88 (2013) 024115.
[179] T. Shun, C. Wan, J. Byrne, A study of work hardening in austenitic Fe- Mn- C and Fe- Mn- Al- C alloys, Acta Metall. Mater 40 (1992) 3407–3412.
[180] K. Haneda, Z. Zhou, A. Morrish, T. Majima, T. Miyahara, Low-temperature stable nanometer-size fcc-Fe particles with no magnetic ordering, Phys. Rev. B 46 (1992) 13832.
[181] L. Del Bianco, C. Ballesteros, J. Rojo, A. Hernando, Magnetically ordered fcc structure at the relaxed grain boundaries of pure nanocrystalline Fe, Phys. Rev. Lett. 81 (1998) 4500.
[182] W.A. Macedo, F. Sirotti, G. Panaccione, A. Schatz, W. Keune, W.N. Rodrigues, G. Rossi, Magnetism of atomically thin fcc Fe overlayers on an expanded fcc lattice: Cu 84 Al 16(100), Phys. Rev. B 58 (1998) 11534.
[183] Y. Tsunoda, Y. Nishioka, R. Nicklow, Spin fluctuations in small γ-Fe precipitates, J. Magn. Magn. Mater 128 (1993) 133–137.
[184] T. Hickel, S. Sandlöbes, R.K. Marceau, A. Dick, I. Bleskov, J. Neugebauer, D. Raabe, Impact of nanodiffusion on the stacking fault energy in high-strength steels, Acta Mater 75 (2014) 147–155.
[185] K.R. Limmer, First-principles Investigations of Iron-based Alloys and Their Properties, Missouri University of Science and Technology, 2014.
[186] W.S. Choi, B.C. De Cooman, S. Sandlöbes, D. Raabe, Size and orientation effects in partial dislocation-mediated deformation of twinning-induced plasticity steel micro-pillars, Acta Mater 98 (2015) 391–404.
[187] K. Irvine, T. Gladman, F. Pickering, The strength of austenitic stainless steels, J. Iron Steel. Inst. 207 (1969) 1017–1028.
[188] P. Kusakin, A. Belyakov, D.A. Molodov, R. Kaibyshev, On the effect of chemical composition on yield strength of TWIP steels, Mater. Sci. Eng. A 687 (2017) 82–84.
[189] J.-H. Kang, T. Ingendahl, J. von Appen, R. Dronskowski, W. Bleck, Impact of short-range ordering on yield strength of high manganese austenitic steels, Mater. Sci. Eng. A 614 (2014) 122–128.
[190] D. Parris, R.B. McLellan, The diffusivity of carbon in austenite, Acta Metall. 24 (1976) 523–528.
[191] R.B. McLellan, Cell models for interstitial solid solutions, Acta Metall. 30 (1982) 317–322.
[192] S.-J. Lee, D.K. Matlock, C.J. Van Tyne, Carbon diffusivity in multi-component austenite, Scr. Mater 64 (2011) 805–808.
[193] B.C. De Cooman, K.-G. Chin, J. Kim, High Mn TWIP Steels for Automotive Applications, New Trends and Developments in Automotive System Engineering, InTech, 2011.
[194] M. Kang, W. Woo, Y.-K. Lee, B.-S. Seong, Neutron diffraction analysis of stacking fault energy in Fe-18Mn-2Al-0.6 C twinning-induced plasticity

Please cite this article in press as: B.C. De Cooman, et al., Twinning-induced plasticity (TWIP) steels, Acta Materialia (2017), http://dx.doi.org/10.1016/j.actamat.2017.06.046

steels, Mater. Lett. 76 (2012) 93–95.
[195] T.S. Shun, C. Wan, J. Byrne, Serrated flow in austenitic Fe-Mn-C and Fe-Mn-Al-C alloys, Scr. Metall. Mater 25 (1991) 1769–1774.
[196] X. Tian, Y. Zhang, Effect of Si content on the stacking fault energy in γ-Fe-Mn-Si-C alloys: Part I. X-ray diffraction line profile analysis, Mater. Sci. Eng. A 516 (2009) 73–77.
[197] B. Huang, X. Wang, L. Wang, Y. Rong, Effect of nitrogen on stacking fault formation probability and mechanical properties of twinning-induced plasticity steels, Metall. Mater. Trans. A 39 (2008) 717–724.
[198] B. Jiang, X. Qi, S. Yang, W. Zhou, T. Hsu, Effect of stacking fault probability on γ-ε martensitic transformation and shape memory effect in Fe-Mn-Si based alloys, Acta Mater 46 (1998) 501–510.
[199] S. Lua, W. Lib, S.K. Kwon, K. Kokkoa, Q.M. Hud, S. Hertzman, L. Vitos, Scripta Materialia, 2015.
[200] S. Lee, J. Kim, S.-J. Lee, B.C. De Cooman, Effect of Cu addition on the mechanical behavior of austenitic twinning-induced plasticity steel, Scr. Mater 65 (2011) 1073–1076.
[201] M. Müller, An antiferromagnetic temperature-compensating elastic Elinvar-alloy on the basis of Fe-Mn, J. Magn. Magn. Mater 78 (1989) 337–346.
[202] G. Hausch, Elastic and magnetoelastic effects in invar alloys, J. Magn. Magn. Mater 10 (1979) 163–169.
[203] S. Reeh, D. Music, T. Gebhardt, M. Kasprzak, T. Jäpel, S. Zaefferer, D. Raabe, S. Richter, A. Schwedt, J. Mayer, Elastic properties of face-centred cubic Fe-Mn-C studied by nanoindentation and ab initio calculations, Acta Mater 60 (2012) 6025–6032.
[204] H. Yang, V. Doquet, Z. Zhang, Micro-scale measurements of plastic strain field, and local contributions of slip and twinning in TWIP steels during in situ tensile tests, Mater. Sci. Eng. A 672 (2016) 7–14.
[205] T. Gebhardt, D. Music, D. Kossmann, M. Ekholm, I.A. Abrikosov, L. Vitos, J.M. Schneider, Elastic properties of fcc Fe-Mn-X (X= Al, Si) alloys studied by theory and experiment, Acta Mater 59 (2011) 3145–3155.
[206] D. Pierce, K. Nowag, A. Montagne, J. Jiménez, J. Wittig, R. Ghisleni, Single crystal elastic constants of high-manganese transformation-and twinning-induced plasticity steels determined by a new method utilizing nano-indentation, Mater. Sci. Eng. A 578 (2013) 134–139.
[207] M. van Schilfgaarde, I. Abrikosov, B. Johansson, Origin of the Invar effect in iron-nickel alloys, Nature 400 (1999) 46–49.
[208] S. Pugh, XCII, Relations between the elastic moduli and the plastic properties of polycrystalline pure metals, the London, Edinburgh, and Dublin, Philos. Mag. J. Sci. 45 (1954) 823–843.
[209] D. Pettifor, Theoretical predictions of structure and related properties of intermetallics, Mater. Sci. Tech. 8 (1992) 345–349.
[210] I.C.Jung, Doctoral Thesis, Pohang University of Science and Technology, 2013, South Korea.
[211] S. Wu, H. Yen, M. Huang, A. Ngan, Deformation twinning in submicron and micron pillars of twinning-induced plasticity steel, Scr. Mater 67 (2012) 641–644.
[212] Q. Yu, Z.-W. Shan, J. Li, X. Huang, L. Xiao, J. Sun, E. Ma, Strong crystal size effect on deformation twinning, Nature 463 (2010) 335–338.
[213] S. Allain, O. Bouaziz, J. Chateau, Thermally activated dislocation dynamics in austenitic FeMnC steels at low homologous temperature, Scr. Mater 62 (2010) 500–503.
[214] J.N. Wang, A new modification of the formulation of Peierls stress, Acta Mater 44 (1996) 1541–1546.
[215] J. Wang, Prediction of Peierls stresses for different crystals, Mater. Sci. Eng. A 206 (1996) 259–269.
[216] O. Majidi, B.C. De Cooman, F. Barlat, M.-G. Lee, Y.P. Korkolis, Thermo-mechanical response of a TWIP steel during monotonic and non-monotonic uniaxial loading, Mater. Sci. Eng. A 674 (2016) 276–285.
[217] G. Dini, A. Najafizadeh, R. Ueji, S. Monir-Vaghefi, Tensile deformation behavior of high manganese austenitic steel: the role of grain size, Mater, Des 31 (2010) 3395–3402.
[218] C. Scott, B. Remy, J.-L. Collet, A. Cael, C. Bao, F. Danoix, B. Malard, C. Curfs, Precipitation strengthening in high manganese austenitic TWIP steels, Int. J. Mater. Res. 102 (2011) 538–549.
[219] S.Lee, B.C.De Cooman, unpublished research results.
[220] Y. Shen, N. Jia, R. Misra, L. Zuo, Softening behavior by excessive twinning and adiabatic heating at high strain rate in a Fe-20Mn-0.6 C TWIP steel, Acta Mater 103 (2016) 229–242.
[221] H. Gwon, MS Thesis, Pohang University of Science and Technology, South Korea, 2017.
[222] J.-H. Kang, S. Duan, S.-J. Kim, W. Bleck, Grain boundary strengthening in high Mn austenitic steels, Metall. Mater. Trans. A 47 (2016) 1918–1921.
[223] J. Li, Y. Chou, The role of dislocations in the flow stress grain size relationships, Metall. Mater. Trans. 1 (1970) 1145.
[224] F. De Las Cuevas, M. Reis, A. Ferraiuolo, G. Pratolongo, L.P. Karjalainen, J. Alkorta, J. Gil Sevillano, Hall-Petch relationship of a TWIP steel, Key Eng. Mat. Trans. Tech. Publ. (2010) 147–152.
[225] S.-H. Wang, Z.-Y. Liu, G.-F. Wang, Influence of grain size on TWIP effect in a TWIP steel, Acta Mater. Sin. 45 (2009) 1083.
[226] T. Lee, M. Koyama, K. Tsuzaki, Y.-H. Lee, C.S. Lee, Tensile deformation behavior of Fe-Mn-C TWIP steel with ultrafine elongated grain structure, Mater. Lett. 75 (2012) 169–171.
[227] J. Chateau, A. Dumay, S. Allain, A. Jacques, Precipitation hardening of a FeMnC TWIP steel by vanadium carbides, J. Phys. Conf. Ser. IOP Publ. (2010) 012023.
[228] H.-W. Yen, M. Huang, C. Scott, J.-R. Yang, Interactions between deformation-induced defects and carbides in a vanadium-containing TWIP steel, Scr. Mater 66 (2012) 1018–1023.
[229] R.Z. Valiev, Y. Estrin, Z. Horita, T.G. Langdon, M.J. Zechetbauer, Y.T. Zhu, Producing bulk ultrafine-grained materials by severe plastic deformation, JOM 58 (2006) 33–39.
[230] Y. Estrin, A. Vinogradov, Extreme grain refinement by severe plastic deformation: a wealth of challenging science, Acta Mater 61 (2013) 782–817.
[231] R. Ueji, N. Tsuchida, H. Fujii, D. Kondo, K. Kunishige, Effect of grain size on tensile properties of TWIP steel, J. Jpn. I. Met. 71 (2007) 815–821.
[232] R. Ueji, N. Tsuchida, D. Terada, N. Tsuji, Y. Tanaka, A. Takemura, K. Kunishige, Tensile properties and twinning behavior of high manganese austenitic steel with fine-grained structure, Scr. Mater 59 (2008) 963–966.
[233] I. Gutierrez-Urrutia, S. Zaefferer, D. Raabe, The effect of grain size and grain orientation on deformation twinning in a Fe-22 wt.% Mn-0.6 wt.% C TWIP steel, Mater. Sci. Eng. A 66 (2010) 3552–3560.
[234] I. Timokhina, A. Medvedev, R. Lapovok, Severe plastic deformation of a TWIP steel, Mater. Sci. Eng. A 593 (2014) 163–169.
[235] G. Fontaine, Doctoral Thesis, Orsay, France, 1968.
[236] J.W. Christian, S. Mahajan, Deformation twinning, Prog. Mater. Sci. 39 (1995) 1–157.
[237] M. Niewczas, Dislocations and twinning in face centred cubic crystals, Disloc. Solids 13 (2007) 263–364.
[238] X. Liao, S. Srinivasan, Y. Zhao, M. Baskes, Y. Zhu, F. Zhou, E. Lavernia, H. Xu, Formation mechanism of wide stacking faults in nanocrystalline Al, Appl. Phys. Lett. 84 (2004) 3564–3566.
[239] J. Narayan, Y. Zhu, Self-thickening, Cross-slip deformation twinning model, Appl. Phys. Lett. 92 (2008) 151908.
[240] Y. Zhu, J. Narayan, J. Hirth, S. Mahajan, X. Wu, X. Liao, Formation of single and multiple deformation twins in nanocrystalline fcc metals, Acta Mater 57 (2009) 3763–3770.
[241] R.J. McCabe, I.J. Beyerlein, J.S. Carpenter, N.A. Mara, The critical role of grain orientation and applied stress in nanoscale twinning, Nat, Commun 5 (2014).
[242] J. Cohen, J. Weertman, A dislocation model for twinning in fcc metals, Acta Metall. 11 (1963) 996–998.
[243] H. Fujita, T. Mori, A formation mechanism of mechanical twins in FCC Metals, Scr. Mater 9 (1975) 631–636.
[244] S. Mahajan, G. Chin, Comments on deformation twinning in silver-and copper-alloy crystals, Scr. Metall. 9 (1975) 815–817.
[245] S. Miura, J.-I. Takamura, N. Narita, Orientation dependence of flow stress for twinning in silver crystals, Trans. Jpn. Inst. Met. 9 (1968) 555–561.
[246] S. Copley, B. Kear, The dependence of the width of a dissociated dislocation on dislocation velocity, Acta Metall. 16 (1968) 227–231.
[247] J. Hirth, On the pole mechanism in FCC metals, Deform. Twinning 25 (1964) 112–115.
[248] J. Venables, On dislocation pole models for twinning, Philos. Mag. 30 (1974) 1165–1169.
[249] J. Venables, The nucleation and propagation of deformation twins, J. Phys. Chem. Solids 25 (1964) 693–700.
[250] M. Niewczas, G. Saada, Twinning nucleation in Cu-8 at.% Al single crystals, Philos. Mag. A 82 (2002) 167–191.
[251] J. Liu, X. Liu, W. Liu, Y. Zeng, K. Shu, Transmission electron microscopy observation of a deformation twin in TWIP steel by an ex situ tensile test, Philos. Mag. 91 (2011) 4033–4044.
[252] I. Karaman, H. Sehitoglu, K. Gall, Y.I. Chumlyakov, H. Maier, Deformation of single crystal Hadfield steel by twinning and slip, Acta Mater 48 (2000) 1345–1359.
[253] S. Martin, C. Ullrich, D. Šimek, U. Martin, D. Rafaja, Stacking fault model of ϵ-martensite and its DIFFaX implementation, J. Appl. Crystallogr. 44 (2011) 779–787.
[254] I. Beyerlein, C. Tomé, A probabilistic twin nucleation model for HCP polycrystalline metals, Proc. R. Soc. A 466 (2010) 2517–2544.
[255] A. Vinogradov, E. Vasilev, D. Merson, Y. Estrin, A phenomenological model of twinning kinetics, Adv. Eng. Mater 19 (2017) 1–10.
[256] N. Narita, J. Takamura, Deformation twinning in silver-and copper-alloy crystals, Philos. Mag. 29 (1974) 1001–1028.
[257] H. Suzuki, C. Barrett, Deformation twinning in silver-gold alloys, Acta Metall. 6 (1958) 156–165.
[258] M. Meyers, O. Vöhringer, V. Lubarda, The onset of twinning in metals: a constitutive description, Acta Mater 49 (2001) 4025–4039.
[259] K. Phiu-on, W. Bleck, Deformation Mechanisms and Mechanical Properties of Hot Rolled Fe-mn-c-(Al)-(Si) Austenitic Steels, Lehrstuhl und Institut für Eisenhüttenkunde, 2008.
[260] A.A. Mohammed, E.A. El-Danaf, A.-K.A. Radwan, Equivalent twinning criteria for FCC alloys under uniaxial tension at high temperatures, Mater. Sci. Eng. A 457 (2007) 373–379.
[261] S.A. Kibey, L.-L. Wang, J. Liu, H. Johnson, H. Sehitoglu, D.D. Johnson, Quantitative prediction of twinning stress in fcc alloys: application to Cu-Al, Phys. Rev. B 79 (2009) 214202.
[262] G. Dini, R. Ueji, A. Najafizadeh, S. Monir-Vaghefi, Flow stress analysis of TWIP steel via the XRD measurement of dislocation density, Mater. Sci. Eng. A 527 (2010) 2759–2763.
[263] K. Rahman, N. Jones, D. Dye, Micromechanics of twinning in a TWIP steel, Mater. Sci. Eng. A 635 (2015) 133–142.
[264] I. Karaman, H. Sehitoglu, A. Beaudoin, Y.I. Chumlyakov, H. Maier, C. Tome,

Please cite this article in press as: B.C. De Cooman, et al., Twinning-induced plasticity (TWIP) steels, Acta Materialia (2017), http://dx.doi.org/10.1016/j.actamat.2017.06.046

Modeling the deformation behavior of Hadfield steel single and polycrystals due to twinning and slip, Acta Mater 48 (2000) 2031–2047.
[265] D. Barbier, Doctoral Thesis, Université Paul Verlaine de Metz, France.
[266] J. Kim, Doctoral Thesis, Pohang University of Science and Technology, South Korea.
[267] A. Soulami, K.S. Choi, Y. Shen, W.N. Liu, X. Sun, M.A. Khaleel, On deformation twinning in a 17.5% Mn-TWIP steel: a physically based phenomenological model, Mater. Sci. Eng. A 528 (2011) 1402–1408.
[268] C. Haase, L.A. Barrales-Mora, F. Roters, D.A. Molodov, G. Gottstein, Applying the texture analysis for optimizing thermomechanical treatment of high manganese twinning-induced plasticity steel, Acta Mater 80 (2014) 327–340.
[269] J.C. Fisher, E.W. Hart, R.H. Pry, Phys. Rev. 79 (1950) 722.
[270] V. Shterner, A. Molotnikov, I. Timokhina, Y. Estrin, H. Beladi, A constitutive model of the deformation behaviour of twinning induced plasticity (TWIP) steel at different temperatures, Mater. Sci. Eng. A 613 (2014) 224–231.
[271] G. Piercy, R. Cahn, A. Cottrell, A study of primary and conjugate slip in crystals of alpha-brass, Acta Metall. 3 (1955) 331–338.
[272] T. Leffers, Deformation rate dependence of rolling texture in brass containing 5% zinc, Scr. Metall. 2 (1968) 447–452.
[273] T. Leffers, R. Ray, The brass-type texture and its deviation from the copper-type texture, Prog. Mater. Sci. 54 (2009) 351–396.
[274] S. Sato, E.-P. Kwon, M. Imafuku, K. Wagatsuma, S. Suzuki, Microstructural characterization of high-manganese austenitic steels with different stacking fault energies, Mater. Charact. 62 (2011) 781–788.
[275] I. Gutierrez-Urrutia, D. Raabe, Study of deformation twinning and planar slip in a TWIP steel by electron channeling contrast imaging in a SEM, Mater. Sci. Forum (2012) 523–529.
[276] D. Geissler, J. Freudenberger, A. Kauffmann, M. Krautz, H. Klauss, A. Voss, J. Eickemeyer, L. Schultz, Appearance of dislocation-mediated and twinning-induced plasticity in an engineering-grade FeMnNiCr alloy, Acta Mater. 59 (2011) 7711–7723.
[277] E.I. Kuprekova, Y.I. Chumlyakov, I.P. Chernov, Dependence of critical cleavage stresses as a function of orientation and temperature in single crystals of Fe-18% Cr-14% Ni-2% Mo austenitic stainless steel containing hydrogen, Met. Sci. Heat. Treat. 50 (2008) 282–288.
[278] P. Yang, Q. Xie, L. Meng, H. Ding, Z. Tang, Dependence of deformation twinning on grain orientation in a high manganese steel, Scr. Mater 55 (2006) 629–631.
[279] A. Prakash, T. Hochrainer, E. Reisacher, H. Riedel, Twinning models in self-consistent texture simulations of TWIP steels, Steel Res. Int. 79 (2008) 645–652.
[280] B.C. De Cooman, J. Kim, S. Lee, Heterogeneous deformation in twinning-induced plasticity steel, Scr. Mater 66 (2012) 986–991.
[281] J. Hirsch, K. Lücke, Overview no. 76: mechanism of deformation and development of rolling textures in polycrystalline fcc metals—I. Description of rolling texture development in homogeneous CuZn alloys, Acta Metall. 36 (1988) 2863–2882.
[282] J. Hirsch, K. Lücke, M. Hatherly, Overview No. 76: mechanism of deformation and development of rolling textures in polycrystalline f.c.c. Metals—III. The influence of slip inhomogeneities and twinning, Acta Metall. 36 (1988) 2905–2927.
[283] R. Smallman, D. Green, The dependence of rolling texture on stacking fault energy, Acta Metall. 12 (1964) 145–154.
[284] I. Dillamore, The stacking fault energy dependence of the mechanisms of deformation in fcc metals, Metall. Trans. 1 (1970) 2463–2470.
[285] K. Morii, H. Mecking, Y. Nakayama, Development of shear bands in fcc single crystals, Acta Metall. 33 (1985) 379–386.
[286] C. Donadille, R. Valle, P. Dervin, R. Penelle, Development of texture and microstructure during cold-rolling and annealing of FCC alloys: example of an austenitic stainless steel, Acta Metall. 37 (1989) 1547–1571.
[287] F. Roters, P. Eisenlohr, L. Hantcherli, D.D. Tjahjanto, T.R. Bieler, D. Raabe, Overview of constitutive laws, kinematics, homogenization and multiscale methods in crystal plasticity finite-element modeling: theory, experiments, applications, Acta Mater 58 (2010) 1152–1211.
[288] D. Barbier, V. Favier, B. Bolle, Modeling the deformation textures and microstructural evolutions of a Fe-Mn-C TWIP steel during tensile and shear testing, Mater. Sci. Eng. A 540 (2012) 212–225.
[289] T. Leffers, Computer simulation of the plastic deformation in face-centred cubic polycrystals and the rolling texture derived, Phys. Status Solidi B 25 (1968) 337–344.
[290] I. Dillamore, H. Katoh, A comparison of the observed and predicted deformation textures in cubic metals, Met. Sci. 8 (1974) 21–27.
[291] Y. Lü, D.A. Molodov, G. Gottstein, Recrystallization kinetics and microstructure evolution during annealing of a cold-rolled Fe-Mn-C alloy, Acta Mater 59 (2011) 3229–3243.
[292] Y. Lü, B. Hutchinson, D.A. Molodov, G. Gottstein, Effect of deformation and annealing on the formation and reversion of ε-martensite in an Fe-Mn-C alloy, Acta Mater 58 (2010) 3079–3090.
[293] R. Ray, J.J. Jonas, R. Hook, Cold rolling and annealing textures in low carbon and extra low carbon steels, Int. Mater. Rev. 39 (1994) 129–172.
[294] L. Bracke, K. Verbeken, L. Kestens, J. Penning, Microstructure and texture evolution during cold rolling and annealing of a high Mn TWIP steel, Acta Mater 57 (2009) 1512–1524.
[295] L. Bracke, K. Verbeken, L.A. Kestens, Texture generation and implications in TWIP steels, Scr. Mater 66 (2012) 1007–1011.
[296] L. Barrales-Mora, Y. Lü, D. Molodov, Experimental determination and simulation of annealing textures in cold rolled TWIP and TRIP steels, Steel Res. Int. 82 (2011) 119–126.
[297] Y. Estrin, L. Kubin, Spatial Coupling and Propagative Plastic Instabilities, Continuum Models for Materials with Microstructure, 1995, pp. 395–450.
[298] M. Dao, L. Lu, Y. Shen, S. Suresh, Strength, strain-rate sensitivity and ductility of copper with nanoscale twins, Acta Mater 54 (2006) 5421–5432.
[299] L. Chen, J.K. Kim, S.K. Kim, G.S. Kim, K.G. Chin, B. De Cooman, Stretch-flangeability of high Mn TWIP steel, Steel Res. Int. 81 (2010) 552–568.
[300] L. Xu, L. Chen, B. De Cooman, D. Steglich, F. Barlat, Hole expansion of advanced high strenth steel sheet sample, Inter. J. Mater. Form. 3 (2010) 247–250.
[301] J.-K. Kim, L. Chen, H.-S. Kim, S.-K. Kim, Y. Estrin, B. De Cooman, On the tensile behavior of high-manganese twinning-induced plasticity steel, Metall. Mater. Trans. A 40 (2009) 3147–3158.
[302] L. Qian, P. Guo, J. Meng, F. Zhang, Unusual grain-size and strain-rate effects on the serrated flow in FeMnC twin-induced plasticity steels, J. Mater. Sci. 48 (2013) 1669–1674.
[303] A. Saeed-Akbari, A.K. Mishra, J. Mayer, W. Bleck, Metall. Mater. Trans. A 43 (2012) 1705–1723.
[304] A. Bäumer, W. Bleck, Proceeding of IDDRG 2007, M.Tisza Editor, 2007, 47.
[305] K. Renard, S. Ryelandt, P. Jacques, Characterisation of the Portevin-Le Châtelier effect affecting an austenitic TWIP steel based on digital image correlation, Mater. Sci. Eng. A 527 (2010) 2969–2977.
[306] L. Chen, H.-S. Kim, S.-K. Kim, B. De Cooman, Localized deformation due to Portevin-LeChatelier effect in 18Mn-0.6 C TWIP austenitic steel, ISIJ Int. 47 (2007) 1804–1812.
[307] H. Karabulut, S. Gündüz, Effect of vanadium content on dynamic strain aging in microalloyed medium carbon steel, Mater. Des. 25 (2004) 521–527.
[308] L. Kubin, Y. Estrin, The critical conditions for jerky flow. Discussion and application to CuMn solid solutions, Phys. Status Solidi B 172 (1992) 173–185.
[309] S.D. Andrews, H. Sehitoglu, I. Karaman, Constriction energy in the presence of a solute field, J. Appl. Phys. 87 (2000) 2194–2203.
[310] M. Koyama, T. Sawaguchi, K. Tsuzaki, Deformation twinning behavior of twinning-induced plasticity steels with different carbon Concentrations-Part 2: proposal of dynamic-strain-aging-assisted deformation twinning, ISIJ Int. 55 (2015) 1754–1761.
[311] A. Van den Beukel, Theory of the effect of dynamic strain aging on mechanical properties, Phys. Status Solidi A 30 (1975) 197–206.
[312] S. Allain, O. Bouaziz, T. Lebedkina, M. Lebyodkin, Relationship between relaxation mechanisms and strain aging in an austenitic FeMnC steel, Scr. Mater 64 (2011) 741–744.
[313] N. Tsuji, Y. Ito, Y. Saito, Y. Minamino, Strength and ductility of ultrafine grained aluminum and iron produced by ARB and annealing, Scr. Mater 47 (2002) 893–899.
[314] S. Kang, Y.-S. Jung, J.-H. Jun, Y.-K. Lee, Effects of recrystallization annealing temperature on carbide precipitation, microstructure, and mechanical properties in Fe-18Mn-0.6 C-1.5 Al TWIP steel, Mater. Sci. Eng. A 527 (2010) 745–751.
[315] G. Dini, A. Najafizadeh, R. Ueji, S. Monir-Vaghefi, Improved tensile properties of partially recrystallized submicron grained TWIP steel, Mater. Lett. 64 (2010) 15–18.
[316] O. Bouaziz, C. Scott, G. Petitgand, Nanostructured steel with high work-hardening by the exploitation of the thermal stability of mechanically induced twins, Scr. Mater 60 (2009) 714–716.
[317] C. Haase, L.A. Barrales-Mora, D.A. Molodov, G. Gottstein, Tailoring the mechanical properties of a twinning-induced plasticity steel by retention of deformation twins during heat treatment, Metall. Mater. Trans. A 44 (2013) 4445–4449.
[318] C. Haase, L.A. Barrales-Mora, D.A. Molodov, G. Gottstein, Application of texture analysis for optimizing thermo-mechanical treatment of a high Mn TWIP steel, Adv. Mat. Res. (2014) 213–218.
[319] C. Haase, T. Ingendahl, O. Güvenç, M. Bambach, W. Bleck, D.A. Molodov, L.A. Barrales-Mora, On the applicability of recovery-annealed twinning-induced plasticity steels: potential and limitations, Mater. Sci. Eng. A 649 (2016) 74–84.
[320] T. Niendorf, C. Lotze, D. Canadinc, A. Frehn, H. Maier, The role of monotonic pre-deformation on the fatigue performance of a high-manganese austenitic TWIP steel, Mater. Sci. Eng. A 499 (2009) 518–524.
[321] A. Hamada, L. Karjalainen, A. Ferraiuolo, J.G. Sevillano, F. De Las Cuevas, G. Pratolongo, M. Reis, Fatigue behavior of four high-Mn twinning induced plasticity effect steels, Metall. Mater. Trans. A 41 (2010) 1102–1108.
[322] Y. Estrin, A. Vinogradov, Fatigue behaviour of light alloys with ultrafine grain structure produced by severe plastic deformation: an overview, Int. J. Fatigue 32 (2010) 898–907.
[323] A.S. Hamada, L.P. Karjalainen, J. Puustinen, Fatigue behavior of high-Mn TWIP steels, Mater. Sci. Eng. A 517 (2009) 68–77.
[324] L.P. Karjalainen, A. Hamada, R.D.K. Misra, D.A. Porter, Some aspects of the cyclic behavior of twinning-induced plasticity steels, Scr. Mater 66 (2012) 1034–1039.
[325] T. Niendorf, F. Rubitschek, H. Maier, J. Niendorf, H. Richard, A. Frehn, Fatigue crack growth-Microstructure relationships in a high-manganese austenitic TWIP steel, Mater. Sci. Eng. A 527 (2010) 2412–2417.

Please cite this article in press as: B.C. De Cooman, et al., Twinning-induced plasticity (TWIP) steels, Acta Materialia (2017), http://dx.doi.org/10.1016/j.actamat.2017.06.046

[326] Y.W. Kim, G. Kim, S.-G. Hong, C.S. Lee, Energy-based approach to predict the fatigue life behavior of pre-strained Fe-18Mn TWIP steel, Mater. Sci. Eng. A 528 (2011) 4696–4702.
[327] A. Hamada, A. Järvenpää, M. Honkanen, M. Jaskari, D. Porter, L. Karjalainen, Effects of cyclic pre-straining on mechanical properties of an austenitic microalloyed high-Mn twinning-induced plasticity steel, Procedia Eng. 74 (2014) 47–52.
[328] Y. Ha, H. Kim, K.H. Kwon, S.-G. Lee, S. Lee, N.J. Kim, Microstructural evolution in Fe-22Mn-0.4 C twinning-induced plasticity steel during high strain rate deformation, Metall. Mater. Trans. A 46 (2015) 545–548.
[329] A. Hamada, L. Karjalainen, M. Somani, The influence of aluminum on hot deformation behavior and tensile properties of high-Mn TWIP steels, Mater. Sci. Eng. A 467 (2007) 114–124.
[330] Y. Tomota, M. Strum, J. Morris, The relationship between toughness and microstructure in Fe-high Mn binary alloys, Metall. Trans. A 18 (1991) 1073–1081.
[331] G. Gigacher, W. Krieger, P.R. Scheller, C. Thomser, Non-metallic inclusions in high-manganese-alloy steels, Steel Res. Int. 76 (2005) 644–649.
[332] M. Whiteman, A. Troiano, The influence of hydrogen on the stacking fault energy of an austenitic stainless steel, Phys. Status Solidi B 7 (1964).
[333] A.E. Pontini, J.D. Hermida, X-ray diffraction measurement of the stacking fault energy reduction induced by hydrogen in an AISI 304 steel, Scr. Mater 37 (1997) 1831–1837.
[334] P. Rozenak, D. Eliezer, Phase changes related to hydrogen-induced cracking in austenitic stainless steel, Acta Metall. 35 (1987) 2329–2340.
[335] N. Narita, C. Altstetter, H. Birnbaum, Hydrogen-related phase transformations in austenitic stainless steels, Metall. Mater. Trans. A 13 (1982) 1355–1365.
[336] J. Rigsbee, R. Benson, A TEM investigation of hydrogen-induced deformation twinning and associated martensitic phases in 304-type stainless steel, J. Mater. Sci. 12 (1977) 406–409.
[337] E. Astafurova, G. Zakharova, H. Maier, Hydrogen-induced twinning in< 001> Hadfield steel single crystals, Scr. Mater 63 (2010) 1189–1192.
[338] B.J. Lee, J.W. Jang, A modified embedded-atom method interatomic potential for the Fe-H system, Acta Mater 55 (2007) 6779–6788.
[339] J. Jung, O. Lee, Y. Park, D. Kim, K. Jin, S. Kim, K. Song, Microstructure and mechanical properties of high Mn TWIP steels, Korean J. Met. Mater 46 (2008) 627–633.
[340] K.H. So, J.S. Kim, Y.S. Chun, K.-T. Park, Y.-K. Lee, C.S. Lee, Hydrogen delayed fracture properties and internal hydrogen behavior of a Fe-18Mn-1.5 Al-0.6 C TWIP steel, ISIJ Int. 49 (2009) 1952–1959.
[341] Y.S. Chun, J.S. Kim, K.T. Park, Y.K. Lee, C.S. Lee, Role of ε martensite in tensile properties and hydrogen degradation of high-Mn steels, Mater. Sci. Eng. A 533 (2012) 87–95.
[342] Y.S. Chun, J. Lee, C.M. Bae, K.-T. Park, C.S. Lee, Caliber-rolled TWIP steel for high-strength wire rods with enhanced hydrogen-delayed fracture resistance, Scr. Mater 67 (2012) 681–684.
[343] Y.S. Chun, K.-T. Park, C.S. Lee, Delayed static failure of twinning-induced plasticity steels, Scr. Mater 66 (2012) 960–965.
[344] I.-J. Park, K.-H. Jeong, J.-G. Jung, C.S. Lee, Y.-K. Lee, The mechanism of enhanced resistance to the hydrogen delayed fracture in Al-added Fe-18Mn-0.6 C twinning-induced plasticity steels, Int. J. Hydrogen Energy 37 (2012) 9925–9932.
[345] Y.J. Kwon, T. Lee, J. Lee, Y.S. Chun, C.S. Lee, Role of Cu on hydrogen embrittlement behavior in Fe-Mn-C-Cu TWIP steel, Int. J. Hydrogen Energy 40 (2015) 7409–7419.
[346] S.-M. Lee, I.-J. Park, J.-G. Jung, Y.-K. Lee, The effect of Si on hydrogen embrittlement of Fe-18Mn-0.6 C-xSi twinning-induced plasticity steels, Acta Mater 103 (2016) 264–272.
[347] J.H. Ryu, S.K. Kim, C.S. Lee, D.W. Suh, H.K.D.H. Bhadeshia, Effect of aluminium on hydrogen-induced fracture behaviour in austenitic Fe-Mn-C steel, Proc. R. Soc. A 469 (2015) 20120458.
[348] J. Ronevich, S. Kim, J. Speer, D. Matlock, Hydrogen effects on cathodically charged twinning-induced plasticity steel, Scr. Mater 66 (2012) 956–959.
[349] L. Chen, S.-J. Lee, B.C. De Cooman, Mechanical properties of H-charged Fe-18Mn-1.5 Al-0.6 C TWIP steel, ISIJ Int. 52 (2012) 1670–1677.
[350] M. Koyama, E. Akiyama, K. Tsuzaki, Effect of hydrogen content on the embrittlement in a Fe-Mn-C twinning-induced plasticity steel, Corros. Sci. 59 (2012) 277–281.
[351] M. Koyama, E. Akiyama, T. Sawaguchi, D. Raabe, K. Tsuzaki, Hydrogen-induced cracking at grain and twin boundaries in an Fe-Mn-C austenitic steel, Scr. Mater 66 (2012) 459–462.
[352] M. Koyama, E. Akiyama, K. Tsuzaki, Hydrogen-induced delayed fracture of a Fe-22Mn-0.6C steel pre-strained at different strain rates, Scr. Mater 66 (2012) 947–950.
[353] M. Koyama, E. Akiyama, K. Tsuzaki, D. Raabe, Hydrogen-assisted failure in a twinning-induced plasticity steel studied under in situ hydrogen charging by electron channeling contrast imaging, Acta Mater 61 (2013) 4607–4618.
[354] R. Van Tol, L. Zhao, H. Schut, J. Sietsma, Experimental investigation of structural defects in deep-drawn austenitic Mn-based TWIP steel, Mater. Sci. Tech. 28 (2012) 348–353.
[355] C. Beal, X. Kleber, D. Fabregue, M. Bouzekri, Embrittlement of a zinc coated high manganese TWIP steel, Mater. Sci. Eng. A 543 (2012) 76–83.
[356] D. Fabrege, C. Béal, X. Kleber, M. Bouzekri, Proc. 1st Int. Conf. on High Mn Steels, Seoul, 2011, B-44.
[357] C. Béal, Mechanical Behaviour of a New Automotive High Manganese TWIP Steel in the Presence of Liquid Zinc, INSA, Lyon, 2011.
[358] H. Kang, L. Cho, C. Lee, B.C. De Cooman, Zn penetration in liquid metal embrittled TWIP steel, Metall. Mater. Trans. A 47 (2016) 2885–2905.
[359] M. Krishtal, the formation of dislocations in metals on diffusion of surface-active substances in connection with the effect of adsorption embrittlement, Sov. Phys. Dokl. (1970) 614.
[360] P. Gordon, H.H. An, The mechanisms of crack initiation and crack propagation in metal-induced embrittlement of metals, Metall. Trans. A 13 (1982) 457–472.
[361] N. Stoloff, T. Johnston, Crack propagation in a liquid metal environment, Acta Metall. 11 (1963) 251–256.
[362] A. Westwood, M. Kamdar, Concerning liquid metal embrittlement, particularly of zinc monocrystals by mercury, Philos. Mag. 8 (1963) 787–804.
[363] C. Scott, S. Allain, M. Faral, N. Guelton, The development of a new Fe-Mn-C austenitic steel for automotive applications, Rev. Metall. 103 (2006) 293–302.
[364] W. Bleck, K. Phiu-on, C. Heering, G. Hirt, Hot workability of as-cast high manganese-high carbon steels, Steel Res. Int 78 (2007) 536–545.
[365] P. Lan, J. Zhang, Thermophysical properties and solidification defects of Fe-22Mn-0.7C TWIP Steel, Steel Res. Int. 87 (2016) 250–261.
[366] K.H. Spitzer, F. Rüppel, R. Viščorová, R. Scholz, J. Kroos, V. Flaxa, Direct strip casting (DSC)-an option for the production of new steel grades, Steel Res. Int. 74 (2003) 724–731.
[367] H. Hoffmann, B. Engl, M. Menne, T. Heller, W. Zimmermann, Highly stable, strips or steel sheets cold-formed, method for the production of steel strips and uses of said steel, US Patent US 20030145911 A1 (2003).
[368] T.W. Kim, Y.G. Kim, S.H. Park, Process for manufacturing high manganese hot rolled steel sheet without any crack, US Patent US 5647922 A (1997).

Please cite this article in press as: B.C. De Cooman, et al., Twinning-induced plasticity (TWIP) steels, Acta Materialia (2017), http://dx.doi.org/10.1016/j.actamat.2017.06.046